Proc. Symp. Ultrason. Electron., Vol. 26, (2005) pp. 193-194
16-18 November, 2005

Low-loss and Constant-Group-Delay SAW Filters Employing Cu-Based R-SPUDTs

H.L Li, J.G. Wen, K. Hashimoto, T. Omori, and M. Yamaguchi (Chiba University)

1. Introduction

Recently, much of an effort has been made to develop low loss surface acoustic wave (SAW) filters with constant group delay[1,2,3].

The transversal-type filters designed by the apodization of an interdigital transducer (IDT) offer superior group delay provided that relatively large insertion loss is accepted. It is known that a single-phase unidirectional transducers (SPUDTs) is an effective countermeasure for reducing the insertion loss. However, the group delay deteriorates with a decrease in the insertion loss [3].

The authors recently proposed[4] that low-loss and constant-group-delay filters can be developed by using a resonant SPUDT (R-SPUDT)[5], and showed how the technique is effective by an experiment using Al-electrode/128^{o}YX-LiNbO$_3$ -substrate structure. However, because of a small reflectivity of an Al electrode, the variable range in ~~of~~ the reflectivity is limited unless an extraordinary large film thickness (>0.09λ) is employed. The limitation results in poor device performance.

The paper describes the use of Cu as an electrode material aiming at designing low-loss and constant-group-delay SAW filters of excellent performance.

Theoretical analysis shows that a reflectivity of a Cu electrode is about two times larger than that of an Al electrode of the same thickness. Because of this, Cu is effective in widening the variable range in the reflectivity. In addition, the electric conductivity of Cu is about two times larger than that of Al, it is also beneficial for reducing an ohmic loss.

The constant-group-delay filter is designed and fabricated. Experimental results are in fairly good agreement with the design; the group delay deviation of 30 ns was realized over the range of ±6.5 MHz at the center frequency of 490 MHz. The minimum insertion loss and -3 dB bandwidth were 6.1 dB and 8.5 MHz, respectively.

2. Theoretical analysis

The input admittance of infinitely long EWC/SPUDTs (see Fig. 1) was calculated for Al and Cu electrodes on 128^{o}YX-LiNbO$_3$ substrate.

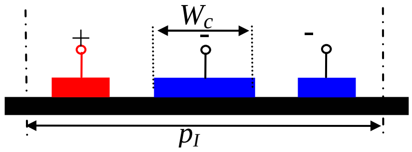

Fig.1 unit section of EWC/SPUDT

The software MSYNC[6] was used for the numerical calculation. Then, the normalized reflectivity ($|\kappa_{12}|p_I/\pi$) (p_I: periodicity) was estimated from the calculated admittance by using the technique described in [6] for a given metallization ratio W_c/p_I (W_c: center electrode width, see Fig. 1) and electrode thickness h/p_I. The width of the side electrodes is $0.125p_I$, and the center-to-center distance between the electrodes are $0.375p_I$.

Figs.2 (a) and (b) show the estimated reflectivity of the SPUDT for Al and Cu electrodes, respectively. It is seen that the variable range in the reflectivity of Cu electrodes is expanded to be about two times larger than that of Al electrodes for a given film thickness.

Next, it was investigated how filter performance~~s~~ is improved by the expanded variable range in $|\kappa_{12}|$ of Cu.

For the optimization, the electrode thickness was fixed at 3%λ, and the following specifications were used as constraints: insertion loss less than 2 dB, -3 dB fractional passband larger than 1.8%, group delay error less than 20 ns and IDT length less than 52 periods.

Results of the optimization are shown in Fig. 3(a). It is seen that the insertion loss for Cu (dashed line) is about 2 dB smaller than that for Al (dotted line). The difference is mainly due to the power leakage to the backward direction of the SPUDTs. Fig. 3(b) shows the group delay for Cu (dashed line). It is almost constant in transition bands as well as in a passband. The group delay deviation is about 20 ns and does not seem to be badly affected by the increased $|\kappa_{12}|$.

The designed device was fabricated on a 128^{o}YX-LiNbO$_3$ substrate. Experimental results are also shown in Fig. 3(a) and (b) by solid lines, where the minimum insertion loss at the centre frequency of 490 MHz and -3 dB bandwidth were 6.1 dB and

8.5 MHz, respectively. The group delay deviation of 30 ns was realised over the range of ±6.5MHz.

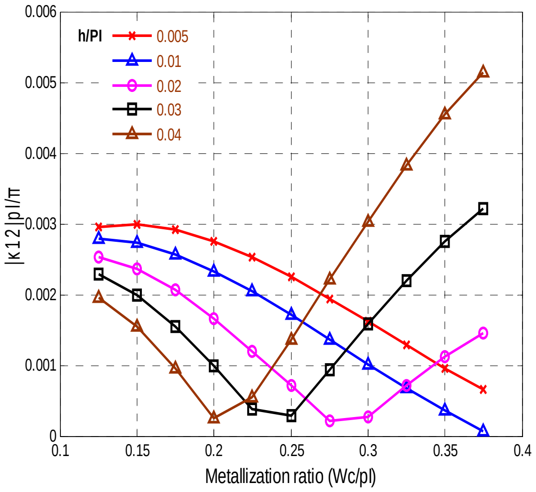

(a) Al electrodes

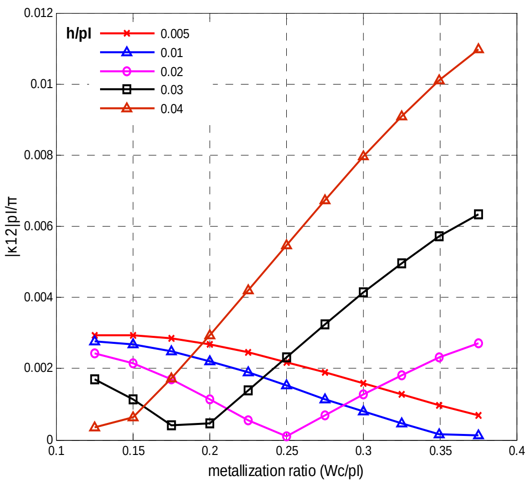

(b) Cu electrodes

Fig. 2 Reflectivity per period of Cu and Al electrodes on 128°LN substrate

3. Conclusion

This paper described the application of Cu to the development of low-loss SAW filters with constant group delay in transition bands as well as in a passband. Theoretical analysis suggested that Cu electrodes could offer the expanded variable range in the reflectivity, which is two times larger than Al electrodes of the same film thickness.

A low-loss SAW filter with constant group delay was designed and fabricated. Experimental results were fairly agreeable with the design, and small group delay deviation of 30 ns was realised over the range of ±6.5MHz at the center frequency of 490MHz.

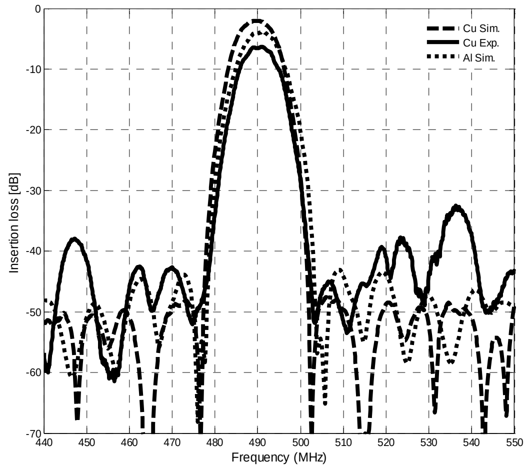

(a)Amplitude response

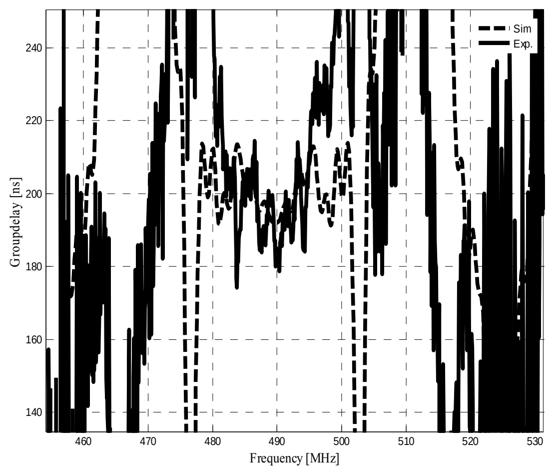

(b) Group delay response

Fig. 3 The theoretical and experimental frequency response of RSPUDT filter

Acknowledgement

This work was partially supported by the Grant-in-Aids for Fundamental Scientific Research from the Ministry of Education, Sports, Science and Culture.

References

1. G.Martin, F.Z.Bi, D.P.Chen, and C.S.Lam:Proc. IEEE Ultrason. Symp., (1998) p.165
2. Hiromi Yatsuda:IEEE Trans. Ultrason., Feroelec., Freq. Contr., **45**, No.1(1998) p.41.
3. C.S.Hartmann and B.P.Abbott: Proc. IEEE Ultrason. Symp., (1989) p.79
4. H.L Li, J.G. Wen, K. Hashimoto, T. Omori, and M. Yamaguchi: Proc. IEEE Ultrason. Symp., (2005) [to be published]
5. P. Ventura, M. Solal, P. Dufilie, J. M. Hode and F. Roux: Proc. IEEE Ultrason. Symp., (1994) p.1
6. K.Hashimoto. J.Koskela and M.Salomaa: Proc. IEEE Ultrason. Symp., (1999) p.93

E-2
Proc. Symp. Ultrason. Electron., Vol. 26, (2005) pp. 195-196
16-18 November, 2005

Ultrasonic Linear Actuator Using Elastic Hinge Structure

Masahiro Takano, Akichika Nakashima*, Mitsuhiko Taka* and Takaaki Ishii***
(**Industrial Research Institute of Ishikawa, **University of Yamanashi*)

1. Introduction

In recent years, downsizing is the trend in the field of electronic and machine industries and high resolution of nanometer level is required for measurement and manufacturing. To realize such demand, precise actuator is strongly required. In addition to high resolution, some special conditions such as non-magnetic interference, use in vacuum, have to be considered. For that purpose, ultrasonic actuator is one of the candidates[1-3]. Especially, ultrasonic linear actuators are in strong demand.

The objective of this research is to realize the ultrasonic linear stage using ultrasonic linear actuator with high resolution and high thrust. The effective method to obtain ultrasonic elliptical motion was intensively investigated. Then the proposed actuator was manufactured and was applied to the linear stage. Its characteristics were measured and discussed.

2. Design of the ultrasonic actuator.

2.1 Driving principle of the ultrasonic actuator.

Driving principle of the ultrasonic linear actuator is shown in figure 1. Elliptical motion of the tip attached to the slider intermittently drives it. The rotation direction determines the moving direction of the slider.

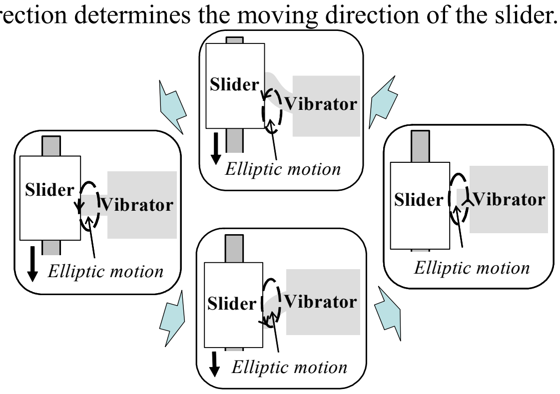

Fig. 1 Driving principle of the ultrasonic linear actuator.

2.2 Elastic hinge structure.

Two standing waves with 90 degrees phase shift have to be excited to obtain a traveling wave. In general, piezoelectric actuators are used to excite the vibration and they were rigidly fixed to the vibrator by glue or bolt. However, the structure of the actuator sometimes becomes complicated because some pieces of piezoelectric element are used and vibration mode analysis also becomes complicated because of its sophisticated structure and coupling vibrations. Therefore, elastic hinge structure was proposed for actuator design to isolate each vibration mode. Elastic hinge has low stiffness, hence coupling vibration will be isolated. Almost pure longitudinal vibration mode will be excited in the Langevin transducers. Effective excitation and energy transmission will be expected.

takano@irii.go.jp, ishii@ms.yamanashi.ac.jp

2.3 Effect of the elastic hinge structure.

ANSYS 8.1 was used for finite element method (FEM) analysis. Langevin transducers were used for excitation. The analysis model is shown in figure 2. Resonance frequency was 63 kHz and vibration modes with elastic hinge and without elastic hinge are summarized in figures 3 and 4. In figure 3, coupling vibration was excited. On the other hand in figure 4, almost independent vibration modes were obtained with elastic hinge structure. The piezoelectric response was simulated by FEM under the condition that both transducers were excited with 90 degrees phase shift. It is shown in figure 5. The displacement at the end of PZT as a function of driving frequency was estimated. The larger displacement can be obtained with hinge structure. The elliptical motion was formed in both conditions with elastic hinge and without elastic hinge. Figure 6 shows the example of the elliptic locus.

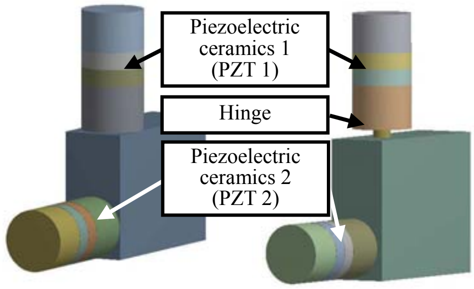

(a) Without elastic hinge (b) With elastic hinge
Fig. 2 Basic configuration of the ultrasonic actuators.

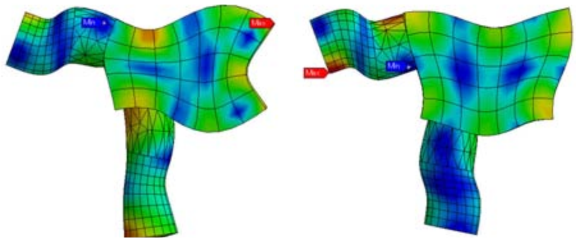

(a) Longitudinal mode α (b) Longitudinal mode β
Fig. 3 Natural modes of the actuators without elastic hinge.

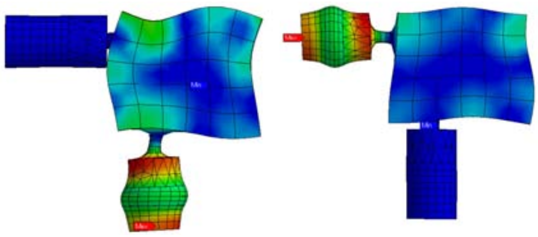

(a) Longitudinal mode α (b) Longitudinal mode β
Fig. 4 Natural modes of the actuators with elastic hinge.

2.4 Manufacturing of the ultrasonic actuator.

Figure 7 shows the proposed ultrasonic linear actuator using four Langevin transducers. As discussed above, the elastic hinge is made between vibration coupler and Langevin transducer. Four Langevin transducers were bolted symmetrically on the coupler. The shape of the coupler was designed by the FEM to match the resonance frequencies of two longitudinal vibration modes. The phase difference of the applied voltage among four transducers were described in figure 7.

Figure 8 is the picture of the actuator installed in the stage system. The cross roller guide type precision stage is used as slider. The contact surface on the slider side was hard anodized 30μm in thickness for anti-ware property. The actuator was held at the nodal point of the coupler with spring, and pressed onto the contact surfaces with 30 N normal force. Driving frequency was 62.7 kHz. Stage displacement was measured by the capacitance type displacement meter. The applied voltage was 60 V and driven by burst mode containing 50 cycles. As shown in figure 9, about 4 nm-resolution was obtained. Figure 10 shows the relationship between stage displacement and applied voltage. Although we can see insensitive range below 60 V, almost linear relation was obtained.

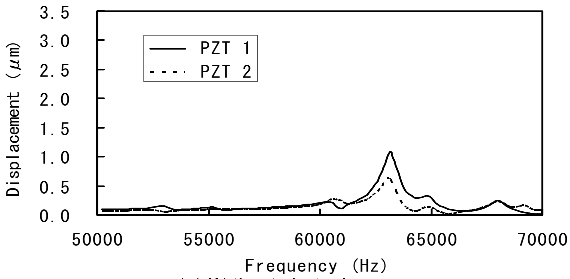

(a) Without elastic hinge.

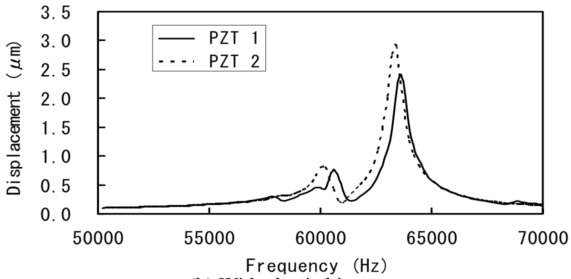

(b) With elastic hinge.

Fig. 5 Displacement at the end of PZT as functions of driving frequencies.

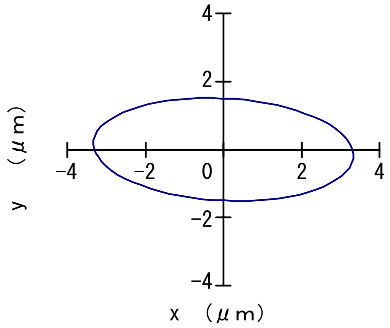

Fig. 6 Lissajous figure at the edge of the vibrator (With elastic hinge).

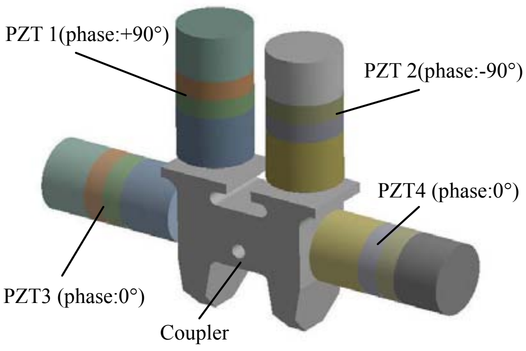

Fig. 7 Structure of the ultrasonic actuator.

3. Conclusions

High resolution linear stage was realized using precision ultrasonic linear actuator. The elastic hinge structure between piezoelectric element and vibration coupler was proposed. This structure was simulated by the FEM. Its effective roles to isolate each vibration mode and to obtain larger displacement have been confirmed. The actuator was manufactured and installed in the stage system. As a result, the maximum velocity of 100 mm/s and resolution of less than 10 nm were obtained.

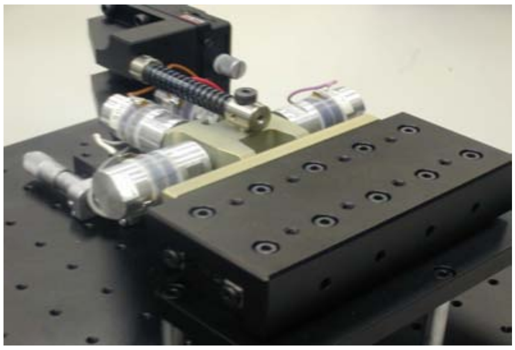

Fig. 8 Ultrasonic linear stage.

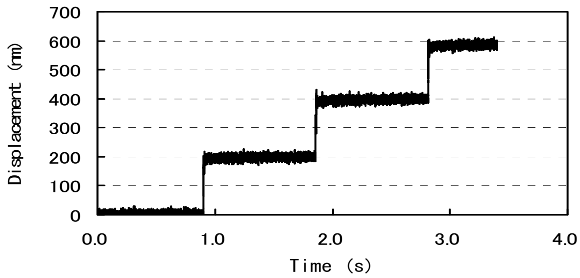

Fig. 9 Stage displacement.
(Input voltage : 60 [V_{p-p}], cycles : 50)

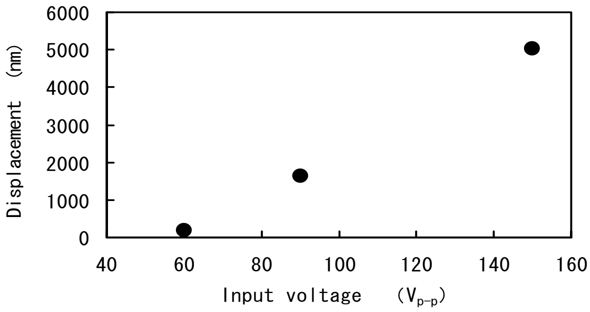

Fig. 10 Stage displacement as a function of input voltage.
(Cycles : 50)

References

1) T. Funakubo, T. Tsubata, Y. Taniguchi, K. Kumei, T. Fujiwara and C. Abe : Ultrasonic Linear Motor Using Multilayer Piezoelectric Actuators, Jpn. J. Appl. Phys., 34 Part 1, No.5B (1995) 2756
2) T. Furukawa et. al., J. Acoustical Society of Japan, 55-8 (1999) 554 (in Japanese)
3) C, Yun, T. Ishii, K. Nakamura, S. Ueha and K. Akashi : A High Power Ultrasonic Linear Motor Using a Longitudinal and Bending Hybrid Bolt-Clamped Langevin Type Transducer, Jpn. J. Appl. Phys., 40 (2001) 3773.

E-3

Proc. Symp. Ultrason. Electron., Vol. 26, (2005) pp. 197-198
16-18 November, 2005

A Miniature Multi-Degree-of-Freedom Ultrasonic Motor

◎Yasuyuki Gouda, Daisuke Koyama, Kentaro Nakamura, and Sadayuki Ueha
(P & I Laboratory, Tokyo Inst. of Tech.)

1 Introduction

There are various demands for small-sized Multi-Degree-of-Freedom (MDOF) actuator. Conventional MDOF actuator consists of electromagnetic motors and gears, and it has some problems of noise, complex structure, and large size. Ultrasonic actuator has been studied for its advantages in silent operation, simple structure, small size, and having a holding force. MDOF ultrasonic actuator has been prototyped using a combination of a longitudinal vibration and two orthogonal bending vibrations of a rod[1][2].

In this study, we aim to miniaturize the MDOF ultrasonic actuator and discuss the structure suitable for fabricating on a substrate with the minimum number of PZT elements. The actuator consists of a cylinder fixed on a substrate and a PZT ring. Electrode of the PZT is divided into four parts and they are driven by the phased voltages to excite the 1st longitudinal and 2nd bending vibrations simultaneously. Height and diameter of the cylinder are decided so as to tune the resonance frequency of the 1st longitudinal vibration to the 2nd bending one. Actuator performances are evaluated experimentally for a prototype of a 7-mm-diameter stainless steel cylinder with a 0.5-mm thickness PZT ring. We confirmed the rotation of the ball rotor for each of the three axes and obtained 15.8 rps using a 6-mm ball rotor.

2 Structure and the operation principle

The actuator consists of a stainless steel cylinder fixed on a substrate and a PZT ring as shown in Fig. 1. The PZT ring is uniformly polarized in the thickness direction, and bonded close to the bottom of the cylinder. Electrode of the PZT ring is divided into four parts, and we can excite a longitudinal vibration and two orthogonal bending vibrations simultaneously by selecting the electrodes. By combining these vibrations, elliptical motion takes place at the top surface of the cylinder, and a ball rotor located on the cylinder rotates because of the friction force. Figure 2 shows the method to excite each vibration. To excite the X-bending vibration, we apply voltages with the phase difference of 180 degrees to two electrodes that are diagonally located each other. The Y-bending vibration is excited in the same way as the X-axis vibration but a pair of electrodes of 90°-shifted is selected. To excite the Z-longitudinal vibration, we apply the same voltages to all the divided electrodes. Figure 3 shows the method to rotate the ball rotor. To achieve the X-axis rotation, we utilize the Y-bending vibration and the Z-longitudinal vibration. To achieve the Y-rotation, we use the X-bending vibration and the Z-longitudinal vibration. To achieve the Z-axis rotation, we use the X-bending vibration and the Y-bending vibration. In each case, the phase difference between the two selected vibrations should be 90° to obtain elliptical vibration locus.

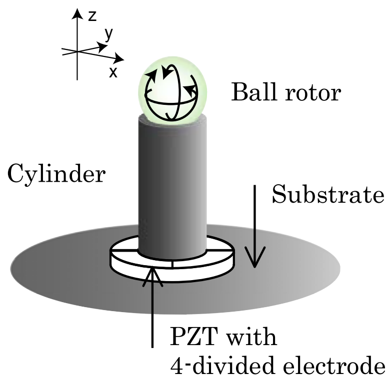

Fig. 1 Proposed structure of the multi-degree-of-freedom ultrasonic actuator.

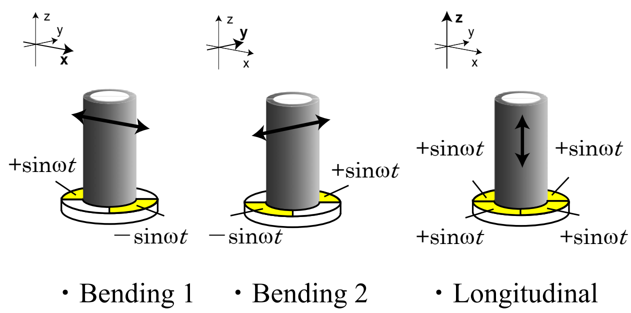

Fig. 2 Method to excite each vibration.

gouda@sonic.pi.titech.ac.jp

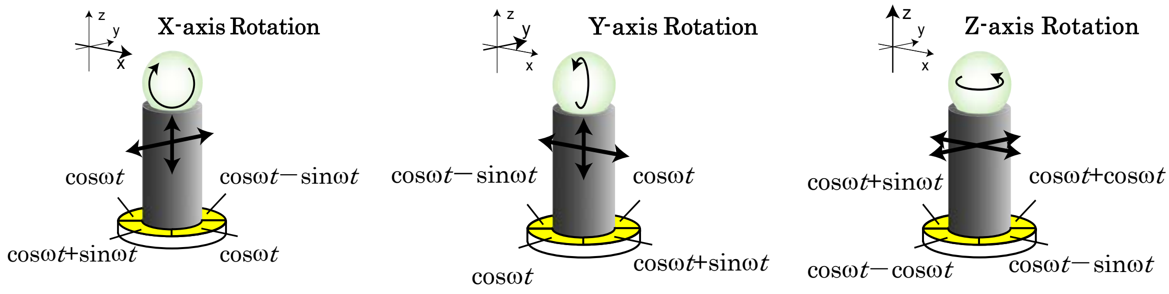

Y-bending and Z-longitudinal X-bending and Z-longitudinal X-bending and Y-bending

Fig. 3 Method to rotate the ball rotor.

3 Frequency design

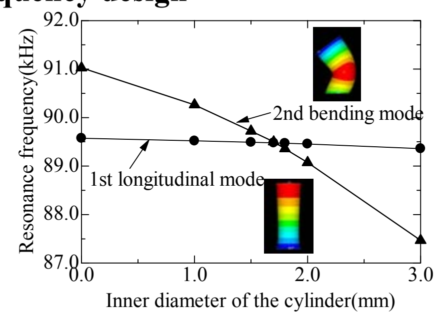

Fig. 4 Resonance frequencies of the cylinder.

To drive the actuator effectively, we have to match the resonance frequencies of the 1st longitudinal vibration and the 2nd bending vibration[2]. We analyzed these resonance frequencies of a fixed-free cylinder through finite element method. The stainless steel cylinder of 7 mm in diameter and 14 mm in height is assumed to be fixed on a rigid substrate. As shown in Fig. 4, these resonance frequencies match at 89.469 kHz when the inner diameter is 1.711 mm.

4 Operating characteristics

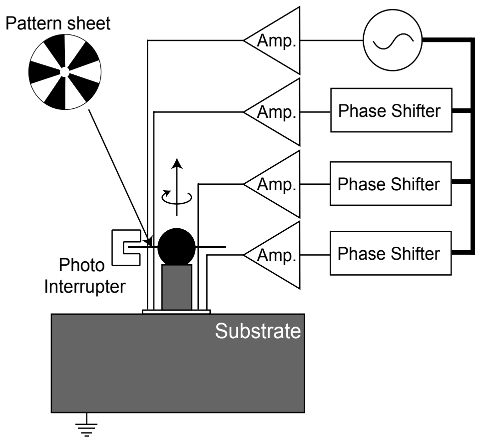

Fig. 5 Experimental setup.

According to the analysis results, we made a prototype actuator using a cylinder with the inner diameter of 1.7 mm and a PZT ring with 0.5-mm-thickness. We confirmed the X-axis rotation and Y-axis rotation at 84.920 kHz, as well as the

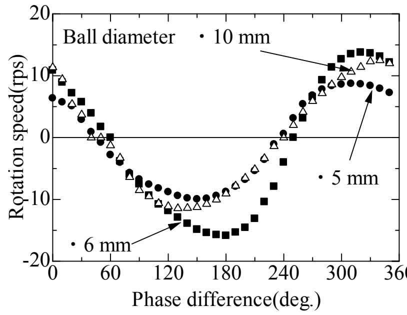

Fig. 6 Rotation speed vs. the phase difference.

Z-axis rotation at 84.833 kHz. Using the setup shown in Fig. 5, we measured the rotation speed of the ball rotor as a function of the phase difference between the electrodes. Rotation speed and direction are changed according to the phase difference as shown in Fig. 5, and we obtained 15.8 rps for clockwise direction and 13.8 rps for counterclockwise direction with the ball rotor of 6 mm in diameter.

5 Conclusions

We proposed a new structure of multi-degree-of-freedom ultrasonic motor suitable for miniaturization, and confirmed the X-axis rotation and Y-axis rotation at 84.920 kHz, and Z-axis rotation at 84.833 kHz. For the Z-axis rotation, we obtained 15.8 rps using a 6-mm-diameter ball rotor.

6 Acknowledgements

A part of this study was supported by the Grant-in-Aid for Scientific Research of Japan Society for the Promotion of Science, #17360038.

References

[1]Takefumi Amano, et al. “An Ultasonic Actuator with Multi-Degree-of-Freedom Using Bending and Longitudinal Vibrations of A Single Stator”, Proc. IEEE Int. Ultrasonic Symp., pp667-670, 1998.

[2]M. Aoyagi, et al. “A Novel multi-Degree-of-Freedom Thick-Film Ultrasonic Motor” IEEE Transactions on Ultrasonics, Ferroelectrics, and Frequency Control, vol. 49, No. 2, 2002.

E-4

Proc. Symp. Ultrason. Electron., Vol. 26, (2005) pp. 199-200
16-18 November, 2005

A piezoelectric rod micro ultrasonic motor with shear-bending modes

Cunyue Lu, Tieying Zhou, Yu Chen, Kai Lu

Department of Physics, Tsinghua University, Beijing 100084, P R China

This paper proposed a new mechanism for exciting shear-bending vibration in a piezoelectric ceramic rod. A mini-ultrasonic motor prototype with this concept was designed. Both finite element method (FEM) analyses and experimental results demonstrate the concept.

KEYWORDS: ultrasonic motor; shear-bending mode; piezoelectric ceramic rod

Recently, mini/micro ultrasonic motors have been of significant research interests. Compared with ordinary traveling wave type and standing wave type ultrasonic motors, the shaking head type ones have such advantages as simple configuration, lower cost and easy to be miniaturized. So many reported mini ultrasonic motors belong to shaking head type ones, which use the axial bending-vibration modes of the stator as the working modes.[1-4] For the purpose of simplify the construction, mini ultrasonic motors often use directly a piezoelectric ceramic rod or tube as a stator. Commonly, previous designs have used the piezoelectric d_{31} or d_{33} effect to generate bending vibration. The constant value for d_{31} or d_{33} has a lower value compared with shear piezoelectric constant d_{15}. Also, the values of electromechanical coupling coefficient k_{31} and k_{33} are smaller than that of the shear electromechanical coupling coefficient k_{15}.

A design for an ultrasonic motor based on the shear coefficients has the potential for superior performance, relative to conventional d_{31} and d_{33} based ones. Thus, this paper presents a special design for an electrode distribution on a piezoelectric ceramic rod by using the shear piezoelectric d_{15} effect to excite the bending vibration modes of the stators.

If an electric field applied to a piezoelectric ceramic is vertical to the direction of polarization, a shearing strain should be inspired on the piezoelectric ceramic. Figure 1(a) shows a solid piezoelectric ceramic rod which is polarized along its axial direction. The cylindrical surface of the rod is plated with nickel as electrode. The cylindrical surface electrode was divided into four pairs (AB, CD, EF and GH) by acid eroding and each pair has two parts symmetrically along the axes. For example, the pair AB has part A and part B. By use of an alternating current (AC) voltage signals (positive and negative), separately on one pair electrodes, a bending vibration was generated at the stator's resonance frequency. Figure 1(a) shows the driving method. Excitation signal $A\sin(\omega t)$ are applied to electrode A, while excitation signal $-A\sin(\omega t)$ are applied to electrode B. At the same time, on the symmetrical pair of electrodes, excitation signal $-A\sin(\omega t)$ are applied to electrode C, and excitation signal $A\sin(\omega t)$ are applied to electrode D. Thus A bending vibration of a piezoelectric rod is excited as shown in figure 1(b). Similarly, if a $A\cos(\omega t)$ voltage signal are applied to electrode E and H, while a $-A\cos(\omega t)$ voltage signal are applied to electrode F and G, the other bending vibration on the piezoelectric rod is excited. The directions of the two vibrations are vertical to each other. By use of a pair of alternating voltage signals (sine and cosine) on four pairs of electrodes, a shaking head vibration (wobbling motion) was generated circumferentially. Because the polarization is along the axial direction, the piezoelectric ceramic rod can be well polarized.

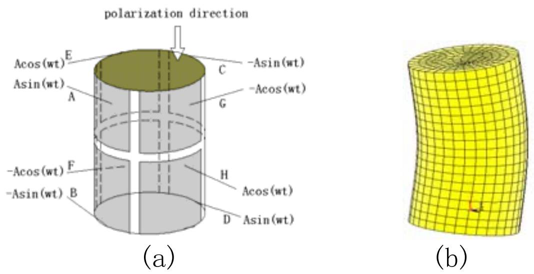

Fig.1 The electrode distribution and working principle of the piezoelectric ceramic rod. (a) The electrode distribution. (b) Vibrating mode.

As a prototype example, a compact ultrasonic motor based on bending vibrating modes of the piezoelectric rod was fabricated, as illustrated in Figure 2(a).

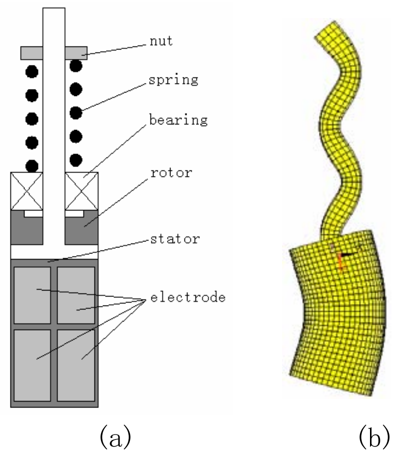

Fig.2 The configuration of a micro motor and its vibrating mode.

It consists of a piezoelectric ceramic stator, a rotor, and a pressing mechanism including a nut, a spring and a bearing. A copper plate with a slender shaft is bonded to one end of the piezoelectric ceramic rod. The working bending vibration modes of the stator are as shown in figure 2(b). The local bending vibrating resonance modes of the piezoelectric ceramic part should be its 1st local bending vibrating resonance modes.

The role of a piezoelectric stator is to transform the input electric energy into a mechanical energy. This transformation of energy can be described by an effective electromechanical coupling coefficient, k_{eff}, given as

$$K_{eff}^2 = \frac{f_a^2 - f_r^2}{f_a^2}$$

where f_r is the resonant frequency, and f_a is the anti-resonant frequency. An ultrasonic motor needs a large electromechanical coupling factor. The electromechanical coupling coefficient of the piezoelectric stator can be modeled using Ansys software. Fig.3 shows the predicted k_{eff} of the bending modes as functions of the diameter and the length of the piezoelectric rod. It can be found from Fig.3 that coefficient k_{eff} increases with the diameter of stator, and decreases with the length of stator. This modeling revealed that a piezoelectric rod with a larger diameter and a smaller length would have a larger value of k_{eff}. Thus such a special design presented in this paper for the electrode distribution on the piezoelectric ceramic rod is well suitable to a structure of the short fat stator with a larger value of k_{eff}.

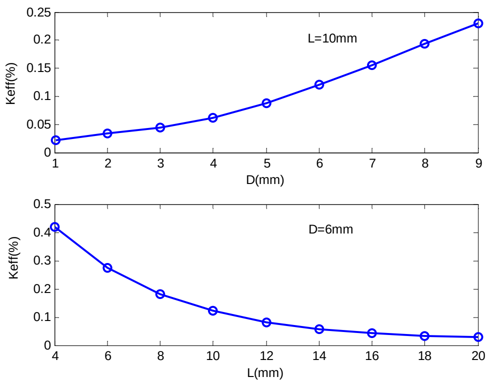

Fig.3 Calculated k_{eff} as a function of diameter (D) and lenght (L) of the stator.

Because of the fact that the calculated value of 0.12 for k_{eff} in the bending mode is much smaller than the value for k_{15} of the piezoelectric material itself, it is quite reasonable to believe that there would be a better configuration for a micro ultrasonic motor to yield a significantly higher k_{eff}.

In our design, the piezoelectric rod is 6mm in diameter, 10mm long and made with PZT-5h soft-type material. The frequency response characteristic of the rod measured with impedance analyzer is shown in figure 4. The resonant frequency of the working bending vibration modes is 72.3 kHz.

The rotational speed of the motor varies proportionally with an applied voltage. This result is in agreement with a no-load working condition of the rotor, as shown in figure 5.

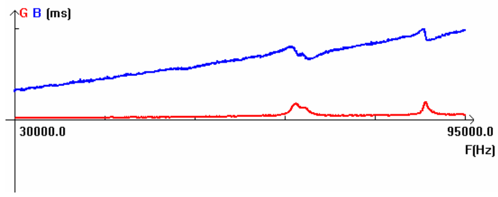

Fig.4 The measured resonant frequency of the motor

The driving electric voltage of the motor is about 50 V in rms. Fig.5 also shows the relation between the rotation speed and the drive frequency. At a resonant frequency of 72.5 kHz, the motor has a maximum rotation speed of 109.5 rpm. Under optimum conditions, the maximum speed was slightly increased to 200 rpm. In the frequency range from 73 to 75 kHz, the motor speed decreases linearly with the increasing of drive frequency.

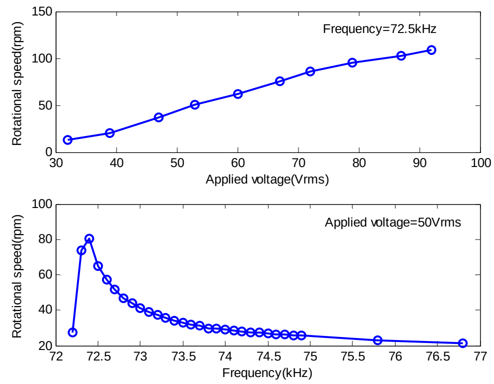

Fig.5 Characteristics of shear-bending mode motor.

This paper proposed a new mechanism for exciting shear-bending vibration in a piezoelectric ceramic rod. A mini-motor prototype with this concept and a diameter of 6mm was designed, and its characteristics were measured experimentally. The design concept presented in this paper is much promising for the applications in smaller motors and especially in these motors with piezoelectric ceramic rod stators with a large diameter-length ratio. There is still much space to improve for higher efficiency and smaller size of motor, although both FEM analyses and experimental results have demonstrated the concept.

The authors thanks for the financial supports from the National Natural Science Foundation of China (No.50235010) and State Key Laboratory of Acoustics, Institute of Acoustics, CAS (No.200506).

1. S. Dong, Siak P. Lim, Kwork H. Lee, J. Zhang, Leong C. Lim, K. Uchino: UFFC. 50 (2003) 361.
2. T. Morita, M. Kurosawa, T. Higuchi: Ultrasonics. 38 (2000) 33.
3. S. Cagatay, B. Koc, K. Uchino: UFFC. 50 (2003) 782.
4. T. Zhou, K. Zhang, Y. Chen: Chinese Science Bulletin. 50 (2005) 826.

Proc. Symp. Ultrason. Electron., Vol. 26, (2005) pp. 201-202
16-18 November, 2005

Piezocomposite Ultrasonic Transducer for High-Frequency Wire-Bonding of Microelectronics Devices

Siu Wing Or* and Helen Lai Wa Chan (The Hong Kong Polytechnic University)
Peter Chou Kee Liu (ASM Assembly Automation Ltd.)

1. Introduction

High-frequency (≥100 kHz) ultrasonic wire bonding is an urgently needed technology to produce smaller wire bonds of higher quality in a shorter time as IC packages in the microelectronics industry are rapidly reducing in size and increasing in volume. To enable a complete fine-pitch (<50 μm) and high-speed (>20 wires/s) process, axial-mode transducers operating at a few kiloherz with a moderately high mechanical qaulity factor (Q_m~300) are of prime importance [1]. While the hard PZT piezoceramic rings used in state-of-the-art transducers have large axial coupling (k_t~0.38 for PKI804), they also have large lateral coupling (k_{31}~-0.38) and high Q_m (~1500). The resulting transducers thus exhibit strong lateral coupling with many non-axial and spurious modes distributed over the hundred kiloherz range. This causes the supplied energy to be drained from the desired axial modes into these undesribable modes, thereby reducing the purity of axial motion of transdcuers. Moreover, high Q_m transducers have sharp resonances with limited bandwidths; they are sensitive to load changes and impose difficulties in frequency tuning and mode locking. Therefore, we have developed novel ultasonic transducers possessing low lateral coupling and broadband charactersitics to alleivate the drawbacks intrinsic in PZT transducers based on the PZT/epoxy 1-3 piezocomposite technology [2]. In this paper, a 136 kHz composite transducer is described and its electrical and vibrational characteristics are reported, together with a PZT transducer of similar structure.

2. Structure of Ultrasonic Transducers

Figure 1(a) shows the solid model of the composite transducer. The transducer has a length of 47.38 mm and is composed of a Langevin-type piezodriver (12.46 mm long), an ultrasonic horn (34.92 mm long) and a bonding tool. The piezodriver has a pair of composite rings, each of 12.65 mm outer diameter, 5.03 mm inner diameter and 1.70 mm thickness, connected electrically in parallel, mechanically in series and preloaded by a prestress mechanism formed by two 4.47 mm thick SST304 slabs and a SST304 prestress screw. Three pieces of 0.04 mm thick, ring-shaped Cu electrodes are inserted between the driver components for electrical connections. The composite rings are self-made PKI804/Araldite LY5210/HY2954 1-3 piezocomposite with 0.89 PZT volume fraction. They have sufficiently small epoxy width of 77 μm and can be treated as an effective homogeneous material for frequencies up to 10 MHz [3]. The ultrasonic horn is formed by two SST304 half-wave sectional horns. The section next to the piezodriver has a cylindrical rod (13.06 mm long, 8.2 mm diameter) attached to the small end of a conical horn (3 mm long). The second section is a conical horn (18.86 mm long) with its smaller end (3.6 mm diameter) affixed with a bonding tool by a screw. The entire horn is capable of amplifying 2.6 folds the axial displacement output from the piezodriver. Figure 1(b) shows the fabricated composite transducer along with a PKI804 PZT transducer.

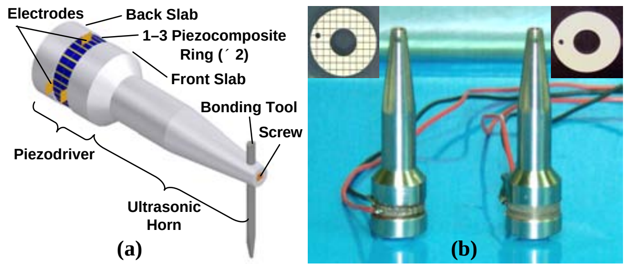

Fig. 1. (a) Solid model of the 136-kHz composite transducer and (b) photograph of the fabricated composite (left) and PZT (right) transducers. The two insets of (b) are the composite and PZT rings.

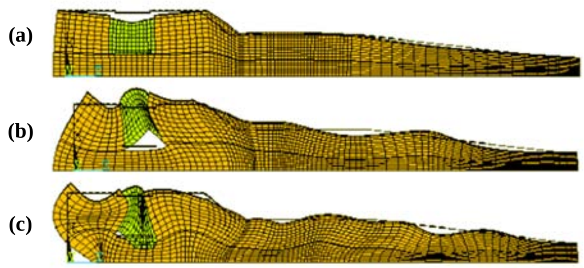

Fig. 2. Deformed shapes of three major natural modes governed by (a) axial, (b) radial and (c) wall-thickness excitations of the piezoelectric ring stack.

3. Electrical Resonance Characteristics

The electrical impedance spectra of the composite and PZT transducers were measured using an Agilent 4294A impedance analyzer. By associating the measured series and parallel resonance frequencies with the resonance and antiresonance frequencies computed using an ANSYS finite element model, the nature of most experimental resonance modes was identified and grouped into three categories according to the excitation forces governed by the piezoelectric ring stack. These categories include: 1) axial excitation [Fig. 2(a)]; 2) radial excitation [Fig. 2(b)]; and 3) wall-thickness excitation [Fig. 2(c)].

As shown in Fig. 3(a), the composite transducer has the strongest resonance at 135.1 kHz, which is the designated working mode of the transducer and also is the 3rd axial mode (M3) with 1.5 longitudinal wavelengths [Fig. 2(a)]. The two lower modes at 54.5 (M1) and 103.5 kHz (M2) are the 1st and 2nd axial modes with 0.5 and 1 longitudinal wavelength, respectively. The two higher modes at 181.8 (M4) and 193.7 kHz (M5) are a pair of the 4th quasi-axial modes. The one observed at 225.9 kHz (M6) is the 5th

---

* E-mail: apswor@polyu.edu.hk

quasi-axial mode. After that, no prominent resonances are found. Consequently, the impedance spectrum is very pure in that the axial modes are promoted by impeding non-axial and spurious modes in the composite ring stack.

For the PZT transducer [Fig. 3(b)], the working axial mode is found at 135.7 kHz (M3), while the two lower axial modes, M1 and M2, and the three higher quasi-axial modes, M4, M5 and M6, are located at 54.4, 105.1, 184.5, 195.1 and 227.6 kHz, respectively. Besides, very complicated resonance characteristics covering two broad frequency ranges of 250-350 kHz and 400-600 kHz originate from the radial [Fig. 2(b)] and wall-thickness [Fig. 2(c)] activities of the PZT ring stack. Thus, when this highly laterally coupled transducer is used in a bonding operation, the non-axial and spurious resonance modes, especially for those with frequencies very close to the working axial mode or equal to its higher frequency harmonics, are likely to be excited simultaneously, leading to a reduction in the purity of axial motion and hence in the bonding stability and yield.

Due to the effect of epoxy damping, the measured Q_m of the composite transducer at M3 is 296, corresponding to a 3-dB bandwidth of 456 Hz [the insert of Fig. 3(a)]. The PZT transducer has ~2.4 times increased in Q_m (= 710), thus giving a smaller 3-dB bandwidth of 191 Hz [the insert of Fig. 3(b)]. Under such a low Q_m operation, the composite transducer will be more adaptable to various types of bonding surfaces so that a relaible working platform can be created for high-frequency bonding.

4. Vibrational Characteristics

The vibrational characteristics of both transducers were evaluated with a Polytec OFV-303/OFV-3001 laser Doppler vibrometer. An ASM PC-BQM ultrasonic board operating in a constant voltage, digital phase-locked-loop mode was used to drive the transducers. To initiate an optimal bonding condition, a 0.15-W burst in 15 ms with a duty cycle of 13% was supplied to each transducer at resonance (~136 kHz). The temporal profile of axial displacement at the tip of the ultrasonic horn was examined by measuring the temporal profile of axial velocity. By applying FFT to the steady-state portion of the displacement waveform, the corresponding amplitude spectrum (in dBm re 50 Ω 1 mW) was obtained.

From the waveforms in Fig. 4, the composite transducer has a rise/fall time of ~50% shorter than the PZT transducer due to its heavily damped nature as have been seen in its lower Q_m (Fig. 3). Importantly, shortening the rise time can directly shorten the time required to form a bond. This is definitely an advantage for promoting high-speed bonding.

The amplitude spectra (the inserts of Fig. 4) reveal that excitations of other frequency components (i.e. higher-order harmonics and sub-harmonics to the fundamental) are ~10 dBm lower in the composite transducer, except the fundamental amplitude (16 dBm or 295 nm) – It is almost equal to that of the PZT transducer (16.1 dBm or 297 nm). Hence, the purity of axial excitation of ~95 % is obtained for the composite transducer but only ~86 % for the PZT transducer, reflecting again the low lateral coupling nature of the composite-based transducers.

5. Conclusion

A 136-kHz composite ultrasonic transducer for high-frequency microelectronics wire bonding has been successfully developed using ring-shaped PKI804/Araldite LY5210/HY2954 1-3 piezocomposite rings having 77 µm epoxy width and 0.89 PZT volume fraction. Comparing to its PZT transducer counterpart, the composite transducer has superior characteristics of low lateral coupling and reduced Q_m, which made it a promising transducer for use in high-frequency wire bonding. Process tests have showed that an ultrasonic wire bonder when equipped with the composite transducer possesses a wider operating window and a shorter bonding time, thereby promoting the fine-pitch and high-speed capabilities of the machine.

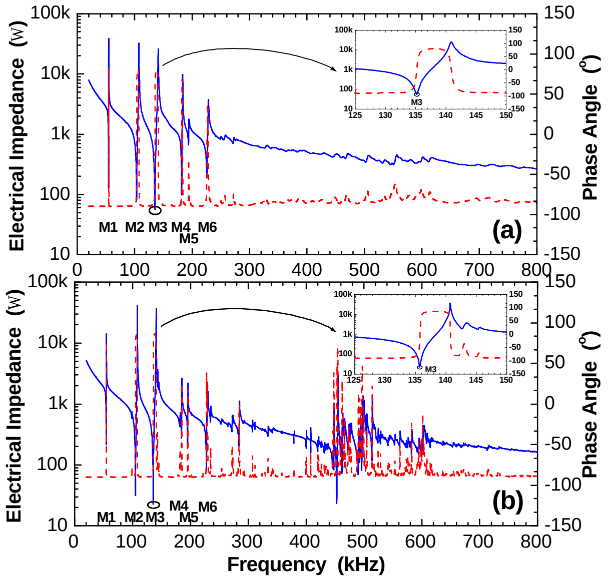

Fig. 3. Electrical impedance spectra for the (a) composite and (b) PZT transducers.

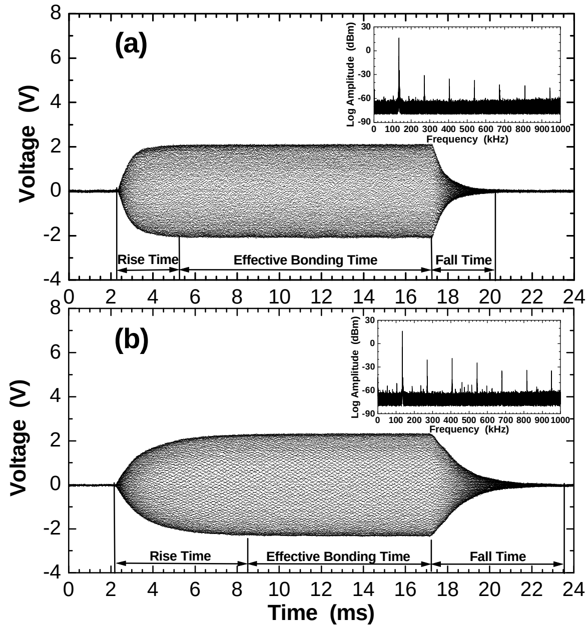

Fig. 4. Axial vibration responses at the horn tip for the (a) composite and (b) PZT transducers, where 1 V = 10 dBm = 147 nm.

Acknowledgments

This work was supported by the Innovation and Technology Fund (UIM/117) of the HKSAR Government and the Centre for Smart Materials of The Hong Kong Polytechnic University.

References

1. S.W. Or: PhD Thesis (The HK Polytechnic University, 2001).
2. H.L.W. Chan, S.W. Or, K.C. Cheng and C. L. Choy: US Patent **US 6,190,497 B1** (2001).
3. S.W. Or and H.L.W. Chan: J. Appl. Phys. **90** (2001) 4122.
4. ASM Assembly Automation Ltd.: Private Communications (2004).

F-1

Proc. Symp. Ultrason. Electron., Vol. 26, (2005) pp. 203-204
16-18 November, 2005

A Study on the Behavior of Heating due to Absorption of Ultrasound in Medium

◎ Chiaki YAMAYA and Hiroshi INOUE (Akita Univ.)

1 Introduction

Recently, the ultrasound wave has been put to practical use not only the diagnostic equipment but also the thermotherapy that uses the effect of ultrasound wave in living body. The analysis of temperature rise due to absorption of ultrasound in the soft tissue medium are important analyzing object for the clarification of the affect in biological tissue[1, 2] and the estimation of medium constants. Three dimensional simulation by FDTD(Finite-Difference Time-Domain) method has been executed by the equations that considers the absorption attenuation based on the acoustic basic equations(ABE)[3–5]. The Westervelt equation exists as an equation that describes the absorption attenuation of the ultrasound, too[6–8]. Acoustic field distribution is calculated respectively by these equations, internal heat generation in the medium is calculated from ultrasonic intensity and heat analysis is executed.

2 Analysis method

ABE(eq.(1) and (2)) and Westervelt equation(eq.(3)) are as the followings.

$$\frac{\partial p}{\partial t} = -K\nabla \cdot \boldsymbol{v} \tag{1}$$

$$-\rho\frac{\partial \boldsymbol{v}}{\partial t} = \nabla p + \eta \boldsymbol{v} \tag{2}$$

$$\nabla^2 p - \frac{1}{c^2}\frac{\partial^2 p}{\partial t^2} + \frac{\delta}{c^4}\frac{\partial^3 p}{\partial t^3} + \frac{\beta}{\rho c^4}\frac{\partial^2 p^2}{\partial t^2} = 0 \tag{3}$$

The Westervelt equation cannot be derived from ABE. For ABE, p is the sound pressure, $\boldsymbol{v}$=(v_x, v_y, v_z) is the particle velocity, K is the volume elasticity, ρ is the density, η is the attenuation coefficient assumed to be proportional to particle velocity[3][4], where

$$\eta = \frac{2k\alpha\rho c}{\sqrt{k^2 - \alpha^2}}, \tag{4}$$

k is the wave number, α is the absorption coefficient, c is the sound velocity. For Westervelt equation(eq.(3)), δ is the acoustic diffusivity, where

$$\delta = \frac{2c^3\alpha}{\omega^2} \tag{5}$$

ω is the angular frequency. $\beta = 1 + B/2A$ is the coefficient of nonlinearity with B/A being the nonlinearity parameter of the medium[9]. In eq.(3), The first and second terms, the third term and the fourth term describe linear lossless wave propagation, the loss term and the nonlinear term, respectively. In this simulation, the nonlinear term is ignored in the Westervelt equation . The absorption attenuation is considered by eq.(4) and (5).

Heat conduction equation(HCE)(eq.(6)) and connection equation(eq.(7)) are as the followings.

$$\frac{\partial T}{\partial t} = \kappa\nabla^2 T + \frac{H}{\rho C} \tag{6}$$

$$H = 2\alpha I \tag{7}$$

In HCE (eq.(6)), T is the temperature, H is the internal heat generated by source, C is the specific heat, κ is the thermal diffusivity, where

$$\kappa = \frac{\lambda}{\rho C}, \tag{8}$$

λ is the thermal conductivity. In eq.(7), I is the ultrasonic intensity.

$$I_x = \frac{1}{T_p}\int_0^{T_p} p(t)v_x(t)dt = \frac{1}{T_p}\int_0^{T_p}\frac{p^2(t)}{\rho c}dt \tag{9}$$

I_x is the intensity which passes a unit area perpendicular to the propagation direction of an ultrasound x at unit time, T_p is the integral multiple of one cycle of an ultrasonic wave or time longer enough than a cycle. The spatial region for analysis in water and the value of medium constants are shown in **Fig.1** and **Table 1**, respectively. The absorbing medium is placed at near field length[10] for sinusoidal wave, X_0=$\frac{a^2}{\lambda_{wl}}$(λ_{wl} is the wave length, a is the radius of sound source), from the sound source. The size of the absorbing medium is 60×60×60mm^3. The sound source is assumed as the circular of 9mm in radius. The sound source excites a sinusoidal wave of 1MHz and 100kPa.

The cell size is one edge 70 μm as a cubic cell in both ABE and Westervelt equations. The absorbing boundary condition(ABC) of ABE and that of Westervelt equation are first order Mur's ABC and second order Mur's ABC, respectively. This reason is that the reflection from ABC appeared remarkably in the Westervelt equation.

3 Result and discussion

Acoustic field distributions on the center axis of sound source are shown in **Fig. 2**. The result of FDTD analysis by Westervelt equation is in good agreement with that of ABE. This shows that a similar analytical result of acoustic field is obtained though these are different equations. It is

yamaya@venus.ee.akita-u.ac.jp

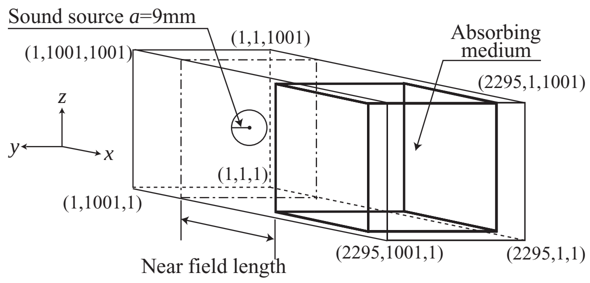

Fig. 1 Analytic region

Table 1 medium constants

	Water	Absorbing medium
Volume elasticity K [$\times 10^9$ N/m^2]	2.22	2.23
Density ρ [kg/m^3]	1000	960.0
Specific heat C [J/kg·K]	4186	2149
Thermal conductivity λ [W/m·K]	0.596	0.18
Thermal diffusivity κ [$\times 10^{-7}$ m^2/s]	1.42	0.872
Absorption coefficient α [dB/m]	25.3×10^{-3}	6.5

confirmed that the attenuation in the absorbing medium is the diffusion attenuation when the absorption medium is not put and the absorption attenuation with the medium.

Fig. 3 shows temperature distribution in the absorbing medium on each irradiation time at center axis of sound source. These results are normalized by each peak temperature on irradiation time 5s. Because similar acoustic field distribution had been obtained from two equations, a corresponding result was obtained in the temperature distribution.

The Westervelt equation is calculated by one element(the sound pressure) though four elements (the sound pressure(scalar:one element) and the particle velocity(vector:three elements)) are needed in ABE. However, it is necessary to store the sound pressure in front of 1$\sim$5 steps from the formulation of the Westervelt equation for FDTD. The FDTD calculation memory in the propagation of ultrasound of ABE and Westervelt equation are 46.1GB and 62.8GB, respectively. The calculation in Westervelt equation needs more calculation memories.

4 Conclusion

In this study, the temperature distribution was examined by ABE and Westervelt equation that models absorption of ultrasound that becomes factor of temperature rise when ultrasound is irradiated. The calculation memory in Westervelt equation is larger than ABE though a result corresponding to ABE is obtained by only one element in Westervelt equation. In a future work, a detailed examination for the heating behavior of ultrasound by the experiment is enumerated.

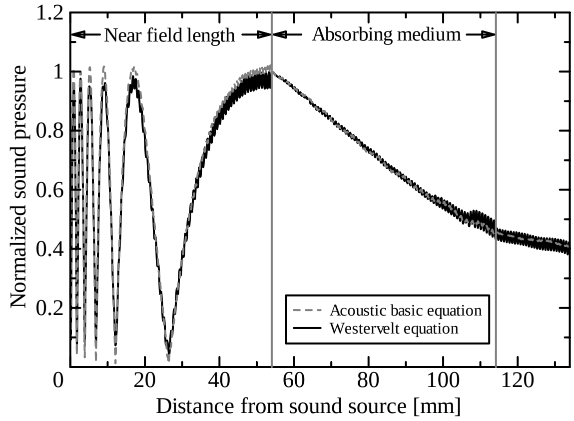

Fig. 2 Acoustic field distribution

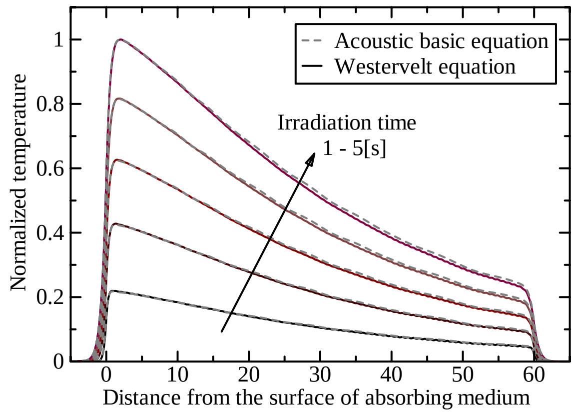

Fig. 3 Heat distribution on each irradiation time

Acknowledgment This study were supported by a supercomputer resources at Information Synergy Center, Tohoku University, and General Information Processing Center, Akita University.

References

[1] J. L. Drewniak and F. Dunn : J. Acoust. Soc. Jpn. **13** (1992) 115.
[2] Y. Saito, T. Ishizeki, T. Tsuchiya and N. Endoh : Jpn. J. Appl. Phys. **44** (2005) 4600.
[3] H. Inoue and F. Yoshida : Proc. Spring Meet. Acoust. Soc. Jpn. (2002) 1057.
[4] H. Inoue and F. Yoshida : Tech. Report of IEICE, EMD2001-93, (2002) 13.
[5] C. Yamaya and H. Inoue : in Proc. Int. Fed. Med. Bio. Eng. APCMBE2005, **8** (2005)
[6] I.M. Hallaj and R.O. Cleveland : J. Acoust. Soc. Am., **105** (1999) 7.
[7] I.M. Hallaj *et al.* : J. Acoust. Soc. Am., **109** (2001) 2245.
[8] J. Huang *et al.* : J. Acoust. Soc. Am., **116** (2004) 2451.
[9] T. Kamakura, “Fundamentals of Nonlinear Acoustics”, AICHI PUBLISHING CO.,LTD., TOKYO (1996)
[10] Ultrasound handbook edit committee, “Ultrasound Handbook”, MARUZEN CO.,LTD., TOKYO (1999)

F-2

Proc. Symp. Ultrason. Electron., Vol. 26, (2005) pp. 205-206
16-18 November, 2005

Brillouin Scattering Study of Liquid Glass Transition in Lithium Borate Glass

◎Yuji Ike*, Seiji Kojima (PAS, Univ. Tsukuba, Japan)

1. Introduction

Since the properties of alkali metal borate glasses have anomalous behavior against molar fraction, the composition dependence of structural and physical properties are strongly interested. The anomalous behavior has been deduced from the changes in B_2O_3 structural units. The random network of B_2O_3 glass is mostly constructed by BO_3 planar triangle units. The addition of alkali metal oxide to the B_2O_3 glass causes the formation of BO_4 tetrahedral groups by crosslink between the BO_3 group units building the glass network. Such properties have been studied by several experimental techniques (NMR, Raman spectroscopy, etc.) [1, 2]. Also the elastic parameters are sensitive and indicative to the structure of glass network, thus it plays a significant role in understanding the structural characteristics of glass network. The change in borate units affects the B_2O_3 glass network and it causes a stiffening of the structure. This tendency is indicated by the increase of the elastic moduli [3]. However, the information of elastic properties in a high temperature region is scarce. The elastic properties such as velocity, elastic modulus and attenuation in high temperature, especially at the glass transition temperature have much attracted in the study of glass transition. In the present study, different compositions of lithium borate glass system are investigated by micro-Brillouin scattering technique [4].

2. Experimental

The composition formula of lithium borate glass is denoted by x $Li_2O \cdot (1-x)\ B_2O_3$, where x indicates the mole fraction of Li_2O. All glasses were prepared with high homogeneity in order to investigate the inherent nature of binary mixture in lithium borate glasses. Details of high homogeneity glass preparation method can be seen elsewhere [3].

One of the techniques measuring the elastic property, Brillouin scattering is known to be a powerful tool to examine the transparent condensed materials not only the probe of high frequency elastic property, but also the ability to explore in an extremely wide temperature range. The experimental setup of a micro-Brillouin scattering apparatus is shown in Fig. 1. The Brillouin scattering spectra were measured at backward scattering geometry. The Sandercock-type 3 + 3 passes tandem Fabry-Perot Interferometer (FPI) was combined with microscope and operated to acquire the spectra of the scattered light. A free spectral range of 60 GHz was applied to measure the Brillouin spectra between ±50 GHz. The temperature was controlled and started from 25 ºC to 600 ºC. Temperature stability was within ±0.1 ºC below 500 ºC.

3. Results and Discussion

The acquired Brillouin spectra of the lithium borate glasses showed one longitudinal acoustic (LA) mode. Brillouin shifts and full width at half maximum (FWHM) have been obtained from the spectra by using the fitting function which takes account the instrumental function. The longitudinal velocity of sound V_l was obtained from the Brillouin shift ν ($=qV_l/2\pi$) and the scattering wave vector q ($=2\pi n\sin(\theta/2)/\lambda$), where n, λ and θ are the refractive index of the sample, the wavelength of the laser and scattering angle, respectively. The longitudinal elastic modulus M is derived by $M = \rho V_l^2$, where ρ is the density. The LA mode absorption coefficient α can be determined by FWHM of Brillouin component using the equation, $\alpha = \pi\Gamma/V_l$ where Γ is FWHM. The temperature dependence of M are plotted as shown in Fig. 2. The figure indicates M becomes larger with increasing mole fraction of Li_2O. Larger the elastic modulus indicates the stiffer the network and this behavior is due to the modification in some amount of cross-linking borate units from triangle BO_3 to tetrahedral BO_4 by addition of Li_2O. Also we clearly observed the kink in the present temperature range. The temperature dependence above and below the kink are significantly different. The marked decrease above T_g is similar to B_2O_3 and other

* e-mail: s-ike@ims.tsukuba.ac.jp

glasses [5, 6]. Above the temperature M decreases with increasing temperature and it indicates the decrease of the elasticity of glass network. The kinked point temperature can be a glass transition temperature, T_g, and this temperature shifted to higher temperature by adding the Li_2O. This tendency is also related to the glass network variation and higher T_g describes tighter the glass network by the change of coordination number of boron atoms. Above T_g, the slope of the curve becomes steeper hence the glasses are softened by increasing temperature, while the dependence below T_g is small and nearly constant. Another elastic parameter of absorption coefficient α exhibits the close relation to the temperature dependence of M and shows a huge increase beyond T_g, in a supercooled temperature region. We observed this behavior is in common with all different concentration of lithium borate glasses. Further analysis to understand the relaxation process of the present glass system, the temperature limitation is the problem at the moment.

4. Summary

We investigated the elastic properties of lithium borate glasses in a wide temperature range. At the glass transition temperature the elastic modulus and also absorption coefficient of LA mode obviously show anomaly. The glass transition temperatures increase remarkably with the increase of the mole fraction of Li_2O. These results are well indicated by the change in some amount of cross-linking borate units of triangle BO_3 to tetrahedral BO_4 units. This transformation of glass network leads to the glass more rigid in comparison with a pure borate glass and causes the increase of glass transition temperatures.

References

[1] G. Carini, M. Cutroni, A. Fontana, G. Mariotto, F. Rocca, Phys. Rev. B **29** (1984) 3567.
[2] J. Zhong, P. J. Bray, J. Non-Cryst. Solids **111** (1989) 67.
[3] M. Kodama, T. Matsushita, S. Kojima, Jpn. J. Appl. Phys. **34** (1994) 2570.
[4] F. Jiang and S. Kojima, Appl. Phys. Lett. **77** (2000) 1271.
[5] R. E. Youngman, J. Kieffer, J. D. Bass, L. Duffrène, J. Non-Cryst. Solids **222** (1997) 190.
[6] H. Anwar, S. Kojima, M. Kodama, B. Whittington, M. Olesiak, M. Affatigato and S. A. Feller, Jpn. J. Appl. Phys. (to be published).

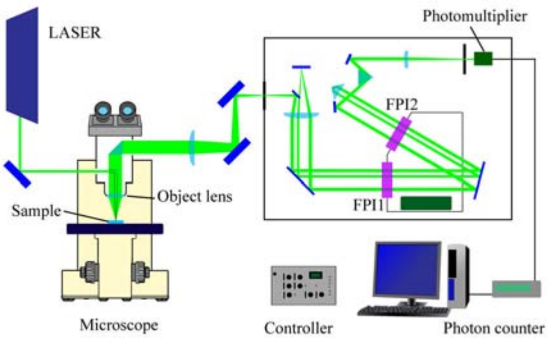

Fig. 1 Schematic diagram of the micro-Brillouin apparatus. The object lens focuses an incident laser beam on to a sample and also corrects scattered light from a sample. Collimated scattered light passes through two Fabry-Perot interferometers (FPI 1&2) and detected by a photomultiplier tube.

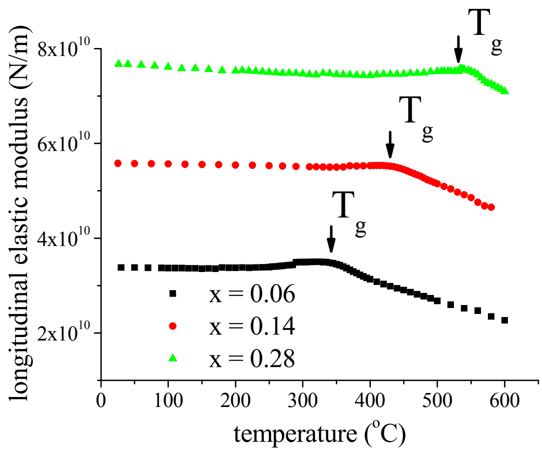

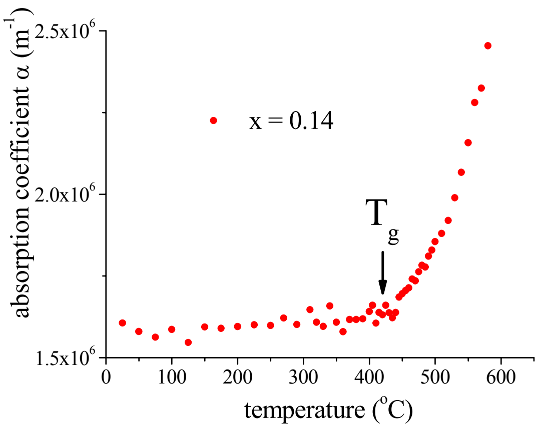

Fig. 2 Temperature dependence of longitudinal elastic modulus and absorption coefficient of lithium borate glasses.

INV-1

Proc. Symp. Ultrason. Electron., Vol. 26, (2005) pp. 207-208
16-18 November, 2005

Discovery of ATP motor and its mechanism

Masasuke Yoshida (Chemical Resources laboratory, Tokyo Institute of Technology)

All living organisms on the earth rely solely on a single molecule as an energy currency, ATP (adenosine triphosphate). This small molecule supports nearly all the cellular activities that require energy, and our body synthesizes roughly as much ATP every day as our body weight. In the biological world, ATP synthesis is certainly the most prevalent chemical reaction and the enzyme, ATP synthase, responsible for most of this task, is one of the most ubiquitous, abundant proteins on the earth. ATP synthase uses physical rotation of its own subunits as a step of catalysis－a novel mechanism, different from any other known enzymes. Rotation is not a favourite motion in living organisms; there is no animal with wheels, no bird with a propeller, and no fish with a screw. On a molecular scale, besides ATP synthase only bacterial flagella are known as a rotary motor. The crystal structures of the main part of ATP synthase show in atomic detail how the appearance of this world tiniest motor made of protein is remarkably reminiscent of the man-made motors. The driving force that spins ATP synthase is gradient of hydrogen ion concentration across membranes that in turn is made by respiration (burning the food) or by sunshine. We have video-imaged the rotary motion of ATP synthase that spins as fast as several hundreds revolutions per second. The mechanism of the motor is completely different from the man-made motor. ATP synthase is two-particle structure connected with a common rotary shaft. The flow of hydrogen ions through the lower particle drives the rotation of the central rotor that then forces upper particle to make the bending motion for synthesis of ATP. Imagine billions of billion rotary motors are spinning in our body, day and night, without rest. When the motors stop, we die.

～ *Memo* ～

INV-2

Proc. Symp. Ultrason. Electron., Vol. 26, (2005) pp. 209-212
16-18 November, 2005

Simulation of Surface Acoustic Wave Devices, Review

Ken-ya Hashimoto

2005-2006 IEEE UFFC Society International Distinguished Lecturer
Faculty of Engineering, Chiba University

1. Introduction

Presently, surface acoustic wave (SAW) filters are mass-produced and widely used in various consumer products and communication equipment. For their research and development, use of fast and precise simulation and design tools is essential, and much effort has been paid for their enhancement for many years.

Fortunately, recent rapid progress of computer technologies has made it possible to deal with large-scale problems using small personal computers. So as for computers, anyone can set up the latest research environment with small investment. The remaining task is to establish simulation and design software tools.

This lecture reviews simulation technologies used in the research and development of modern SAW devices from various aspects.

2. Role and Flow of Numerical Simulation

For the research and development of SAW devices, the numerical simulation has been widely used for various purposes such as (a) understanding underlying physics, (b) reducing the number of trials, (c) improving the production yield, and (d) optimizing the device design.

Although a number of simulation techniques have been developed, none of them are perfect. So we must select appropriate one for each purpose with the trade-off between computation speed and precision.

Theoretically, rigorous three-dimensional analysis is applicable for the whole device structure. However, this approach is not realistic because of required computer speed and memory size.

Fig. 1 shows a typical SAW device structure called the one-port SAW resonator. The SAW is generated by an interdigital transducer (IDT), and resonates between two Bragg reflectors. Usually the IDT and reflectors are uniform laterally, and their aperture is much larger than the SAW wavelength. So lateral SAW propagation on the surface is a minor effect, and its influence is often ignored.

Now the problem under concern becomes two-dimensional, and the rigorous analysis is possible for the whole structure by the use of current computer power.

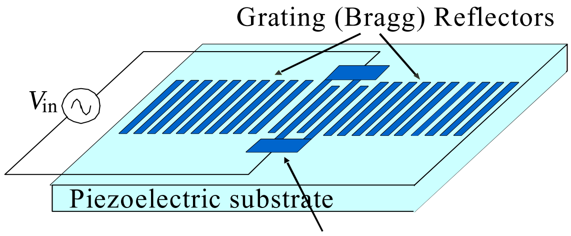

Fig. 1 Typical SAW device structure

However, the simulation is still too slow to use in practical device design. So further simplification is necessary.

In the device design, rigorous SAW field is out of interest and only electrical properties are necessary to know. So SAW propagation and excitation are modeled in behavior basis rather than physical one, reducing to a one-dimensional problem.

This type of simulators called the behavior model analysis is mainly used in the optimization process. In this case, the calculation speed is very crucial because the same simulator will be executed for a huge number of iterations to search the optimal solution.

Accuracy of the simulation is critically dependent upon parameters used in the model. Two-dimensional full-wave analyses are often used for the extraction of the parameters. In this case, accuracy is more important than the calculation speed.

Sometimes SAW oblique propagation on the substrate surface is taken into account after the one-dimensional analysis. Again use of behavior models is essential, and simplified two-dimensional analysis is applied for the extraction of simulation parameters. Since the oblique propagation is usually a minor effect, not so high accuracy may not be required.

Finally, influence of parasitic impedances, such as bonding pads, wires, package, etc., must be taken into account. This is because even tiny wire inductances give significant influences to device performances in GHz range. Parasitic impedances are estimated experimentally or by the use of commercial tools.

3. Simulation Based on Behavior Model[1]

As the behavior models, the coupling-of-modes (COM), p-matrix and equivalent circuit models are widely used. Difference in these models is how one period of the IDT is expressed in a three-port element shown in Fig. 2, where $U_{\pm}(x)$ is the SAW amplitude propagating to the $\pm x$ direction, and V and I are the applied voltage and current, respectively.

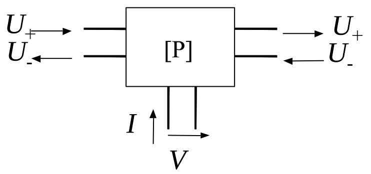

Fig. 2 Three-port element model for IDT

Once each period is modeled, the whole IDT is expressed in the same three-port structure by the mutual-connection.

It should be noted that short-circuited (SC) and open-circuited (OC) gratings are equivalent to IDTs where all electrodes are short-circuited or isolated electrically from bus-bars, respectively.

Here the COM model is introduced because of its simplicity and existence of the number of references.

In the model, $U_{\pm}(x)$ and the current $I(x)$ on the bus-bar are assumed to be governed by the following simultaneous linear equations:

$$\frac{\partial U_{+}(x)}{\partial x} = -j\theta_u U_{+}(x) - j\kappa_{12} U_{-}(x) + j\zeta V, \qquad (1)$$

$$\frac{\partial U_{-}(x)}{\partial x} = +j\kappa_{12}^{*} U_{+}(x) + j\theta_u U_{-}(x) - j\zeta^{*} V, \qquad (2)$$

and

$$\frac{\partial I(x)}{\partial x} = -4j\zeta^{*} U_{+}(x) - 4j\zeta U_{-}(x) + j\omega C V, \qquad (3)$$

where V is the applied voltage, C, κ_{12} and ζ are the static capacitance, and the reflection and the excitation coefficients per unit length, respectively. And θ_u (=β_u-$2\pi/p_I$) is the detuning factor corresponding to deviation of the SAW wavenumber β_u from the Bragg condition (β_u=$2\pi/p_I$) under a situation where κ_{12}=0, namely the SAW reflection is ignored. And p_I is the IDT period.

When θ_u, κ_{12}, ζ and C are uniform (independent of x), the general solution of Eqs. (1) and (2) is given by

$$U_{+}(x) = a_{+} e^{-j\theta_p x} + \Gamma_{-} a_{-} e^{+j\theta_p x} + j\xi_{+} V \qquad (4)$$

and

$$U_{-}(x) = \Gamma_{+} a_{+} e^{-j\theta_p x} + a_{-} e^{+j\theta_p x} + j\xi_{-} V, \qquad (5)$$

where Γ_{+}=(θ_u- θ_u)/κ_{12}, Γ_{-}=(θ_u- θ_u)/κ_{12}^{*},
ξ_{+}=($\zeta\theta_u$- $\zeta^{*}\kappa_{12}$)/θ_p^2, ξ_{+}=($\zeta^{*}\theta_u$- $\zeta\kappa_{12}^{*}$)/θ_p^2, and

$$\theta_p = \beta_p - 2\pi/p_I = \sqrt{\theta_u^2 - |\kappa_{12}|^2}. \qquad (6)$$

In the equation, β_p is the SAW wavenumber in the IDT with V=0, which is equivalent to the SC grating.

Note that β_p for the OC grating is given by

$$\beta_p = 2\pi/p_I + \sqrt{(\theta_u - 4|\zeta|^2/\omega C)^2 - |\kappa_{12} - 4\zeta^2/\omega C|^2} \qquad (7)$$

from the condition of $I(x)$=0.

Total current I is calculated by the substitution of the general solution into the following equation:

$$I = \int \frac{\partial I(x)}{\partial x} dx = \int (-4j\zeta^{*} U_{+} - 4j\zeta U_{-} + j\omega C V) dx. \quad (8)$$

Simple rearrangement of these results and application of boundary conditions give the three-port model shown in Fig. 2 for the uniform IDT.

When the IDT is not uniform and the simulation parameters are dependent on x, Eqs. (4)-(6) can be solved numerically.

Then the whole structure of a one-port SAW resonator is expressed as an array of the three-port model as shown in Fig. 3. In the figure, Gaps represent structural discontinuities between the IDT and the reflector, and are usually regarded as a simple delay line.

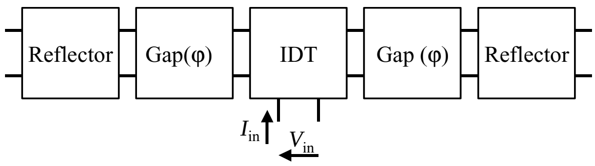

Fig. 3 Behavior model for one-port SAW resonator

Then device characteristics can be readily calculated, provided that parameters κ_{12}, ζ, C and θ_u are determined in advance.

Usually, κ_{12}, ζ and C are almost constant in certain wide range of frequencies. On the other hand, θ_u changes almost linearly with the frequency. So θ_u is often expressed in a following form:

$$\theta_u = \omega / V_g - 2\pi / p_I + \kappa_{11}, \qquad (9)$$

where V_g is the SAW group velocity and k_{11} is a constant called the self-coupling coefficient.

As it will be shown later, this analysis offers fairly good accuracy, especially for devices employing conventional Rayleigh-type SAWs. Of course, accuracy of the analysis is critically dependent upon that of the parameters κ_{12}, ζ, C, V_g and k_{11}.

Here one question arises. How shall we determine these parameters? Ideally, they are determined from SAW propagation characteristics in infinitely long SC and OC gratings. In former days, they were determined experimentally. Presently, various rigorous numerical techniques have been developed and are now widely used for this purpose.

4. Full-Wave Simulation[2]

In this category, the finite element method (FEM), the boundary element method (BEM), the spectral domain analysis (SDA) and their combinations are representative.

Attention should be paid for their use in the simulation of SAW devices. It is known that charge $q(x)$ on IDT fingers concentrates at the electrode edges and diverges in a form of $x^{-0.5}$. Since conventional simulation software assumes continuity of field variables such as the electric flux, the divergence results in very slow convergence of the calculation accuracy with respect to the number of variables.

Fig. 4 shows, as an example, the static capacitance C_0 of the IDT calculated by the BEM. When a piece-wise function is employed to express $q(x)$, the conversion is very bad, and the calculation error decreases in a form of N^{-1}, where N is the number of variables.

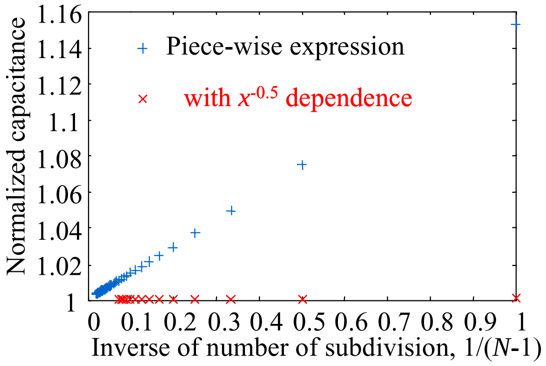

Fig. 4 Static capacitance calculated by BEM.

The figure also shows another calculation where the following expansion functions are used:

$$q(x)=\sum_{n=0}^{N-1}\frac{a_n T_n(2x/w)}{\sqrt{1-(2x/w)^2}}, \quad (10)$$

where $T_n(x)$ is the n-th order Chebyshev function, w is the electrode width, and a_n is the coefficients to be determined. In this case, convergence is very fast. This indicates that the charge divergence must be taken into account appropriately for fast calculation.

It should be noted that conventional FEM tools are based on continuity of field variables and exhibit slow convergence for this kind of problems.

The author and coworkers developed a simulation tool called the FEMSDA for the calculation of SAW excitation and propagation properties of infinitely long gratings with finite electrode thickness h. The SDA is applied for the substrate region. This allows to speed up the calculation, while the substrate surface is required to be flat. On the other hand, the FEM is employed only for the electrode region because it allows arbitrary electrode cross-section and/or structure.

From the FEM/SDA analysis, an effective permittivity is calculated for the structure. Then it is used to determine electrical properties by applying a method proposed Blϕtekær, et al., which allows to take the influence of the charge concentration into account skillfully for infinitely long gratings.

Fig. 5 shows, as an example, calculated SAW phase velocity V_p (=ω/Re(β_p)) and attenuation α (=$-40\pi\log e\times$Im(β_p)/Re(β_p)) with propagation in infinite gratings on a 128°YX-$LiNbO_3$ substrate. As an electrode film, Al was chosen. There is a frequency region where V_p changes linearly and α becomes large. This region is called the stopband where the Bragg reflection occurs.

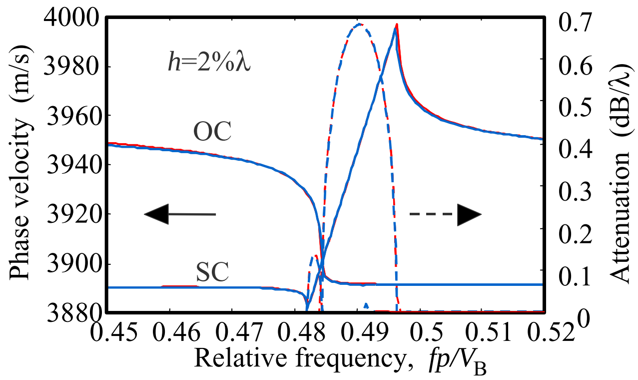

Fig. 5 Calculated SAW phase velocity and attenuation on Al/128°YX-$LiNbO_3$. Thin lines: FEMSDA, and Bold lines: COM. In the figure, V_B=4,025 m/s.

The COM parameters are determined by fitting calculated β_p with that given Eqs. (6) or (7). The figure also shows V_p and α calculated by using Eqs. (6) and (7) with the determined COM parameters. It is seen that these two calculations agree extremely well. This indicates that the COM analysis described in 3 is effective for the simulation of Rayleigh-type SAWs.

So we can construct practical simulators provided that the COM parameters are evaluated as a function of design parameters such as film thickness and width in advance, and the data are stored in an appropriate form for the access at the simulation.

Attention should be paid to the fact that the full-wave analyses require material constants for the electrode film, and they deviate considerably with deposition and etching techniques, equipment and conditions. Material constants for the substrate also change with the wafer supplier and lot. So the estimated COM parameters must be corrected for individual fabrication process by the fitting with experiments.

5. Simulation of SH-SAW Devices[3]

Presently, shear-horizontal (SH) type SAWs are widely used in low-loss RF filters instead of the Rayleigh-type ones. Although behavior-models described in 3 are also applicable to the SH-type SAWs, influence of the bulk acoustic waves (BAWs) must be taken into account for the precise simulation.

Fig. 6 shows, as an example, calculated V_p and α in infinite gratings on a 42°YX-$LiNbO_3$ substrate. As an electrode film, Al was chosen. At first look, their variation with the frequency seems similar to that shown in Fig. 5 at frequencies lower than the upper edge of the stopband. It is seen that α remains relatively large at frequencies higher than the stopband. This attenuation is due to the Bragg reflection (backscattering) of the incident SAW to BAWs.

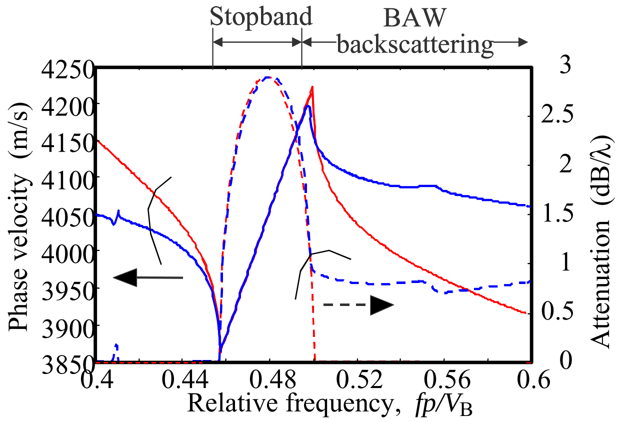

Fig. 6 Calculated SAW phase velocity and attenuation on Al (h=10%λ) /42°YX-$LiTaO_3$. Bold lines: FEMSDA, and thin lines: COM. In the figure, V_B=4,226 m/s.

The figure also shows V_p and α calculated by using Eqs. (6) and (7) with the COM parameters determined by the method described above. In this case, the agreement is poor. This is due to significant reduction of the SAW velocity in the stopband. That is, below the cutoff frequency of the BAW reflection, the scattered BAWs cancel each other, and the cancellation results in reduction in the SAW velocity (energy storing effect). On the other hand, this effect diminishes above the cutoff frequency due to the BAW radiation. Note that scattering amplitude takes a maximum near the cutoff frequency, resulting in maximum velocity reduction.

Various techniques were proposed for taking this effect into account in the behavior model, and are widely used in the design of current RF SAW devices.

It was also shown that the electromechanical coupling strength for the SAW varies significantly near the cutoff frequency of the BAW reflection. Namely, there is a situation where portion of energy radiated as the SAW is converted as the BAW at the grating fingers and is detected by the IDT or vice versa.

Fig. 7 shows the admittance of a one-port resonator on 42°YX-$LiTaO_3$ calculated by taking these effects into account. In the figure, experimental one is also shown. It is seen that their agreement is excellent.

Although the simulation seems perfect, there still remains a room for further improvement. First, the calculation is too slow to use in the computer optimization. Second, it cannot simulate behavior at structural discontinuities properly where the energy storing effect changes abruptly. So our goal is far beyond.

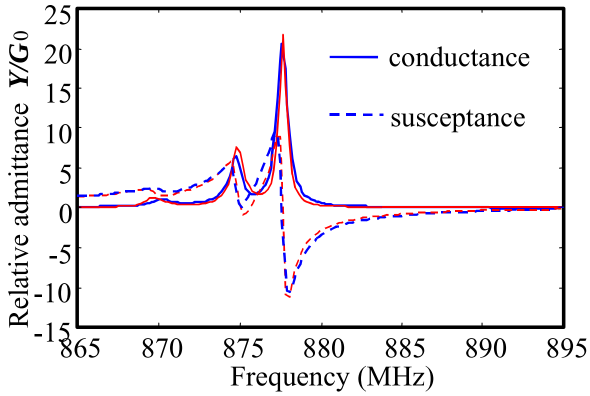

Fig. 7 Admittance of one-port resonator on 42°YX-$LiTaO_3$.Thick lines: experiments, and thin lines: theory.

6. Remaining Tasks

In this paper, the simulation technologies for the RF SAW devices were reviewed.

Once simulation tools are ready, it is a starting point of a trial road. This is because minor effects in former days become obvious after evolution, and further improvement is always necessary.

For example, a little discrepancy can be seen in the conductance just above the resonance. in Fig. 7, this is due to the lateral SAW leakage, and its suppression is one of the hottest topics in the simulation of RF SAW devices.

In addition, although certain amount of additional SAW propagation loss was assumed in the simulation, there is no clear answer where and how the loss occurs. Once the origin is revealed, one may find proper countermeasure which results in further reduction of the device insertion loss. Precise simulators may be also powerful for such investigation.

Acknowledgement

The author thanks to Prof. Yamaguchi, Dr. Omori and all lab members for their cooperation. This talk is given as a part of the international distinguished lecturer program sponsored by the Ultrasonics, Ferroelecctrics and Frequency Control (UFFC) society, the Institute of Electrical and Electronics Engineers (IEEE), Inc.

References

[1] K.Hashimoto: “Surface Acoustic Wave Devices in Telecommunications” (Springer-Verlag, 2000)

[2] K.Hashimoto, T.Omori and M.Yamaguchi: “Analysis of SAW Excitation and Propagation Under Periodic Metallic Grating Structures”, in *Advances in Surface Acoustic Wave Technology, Systems and Applications, Vol. 1*, edited by C.C.W.Ruppel and T.A.Fjeldly, (World Scientific, 2000) pp. 133-182.

[3] K.Hashimoto, T.Omori and M.Yamaguchi: “Modelling of Shear-Horizontal-Type Surface Acoustic Waves and its Application to COM-Based Device Simulation”, Proc. IEEE Ultrason. Symp, (2001) pp. 127-132.

P2-1

Proc. Symp. Ultrason. Electron., Vol. 26, (2005) pp. 213-214
16-18 November, 2005

Probabilistic Superposition of Energy Modes for Treating 2*n*-Layered Mechanical Impedance Mismatch System

Michio Ohki, *Natl. Def. Acad., Japan*

1. Introduction

The existence of mechanical impedance mismatch layers inside an elastic resonance system causes the shift of resonance frequencies and makes the analysis of the system complicated. In this study, a systematic analysis of this problem is performed by considering $2n$ energy modes or complex dynamical variables, η_1, η_2, …, η_{2n}, on the circuit structure representing $2n$-layered system, as shown in **Figs. 1(a)** and **1(b)**.

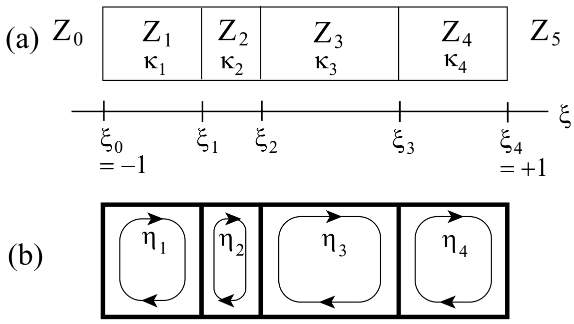

Fig. 1 (a) Resonance system with $2n$ (n =1,2,3,..) mechanical impedance mismatch layers. The i-th (i =1,2,…,$2n$) domain has the mechanical impedance Z_i and the drive ability κ_i. (See ref. 1 with regard to the drive ability.) ξ is a propagation-time-based coordinate. The case of 4-layered system is illustrated. (b) Circuit structure representing (a), in which the energy mode η_i flows clockwise in the i-th block.

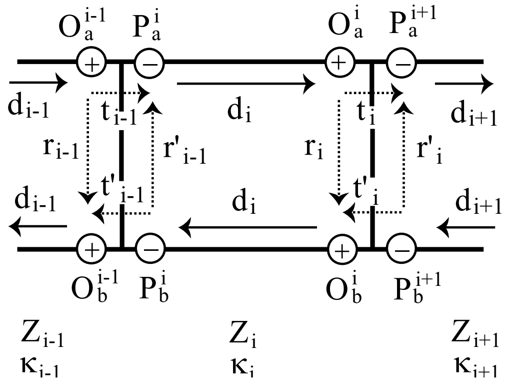

Fig. 2 Behavior of η_i. Terminals P_a^i, O_a^i, O_b^i and P_b^i are located on the i-th circuit block and used for inputting and outputting η_i in which η_i is multiplied by $+\kappa_i$ at O_a^i and O_b^i, and by $-\kappa_i$ at P_a^i and P_b^i. When η_i flows in the circuit, it is also multiplied by d_i, r_i, t_i, r'_{i-1}, t'_{i-1} that represent energy transfer and exchange.

E-mail: michio_ohki@ieee.org

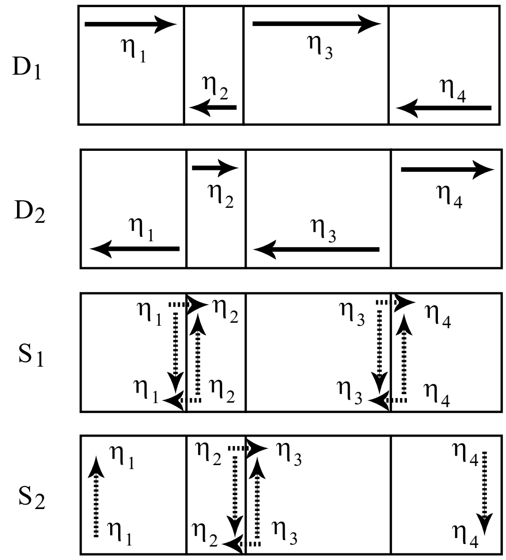

Fig. 3 Operation of matrices D_1, D_2, S_1 and S_2, by which $\boldsymbol{\eta} = (\eta_1, \eta_2, \eta_3, \eta_4)^T$ is multiplied.

2. Formulation of Energy Transfer and Exchange in 2*n*-Layered System

The behavior of η_i is illustrated in **Fig. 2**, in which η_i is multiplied by appropriate multiplication factors. Let us consider a column vector

$$\boldsymbol{\eta} = (\eta_1, \eta_2, \ldots, \eta_{2n})^T \quad \text{(T: transpose)}$$

as a collection of $2n$ energy modes.

We define the matrices D_1, D_2, S_1 and S_2, by which $\boldsymbol{\eta}$ is multiplied, to deal with the behavior of energy modes collectively. The operation of these matrices is illustrated in **Fig. 3** in the case of 4-layered system, and entries of those matrices are given by

$$D_1 = \begin{pmatrix} d_1 & & & \\ & d_2 & & \\ & & d_3 & \\ & & & d_4 \end{pmatrix}, \quad D_2 = D_1 \tag{1}$$

where

$$d_i = \exp(-\mathrm{j}\omega(\xi_i - \xi_{i-1})\pi/(2\omega_0) - \alpha_i), \tag{2}$$

(ω_0 is the characteristic frequency, and α_i is the dissipation factor that is regarded as being in proportion to $\xi_i - \xi_{i-1}$ for the present), and

$$S_1 = \begin{pmatrix} r_1 & t_1' & & \\ t_1 & r_1' & & \\ & & r_3 & t_3' \\ & & t_3 & r_3' \end{pmatrix}, \quad S_2 = \begin{pmatrix} r_0' & & & \\ & r_2 & t_2' & \\ & t_2 & r_2' & \\ & & & r_4 \end{pmatrix}, \qquad (3)$$

with

$$r_i = \frac{Z_i - Z_{i+1}}{Z_i + Z_{i+1}}, \quad r_i' = -r_i, \quad t_i = t_i' = \sqrt{1 - r_i^2}\,. \qquad (4)$$

Since {η_1, η_3} and {η_2, η_4} are considered in a "spatially alternating" manner in the input and output processes, we prepare matrices K_1 and K_2:

$$K_1 = \begin{pmatrix} -\kappa_1 & & & \\ & +\kappa_2 & & \\ & & -\kappa_3 & \\ & & & +\kappa_4 \end{pmatrix}, \quad K_2 = \begin{pmatrix} +\kappa_1 & & & \\ & -\kappa_2 & & \\ & & +\kappa_3 & \\ & & & -\kappa_4 \end{pmatrix}. \qquad (5)$$

The extension of the above formulation into the case of a general $2n$-layered system is easy.

An appropriate matrix product that operates on $\boldsymbol{\eta}$ is expected to represent the "path" of $\boldsymbol{\eta}$ in a *probabilistic* manner, and we regard the superposition of those energy modes, each undergoing one of all possible paths, as a characteristic function of the system, which can be formulated by the infinite geometric series of matrix, Neumann series, as

$$\boldsymbol{\eta}(\omega) = \sum_j K_{\mathrm{out}(j)} (A_{0(j)} + R_{(j)} A_{0(j)} + R_{(j)}{}^2 A_{0(j)} + \cdots) K_{\mathrm{in}(j)} \boldsymbol{\eta}_0 \qquad (6)$$

as a function of ω, where j is an index to classify the path, $A_{0(j)}$ and $R_{(j)}$ are the *initial term* and the *common ratio*, respectively, of the infinite geometric series that represents the superposition of "possible paths," $K_{\mathrm{in}(j)}$ and $K_{\mathrm{out}(j)}$ are multiplication factors for input and output processes, respectively, and $\boldsymbol{\eta}_0 = (1, 1,\ldots,1)^{\mathrm{T}}$ is an initial value of $\boldsymbol{\eta}$.

Consideration of all possible paths, by inspecting Figs. 2 and 3, leads to the construction of 16 cases of $A_{0(j)}$, $R_{(j)}$, $K_{\mathrm{in}(j)}$ and $K_{\mathrm{out}(j)}$, as listed in **Table I**.

3. Calculation Results and Their Interpretation

We investigate a few examples of 4-layered system, #1, #2 and #3, illustrated in **Fig. 4**. The #2 and #3 are physically identical. The resonance frequencies and the resonance intensities (normalized appropriately) of the system are calculated from eq. (6), which is summarized in **Table II**. The summation of η_i over i = 1 to 4, $\Sigma\eta_i$, is also calculated for each case.

Comparing these results with those from Mason's equivalent circuit for 3-layered system,[2] we find that both the resonance frequencies and the resonance intensities are correctly obtained, if we regard $\Sigma\eta_i$ as the resonance intensity of the system. Each η_i indicates the "spatial distribution" of $\boldsymbol{\eta}$.

When layers are such that $2n$ = 2,4,8,16,…, each with $2n$ equal intervals, the methodology of multi-resolution (wavelet) analysis of level 0,1,2,3,…, respectively, for treating spatially inhomogeneous structure[1] can be applied.

Table I 16 cases of matrix parameters in eq. (6) considered using Figs. 2 and 3. $R_1 = D_1S_2D_2S_1$, $R_2 = D_2S_1D_1S_2$, $R_3 = S_1D_1S_2D_2$, and $R_4 = S_2D_2S_1D_1$ below.

j	$A_{0(j)}$	$R_{(j)}$	($K_{\mathrm{in}(j)}$, $K_{\mathrm{out}(j)}$)	j	$A_{0(j)}$	$R_{(j)}$	($K_{\mathrm{in}(j)}$, $K_{\mathrm{out}(j)}$)
1	D_1	R_1	(K_1, K_2)	9	$S_2D_2S_1$	R_4	(K_2, K_1)
2	D_2	R_2	(K_2, K_1)	10	$S_1D_1S_2$	R_3	(K_1, K_2)
3	S_1D_1	R_3	(K_1, K_2)	11	R_4	R_4	(K_1, K_1)
4	S_2D_2	R_4	(K_2, K_1)	12	R_3	R_3	(K_2, K_2)
5	D_2S_1	R_2	(K_2, K_1)	13	R_1	R_1	(K_2, K_2)
6	D_1S_2	R_1	(K_1, K_2)	14	R_2	R_2	(K_1, K_1)
7	$D_2S_1D_1$	R_2	(K_1, K_1)	15	R_3S_1	R_3	(K_2, K_2)
8	$D_1S_2D_2$	R_1	(K_2, K_2)	16	R_4S_2	R_4	(K_1, K_1)

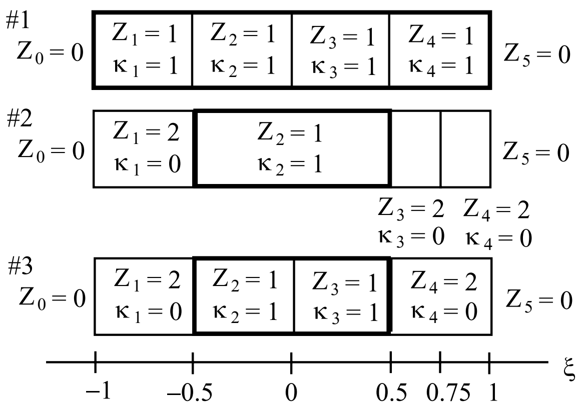

Fig. 4 Boundary conditions of calculation examples.

Table II Calculation results for examples #1-#3 of 4-layered system. ω_{res} is the resonance frequency of the system, normalized as $\omega_0 = 1$.

#	ω_{res}	η_1	η_2	η_3	η_4	$\Sigma\eta_i$
1	1.000	0.144	0.356	0.356	0.144	1.000
	3.000	0.856	-0.356	-0.356	0.856	1.000
2	0.7836	0	0.333	0	0	0.333
	3.2164	0	0.333	0	0	0.333
3	0.7836	0	0.167	0.167	0	0.333
	3.2164	0	0.167	0.167	0	0.333

1) M. Ohki: Jpn. J. Appl. Phys. **44** (2005) 275.
2) M. Ohki and K. Toda: J. J. A. P. **41** (2002) 3413.

Proc. Symp. Ultrason. Electron., Vol. 26, (2005) pp. 215-216
16-18 November, 2005

Control of acoustic streaming induced by a focusing source with two coaxially arranged transducers *

Kazuhisa Matsuda (Sunagawa High School)
Tomoo Kamakura (University of Electro-Communications)
Miyuki Maezawa (Olympus Co. LTD)

1 Introduction

Acoustic streaming occurs because of momentum being transferred from the wave to fluid through energy dissipation in the wave caused by sound absorption. It is evident that the characteristics of acoustic streaming depend temporally and spatially on the characteristics of sound field. This means that it is possible, for example, to control the streaming by changing sound fields appropriately. The present report, therefore, is primarily concerned with some experimenal demonstrations on a simple control method of the streaming by varying the phase difference of two initial ultrasound waves emitted from a focused transducer.

2 Experiments and discussion

An ultrasound transducer as a source consists of two coaxially arranged confocal piezoelectric elements of an inner disc and an outer ring. Their active surfaces are almost the same: the diameter of the disc element is 27.2 mm, and the inner and outer diameters of the ring element are 29.2 mm and 40 mm, respectively. Both the elements have the same resonance frequencies of 3.45 MHz and the same focal lengths of 60 mm. The transducer is flush-mounted on a side wall of a tank filled with fresh water.

Two electric tone-burst signals of 3.45 MHz and of about 50 cycles duration fed from a function generator are power-amplified individually and are applied to the transducer. The amplitudes and phases of the signals can be varied precisely. Let the phase difference between the two signals be θ. When the phase angles are equal: i.e., $\theta = 0$, the signals are in-phase. The signals are out of phase when $\theta = 180°$. A needle-type hydrophone with an active diameter of 0.5 mm that picks up local sound pressure is mounted on a translation stage driven by stepping motors.

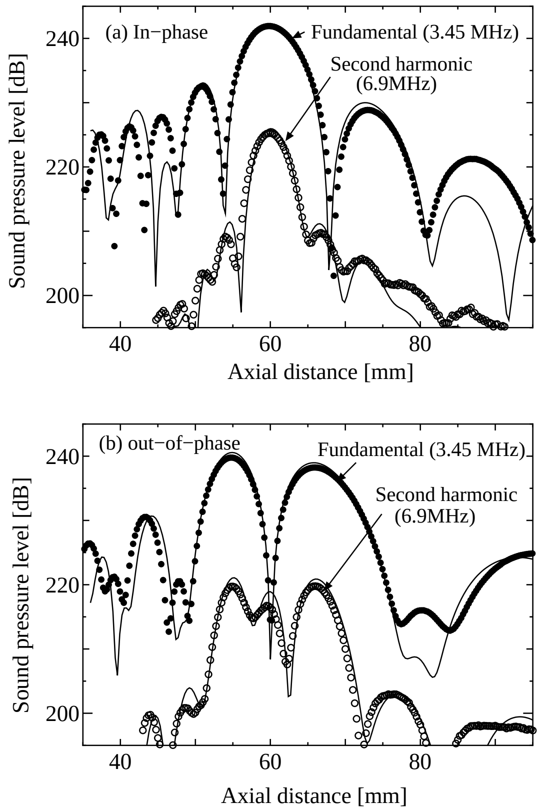

Fig. 1 Fundamental and second harmonic sound pressure levels on the beam axis. Above: in-phase case ($\theta = 0$), bellow: out of phase case ($\theta = 180°$).

Figure 1(a) shows on-axis sound pressure amplitudes of fundamental frequency 3.45 MHz and second harmonic frequency 6.9 MHz for the case where the two electric signals are in-phase. Circle symbols in the figure are all measured data, and solid curves the theoretical prediction based on the spheroidal beam equation (SBE) [1]. As can be seen, the theory agrees very well with the experiment.

Acoustic streaming was observed in the same water tank using laser Doppler velocimetry. Axial distribution of the streaming velocity is shown in Fig. 2. Circles in black and white

* Tachikawa-shi, 190-8583, Tokyo.

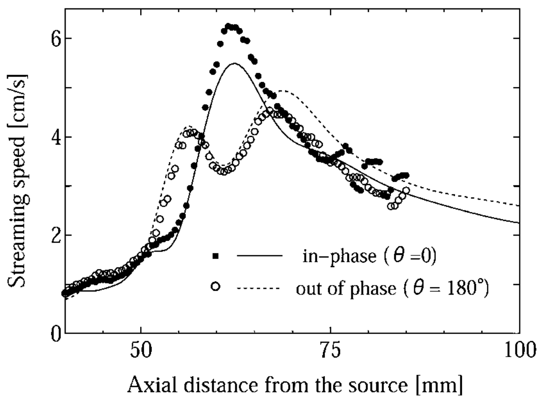

Fig. 2 Axial profiles of streaming speed for $\theta = 0$ and $\theta = 180°$.

are all the measured data, and solid and dotted curves the theoretical data that are numerically predicted by the stream-function vorticity method [2]. Overall, the streaming speed is accurately predicted by the theory. The in-phase excitation accelerates the flow near the focus and attain a maximum speed of 6.3 cm/s at around 62mm just behind the focus. After that, the speed is gradually decreased. The speed profile for the out-of-phase excitation is different: two distinct peaks of the speed appear at 56 mm and 68 mm, and the streaming is slightly faster at the latter point by 5 mm/s.

Axial speed profiles in the plane perpendicular to the axis are given in Fig. 3, where the plane is located at $z = 61.5$ mm, just behind the focal plane. Symbols and notations are the same as those in Fig. 2. In the paraxial region less than 2 mm from the axis, the theoretical predictions accord with the experimental data in a relatively good fashion. Away from the point, however, the measured speeds are overall larger the computed data.

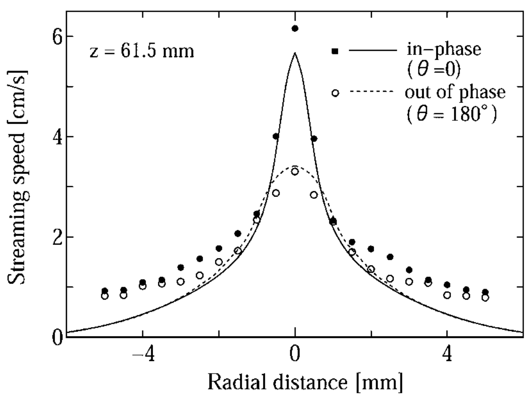

Fig. 3 Axial streaming speed at $z = 61.5$ mm.

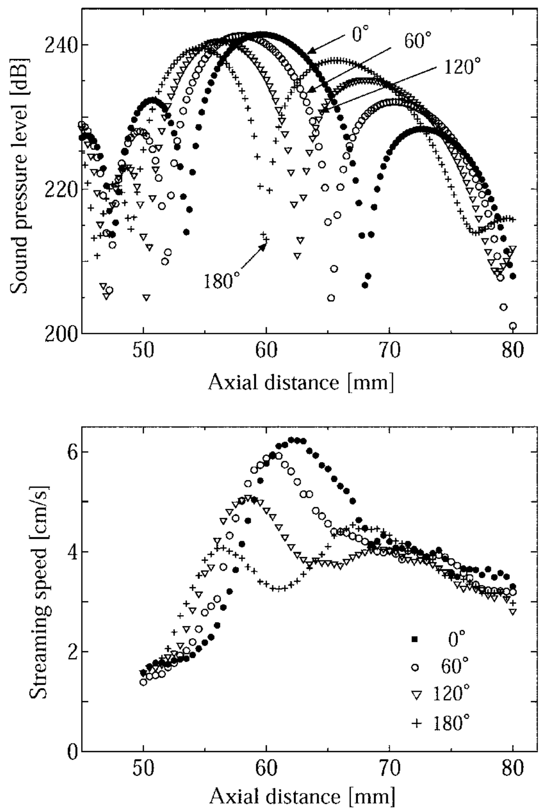

Fig. 4 Measured data of the sound pressure (above) and streaming speed (below) on the axis. The angle is changed 0, 60°, 120°, and 180°.

Experimental data are shown for the sound pressure and speed profiles only when the phase difference θ is changed from 0 to 180° by an increment of 60°. Further measurements were carried out for $\theta = 240°$, 300°, and 360°. However, the data are not shown here because of their similar profiles as Fig. 4. Evidently, these experiments suggest that it is feasible to control the field of acoustic streaming by changing the distribution of sound pressure.

This work is partially supported by the Ministry of Education, Science, Sports and Culture, Grant-in-Aid for Exploratory Research, 16656062.

References

[1] T. Kamakura, T. Ishiwata, and K. Matsuda, "Model equation for strongly focused finite-amplitude sound beams," J. Acoust. Soc. Am. **107**, 3035-3046 (2000).

[2] T. Kamakura, K. Matsuda, Y. Kumamoto, and M. A. Breazeale "Acoustic streaming induced in focused Gaussian beams," J. Acoust. Soc. Am. **97**, 2740-2746 (1995).

P2-3

Proc. Symp. Ultrason. Electron., Vol. 26, (2005) pp. 217-218
16-18 November, 2005

Brillouin Scattering Spectroscopy on α–β Phase Transition of Quartz Using an Angular Dispersion-Type Fabry-Perot Interferometer

◎Shinya Tsukada†, Yuji Ike, Jun Kano and Seiji Kojima (Univ. Tsukuba, PAS, Japan)

1. Introduction

In material sciences, it is important to measure the physical properties of materials without contact and nondestructively. Light scattering measurement is one of them. Brillouin scattering spectroscopy is an optical method to measure the elastic property. In this report, temperature dependence of Brillouin scattering of a well-known quartz crystal was measured in two different geometries using an Angular Dispersion Fabry-Perot Interferometer (ADFPI). ADFPI is the very powerful tool to measure Brillouin scattering [1]. ADFPI has been solved some problems that scanning type FPI has. So far ADFPI has been applied to the measurement of the liquid-glass transition and has shown its excellent ability [2]. For the measurement of solid materials, Brillouin scattering of a quartz crystal, a quartz glass and lithium niobate crystal were measured at room temperature. While no structural phase transition has not yet observed [3]. In this report, we have succeeded the observation of structural phase transition using ADFPI for the first time.

A quartz crystal is one of the most popular crystals as a jewel, piezoelectric device and optical elements and so on. In the point of physics, some unique phenomena are known and they have attracted many physicists. The α-β phase transition is one of the unique phenomena of quartz crystals. It undergoes a phase transition at 573 °C from its low temperature α–phase with point symmetry D_3 to its high temperature β–phase with point symmetry D_6 [4].

2. Experimental

The schematic diagram of the ADFPI is shown in Fig.1. The light source was a diode-pumped solid-state laser (DPSS, Coherent) with a ring cavity operating at 532 nm with 100 mW. The scattered light was collected with the scattering angle of 90°. The interference fringes can be observed after passing through a FPI. ADFPI is composed of a solid etalon which is mechanically stable. Very high reflectivity coating was used for an etalon to obtain high contrast and high resolution. The transmitted light through an etalon was focused onto a CCD detector. The exposure time of CCD detector was 120 seconds which became much shorter than that of the conventional scanning method. The sample temperature was controlled by the tube-shaped furnace.

The combination of a CCD detector, a solid etalon and a light source with high stability of wavelength enables to make acquisition time much shorter than that of a scanning FPI and to make resolution higher.

The synthetic quartz crystal with 6×7×8 mm along the X, Y and Z axes respectively was used as a sample of which six faces were polished to optical grade. A crystal of high quality makes the Rayleigh scattering small and enables to measure lower frequency scattering.

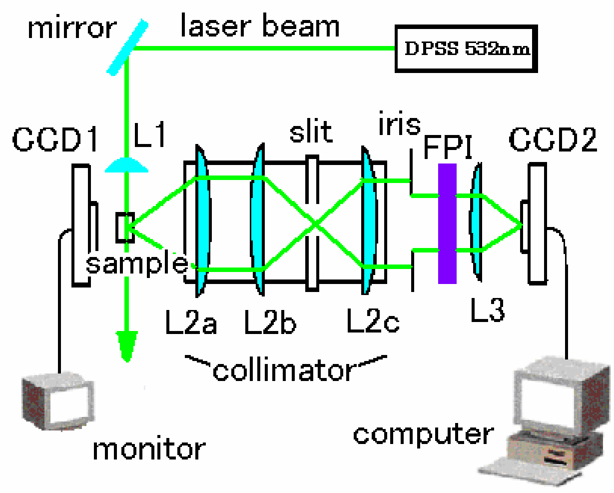

Fig. 1. Schematic diagram of experimental setup of ADFPI.

†s-tsukada@ims.tsukuba.ac.jp

3. Results and discussion

Acoustic phonons propagating in the [100], [010] directions were studied in this report. Fig. 2 shows the spectra with the [010] direction at several temperatures.

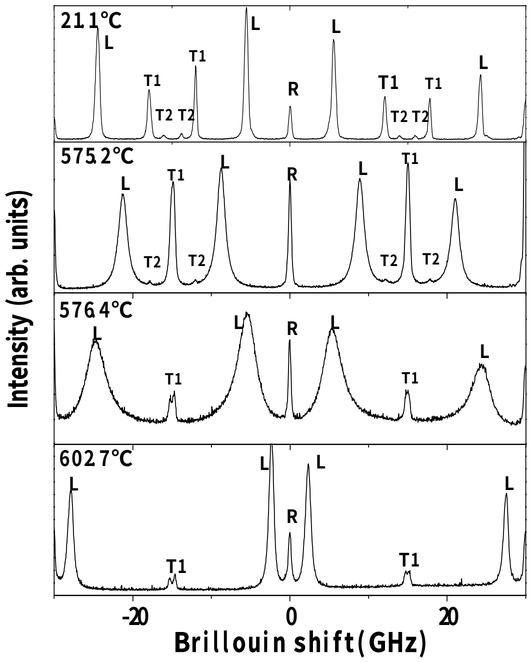

Fig. 2. Brillouin spectra of the phonon propagating the [010] axis of a quartz crystal. L, T1 and T2 denote the Brillouin components scattered by the longitudinal acoustic phonon, transverse acoustic phonons, respectively. R denotes the Rayleigh scattering.

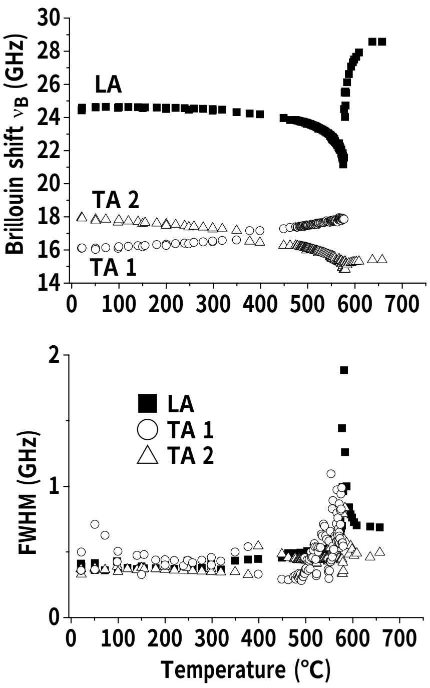

Fig. 3. Temperature dependences of Brillouin shift and full width at half maximum of a quartz crystals.

Shapiro *et al*, already measured Brillouin scattering of quartz [5,6,7] and showed their spectrum at room temperature [6,7]. Compared with their spectrum at room temperature, our spectra had better resolution, because finesse of ADFPI was around 80.

The temperature dependence of Brillouin shift and full width at half maximum (FWHM) of the [010] phonon were obtained from the Lorentzian fitting as shown in Fig. 3. In the vicinity of the $\alpha-\beta$ phase transition temperature, the anomaly of Brillouin shift was clearly observed. In particular, the anomaly of longitudinal wave was apparent. One transverse mode disappeared above the phase transition temperature. It is attributed to the change of the crystal structure into D_6. The transition temperature observed was 574 ^{o}C that is 1 ^{o}C higher than the temperature reported in [4,5]. The FWHM shows a peak at the phase transition temperature. FWHM is related with the damping constant [8], the attenuation of the sound wave became larger above the phase transition temperature. It is known that incommensurate phase exists in the range of 1.4 ^{o}C around the phase transition temperature [9]. Elastic anomaly related to an incommensurate phase between α and β phases could not be obtained in the present experiments.

In summary, we applied ADFPI to the study of structural phase transition for the first time and successfully obtained spectra with the variation of temperatures. In the vicinity of the α-β phase transition temperature, the anomaly of Brillouin shift and FWHM were clearly observed.

References

[1] Jae-Hyeon Ko and Seiji Kojima: Rev. of Sci. Inst. **73** (2002) 4390

[2] Yuji Ike and Seiji Kojima: J. Mol. Struct. **744** (2005) 521

[3] Yuji Ike and Seiji Kojima: J. Kor. phys. soc. **46** (2005) 90

[4] Robert B. Sosman: *The properties of silica*, (The Chemical Catalogu Company, Inc. New York, 1927)

[5] S. M. Shapiro and H. Z. Cummins: Phys. Rev. Lett. **21** (1968) 1578

[6] Stephen M. Shapiro, Robert W. Gammon and Herman Z. Cummins: Appl. Phys. Lett. **9** (1966) 15

[7] Stephen M. Shapiro and Herman Z. Cummins: Proc. the International Conference on Light Scattering Spectra of Solids (1968) 705

[8] Terutaro Nakamura: *Ferroelectricity involved in Structual Phase Transition* (Shokabo Tokyo, 1998)

[9] G. Dolino and P. Bastie: J. Phys. Condens. Matter **13** (2001) 11485

Proc. Symp. Ultrason. Electron., Vol. 26, (2005) pp. 219-220
16-18 November, 2005

Analysis of stress-induced ferroelectric domain structure by ultrasonic atomic force microscopy

◎Seishiro Ide, Toshihiro Tsuji, Kazushi Yamanaka (Tohoku University)

1. Introduction

Ferroelectric materials applied to piezo-actuators are expected to experience combined electrical and mechanical loads. However, only few studies on stress-induced ferroelectric domain structure have been made [1]. In this paper, we report an attempt to analyze ferroelectric domain structure induced using nanoindentation and compare the elastic and piezoelectric properties on the nanoscale.

2. Experimental method

We applied a nanoindentor attached to an atomic force microscope (AFM) with cube cornered diamond tip on polished ferroelectric samples. We prepared PMN-PT single crystal (sample 1) and soft PZT without poling (NEC Tokin, N-21) (sample 2), and indented up to maximum load 1500μN and 1000μN, respectively. We used ultrasonic atomic force microscopy (UAFM) [2-4] and piezo-response force microscopy (PFM) [5] to observe before and after indentations, where we applied 2nd deflection mode in UAFM, which is effective in stiff materials.

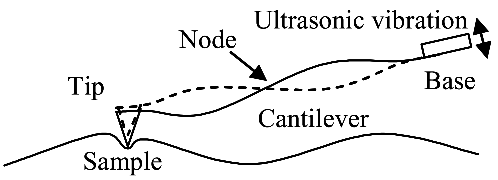

Fig.1. Schematic illustration of UAFM at the 2nd deflection mode.

3. Result and discussion

3.1. PMN-PT single crystal

Figure 2 shows a result of the observation of nanoindentation on sample 1. Fig.2 (a) is AFM topography. The directions of arrows show crystallographic orientations. In spite of using a cube cornered tip, the upheaval around the indentation was of rectangular shape. It may be related to crystallographic structure. Fig.2 (b) is a 3D view around indentation, where grayscale is inverted to highlight the shape of the indentation. Fig.2 (c) and (d) are UAFM images representing the resonance frequency and the amplitude at resonance [3,4]. We observed that both frequency and amplitude were high in the center of the indentation, and low in the periphery of indentation. We consider that the high frequency probably includes an artifact due to the steep slope in the center of indentation, but the low frequency showed elastic property because of gentle

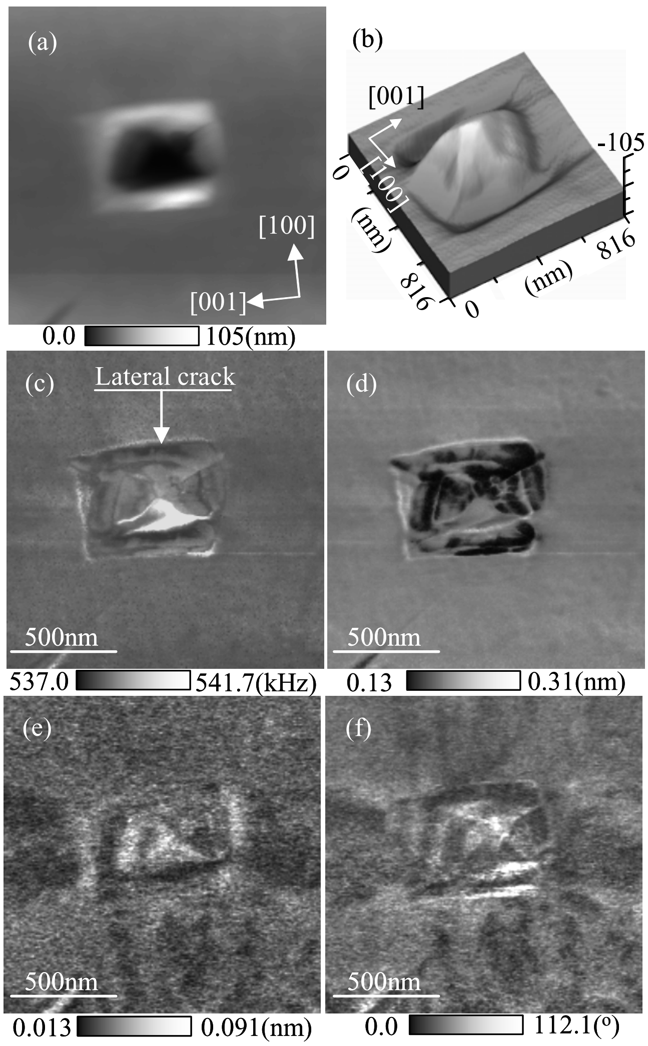

Fig.2. Nanoindentation on PMN-PT single crystal. (a) Topography. (b) 3D view around indentation. Grayscale is inverted. UAFM image representing (c) resonance frequency and (d) amplitude at resonance. PFM image representing (e) amplitude and (f) phase shift.

slope around indentation. The latter can be explained by the decrease of effective stiffness due to lateral cracks [6].

On the other hand, PFM images showed both increase and decrease of amplitude (Fig.2 (e)) and delayed phase (Fig.2 (f)) in the periphery of the indentation.

Around the indentation, we observed the decrease of amplitude and delayed phase expanding towards [100] and [001] directions. Since they had not been observed before indentation, we consider that a crystallographic reorientation caused by the stress field decreased the piezo-response in these regions. They were observed as a slight increase of frequency in UAFM images.

3.2. Soft PZT ceramics

Figure 3 shows the observation of nanoindentation on sample 2, where solid squares show common area. Fig.3 (a) and (b) are AFM topography and 3D view

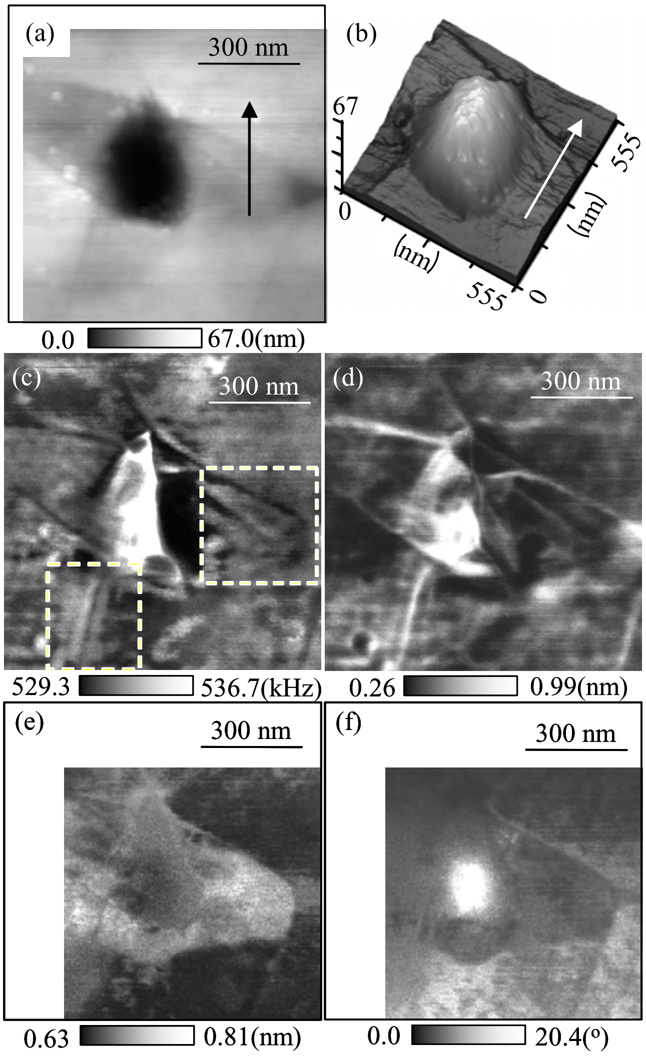

Fig.3. Nanoindentation on soft PZT ceramics. (a) Topography. (b) 3D view around indentation. Grayscale is inverted. UAFM image representing (c) resonance frequency and (d) amplitude at resonance. PFM image representing (e) amplitude and (f) phase shift.

around indentation. There was not a steep edge due to the corner of indentor. Fig.3 (c) and (d) show UAFM images representing resonance frequency and amplitude.

Within the indentation, there was a high frequency region surrounded by a sharp boundary (Fig.3 (c)). In Fig.3 (d), this region showed increase of amplitude. Fig.3 (e) and (f) show PFM images representing amplitude and phase shift. In Fig.3 (e), there was decrease of amplitude within the indentation (Fig.3 (a)). This may be related to the high frequency region in Fig.3 (c). In Fig.3 (f), phase was advanced in the center of the indentation. In the regions around the indentation indicated by broken lines, we observed cyclic changes of frequency (Fig.3 (c)). Since they were not observed in topography (Fig.3 (a)) and UAFM image before indentation, we consider that they are structures induced by stress field during nanoindentation.

3.3. Common structure in both samples

In both samples, we observed stress induced structures around indentations. In PMN-PT, these structures were induced along (100) directions. In PZT, these structures located similarly to PMN-PT. We consider that they are related both to the stress field and to the crystallographic orientation.

4. Conclusions

We compared the elastic and piezoelectric properties of ferroelectric materials on the nanoscale by simultaneous observation within and around nanoindentations using ultrasonic and piezo-response atomic force microscopy. Then a sign of the stress induced ferroelectric domain structures was obtained. We believe that this observation method will be useful for comprehensive evaluation of these materials applied to actuators.

Acknowledgements

This work was supported by the Ministry of Education, Culture, Sports, Science and Technology.

References

[1] D. Liu and K. W. White: Appl. Phys. Lett., **85** (2004) 3459.

[2] K. Yamanaka and S. Nakano: Jpn. J. Appl. Phys., Part 1, **35** (1996) 3738.

[3] T. Tsuji, H. Ogiso, J. Akedo, S. Saito, K. Fukuda and K. Yamanaka: Jpn. J. Appl. Phys., Part 1, **43** (2004) 2907.

[4] T. Tsuji, S. Saito, K. Fukuda, K. Yamanaka, H. Ogiso, J. Akedo and Y. Kawakami: Appl. Phys. Lett., **87** (2005) 071909.

[5] A. Gruverman, O. Auciello and H. Tokumoto: Appl. Phys. Lett., **69** (1996) 3191.

[6] K. Yamanaka, Y. Enomoto and Y. Tsuya: IEEE. Trans. Sonics and Ultrasonics, **32** (1985) 313.

P2-5

Proc. Symp. Ultrason. Electron., Vol. 26, (2005) pp. 221-222
16-18 November, 2005

Study on Layer Mode Device on GaN/Al_2O_3

Manabu Yokota, Chinami Kaneshiro, Kazumi Nishimura*, Naoteru Sigekawa*, and Kohji Hokawa
Kanagawa Institute of Technology, ＊) NTT Photonics Laboratories

I.Introduction

GaN film has many features as semiconductor devices, such as blue light emitting diodes, refractive transistors and ultra violet wave sensors, etc. The system also has piezoelectricity and expected for new semiconductor coupled acoustic wave functional devices in higher frequency range in a future. Layer modes are effective for fabricating higher frequency devices under conditions of the limited fabrication technology for realizing small size pattern. Based on a view point of device design, we studied layer modes on GaN/Al_2O_3 system using result of mode calculations and experiments. The layer mode has shown a relatively wide band characteristics and an interesting response on delay.

II.Experimental conditions of layer mode devices

In order to study actual potential of device performance, we have fabricated delay lines on GaN films (including a commercially available film) and measured device characteristics. Parameters used in the experiment are listed in Table I.

Table I Experimental device parameters

GaN films	4 kinds of films, including commercially available. Film thickness 0.15um, 2 um
Substrate Prop. direction	Sapphire (c-plane) <1-100> and <11-20>
IDT N. of pairs	50 pairs uniform overlap 25 pairs for low freq. device
Line & space	0.8um, 2um, 4um
Path length	2.5 mm, 5 mm

In this experiment, we adopted film thickness smaller than wave length (4 times of line width).

III. Experimental result

A. Effect of propagation direction

The layer mode was sensitive to the orientation of sapphire substrate, namely, propagation direction of waves. Figure 1 and 2 compares dependence of frequency responses on propagation directions. In the case of device with the propagation direction along <11-20>, the layer waves are relatively well confined in a film, because the effective velocity in sapphire substrate is faster than that in GaN. On the other hand, devices with propagation direction <1-100>, energy confinement in layer is relatively low. The layer mode does not exist under the same wave number at which the wave along <11-20> has multi mode transmission ode condition.

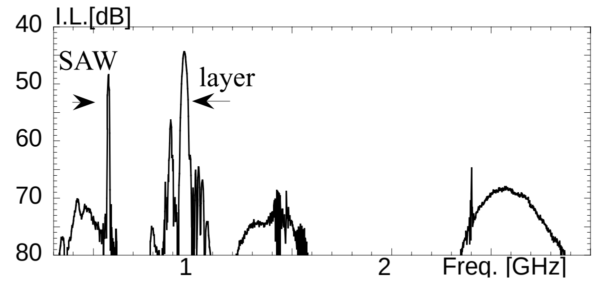

a) Path length=2.5mm LS=2um, kH=1.57

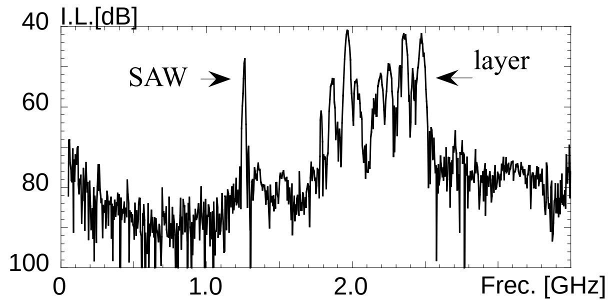

b) Path length=5mm LS=0.8um kH=3.93

Figure 1 Response for <11-20> prop. direction

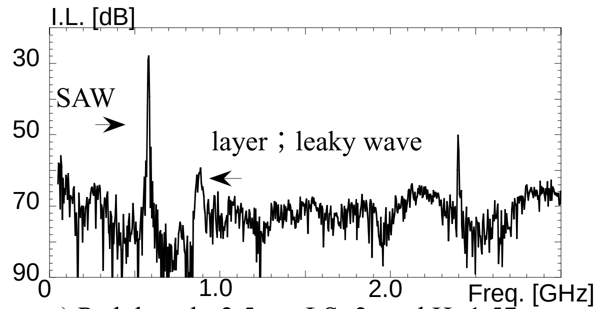

a) Path length=2.5mm LS=2um, kH=1.57

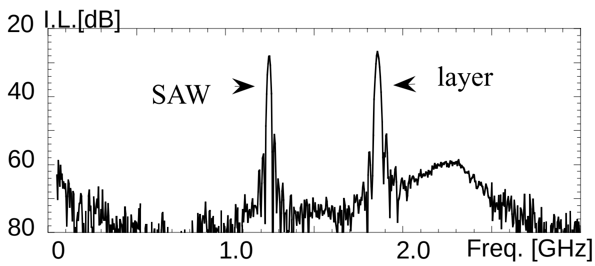

b) Path length=5mm LS=0.8um kH=3.93
Figure 2 Response for <1-100> prop. direction

B. Single mode condition

Experimental result have shown that the single mode operation was stably obtained at the conditions of kH values 1 and 4 for propagation direction of <11-20> and <1-100>, respectively. This condition agrees well with calculation values. At these single mode conditions, the frequency responses are relatively simple. Therefore, we can design by a simple method just including dispersion characteristics on conventional design method used for SAW devices.

C. Multi-mode condition

Figure 4 shows pass band characteristics of layer mode device with the propagation direction of <11-20>. The devices have relatively wide pass band characteristics and group delay characteristics with negative dispersion (delay decrease with frequency increase). These effects could not be estimated by the simple mode calculation. We can explain responses reasonably, if we would define that two layer modes propagates along the layer with different propagation velocity and it couples on the propagation path. In this operation, the frequency response detected by the same output transducer varies depending on the propagation path length from input transducer. The center frequency, at which maximum output signal is obtained, also varies, as shown in the figure 3. In addition, negative dispersion appears by the effective propagation path reduction caused by the interference effects of two modes. By controlling propagation path length and mode interaction, which depends on film thickness, we can design devices with a wideband frequency response.

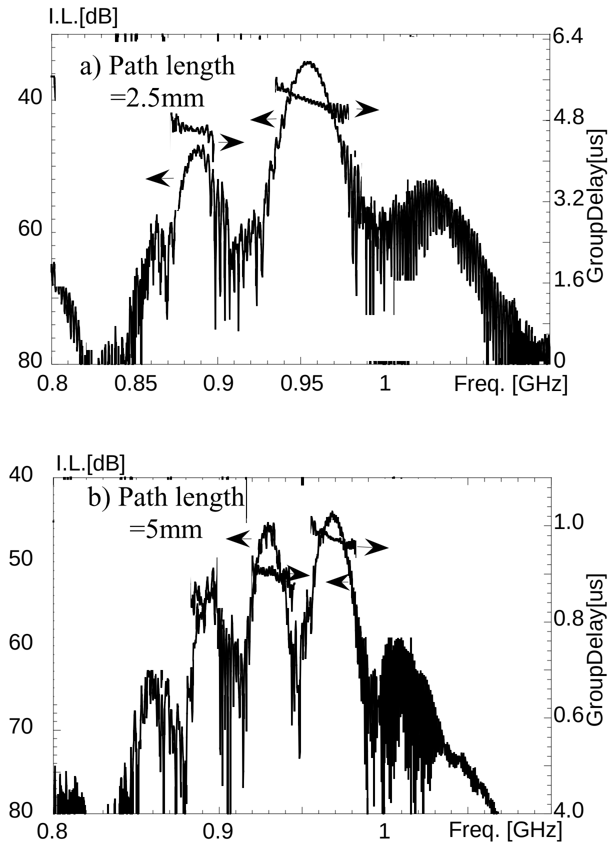

L&S=2um, Thickness 2um, 50-50 pairs IDT

Figure 3 Multimode responses along <11-20>

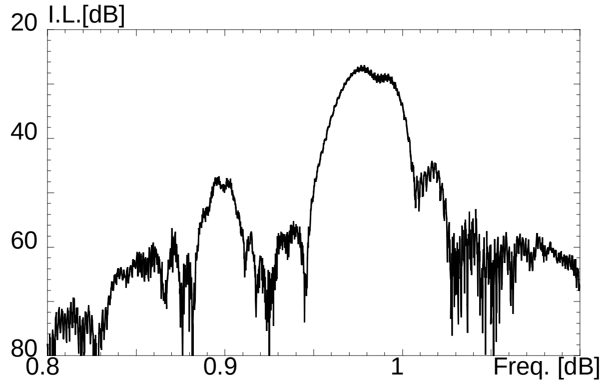

Figure 4 Response of multi mode device with wide bandwidth

fIV. Conclusion

We have experimentally studied layer mode devices on GaN/sapphire substrates. The results clarified that the device is useful for various high frequency devices at the condition of single mode operation. At the multimode condition, layer mode devices showed a relatively flat and negative dispersion characteristic. The devices also have a mode coupling effect, which would be effective for realizing high speed and wide band devices. Future works should be focused on the improving reproducibility.

Acknowledgement

The authors wish to thank Associate professor. Koh for his valuable discussion. This work is supported by the fund for Advance Technology Center from the Ministry of Education, Culture, Sports, Science and Technology.

References

[1] Y. J. Kim, G. H. Lim etc. “SAW Characteristics of GaN Epitaxial Films Deposited on Different Plane,” Proc. IEEE Ultrasonic Symp. **1** 427-430 (2002).

[2] K. Hohkawa, C. Kaneshiro, K. Koh, K. Nishimuru and N. Shigekawa, “Study on Photo-induced Acoustic Charge Transport Effect in GaN Film” IEEE MTS Symp. WE1B, June 15, 2005.

[3] N. Shigekawa, K. Nishimura, H. Yokoyama, “Side gate effect GaN SAW device” USE 2004 Proc. 2-17, pp. 191-192 (2004).

P2-6

Proc. Symp. Ultrason. Electron., Vol. 26, (2005) pp. 223-224
16-18 November, 2005

Acoustic Wave Device Using GaN film with n+ Conduction Layer

Takahiro Mizusawa, Masaya Wada, Keishin Koh, Kazumi Nishimura*, Naoteru Sigekawa*, and Kohji Hokawa
Kanagawa Institute of Technology, ＊) NTT Photonics Laboratories

1. Introduction

By using epitaxially grown highly conductive semiconductor layer, deposited on the insulating semiconductor film, such as GaAs, and GaN, as electrode elements, it is possible to fabricate IDT's without metal electrodes [1], [2]. In addition, if we place the conductive film under layer in multiple epitaxial films, we could obtain new types of functional devices. This paper studies SAW devices having electrode elements consisting of epitaxially grown GaN film with highly conductive layers, and clarify the potentials of this structure.

2. SAW devices with n+ layer electrodes

Since n+ layer has the same nature as that of conductive metals, its role in SAW device is to form electrodes pairs and some kinds of control electrodes. There are two basic structures for applying electrodes of transducer. One is a surface electrode, which is the same as that of conventional metal electrodes of IDT. The other is buried electrode, which would be difficult for conventional metal electrodes to grow piezoelectric film with single crystal semiconductor film with a crystallography good enough to form high performance semiconductor devices. This element makes it possible to control and detect electric field. This nature would lead on SAW devices many improvements stated as follows.

1) We can improve performance of semiconductor SAW coupled devices, such as convolver and programmable devices.
2) This structure allows monolithic fabrication of transducer with transistors using the same layer structure (co-integration).
3) Co-integration would leads new functional device utilizing semiconductor.
4) This enables transducer with lateral field excitation, which extends the fabrication limit of pattern size.

Here, we report some experimental results using epitaxially grown n+ GaN film.

genni@ele.kanagawa-it.ac.jp

We fabricated two kinds of device; namely, 1) n+ layer on the surface; IDT is formed by etching n+ layer as shown in Figure 1, and 2) n+ layer under the piezoelectric layer; metal electrodes are formed on the surface of piezoelectric layer. In this structure, we can estimate two kinds of devices, namely single and dual phase metal electrodes as shown in Figure 2.

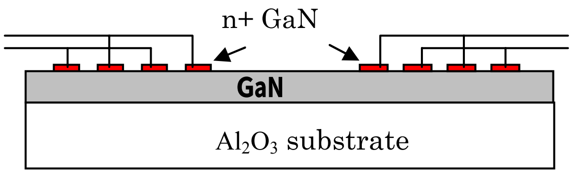

Fig.1 IDT with surface n+ layer

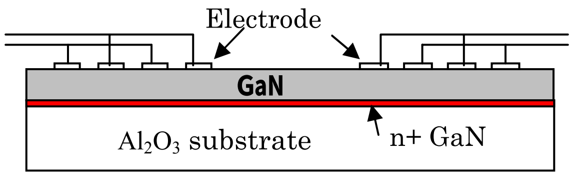

a) Dual electrode

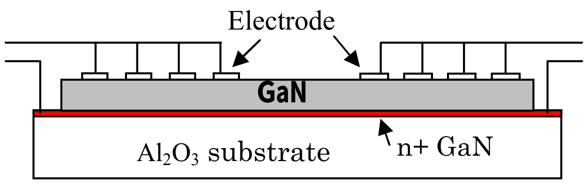

b) Single phase type

Fig.2 Test devices with buried n+ layer

Table I. Parameter of test device

Substrate	GaN on Al_2O_3
Thickness of GaN film	2 μm
Thickness of n+ layer	400 nm
IDT line &space	2μm:2μm / 0.8μm:0.8μm
Overlap. length	800 μm / 400 μm
Number of pairs	50-50 pairs
Prop. length	2.5 mm

3. Experimental results

Table I lists device parameters used for the experiments. We have fabricated a device with IDTs consisting of n+ layer with carrier densities larger than $10^{18}/cm^3$. We have used Cl_2 gas dry etching process for patterning. Compared to the metal electrode, the resistance of semiconductor electrodes is slightly large, but response was almost same as the device with usual metal electrodes. The precise result is reported in reference 2. Figure 3 illustrates experimental result of a device with buried n+ layer device. Compared to the responses of conventional (without n+ layer) device, this device is a comparable insertion loss to that of conventional device at a high frequency range. However, at a lower frequency the insertion loss was relatively large. This difference is mainly caused by the difference in amplitude distribution in the depth direction and also the conductance of layer mode. We also observed the direct feed through can not be reduced even if we connect n+ layer to the ground level. This is also mainly caused by the direct feed through signal path through the n+ layer. This problem is also solved if we decrease resistance of the layer.

The energy loss in lower frequency device is mainly caused by the resistance of n+ layer which closes critical conductance of propagation SAW. The loss would be reduced, if we could enhance conductivity of n+ layer. For the higher frequency device, since the wavelength is comparable with the film thickness and the large fraction of electric field is effectively applied to the film surface and the fraction of electric field in n+ layer become to be weak. (ref. Fig.3 (e) and Fig.3 (d)).

4. CONCLUSION

Experimental result confirms the effectiveness of n+ layer for transducer electrodes. For buried structure the layer, it would be required much more highly conductive layer to isolate from electromagnetic coupling. We have now fabricating a device with circuit structure as shown in Figure 2 (b). The results would be presented in the symposium.

ACKNOWLEDGEMENT

The authors wish to thank Dr. Yokoyama for help with growth of GaN film and Dr. Kaneshiro for her discussion. This work is supported by the fund for Advance Technology Center from the Ministry of Education, Culture, Sports, Science and Technology.

REFERENCES

1) N. Shigekawa, K. Nishimura, H. Yokoyama and K. Hohkawa; Appl. Phys. Lett. 87 084-102 (2005).

2) N. Shigekawa, K. Nishimura, H. Yokoyama and K. Hohkawa; Technical Report of IEICE Oct. (2005).

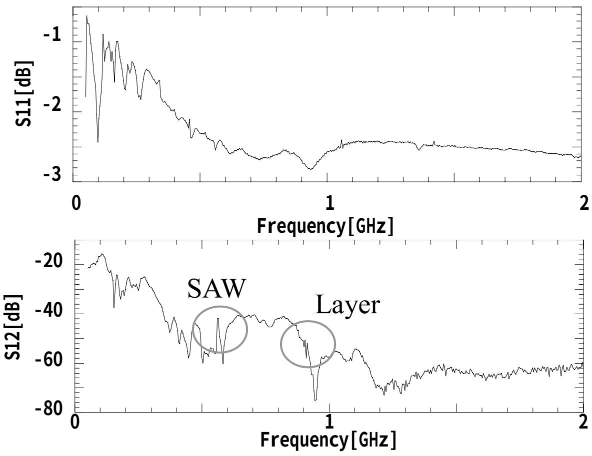

a) Line & space 2μm

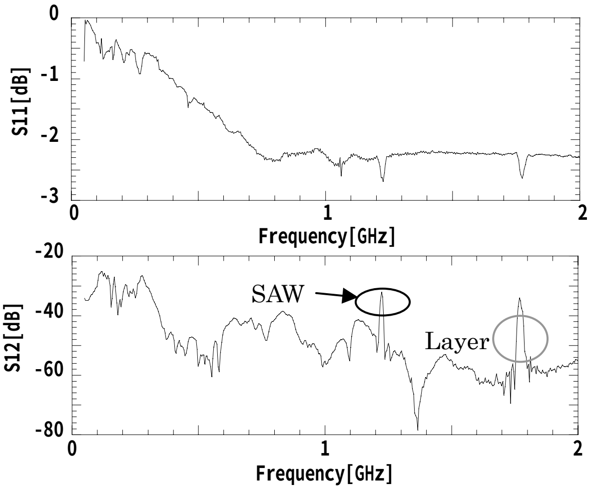

b) Line & space 0.8μm

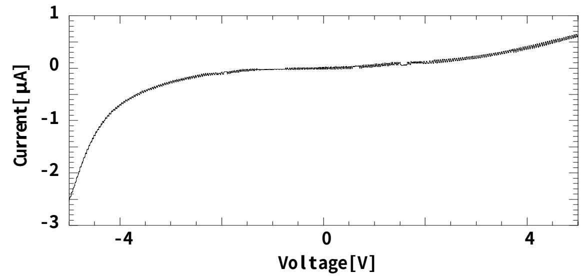

(c) I-V property of IDT with n+ layer (λ=3.2μm)

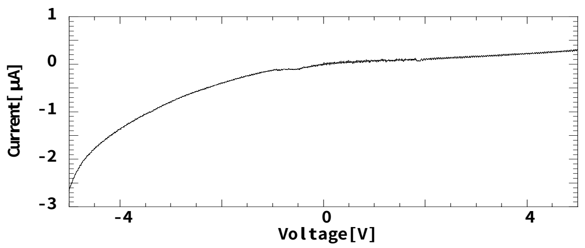

(d) I-V property of IDT with n+ layer λ=8μm)

Fig.3 Frequency characteristics of device with structure as Fig. 2 a)

P2-7

Proc. Symp. Ultrason. Electron., Vol. 26, (2005) pp. 225-226
16-18 November, 2005

Evolutional Research on the Second Harmonic in 50MHz Band Nonlinear Surface Acoustic Wave

Yoshiaki Tokunaga, ○Atsushi Yasuno, Masaki Suzuki (OEDS R&D Center of Kanazawa Inst. Tech.)

1. Introduction

Recently, a barrier among cognitive science, life science, human-social science and nature science has been lowered. Besides, the new academic region called new science (chaos, fractal, nonlinearity, and so on) has attracted lots of interest. In this trend, some researchers attempt to reconsider phenomena in a piezoelectric crystal from a point of view of the complexity[1]. As to the surface acoustic wave generated on the piezoelectric substrate, its behavior easily shifts from a linear region to a nonlinear region because most of its energy is trapped in a depth of a wavelength from the surface of the substrate. Therefore, technologically interesting phenomena which do not emerge in a linear region have been observed. We have studied the complexity of the nonlinear surface acoustic wave (NLSAW) from a point of view of technological application[2)-3)]. Through these studies, we discovered that the second harmonic (2nd harmonic) in 50MHz band NLSAW had soliton-like characteristics. In this paper, we comprehensively report experimental results which we have found out so far.

2. Sample and Measuring Method

128° Y cut X propagation crystals were used as $LiNbO_3$ substrate. IDTs were regular type with 20 pairs. The center frequency of the IDT was around 50MHz because the dissipation between the wave and the thermal phonon bath in the substrate was negligible, and its system could be treated as a conservative system. **Figure 1** shows a diagram of the experimental sample. A 20 mm free space was interspaced between IDT (I) and IDT (II) in order to do light scattering measuring and to evaporate a metal film.

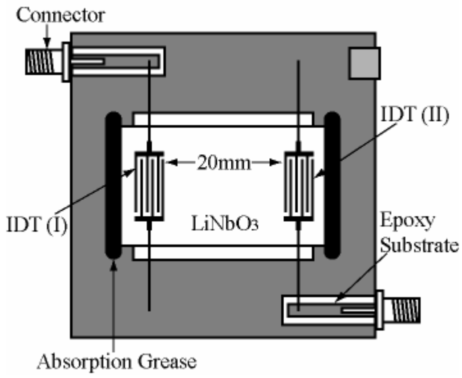

Fig. 1 Diagram of the experimental sample.

3. Results and Discussions

First, the measurement results of velocities of the fundamental and the 2nd harmonic are described. **Figure 2** shows the relationship between the propagation time and the propagation distance of SAW (LSAW) in the linear region. The optical probe was irradiated on the substrate surface at 500 μm intervals in a row, and the temporal process of LSAW was measured. Obtained data were collinear approximated using least–square method, and its velocity was estimated 3996m/s by the slope of line. This velocity agreed fairly with the theoretical value.

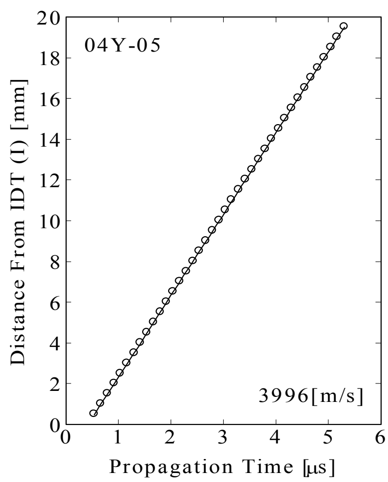

Fig. 2 Velocity of SAW in the linear region.

E-mail: toklab@mlist.kanazawa-it.ac.jp

Secondly, when the input signal was increased, NLSAW was generated, and its velocity was measured in the same way. **Figure 3(a)** and **(b)** show velocities of the fundamental and the 2nd harmonic, respectively. The velocity of the fundamental in NLSAW was 3994m/s, and it was few m/s slower than that of LSAW. Correspondingly, the velocity of the 2nd harmonic was 4000m/s, and it was about 4m/s faster than the velocity of the fundamental in LSAW. This tendency was observed in many measured samples.

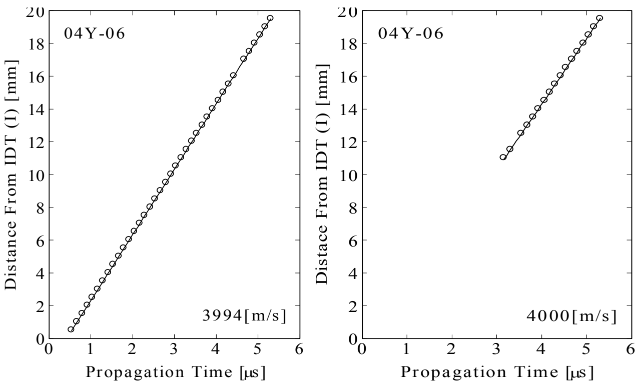

(a) Fundamental. (b) 2nd harmonic.

Fig. 3 Velocities of the fundamental (a) and the 2nd harmonic (b).

Figure 4 shows a comparison between full width at half-maximum (FWHM) of the fundamental and the 2nd harmonic in NLSAW. The FWHM of the fundamental was about 1000 μm, on the other hand, the FWHM of the 2nd harmonic was about 500 μm, and it was about half of the fundamental's.

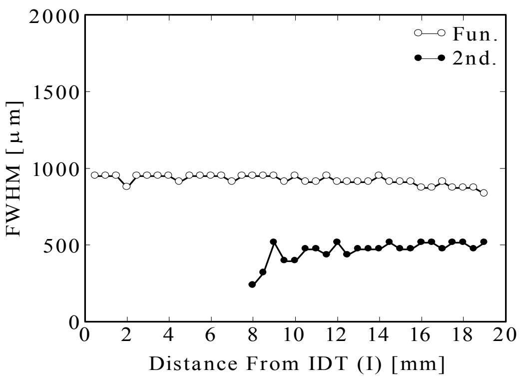

Fig. 4 FWHM of the fundamental and the 2nd harmonic.

By the way, what will happen if NLSAW experiences a metal thin film? We compared FWHM between the case that NLSAW experienced the metal thin film and the case that NLSAW did not experienced it.[3] The value of fundamental in the case that NLSAW experienced the metal thin film was few% bigger than the case that NLSAW did not experience the metal thin film. Correspondingly, the 2nd harmonic was not affected by the metal thin film. In other word, it was conservative. According to these facts, we predicted that the 2nd harmonic might be a kind of soliton. In order to confirm this prediction, a collision experiment of two 2nd harmonics was attempted. **Figure 6(a)** and **(b)** show intensity of observed scattering lights when two NLSAWs which were launched from two spatially opposite IDTs collided head-on at the middle of two IDTs. Because the fundamental lose its shape by the collision, the difference of intensities could not be estimated. On the 2nd harmonic, it was confirmed that its intensity was algebraic sum of two waves at the collision point.

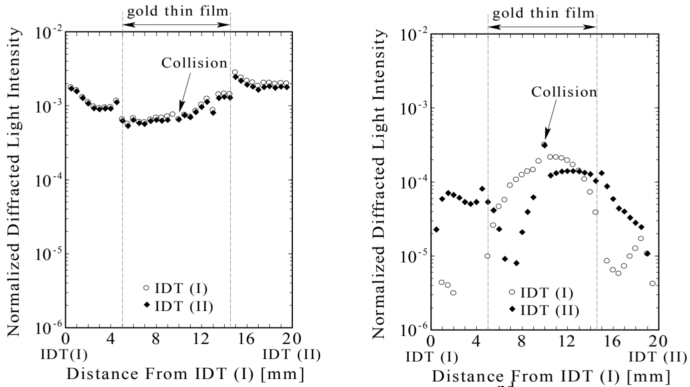

(a) Fundamental. (b) 2nd harmonic.

Fig. 6 Collisions of two fundamentals (a) and two 2nd harmonics (b).

Conclusion

Characteristics of the fundamental and the 2nd harmonic in 50MHz band NLSAW on $LiNbO_3$ substrate were investigated by the optical probing method.

It was found that the 2nd harmonic in NLSAW substantially exhibited soliton-like characteristic.

Acknowledgement

This work was supported by "High-Tech Research Center" Project for Private Universities: matching fund subsidy from MEXT, 2000-2005.

References

1) Y. Tokunaga and Y. Kugo: Jpn. J. Appl. Phys. **39** (2000) 2933.

2) Y. Tokunaga, T. Okayama, et al.: Proc. Symp. Ultrason. Electron., **24**, (2003) 131.

3) Y. Tokunaga, T. Nakaya, et al.: Proc. Symp. Ultrason. Electron., **25**, (2004) 263.

P2-8

Proc. Symp. Ultrason. Electron., Vol. 26, (2005) pp. 227-228
16-18 November, 2005

Application Limitations of Mason Equivalent Circuit as a Linear Coupling Circuit

Michio Ohki, *Natl. Def. Acad., Japan*

1. Introduction

Mason's equivalent circuit has a kind of symmetric structure for representing two different coupling effects, longitudinal (L-) effect and transverse (T-) effect, and it is expected that this structure works successfully when the piezoelectric coupling coefficient is not so large; that is, in the linear region. This study indicates the application limitations of Mason's equivalent circuit as a linear coupling circuit in a semi-quantitative manner.

2. Symmetrical behavior of $-C_0$ and $+C_0$

In Mason's circuit, two kinds of electrical capacitance components, $-C_0$ and $+C_0$, are included, as shown in **Fig. 1**. Two switches SW_- and SW_+ are included in the circuit to explain the behavior of $-C_0$ and $+C_0$ in a symmetric manner. There are four cases with regard to the behaviour of SW_- and SW_+: (i) (SW_-, SW_+) = (open, open), (ii) (open, short), (iii) (short, short), and (iv) (short, open).

Cases (i) and (ii) correspond to the L-effect, and cases (iii) and (iv) correspond to the T-effect in which $-C_0$ is shorted out. Cases (i) and (iv) represents the situation of infinitely large internal resistence in electric source, and cases (ii) and (iii), that of infinitely small internal resistence.

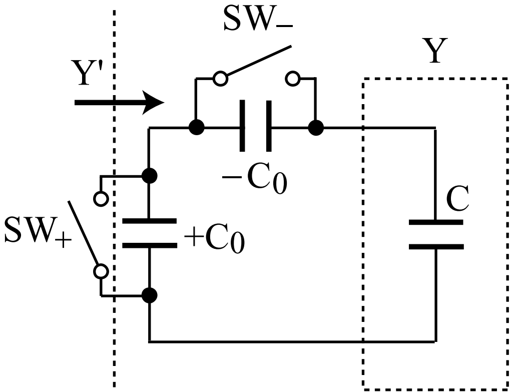

Fig. 1 Framework of Mason's equivalent circuit with dielectric components $-C_0$ and $+C_0$, and with equivalent elastic component C at the frequency $\omega\rightarrow 0$.

E-mail: michio_ohki@ieee.org

In case (i), the resonance frequencies of the total system, ω_{res}, equal those of the mechanical part of the system, the admittance of which is denoted by Y, and those values correspond to the anti-resonance frequencies, ω_A, of the electrically observed admittance denoted by Y'. In this case, $-C_0$ apparently disappears due to the offset to $+C_0$ on the circuit, and the coupling between $-C_0$ and C does not occur, which is the intrinsic state for L-effect. On the other hand, in case (ii) $-C_0$ emerges and is coupled with C, causing the change in ω_{res} from ω_A to ω_R that is the resonance frequencies of Y'. In both cases, the behavior of $-C_0$ determines the resonance of the total system, while $+C_0$ does not work.

The cases (iii) and (iv) in the T-effect correspond to cases (i) and (ii) in the L-effect, respectively, but the behavior of $-C_0$ and $+C_0$ is interchanged; that is, the case (iii) represents the intrinsic state of T-effect, in which the coupling between $+C_0$ and C does not occur, since $+C_0$ is now shorted out, and ω_{res} in this case corresponds to ω_R of Y'; on the other hand, in case (iv), $+C_0$ emerges and is coupled with C, causing the change in ω_{res} from ω_R to ω_A. In both of (iii) and (iv), the behavior of $+C_0$ determines the resonance of the total system, while $-C_0$ does not work.

The symmetrical coexistence of $-C_0$ and $+C_0$ is inevitable in the framework of Mason's circuit.

3. Behavior of Linear Coupling Circuit

We investigate the shift of the resonance frequency of the total system due to the linear coupling between $-C_0$ and C, or between $+C_0$ and C, where the value of C can be calculated by

$$C = \frac{1}{\mathrm{j}} \lim_{\omega\to 0} \frac{\partial Y}{\partial \omega}.$$

Let us consider the type of piezoelectric transducer that is shown in **Fig. 2**.

Figure 3 shows the dependence of the difference

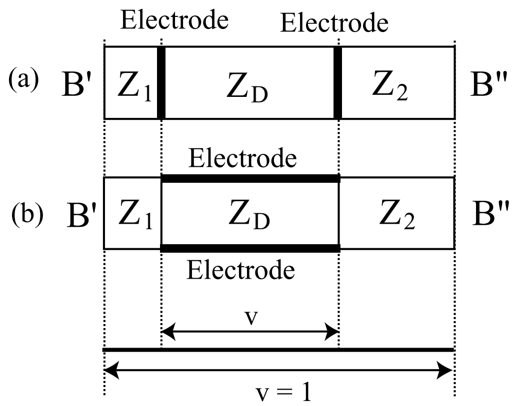

Fig. 2 Piezoelectric transducer for (a) L-effect (b) T-effect. v is the volume ratio of the drive domain to the whole transducer. B' and B'' are mechanical boundaries set free or clamped. Z_1, Z_D, Z_2 are mechanical impedance of the respective domains.

between ω_R and ω_A, $\delta\omega$, on $C/(C_0 + C)$ under the boundary condition of $v = 1$ with (B', B'') = (free, free) for the fundamental mode, based on the calculation using Mason's circuit, in which (a) and (b) are the results for L-effect and T-effect, respectively. In the case of L-effect, the value of $C/(C_0+C)$ cannot exceed 0.5; that is, the value of C never exceeds that of C_0, although material constants composing C and C_0 are thought of as being independent of each other. This unnatural result is caused by the framework of Mason's circuit as a linear coupling circuit in which C and $-C_0$ are linearly coupled. In this case, the total capacitance for the case (ii), $(C^{-1} - C_0^{-1})^{-1}$, must be finite and larger than zero. In a high coupling region in which the satisfaction of the linearity is doubtful, the mathematical result does not reflect the physical situation naturally. Therefore, Mason's circuit is expected to be completely reliable in the region of $C/C_0 \ll 1$.

Since the important and essential factor for this discussion is the ratio of C to C_0, we investigate the dependence of the (normalized) value of C on various boundary conditions, which is shown in **Fig. 4**, in the cases of (a) (B', B'') = (free, free) or (free, clamped) or (clamped, free) and (b) (B', B'') = (clamped, clamped), both for $Z_1 = Z_D = Z_2$ (impedance matching inside the transducer). In each case, the value of C only depends on the value of v; that is, the value of C does not depend on the location of the drive domain in the transducer as long as the volume ratio v is fixed.

In the case of (a) in Fig. 4, the value of C is in

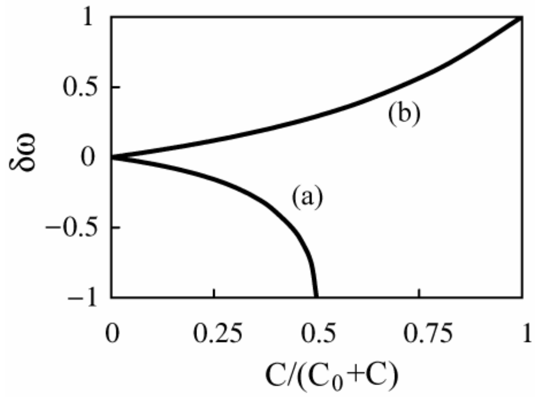

Fig. 3 Relationship between $\delta\omega$, which is the frequency shift due to the linear coupling at the fundamental mode, and $C/(C_0 + C)$, which is a kind of linear coupling parameter, under the condition of $v = 1$ and (B', B'') = (free, free). (a) $\delta\omega = \omega_R - \omega_A$ with $\omega_A = 1$ for L-effect, and (b) $\delta\omega = \omega_A - \omega_R$ with $\omega_R = 1$ for T-effect.

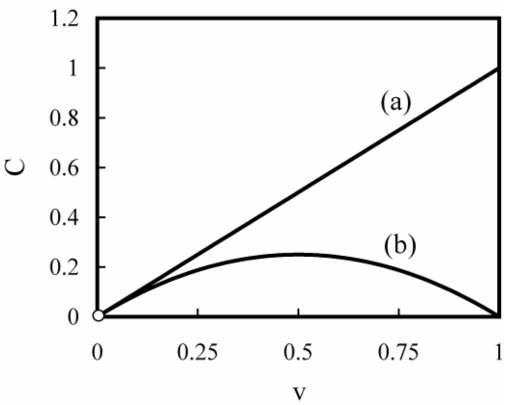

Fig. 4 Dependence of the value of C (normalized) on the volume ratio v. (a) (B', B'') = (free, free) or (free, clamped) or (clamped, free), (b) (B', B'') = (clamped, clamped) for $Z_1 = Z_D = Z_2$. (The dependence of C on v is just identical with the dependence of the "density of resonance pattern" defined in ref. 1 on v.)

proportion to the value of v, which means that the condition of $C/C_0 \ll 1$ is satisfied more easily as v becomes smaller, providing the value of C_0 is fixed. The value of C_0 is actually in inverse proportion to v for the L-effect, as long as the material constant is fixed, while the tendency becomes the inverse for the T-effect. In the case of (b), the situation is the same as in the case of (a) in the region of $v \ll 1$. Therefore, we can expect that the application limitations of Mason's circuit as a linear coupling circuit for L-effect can be removed completely in the situation of $v \to 0$. For T-effect, nothing can be asserted with regard to the present problem in the framework of Mason's circuit.

1) M. Ohki: Jpn. J. Appl. Phys. **44**(2005) 4509.

P2-9

Proc. Symp. Ultrason. Electron., Vol. 26, (2005) pp. 229-230
16-18 November, 2005

Effects of RF Filters on Performance of Power Amplifiers

J.G. Wen, H.L. Li, T.Omori, K. Hashimoto, and M.Yamaguchi (Chiba University)

1. Introduction

RF power amplifiers (PAs) have widely been used in various communication systems, and more and more emphasis has been laid down on high power-added efficiency (PAE) for extending a battery life and reducing heat generation in mobile communication systems.

When RF PAs are operated near a saturation state to get a better PAE, the nonlearity is not neglible, i.e., harmonics may also affect PAE. RF filters are employed for the suppression of unwanted EM radiation and applied to the output network of PAs. For this purpose, the filters based on surface acoustic wave (SAW) and film bulk acoustic resonator (FBAR) technologies are widely used. Independent of the technologies employed, however, the filter function is realised by the frequency dependence of the impedance mismatch with peripheral circuits. This suggests that the input impedance of the filters may badly affect PAE as well as the transmission characteristics of the output network.

From this point of view, this paper discusses how the impedance characteristics of an RF filter affects the PA performance when it is inserted between the PA output and load.

2. Effects of RF filters on PA performance

Fig. 1 shows a circuit used for the discussion. A common emitter Class AB PA was designed to offer optimal output power *(P*$_{out}$) and PAE at a frequncy of 1950MHz with 50Ω termination. The simulation was carried out under Ansoft Designer version 1.1

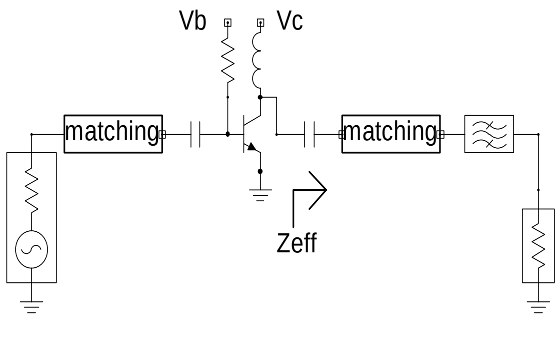

Fig. 1 Circuit topology

As a transistor, NEC 2SC5751 was employed and biased at 3 V and 10 mA. Note in the following simulation that matching elements are assumed to be lossless to clarify the effect of the filter on the PA performance. The performance of the designed PA is: G=12 dB and P_{1dB}=12.7 dBm at P_{in}=1.5 dBm.

An RF FBAR filter for the W-CDMA Tx band (1920-1980MHz) developed by Fujitsu Research Labs was used in the simulation. Fig. 2 shows the frequency response of the filter, where the insertion loss and reflection coefficient are 1.7 dB and -8.0 dB, respectively, at 1,950 MHz.

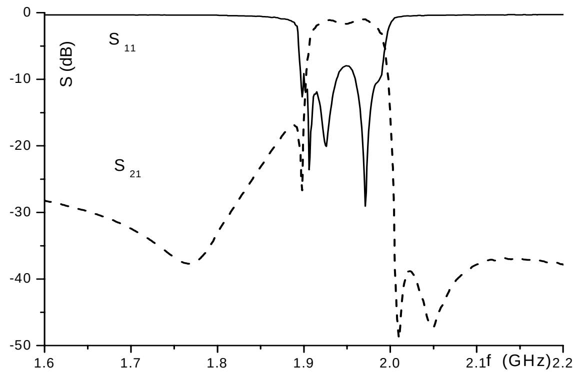

Fig. 2 Frequency response of FBAR filter used in the disucssion

2.1 Effects of S_{11}

Fig. 3 shows P_{out} as a function of the input power P_{in}. When the FBAR filter is short-circuited (Case A), P_{out} is almost proportional to P_{in} when P_{in} is less than –2 dBm. For P_{in}>–2 dBm, P_{out} increases more rapidly and saturates at P_{in}≈ –1 dBm.

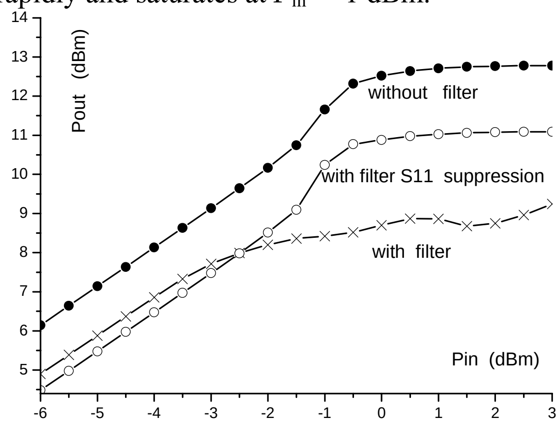

Fig.3 P_{out} as a function of P_{in}

If the filter is inserted (Case B), P_{out} becomes smaller than that in Case A. For P_{in} <–2 dBm, the decrease in P_{out} is mainly caused by S_{21} of the filter, and relatively small (≈ –1.1 dBm). However, the decrease becomes much larger than that expected only by S_{21} when P_{in}>–2 dBm.

The figure also shows the calculated P_{out} when S_{11}

of the filter is set at zero (Case C). Compared Case C with Case A, it is seen that the decrease in P_{out} is almost independent of P_{in}, and that the decrease seems to be simply determined by S_{21}. This suggtests that S_{11}. should significantly affect P_{out} near a saturation state of PA.

To investigate the result shown in Fig. 3 in detail, the dependence of P_{out} on S_{11} was calculated. Although the filter performance used in the calculation is not exactly identical with that shown in Fig. 2, Fig. 4 shows how S_{11} affects P_{out} when S_{11}=–5, –15 and –25 dB.

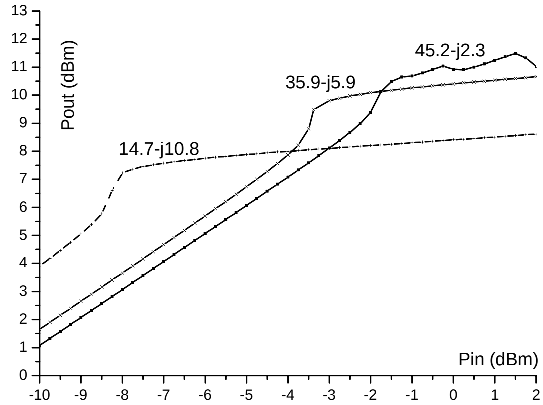

Fig. 3 Influence of $Z_L$of the filter to P_{out}

The result clearly shows that S_{11} considerably reduce P_{out} near a saturation state. Hence, a variation in S_{11} of RF filters must be suppressed sufficiently when they are used with RF PAs.

2.2 Influence of harmonics

It is known that a proper harmonic tuning can increase the output power[2]. From this, it is expected that S_{11} at the harmonic frequencies also affects the PA performance.

Usually, RF filters exhibit reactive input impedances at the rejection bands including harmonic frequencies. Then the real part of the load impedance $Z_{eff}(\omega)$ for the transistor looking toward the output matching circuit (see Fig. 1) can be ideally zero at harmonic frequencies even when the RF filter is connected. In contrast, it is usually nonzero at harmonic frequencies when the matching circuit is simply terminated by a resistive load such as 50Ω.

Fig. 5 shows the calculated P_{in} dependence of P_{out} when $Z_{eff}(\omega)$ for second and third harmonic frequencies are set at a suitable pure imaginary value. For comparison, the result for a 50Ω load is also shown. The result shows that the difference between the two cases is small.

Fig. 6 shows the calculated PAE as a function of P_{in} for these two cases. In contrast to the result for the P_{out} characteristics shown in Fig. 5, PAE is significantly improved by the harmonic tuning at the region where the transistor is almost saturated. The series of the calculation indicate that this PAE enhancement is due to the lack of power consumption for the harmonic components.

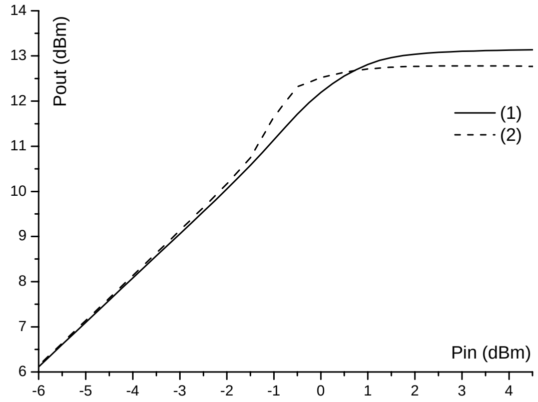

Fig. 4 P_{in} dependence of P_{out}. (1) designed under harmonic-tuning, and (2) designed to 50Ω termination.

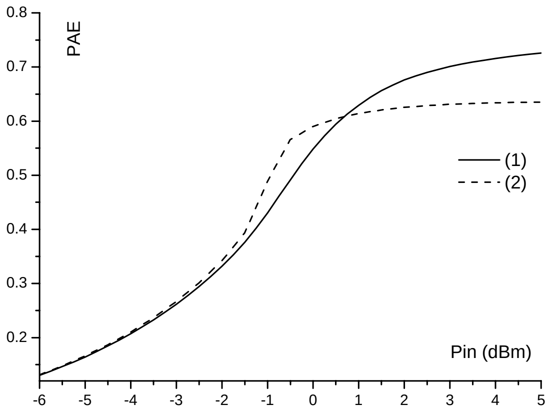

Fig. 5 P_{in} dependence of PAE. (1) designed under harmonic-tuning, and (2) designed to 50Ω termination.

3. Conclusions

It was shown that S_{11} of an RF filter has a significant impact on power amplifier's performance, in particular, near a satuaration state. The effect of S_{11} upon PA performance at harmonic frequencies was also discussed.

Acknowledgment

This work was partially supported by the Grant-in-Aids for Fundamental Scientific Research from the Ministry of Education, Sports, Science and Culture.

References

[1] S.C.Cripps: RF Power Amplifiers for Wireless Communications, Chapter 2, Altech House (1999)

[2] P.Colantonio,P1639, IEEE MTT-S Digest, (2002).

P2-10

Proc. Symp. Ultrason. Electron., Vol. 26, (2005) pp. 231-232
16-18 November, 2005

SAW-Semiconductor UV Sensor Using GaN Film

Keishin Koh, Chinami Kanashiro, and Kohji Hohkawa, Kanagawa Institute of Technology,

Kazumi Nishimura, Naoteru Shigekawa NTT Photonics Laboratories

1. Introduction

GaN material has good semiconductor nature; it not only is used to realize various optical devices such as LD, LED and photodiode, but also it is used to make various electronic devices with high temperature and with high speed. On the other hand, GaN material also has piezoelectric nature; surface acoustic wave (SAW) devices such as filter, oscillator have been studied [1]. Comparing with Si, GaAs material, GaN material has many functional properties and it is expected to realize novel highly functional devices with monolithic structure. In this paper, we will focus on the charge transfer effect in GaN film and investigate basic characteristics of GaN SAW-semiconductor UV sensor based on the transfer effect of charge induced by UV light.

2. SAW-semiconductor UV sensor

Recently, it is strongly required to develop high performances UV sensor. Comparing with UV sensor with vacuum tube structure, the semiconductor UV sensors have better feature such as low cost, low noise and small size. Among them, GaN material is used as material of semiconductor UV sensor since it is wide band energy gap and the UV sensor with MSM structure has been studied [2]. On the other hand, the relationship between traveling SAW and induced carriers in GaN film also has been reported [3]. We also confirmed transports effect of induced carriers by traveling SAW and investigated basic phenomenon. These experimental results indicate possibility of realizing high functional UV sensor using GaN film. Figure 1 shows a cross sectional view of SAW-semiconductor UV sensor device. The GaN film is deposited on a non-piezoelectric substrate (Al_2O_3). When UV light is irradiated on propagation path and carriers (electron and hole) are generated in GaN film, if SAW is not generated and there is not the electric filed in the film,

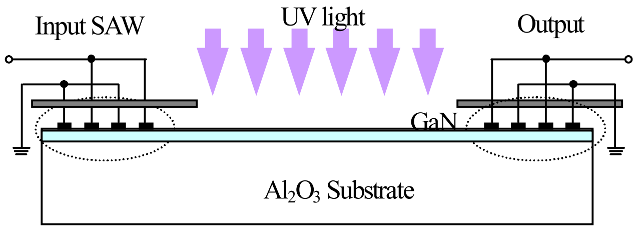

Fig. 1 SAW-semiconductor UV sensor..

so no carriers can transfer. When SAW is generated and the electric filed be formed in the GaN film. The induced carriers are transferred by propagation of potential well caused by traveling SAW and the output signal is detected at output IDT as MSM photodiode with Schottky junction. This UV sensor has feature as following.

1) It has high sensitivity by traveling SAW and has selectivity of UV wavelength
2) The output signal could be selected from DC, amplitude or phase RF signal. Moreover the output signal could be remote controlled.

Here, we report experimental results of the SAW -semiconductor UV sensor using insulating GaN film.

3. Basic experimental results

We deposited the GaN film on the Al_2O_3 substrate grown by MOCVD and fabricated test devices on GaN films. Table 1 shows parameters of test devices. Figure 2 (a) shows the frequency response of the test device, there are two peaks corresponding to SAW mode and Sezawa mode respectively. Figure 2(b) shows I-V characteristics of outprt IDT as a MSM diode, light current caused by induced carriers is observed under UV irradiation.

Table I. Parameter of test device

Substrate	GaN on Al_2O_3
Thickness of GaN film	2 μm insulating film
IDT line &space	2 μm: 2μm / 0.8μm:0.8μm
Overlap. length	800 μm / 400 μm
Number of pairs	50-50 pairs
Propagation length	2.5 mm
Electrode	Al, 100 nm

----

koh@ele.kanagawa-it.ac.jp

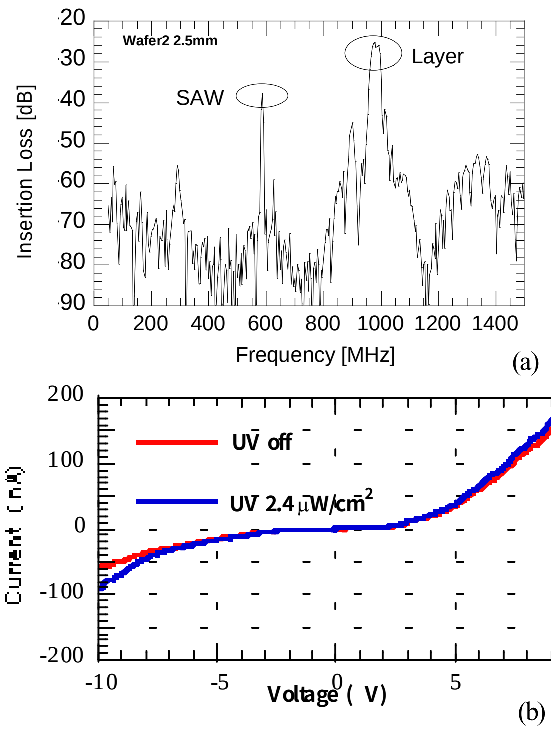

Fig. 2 Basic characteristics of test device. (a) Frequency response, (b) I-V characteristics of IDT.

Figure 3 shows configuration of experimental setup. The UV lamp with 360nm peak was used. We measured the charge function of GaN SAW filter under UV irradiation on the propagation path. Figure 4(a) shows relationship between DC output signal and UV irradiation intensity under different input SAW power. The DC output almost is proportional to UV light power and weak UV light with microwatt order could be detected. It indicates that the charge transfer efficiency is relatively higher than the conductive GaN film. In additional, as the SAW power increase, the DC output level also increases. Fig. 4(b) shows relationship between the DC output and IDT bias voltage, we can find it is effective to enlarge DC output signal.

In experiment, output signal is not stability due to charging up effect. We measured DC output signal at the condition which transferred carriers is completely emitted In future, it is important to design a optimum device structure for emitting carrier.

4. Conclusion

We confirmed the charge transfer effect on the insulating GaN film under UV irradiation and investigated basic characteristics of SAW-semiconductor UV sensor. From a view point of the device application, it is necessary to investigate other basic characteristics such as frequency

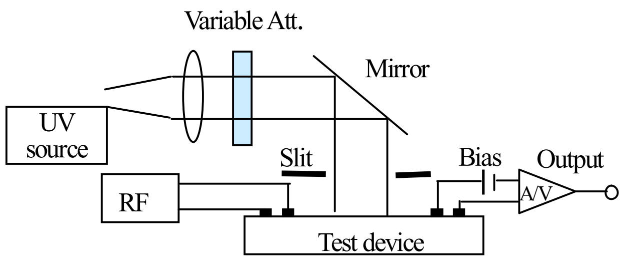

Fig. 3 Experimental set-up

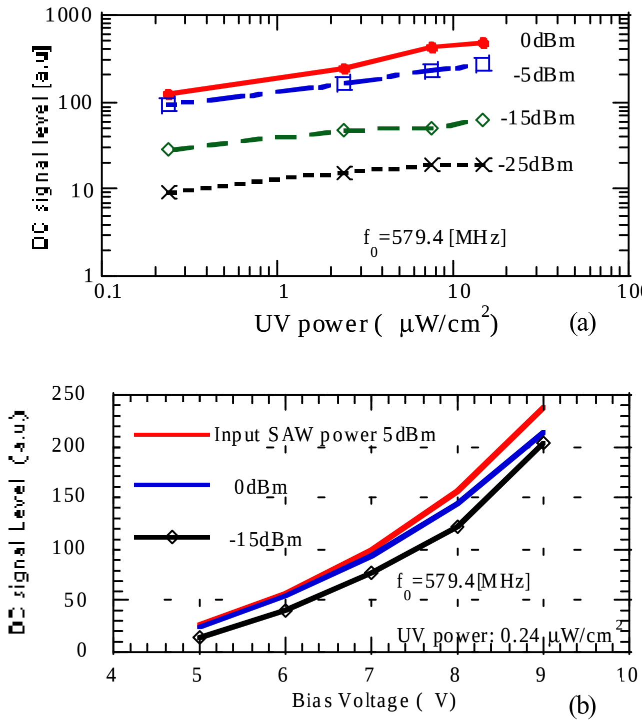

Fig. 4 Basic characteristics of UV sensor.

dependence of film, dependence of UV wavelength. Moreover, we have to find way exactly to control charges in film and study optimization of device structure.

Acknoledgement

The authors wish to thank Dr. Yokoyama for help with growth of GaN film and Mr. Mizusawa for their contributions on measurements. This work is supported by the fund for Advance Technology Center from the Ministry of Education, Culture, Sports, Science and Technology.

References

1) 1. O. Ambacher , Appl. Phys., vol. 31, pp. 2653-2710, 1998.
2) D. Ciplys, R.Rimeika, A. Sereika, R. Gaska, M. S. Shur, J. W. Yang and M. A. Khan, Electron. Lett., vol. 37, no. 8, pp. 545-546, April 2001.
3) T. Palacios, F. Calle, J. Grajal, E. Monroy, M. Eickhoff, O. Ambacher, and F. Omnès, Proc IEEE Ultrason Symp, pp. 57-60 2002.
4) K. Hohkawa, C. Kaneshiro, K. Koh, K. Nishimuru and N. Shigekawa, IEEE MTS 2005, to be pubrised.

P2-11
Proc. Symp. Ultrason. Electron., Vol. 26, (2005) pp. 233-234
16-18 November, 2005

Simple Ultrasonic Anemometer Using a Bended Sound Probe

◎Kosuke KUDO, Koichi MIZUTANI[1] and Masahisa ISHII[2]
[1] Graduate School of Systems and Information Engineering, University of Tsukuba
[2] National Institute for Rural Engineering

1. Introduction

A heat exchange between some spaces is performed via air usually. Winds are ones of the important parameters for advanced environmental controls(1-2). A whole motion of the wind is estimated simply. However, the winds change fluxionally. An adequate value should be estimated from several measurement results at several points during a brief period. Ultrasonic anemometers rapidly measure mean winds in an area(3-6). Conventional ultrasonic anemometers have applied two pairs of transducers at least. Sound reflections have been applied to reduce the transducers7-8). The sound reflection allows the ultrasonic anemometer to reduce the transducers(9). However, the ultrasonic anemometer with the sound reflection was a symmetric shape. The symmetric shape caused some problem to measurement.

This paper described a simple ultrasonic anemometer using a bended sound probe. The bended sound probe allowed the ultrasonic anemometer to measure the wind with a pair of loud speaker and microphone.

2. Principle

A schematic diagram of a simple ultrasonic anemometer is shown in **Fig. 1**. Two sound probes consist of two propagation paths by a loud speaker (SP), microphone (MIC) and acoustic reflector. A bended sound probe is composed by the acoustic reflector. Each device is installed on the apexes of an inequilateral triangle with 30° and 60°. The MIC receives two times of flights (TOF) of the sounds from the SP. The wind velocity is decomposed to *x*-*y* components; w_x and w_y. Using the w_x and w_y, the TOFs along the direct path, t_1, and reflected path, t_2, are expressed as follows:

$$t_1 = \frac{L_1}{c + w_x}, \tag{1}$$

$$t_2 = \frac{L_2}{c + w_x/2 + \sqrt{3}w_y/2} + \frac{L_3}{c + \sqrt{3}w_x/2 - w_y/2}, \tag{2}$$

where L_1, L_2 and L_3 denote lengths of propagation paths, c sound velocity, respectively. Two w_y are derived from eq. (2). **Figure 2** shows typical traces of eq. (2) with L_1 = 2.0 m, L_2 = 1.0 m, L_3 = 1.7 m, w = 5.0 m/s and c = 347.3 m/s. θ are 20, 40 and 60 degrees. The two w_y from one TOF indicate different values by biases of central axes. A correct w_y changes by the wind direction. Estimations of w_y are difficult in the space with extreme changes of the wind. However, the wind direction changes continuously. A correct w_y is estimated using the previous wind velocity and direction in the rapid measurement. Wind velocity, w, and direction, θ, are

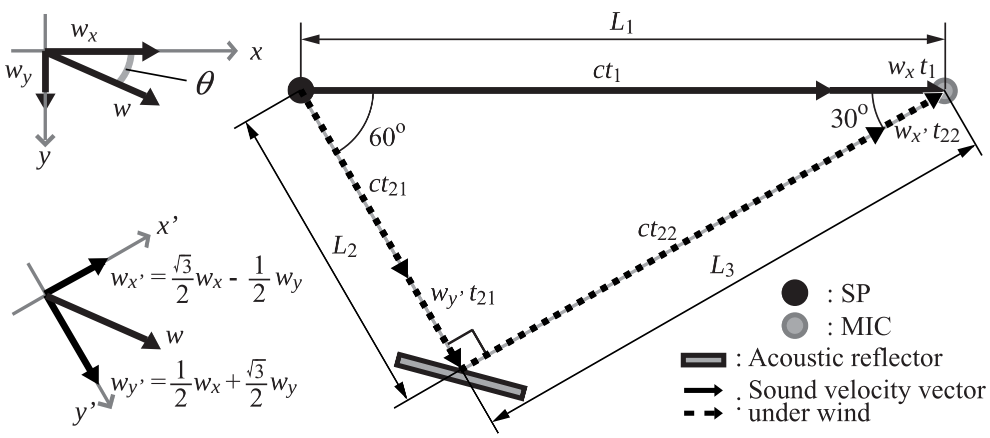

Fig. 1 Parameters for wind measurements. Wind vector is decomposed to two patterns. Apparent sound velocities are composed of sound velocities and wind velocities along propagation paths.

derived from the w_x and w_y.

3. Simulation

Simulations were performed. Parameters were L_1 = 2.0 m, L_2 = 1.0 m, L_3 = 1.7 m, w = 5.0 m/s and c = 347.3 m/s. A sampling frequency of the TOF was 100.0 MHz (0.01 μs). Incident angles of the winds were changed from 0^{o} to 360^{o}. **Figure 4** shows traces of ideal and simulated w_x and w_y. w_x was measured with slight errors. w_y indicated some errors from the ideal w_y. The maximum error was 0.2 m/s at 20^{o}. **Figure 5** shows the wind velocity and direction. w indicated some errors from ideal w. The maximum error was 0.1 m/s. The used TOF were digital values. Half adjusts of ideal TOF caused the errors. In this situation, 0.01 μs difference of TOF corresponded to 0.1 m/s difference of w_y.

4. Conclusion

A simple ultrasonic anemometer using a bended sound probe was described. A SP, MIC and acoustic reflector were composed two propagation paths. In the simulation, good agreement was indicated except to errors caused from digital values. The wind velocity and direction would be measured with the simple ultrasonic anemometer.

Acknowledgment

This work has been supported in part by a Grant-in-Aid for Scientific-Research (B) (No. 17380149) from the Japan Society for the Promotion of Science.

1) S. Wang, M. Yernaux and J. Deltour: J. Agric. Engeng Res., **73** (1999) 189.
2) E. Shilo, M. Teitel, Y. Mahrer and T. Boulard: Agric. Forest Meteorol., **122** (2004) 3.
3) R. E. Corby: Electronics, **23** (1950) 88.
4) G. S. Campbell and M H. Unsworth: J. Appl. Meteoril., **18** (1979) 1072.
5) K. Hamotani and N. Monji: J. Agric. Meteorol., **55** (1999) 109.
6) K. Mizutani, K. Taruishi, Y. Hachisuka, K. Kudo and M. Ishii: Jpn. J. Appl. Phys., **43** (2004) 3099.
7) J. S. Kim and A. Yamada: Jpn. J. Appl. Phys., **41** (2002) 3592.
8) K. Kudo and K. Mizutani: Jpn. J. Appl. Phys., **43** (2004) 3095.
9) K. Kudo, K. Mizutani and K. Itoga: Jpn. J. Appl. Phys., 44 (2005) 4407.

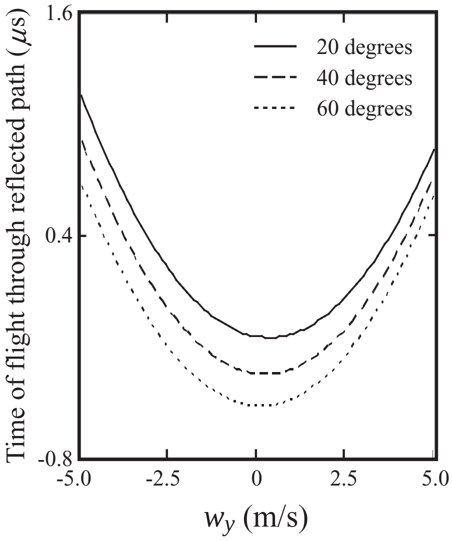

Fig. 2 Typical traces of eq. (2). L_1 = 2.0 (m), L_2 = 1.0 (m), L_3 = 1.7 m and c = 347.3 (m/s). Wind velocity and direction were 5.0 m/s and 20, 40 and 60 degrees.

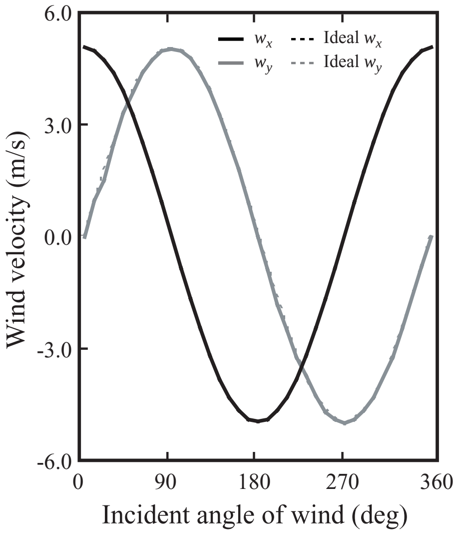

Fig. 3 Simulated wind velocities of x-y component (w_x and w_y). A sampling frequency of TOF was 100.0 MHz (0.01 μs). Ideal w_x and w_y are indicated also.

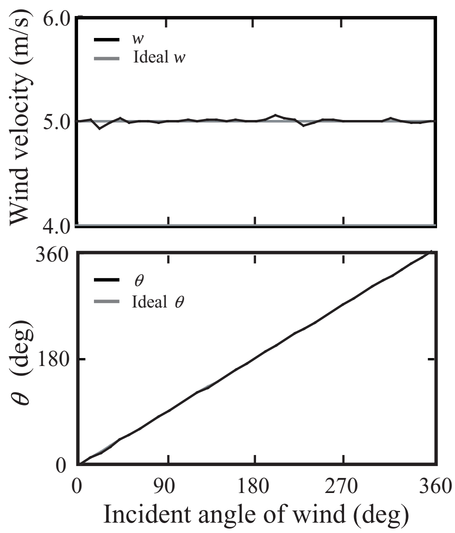

Fig. 4 Simulated wind velocity and direction.

P2-12

Proc. Symp. Ultrason. Electron., Vol. 26, (2005) pp. 235-236
16-18 November, 2005

Measurement of Temperature Distribution Using Acoustic Reflector Array

◎**Satoshi KAWABE and Koichi MIZUTANI** (Univ. Tsukuba)

1. Introduction

In recent years, it has become necessary to control temperature distribution of living space such as office appropriately [(1)] from viewpoint of energy conservation. Measurement of distribution of environmental parameters using sound wave is superior to contact-type sensors in the point that it can measure large area and it is nondestructive and noncontact method. Therefore, many studies on the method have been made [(2-9)]. In case it is hard to install a lot of acoustic sensors in measurement space, the method using acoustic reflectors (hereinafter: reflector) is very effective [(9)].

In this study, we constructed acoustic reflector array and measured spatial mean temperature of divided areas by receiving the reflected waves. Further, we compared the result of measurement with that of thermocouples to evaluate the system.

2. Principle of measurement

Relationship between sound velocity and air temperature is expressed as follows:

$$T = \frac{\mathrm{T_0}}{331.32^2} c^2 - \mathrm{T_0}. \qquad (1)$$

$$\mathrm{T_0} = 273.15\mathrm{K}$$

where T (℃) is the spatial mean temperature along the sound propagation path ,c(m/s) is the sound velocity. Measuring the propagated distance and the time of flight (TOF) of the sound, the sound velocity is obtained. Thus the spatial mean temperature is calculated from eq. (1).

Figure 1 shows the schematic diagram of measurement of temperature distribution using reflector array. The unit with a loud speaker (SP) and a microphone (MIC) is installed at the higher position than reflector array. Reflectors are arrayed at even interval and the height of the center of each reflector is equal .The angles of the reflectors are set so that the perpendicular of each reflector would intersect with SP. The measurement space is divided into several areas on the boundary of reflectors. It is supposed that the temperature is uniform in each area and the sound velocity is uniform too. A torn burst is transmitted from the SP and reflected by each reflector, and received by the MIC. Analyzing the cross correlation between the transmitted signal and the received signal, the TOF of the reflected signals, t_1～ t_i, are obtained. The sound velocity in the Area$_1$, c_1, is expressed as follows:

$$c_1 = \frac{2L_1}{t_1}. \qquad (2)$$

where L_1 is the distance between the center of SP and the center of reflector$_1$. Substituting c_1 for eq. (1), the spatial mean temperature, T_1, is obtained. In addition, using c_1, t_2 is expressed as follows:

$$t_2 = \frac{2L_2}{c_1} + \frac{2L_2}{c_2}. \qquad (3)$$

Eq. (3) is arranged as follows:

$$c_2 = \left(\frac{t_2}{2L_2} - \frac{1}{c_1} \right)^{-1}. \qquad (4)$$

In eq. (4), values included in right side are known. Therefore, c_2 is obtained and the spatial mean temperature in area$_2$ is calculated. Thus the spatial mean temperature of each area is obtained sequentially.

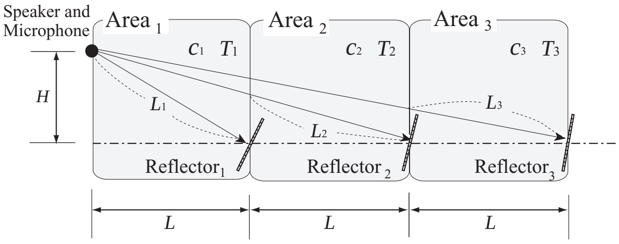

Fig. 1 Schematic of a measurement of temperature distribution using acoustic reflector array. Temperatures and sound velocities are uniform in each area.

3. Experiment

Figure 2 shows an experimental setup. The height of center of the SP is 450 mm higher than those of the reflectors. And three reflectors are arrayed at interval of 900 mm. The sound wave used for measurement was frequency modulated with 10±2 kHz in 10 waves. Transmitting signal was generated by a personal computer (PC) and was radiated from the SP via an amplifier and a digital to analog (D-A) converter (DAQ Card-6062E / National Instruments).

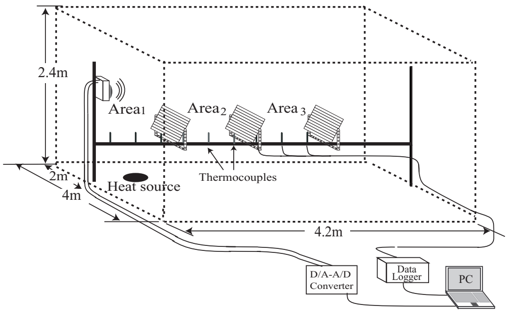

Fig. 2 Experimental setup.

The sound wave reflected by the reflector array is digitized by the PC via the MIC, amplifier and an analog to digital (A-D) converter (DAQ Card-6062E).

Figure 3 shows the waveforms experimentally measured by the system. Figure 3 (a), (b) and (c) are transmitted signal, received signal, and cross correlation result between Fig. 3 (a) and Fig. 3 (b), respectively. In Fig.3 (c), three peaks show the times when the transmitted signal reflected by the three reflectors reached the MIC.

Temperature distribution was experimentally measured in four cases. **Figure 4** shows experimental results. Figure 4 (a), (b), (c) and (d) were without heat source, heat source was installed in the Area$_1$, Area$_2$ and area$_3$, respectively. Rectangles are temperatures measured with the sound wave and black dots show temperatures measured with nine thermocouples. Figure 4 shows that the temperature of the area where the heat source was installed was higher than those of other areas. To evaluate the measurement with sound wave, the product of the area length and the temperature of the area was calculated. In this study, the product is defined as 'amount of heat'. For example, amount of heat of Area$_1$ in Fig. 4 (a) is calculated with 0.9×22.7 = 20.43 (m･℃). Amount of heat measured by the sound probe and those of the thermocouples were corresponding well in the area where no heat source was installed. In the areas where the heat source was installed, the differences were 2.5 % (Area$_1$) 4.2 % (Area$_2$) 6.5 % (Area$_3$). These differences were caused because the thermocouples could not catch precipitous gradient of the temperature. And the differences were caused because the sound velocities were not completely uniform in consequence of a vertical gradient of temperature. However, the measurement system detected the area of heat concentration adequately.

4. Conclusion

The measurement system of the temperature distribution using acoustic reflector array has been proven to be valid for detecting the area of heat concentration. Amount of heat measured by the sound probe and that of the thermocouples have error within 2.5 – 6.5 %, and the experimental result caught the actual temperature distribution well. The system has the advantage that it can be used in life space easily, and the data obtained with this system is useful for energy conservation.

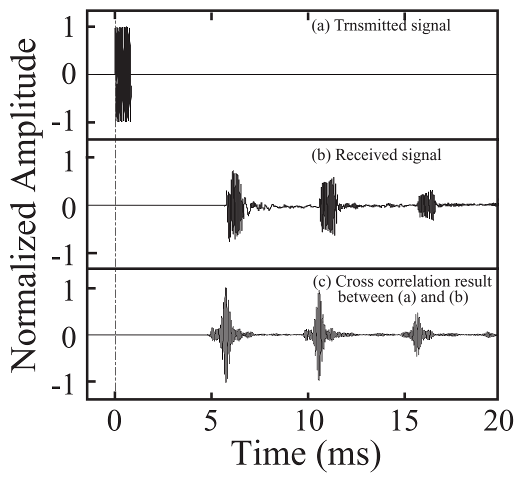

Fig. 3 Measured signals. (a) transmitted signal. (b) received signal. (c) cross correlation result between (a) and (b).

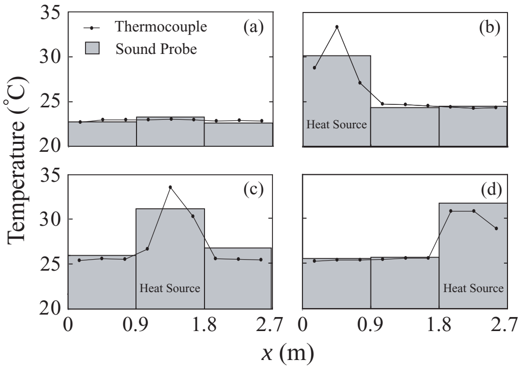

Fig. 4 Temperature distributions measured by sound probe and nine thermocouples.

Acknowledgement

This work has been supported in part by a Grant-in-Aid for Scientific Research (B) (No. 17380149) from the Japan Society for the Promotion of Science.

References

1) F. Engdahl and D. Johansson: Energy and Buildings, **36** (2004) 205.
2) E. C. Shang and Y. Y. Wang : Computer Physics Communications. **65** (1991) 238.
3) I. Basarab-Horwath and M. M. Dorozhevets: Proc. IEEE Ultrasonics Symp (1994) 1891.
4) M. Fujii and X. Zhang: *Proc. 4th World. Conf. Experimental Heat transfer, Fluid mechanics and Thermodynamics*. *Brussels*, *1997*, (1997)169.
5) K. Mizutani, K. Nishizaki, K. Nagai and K. Harakawa: Jpn. J. Appl. Phys. **36** (1997) 3176.
6) A. Funakoshi, K. Mizutani, K. Nagai, and K. Harakawa: Jpn. J. Appl. Phys. **39** (2000) 3107.
7) K. Ikeda: Jpn. J. Appl. Phys. **40** (2001) 3566.
8) E. Ishikawa and K. Mizutani: Jpn. J.Appl. Phys. **42** (2003) 5372.
9) K. Kudo, K. Mizutani, T. Akagami and R. Murayama: Jpn. J. Appl. Phys. **42** (2003) 3189.

P2-13
Proc. Symp. Ultrason. Electron., Vol. 26, (2005) pp. 237-238
16-18 November, 2005

Temperature Measurement Using Network Controlled Acoustic Sensors

◎Kyohei SAWAMURA, Koichi MIZUTANI, Kenichi KASHIWAZAKI and Ikuo ODANAKA (Graduate School of Systems and Information Engineering, University of Tsukuba)

1. Introduction

In recent years, a thermal environmental measurement is required in various fields to maintain an optimum environment for life space, farm, large-scale structure and so on[1,2]. The automated meteorological data acquisition system(AMeDAS) given from the Meteorological Agency is not suitable for the local meteorological data, so the measurement space of the AMeDAS is too large and coarse. Thermometer from the satellite can measure temperature distributions widely, but it is influenced by radiative heat. And the result of measurement is ground temperature and too coarse for local data[3,4]. Therefore, the acoustic sensor has been applied to the measurements of distributions with a small number of sensors without influence of radiative heat[5-7]. As low-frequency can propagate over along distance, measurement of acoustic sensors can apply to large space [8].

In this paper, the purpose is to form the network by many acoustic sensors in the large space and to get temperature data and distributions locally.

2. Principle

Schematic diagram of an acoustic sensor is shown in **Fig. 1**. In the measurement space, two acoustic sensors are set facing each other at the both corner of the baseline. The measurement space along the baseline is equally divided into N cells. In a unit cell, T_n is an air temperature and sound speed c_n is determined by air temperature distribution T_n. $\Delta L = L/N$ are defined. The time of flight (TOF) of the sound wave is described as

$$TOF = \sum_{n=1}^{N} \frac{\Delta L}{c_n} = \frac{L}{\bar{c}}. \qquad (1)$$

Thus, average of sound speed in all section is found. Spatial mean temperature is obtained eqs. (1) and (2).

$$\bar{T} = \frac{T_0}{331.32^2}\bar{c}^2 - T_0. \qquad (2)$$

Here, T_0=273.15K is absolute temperature. An influence of wind is able to remove when sound wave is transmitted two-way at the same time. In this experiment, the TOF is measured by cross-correlation between the received signal and the transmitted signal.

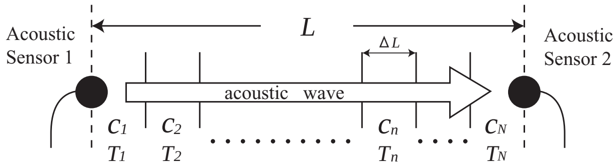

Fig. 1 Schematic diagram of an acoustic sensor

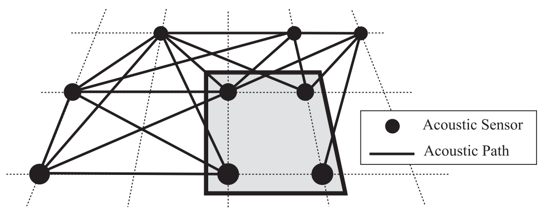

Fig. 2 Layout of the network measurement system

3. Experiment

3.1 Layout of acoustic sensors

Figure 2 shows the future model of network sensing formed by acoustic sensors. As for each sensor, the functions such as signal generating, recording and processing will be installed. And the acoustic sensors are connected by wireless network. The wireless network is IEEE802.11b, which has the advantage of being able to transmit over a long distance. Therefore, measurement function is dispersed.

3.2 Experiment Setup

This time acoustic sensors had not equipped the function of signal generation, recording, and processing yet. So sensors were connected to the PC via an analog-to-digital (A-D) converter and a digital-to-analog (D-A) converter (DAQCard-6062E / National Instruments). Various functions were given to the sensors and the network by wireless LAN (IEEE802.11b) was able to be formed by connecting PC. As the first experiment, four acoustic sensors are set at the corner of the 10×10 ㎡ square in the open air and are formed wireless network. **Figure 3** is the composition of the experiment. For separating from the signal received on each acoustic sensor, two kinds of signals were used. One signal was a ten-wavelength burst sound modulated from 4.5 to 1.5 kHz in linear frequency at sensor 1 and 2, the other was used a ten-wavelength burst sound modulated from 1.5 to 4.5

kHz in linear frequency at sensor 3 and 4. The burst wave was transmitted ten times at the repetition frequency of 2.5Hz in one measurement. TOFs were measured by cross-correlation after averaging the received signal with the number of measurement times. To synchronize the acoustic sensors distributed on the network, trigger lines was set. Because the sampling rate of the A-D/D-A was 250 kHz, the time resolution was 4 μs. This line was wired line. The experiment was carried out at 60s intervals from local time of 23:50 to 0:50 at the University of Tsukuba.

3.3 Measurement results and discussion

Figure 4 shows the measurement results of acoustic path of A, B, C, D, E and F. The solid line represents the time change in the mean spatial temperature. The broken line represents the average of the temperature point measured by ultrasonic anemometer (Model 81000 /Yong).

So the transmitted signal of adjoining sensors were mixed in the received signal, the TOF don't turn out separately. However, the TOF could measure by cross-correlation. This time, by using two kinds of signals and taking cross-correlation between the received signal and the signal transmitted from each sensor, we could get a clear peak that shows the TOF.As for the path A ,the time change of temperature by acoustic sensors and ultrasonic anemometer has a longer periodicity with a maximum range of ±0.4℃ around 23.3 ℃.However, as for the path E, the time change of temperature by acoustic sensors has a short periodicity with a maximum range of ±0.6℃ around 23.3 ℃.This difference is caused by the difference of the spatial mean and the point measurement.

4. Conclusions

In order to measure the temperature distribution of the large space, we formed the wireless network and six acoustic paths by four acoustic sensors in the 10×10 ㎡ square in the open air, as the first experiment. The monitoring system of the temperature was enabled. Applying this system, wind measurements would be realized by using methods of ultrasonic anemometers. In a future work, remote controlling would be required. The remote controlling would be realized via the Internet.

Acknowledgement

This work has been supported in part by a Grant-in-Aid for Scientific Research (B) (No. 17380149) from the Japan Society for the Promotion of Science.

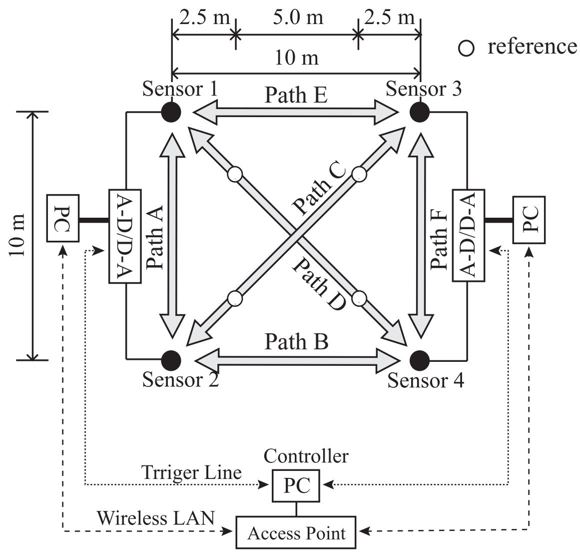

Fig. 3 is the composition of the experiment. The height of baseline was 2.15 m above the ground.

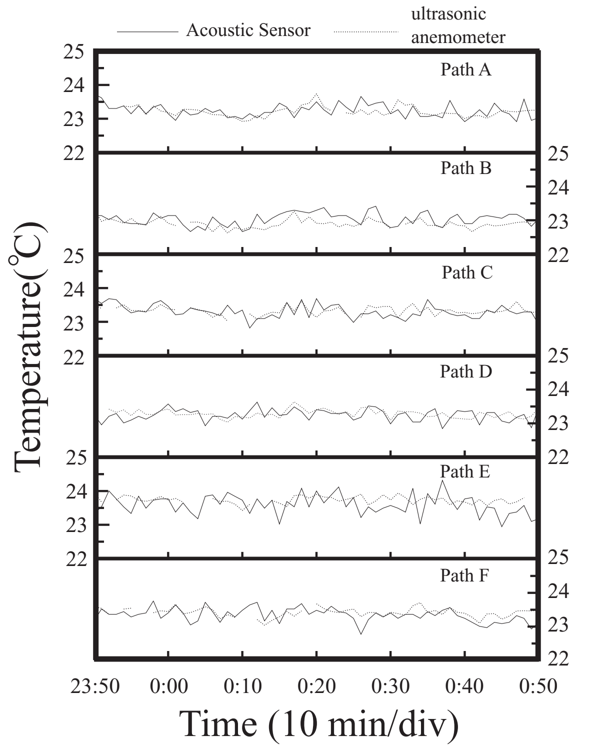

Fig.4 shows the measurement results of acoustic path A, B, C, D, E, F.

1) J. E. Son, J. S. Park and H. Lee: Acta Hort. **578** (2002) 257.
2) D. J. Tanner and N. D. Amos: Acta Hort. **599** (2002) 193.
3) T. Honjo: J. Agric. Meteorol.**56** (2000) 227.
4) X. Wang, T. Kawasumi, H. Tani: J. Agric. Meteorol.**56** (2000) 283.
5) G. Hofelmann, H. O. Luck and P. Beckord: J. Aerosol. Sci. **23** (1992) 51.
6) K. Mizutani, K. Nishizaki, K. Nagai and K. Harakawa: Jpn. J. Appl. Phys.**36** (1997) 3176.
7) E. Ishikawa, K.Mizutani and K. Nagai: Jpn. J. Appl. Phys. **40** (2001) 5446.
8) K. Attenborough *et al.*: J. Acoust. Soc. Am. **97** (1995) 1

P2-14

Proc. Symp. Ultrason. Electron., Vol. 26, (2005) pp. 239-240
16-18 November, 2005

Measurement of the Sound Speed in a Thread

〇Shigemi Saito, Yasuhiro Shibata and Akira Ichiki (Tokai University)

1. Introduction

A sound speed and elastic constant are important parameters to describe the mechanical property of a material. They are often used for identifying materials. Although a certain volume is usually employed for the measurement, some materials such as natural fiber and human hair are found only in a shape of thread. The data of sound speed measured for various materials including biological tissues have been accumulated.[1,2] However the sound speed has scarcely been measured for such materials. Different from a method to use laser for sound excitation that has previously been conducted for ceramic fibers[3], a simple measuring method for the sound speed in a more flexible thread such as human hair is presented in this paper.

2. Transmission and Reception of Ultrasound

The experimental setup for measuring the sound speed in a thread is shown in **Fig.1**. A glass bead with a hole is firmly bonded on each surface of a 300 kHz cylindrical PZT transducer A with a diameter, thickness and weight of 10 mm, 6.5 mm and 3 g so that the hole of each glass bead is parallel to the transducer surface. A thread sample is fixed to one of beads with a thief knot, and a string to hang a plumb is connected to another bead. A bead to fix the thread sample is bonded also to a transducer B of the same type. The transducer B is backed with a cylinder of epoxy-resin and iron-powder mixture (ITW Industry, Devcon B), and the thread sample is hanged underneath. Both the plumb and the weight of the transducer A apply a tensile force to the thread. One cycle 300 kHz voltage with an amplitude from 5 to 60 V is applied to the transducer A. An induced ultrasound propagates in the thread and then generates the voltage across the transducer B. A distance between two transducers, namely a thread length *l*, is measured with a reading microscope.

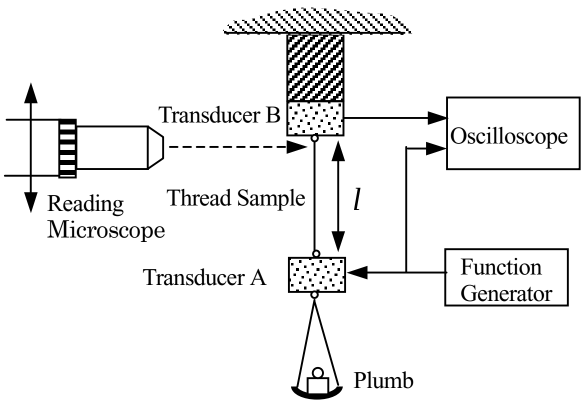

Fig.1. Experimental arrangement.

3. Measurement of Sound Speed

The waveform of the received voltage of the transducer B for the case that a thread is a human hair about 50 mm and 60 μm in length and diameter is shown in **Fig.2**. Although the waveform becomes lengthy with slow transient responses due to the transducer resonance, the propagation of ultrasound is confirmed. The delay time τ from the rising portion S of the driving voltage to the position R of the first trough in the received voltage is measured on a digital oscilloscope.

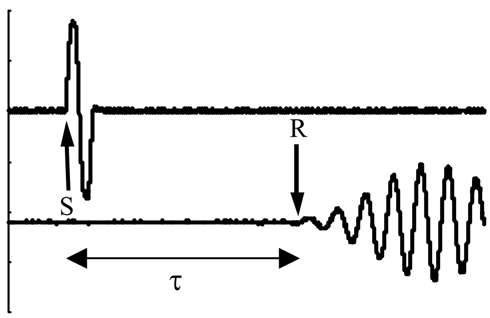

Fig.2. Example of observed waveforms.

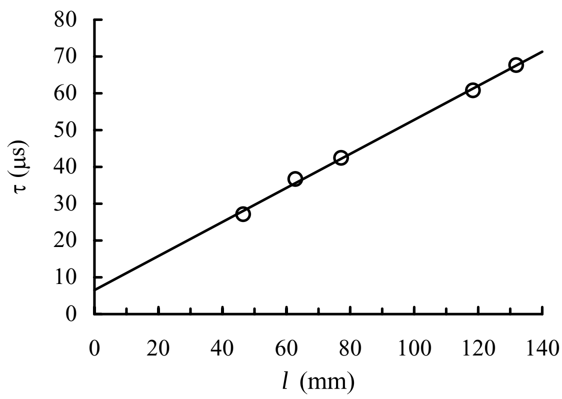

Fig.3. Measured delay for a 60 μm diameter hair.

---

ssaito@scc.u-tokai.ac.jp

An example of measured delay time τ under a 15 gf load including the weight of the transducer A is shown in **Fig.3**. The measured plots are almost on a line. Extrapolation of this line yields a finite value of τ even at l=0. This must be caused by a neglected diameter of glass bead, a small local elasticity of the thief knot and the delay due to reading the first trough. From the reciprocal $dl/d\tau$ of the slope of the line, the sound speed is obtained as 2160 m/s.

Using various weights up to 100 g, the delay time τ was measured for a 70 mm long copper wire 130 μm in diameter. The result is shown in **Fig.4** with a measured l. Although the propagation speed of transversal wave which we call string vibration is proportional to the square root of tension, the measured speed does not change much with the tension. Hence the detected wave is not a transversal wave but a longitudinal wave. In this thread, the load of 100 gf corresponds to a tensile stress of 70 MPa. This is relatively large, but the thread is still within elastic limit.[4]

4. Measured Example

The l-τ relations measured for copper wires with various diameters, a gold wire with 30 μm diameter and a constantan wire with a diameter 100 μm under a load of 25 gf, 3 gf and 25 gf, respectively, are shown in **Fig. 5**. Obtained sound speeds are also indicated in the figures. These values differ from the literature values, which may be calculated with the Young's modulus measured for block specimen. The effect of processing to a thread is expected.

The l-τ relation was measured under a 4.5 gf loading for human hair samples offered from over twenty people. The examples are shown in **Fig.6**. The sound speed disperses in a relatively wide range between 2000 m/s and 2500 m/s due to individual difference. Combining the specific gravity of a hair sample for 45 year old woman measured as 1.22, the Young's modulus is estimated to be $\rho_0 c_0^2 = 4.98\times10^9$ Pa that means a hardness nearly equal to polystyrene. A trend of high sound speed in damaged hair is found for tested samples.

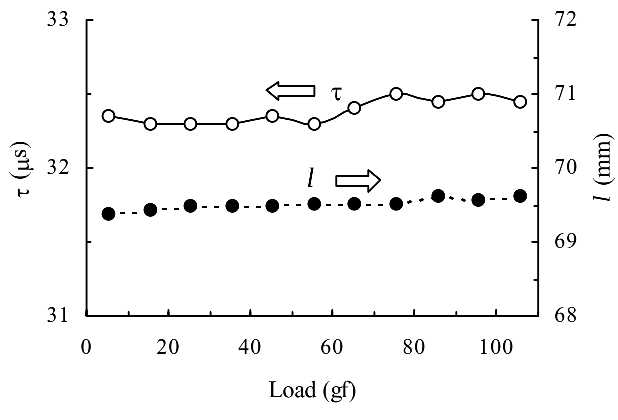

Fig.4. Dependence of τ on the tension in a copper wire.

5. Conclusions

The longitudinal sound speed in a thread was measured with a simple manner. The sound speed in a human hair showed individual differences.

References

1. P.-K. Choi: Ultrasonics Handbook (Maruzen, Tokyo, 1992) p.714.
2. S. A. Goss, R. L. Johnston and F. Dunn: J. Acoust. Soc. Am. **64** (1978) 423.
3. E. A. Lindgren, M. Rosen and K. E. Amin: Ultrasonics **32** (1994) 411.
4. T. Iwatani *et al.*: Fundamental Material Strength. (Maki Publishing, Tokyo, 1996) p.14.

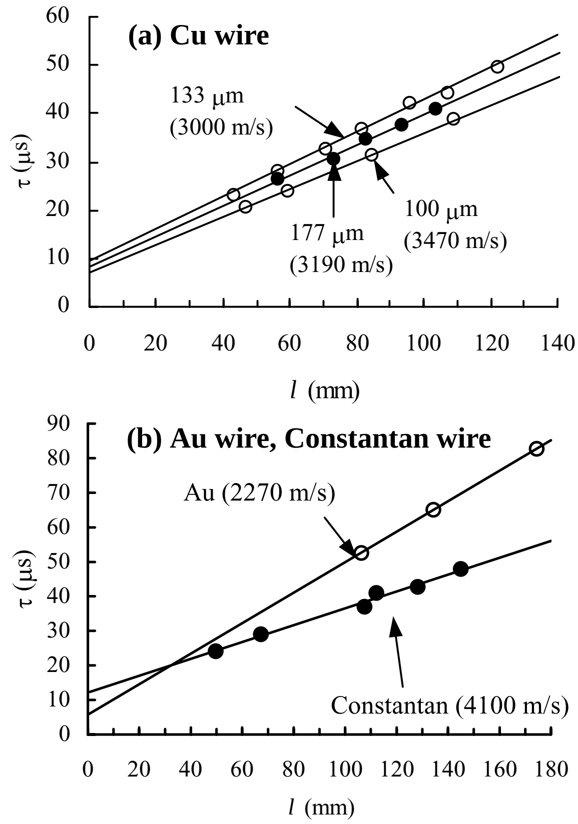

Fig.5. Measured result for metallic wires.

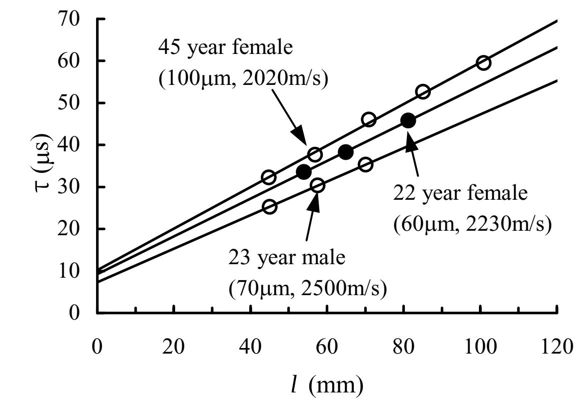

Fig.6. Measured result for human hairs.

P2-15

Proc. Symp. Ultrason. Electron., Vol. 26, (2005) pp. 241-242
16-18 November, 2005

Correlation Characteristic Improvement of Sound Probe Using Inverse Problem

◎Ikuo ODANAKA, Koichi MIZUTANI and Kyohei SAWAMURA
Graduate School of Systems and Information Engineering, University of Tsukuba

1. Introduction

Recently, the importance of a mean temperature measurement of wide area is pointed out from the viewpoint of energy conservation[1-3]. However, to measure the spatial mean temperature, a lot of elements are needed in the temperature measurement element such as thermo-couples of the contact type. They occupy working space and cause heat exchange.

For these reasons, acoustical temperature measurement is suggested. Acoustical temperature measurement uses a sound probe. Advantage of using sound probe is that it has no environmental impact, be able to obtain the spatial mean temperature, with quick response, and without occupy working space[4]. Time of flight (TOF) between two transducers (a loud speaker – microphone) is obtained by using a cross correlation. An impulse response of acoustical system is added to the signal and waveform distortion has occurred. So measurement error in TOF has been finally produced in a cross correlation result[5]. On the other hand, in the field of optical imaging and ultrasonic imaging, a inverse problem is used and imaging accuracy improvement is put into practice by the deconvolution of the impulse response from received signal [6-7]. In this paper, this method is applied to the cross correlation characteristic improvement of sound probe.

2. Time of Flight (TOF) Measurement

Figure 1 shows schematic diagram of a sound probe. The sound probe is consisted by a couple of a loud speaker and a microphone. All of the measurements in this paper are performed in an anechoic room. A distance between transducers L is fixed at 2.1 m. The TOF of the sound probe τ is obtained based on a maximum value of the cross correlation value calculated by

$$\phi = \lim_{T\to\infty} \frac{1}{2T} \int_{-T}^{T} s(t)x(t+\tau)dt \,, \tag{1}$$

Relationship between spatial mean temperature T and

E-mail: odanaka@aclab.esys.tsukuba.ac.jp

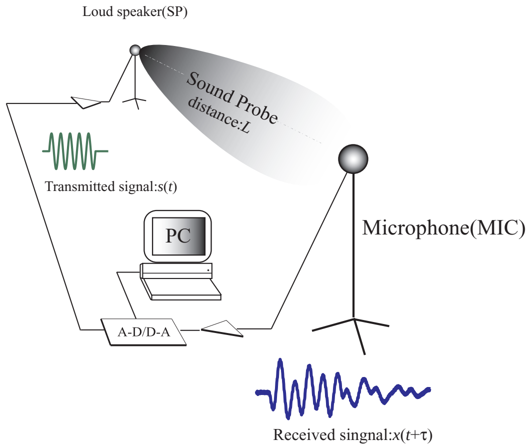

Fig. 1 Schematic diagram of sound probe

the TOF τ is expressed as

$$T = \frac{\mathrm{T}_0}{331.32^2}\left(\frac{L}{\tau}\right)^2 - \mathrm{T}_0 \,. \tag{2}$$

T_0 is 273.15 K. A spatial mean temperature T can be measured by using Eq. (2).

3. Correlation Characteristic Improvement

3.1 Waveform distortion

We should change a condition of a transmitted signal such as a frequency by the change of condition of measuring object. If the sound source of the speaker were point sound source, a precise calculation of the TOF is performed at any frequency. In fact, in an acoustical measurement, an impulse response of the acoustical system is added in the received signal and a waveform distortion has occurred[8]. It causes TOF measuring error.

3.2 Iimprovement

In this paper, sine wave with frequency of 3kHz is used as a transmitted signal. A relational expression of I/O signals of an acoustical system is expressed as

$$x(t) = \int_{-\infty}^{\infty} s(t)h(t-k)dk = s(t)*h(t) \,. \tag{3}$$

In this equation, $s(t)$ is a transmitted signal, $x(t)$ is a received signal and $h(t)$ is an impulse response of the acoustical system. Many researches for the method of acquiring the impulse response have executed because the impulse signal could not be generated in a usual method. Crossing spectrum method, maximum length sequence (MLS) method, and time stretched pulse (TSP) method are typical method[9-11]. In this paper, the impulse response is acquired by using the pulse wave with limited amplitude and short continuance time. This pulse wave has a flat frequency response at least in the demanded range. Compute the Fourier transform of both sides of Eq. (3) and transform it into the shape as

$$S(\omega) = \frac{X(\omega)}{H(\omega)}. \qquad (4)$$

So we can reduce the impulse response of the acoustical system by using Eq. (4).

Figure 2 (a) shows simulation of cross correlation. This figure indicates that an ideal cross correlation result has completely symmetric shape, Fig. 2 **(b)** shows the cross correlation result of transmitted signal: $s(t)$ and received signal $x(t+\tau)$ and Fig. 2 **(c)** shows the cross correlation result of transmitted signal: $s(t)$ and signal $s(t+\tau)$ acquired by the deconvolution of the impulse response of an acoustical system: $h(t)$ from the received signal: $x(t+\tau)$. Shape of Fig. 2 (b) is clearly not symmetric shape, and shape of Fig. 2 (c) is almost symmetric shape.

3.3 Application to TOF measurement

Using Eq. (1), TOF τ can obtained. An actual spatial mean temperature T is 25.03 degrees Celsius (deg C), and the theory value of the TOF at 25.03 deg C: τ is 6. 312 ms. The TOF derived from Fig. 2 (b): τ_1 is 6.296 ms. To compare with theory value, measuring error is 0.016 ms and calculated spatial mean temperature: T_1 is 26.54 deg C. The temperature measuring error is 1.51 deg C. This result suggests that a small number of TOF measuring error causes a lot of temperature measuring error. The TOF derived from Fig. 2 (c): τ_2 is 6.316 ms and calculated spatial mean temperature: T_2 is 24.65 deg C. When τ_1 is compared with τ_2, the accuracy of τ_2 is 0.012 ms better than that of τ_1 and accuracy of T_2 is 1.13 deg C better than that of T_1. From these result, it can be said that accuracy improvement of measuring TOF achieves by using deconvolution.

4. Conclusions

Cross correlation characteristic improvement has performed with inverse problem in this paper. TOF of sound probe has been calculated based on maximum value of cross correlation result, so waveform distortion causes measurement error. This error could have been reduced by the elimination of the impulse response of an acoustical system with deconvolution. And a pulse wave with limited amplitude and short continuance time can be used as an impulse signal.

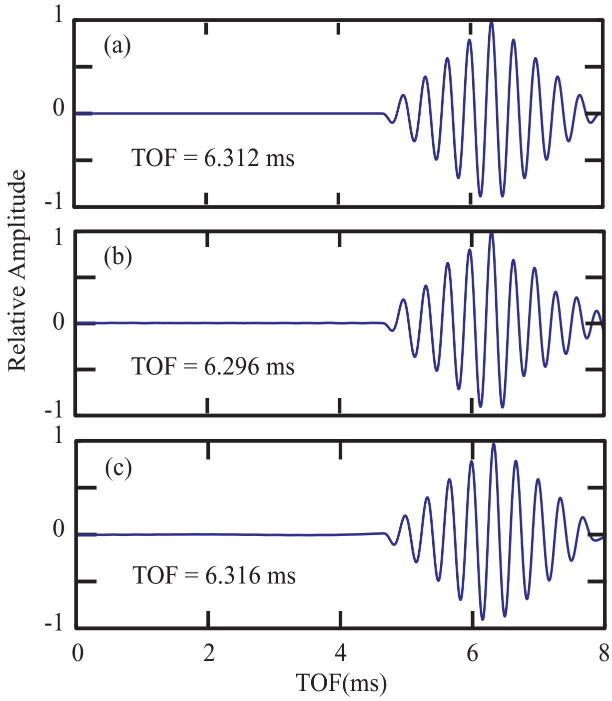

Fig. 2 Results of the cross correlation. (a): The simulation of cross correlation result (b): The cross correlation result of transmitted signal: $s(t)$ and received signal $x(t+\tau)$. (c): The cross correlation result of transmitted signal: $s(t)$ and signal $s(t+\tau)$ acquired by the deconvolution of the impulse response from the received signal

Acknowledgment

This work has been supported in part by a Grant-in-Aid for Scientific Research (B) (No. 17380149) from the Japan Society for the Promotion of Science.

References

(1) C. Boonen, K. Janessens, and D. Berckmans: trans. ASAE 45, 1077-1082 (2002).
(2) T. Boulard, S. Wang, R. Haxaire, C. Kittas, G. Papadakis, and M. Mermier: Acta Hort. 507, 51-59 (1999).
(3) F. L. K. Kempkes, J. C. Bkker, and N. J. van de Braak: Acta Hort. 456, 363-370 (1998).
(4) S. Wang, M. Yernaux and J. Deltour: Journal of Agricultural Engineering Research, Vol. 73, 189-197 (1999).
(5) E. Ishikawa and K. Mizutani: Japanese Journal of Applied Physics, Vol. 42, No. 1, 8, 5372-5373 (2003).
(6) J. Biemond, R. L. Lagendijk and R. M. Mersereau: Proc. IEEE, 78, 5, 856-883 (1990).
(7) B. Haider, P. A. Lewin and K. E. Thomeuus: IEEE Trans. Ultrason. Ferro. & Ferq. Control, 45, 1, 98-113 (1998).
(8) G. H. Glover: Neuroimage, vol. 9, 416-429 (1999).
(9) F. Satou: Proc. Of Forum Acusticum Sevillia 2002 (2002).
(10) N. Aoshima: J. Acoust. Soc. Am., 69, 5, 1485-1488 (1981).
(11) Sinha: D. Reidel Publishing Company (1986).

P2-16

Proc. Symp. Ultrason. Electron., Vol. 26, (2005) pp. 243-244
16-18 November, 2005

Suppression of spurious vibration of cantilever in ultrasonic atomic force microscopy

◎Toshihiro Tsuji, Seishiro Ide, Kazushi Yamanaka (Tohoku University)

1. Introduction

Ultrasonic atomic force microscopy (UAFM) is now being accepted as a practical tool for non-destructive evaluation of mechanical properties and subsurface defects in MEMS devices [1-3]. Since in UAFM and non-contact AFM with atomic resolution [4] resonance vibration of cantilever is measured, spurious vibration (SV) could degrade precision of the measurement. Although it has been recognized as a serious problem in UAFM, origin of the SV has not been clarified so far. In this paper, we propose an effective method for suppression of SV.

2. Spurious vibration

Figure 1 shows amplitude spectra of deflection vibration at the top of the cantilever. Excitation power of piezoelectric vibrator was -35dBm. **Fig.1(a)** is a non-contact spectrum. Although NCD1, 2 and 3 are the 1st, 2nd and 3rd deflection modes, respectively, identified by cantilever vibration theory, there are many SVs. **Fig.1(b)** is a spectrum where the tip is in contact with (100) surface of Si wafer at the load of 500nN. Although CD1 and 2 are the 1st and 2nd modes, they were interfered by SV1 and 2.

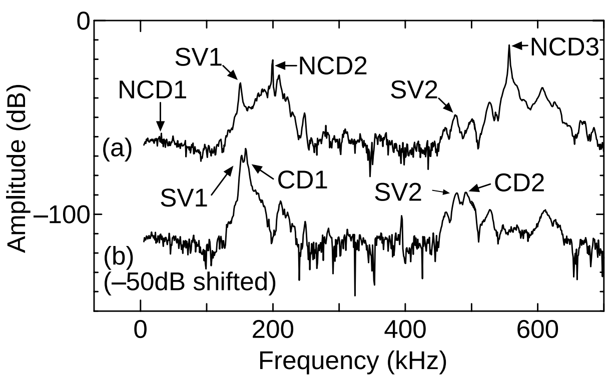

Fig.1 Resonance vibration affected by spurious vibration. (a)Non-contact (b)Contact on Si wafer.

3. Suppression of spurious vibration

First, we propose and verify that SV is originated from bending vibration of the locally clamped base as shown in **Fig.2(a)**. We model this situation as shown by **Fig.2(b)**, where m_n, k_n^*, x_n represent mass, stiffness and position, respectively, and subscript $n = 0,1,2,3$ represent sample stage, cantilever, locally clamped base, and cantilever holder, respectively. Stiffness normalized by k_1 is expressed by

$$k_n^*/k_1 = r_n^e + r_n^v(\Omega/Q_1)i \qquad (1),$$

$$\Omega = \omega/\sqrt{k_1/m_1}\ , Q_1 = \sqrt{m_1/k_1}/\left(k_1 r_1^v(\Omega/Q_1)\right),$$

where r_n^e, r_n^v are relative stiffness and viscosity, Ω is frequency ω normalized by the resonance frequency of the cantilever, and Q_1 is the quality factor related to the cantilever, respectively. r_0^e is called as relative contact stiffness. Position x_1 and x_2 are expressed by

$$\begin{pmatrix} x_1 \\ x_2 \end{pmatrix} = \frac{1}{AC - B^2}\begin{pmatrix} A & B \\ B & C \end{pmatrix}\begin{pmatrix} D \\ E \end{pmatrix} \qquad (2)$$

$A = 1 + r_0^e - \Omega^2 + (1 + r_0^v)(\Omega/Q_1)i$, $B = 1 + (\Omega/Q_1)i$,
$C = 1 + r_2^e - M\Omega^2 + (1 + r_2^v)(\Omega/Q_1)i$, $M = m_2/m_1$,
$D = (r_0^e + r_0^v(\Omega/Q_1)i)x_0$, $E = (r_2^e + r_2^v(\Omega/Q_1)i)x_3$,

where the boundary condition of $x_0 = 0$ and $x_3 = ae^{i\omega t}$ corresponds to the situation of the UAFM. On the other hand, the boundary condition of $x_0 = ae^{i\omega t}$ and $x_3 = 0$ corresponds to the situation of atomic force acoustic microscopy [5].

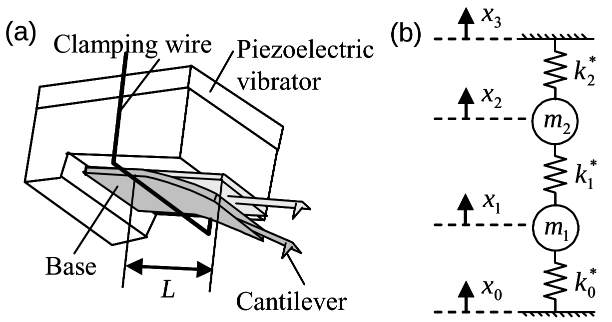

Fig.2 Model of spurious vibration. (a)Schematics of cantilever holder. (b)Mass-spring model.

Figure 3 shows amplitude spectra calculated by Eq.2 with the boundary condition of UAFM, where parameters are $r_0^e = 10$, $Q_1 = 100$, $M = 1\times10^4$, $r_0^v = 1$ are common. **Fig.3(a)** shows the dependence of spectra on r_2^e, where $r_2^v = 1$. When $r_2^e = 1\times10^5$ (solid curve), SVI interferes the resonance due to r_0^e, represented by CR. When r_2^e is 1/8 times lower (chained curve) or 8 times higher (dashed curve), the interference can be avoided (SVII, SVIII). Because r_2^e is approximately proportional to the third power of the thickness of the base, the increase of r_2^e can be realized easily. Moreover, the fabrication of the holder that clamps whole part of the base is effective because r_2^e is enhanced.

Figure 3(b) shows the dependence of spectra around CR on r_2^v, where $r_2^e = 1\times10^5$. Solid curve shows the same case as Fig.3(a). When r_2^v is in the range of 10e5 to, 10e6, the SV is almost damped (dashed and chained curves, respectively). In order to realize large value of r_2^v, not only the selection of the base material but also the effective design of the cantilever holder is important.

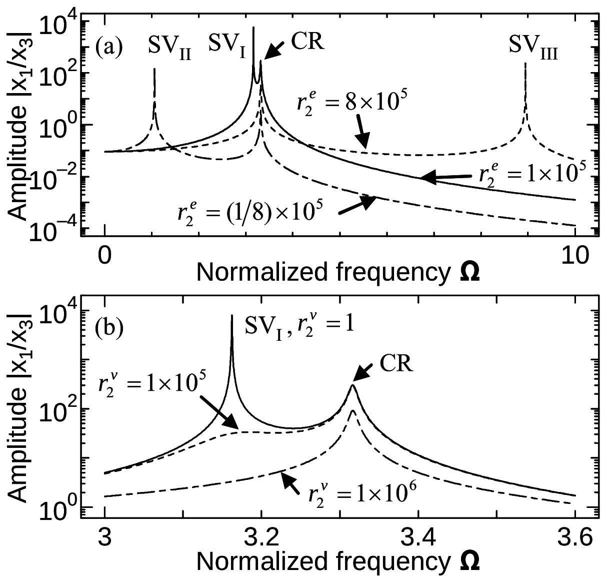

Fig.3 Variation of spurious vibration in resonance spectra. Dependence on (a) relative stiffness and (b) relative viscosity of the base..

4. Experimental verification

When the length of base L is changed (Fig.2(a)), we can decrease r_2^e. Dashed lines in **Fig.4** represent contact resonance frequency (CD1,2). As L increased, SV was shifted to lower frequency (SV1,2).

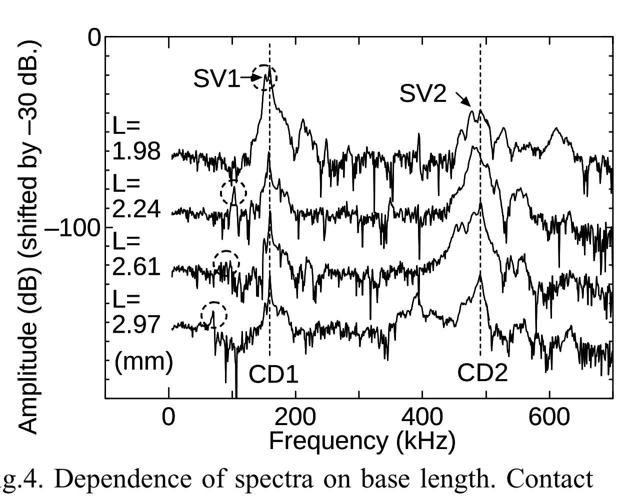

Fig.4. Dependence of spectra on base length. Contact on Si wafer.

The behavior of SV1 can be explained by analytical solution of deflection vibration of thick plate (Dashed circles) [6]. However, other SVs may affect CD1,2.

Aiming to remove all affection, we fabricated prototypical holder that clamps whole part of the base by a stainless steel cover (modified holder). **Fig. 5** shows a result. Most of SVs shown in Fig.1 were suppressed, which indicates that the cover is effective to the suppression of not only deflection modes but also other vibration modes, such as torsional and lateral modes.

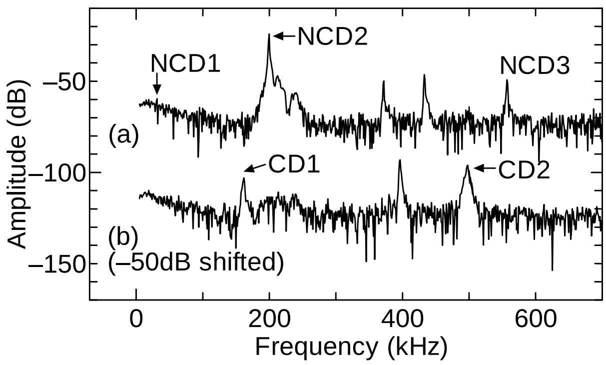

Fig.5. Suppression of spurious vibration shown in Fig.1 by modified holder. (a)Non-contact and (b) Contact on Si wafer.

5. Conclusions

We showed the effective method for the suppression of spurious vibration in UAFM, based on the analysis of coupled vibration system. The holder that clamps whole part of the base and the increase of the base thickness are promising method. We verified that the modified holder effectively suppressed the spurious vibration.

Acknowledgement

This work was supported by the Ministry of Education, Culture, Sports, Science and Technology.

References

1. K. Yamanaka and S. Nakano: Jpn. J. Appl. Phys., Part 1, **35** (1996) 3787.
2. T. Tsuji, H. Ogiso, J. Akedo, S. Saito, K. Fukuda and K. Yamanaka: Jpn. J. Appl. Phys., Part 1, **43** (2004) 2907.
3. T. Tsuji, S. Saito, K. Fukuda, K. Yamanaka, H. Ogiso, J. Akedo, and Y. Kawakami: Appl. Phys. Lett. **87** (2005) 071909.
4. Y. Sugawara, M. Ohota, H. Ueyama and S. Morita: Science **270** (1995) 1646.
5. U. Rabe, K. Janser and W. Arnold: Rev. Sci. Instrum. **67** (1996) 3281.
6. S. P. Timoshenko, D. H. Young and W. Weaver, Jr.: *Vibration Problems in Engineering* (Willey, New York 1974) p. 492.

P2-17

Proc. Symp. Ultrason. Electron., Vol. 26, (2005) pp. 245-246
16-18 November, 2005

Effect of temperature on the response of ball SAW hydrogen gas sensor

Kazushi Yamanaka[1], ○Takuji Abe[1], Naoya Iwata[1], Toshihiro Tsuji[1], Tsuyoshi Mihara[1], Kanwar Jit Singh[1], Shingo Akao[2], Noritaka Nakaso[2], Tsuneo Ohgi[2], Dong Youn Sim[3] , Yusuke Ebi [4], Takeshi Fukiura[4], Hidekazu Tanaka[4]
1. Tohoku University, 2. Toppan Printing, 3. Ball Semiconductor, 4. Yamatake

1. Introduction

Hydrogen fuel cells are expected as the most promising clean energy source. However, since hydrogen is an explosive gas, security of fuel cells requires hydrogen sensor with wide sensing range, fast response. Hence, we have developed a single element hydrogen sensor using surface acoustic wave (SAW) on a sphere with multiple roundtrips of collimate beam [1,2] It realized wider sensing range than other SAW sensors [3,4] or FET sensor[5]. In this paper, we report effect of temperature on the response of the ball SAW hydrogen sensor.

2. Equipment for sensor evaluation

Figure 1 shows a setup. We deposited a 40nm-thick Pd-Ni alloy thin film on a Langasite ball of 10 mm diameter. The ball was exposed to hydrogen at concentrations from 0.1 % to 3% by using a flow cell using mass flow controllers (MFCs). Since the MFC does not tolerate high temperature (> 100 ℃), the gas was rapidly heated after passing through the MFC. The heater consist of a densely wire together with a temperature regulator.

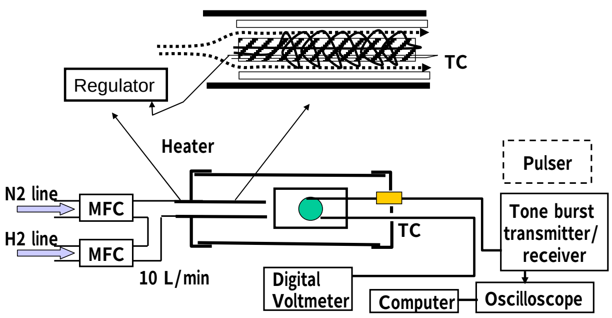

Fig.1. Setup of Ball SAW sensor evaluation

The SAW was excited and detected by an IDT. The measurement was performed either by a short pulse excitation (dotted box) [1,2] or by a tone burst transmitter and receiver with a quadrature and envelop demodulator, constructed for an acoustic microscopy [6].

3. Experimental results

Figure. 2 shows an envelop signal of 34 MHz tone burst at (a) 1 to 73 turns, (b) 60 to 68 turns and (c) 65 turns. The vertical axis is 1.6 $\log_{10}$ (V), where V is the received signal. From this figure, the Q factor was evaluated as ~37,000. In (c), five curves were obtained, just before and after introduction of 1.8 % H_2 at 23 ℃. It is noted that the amplitude decrease was completed within the sampling interval (2s).

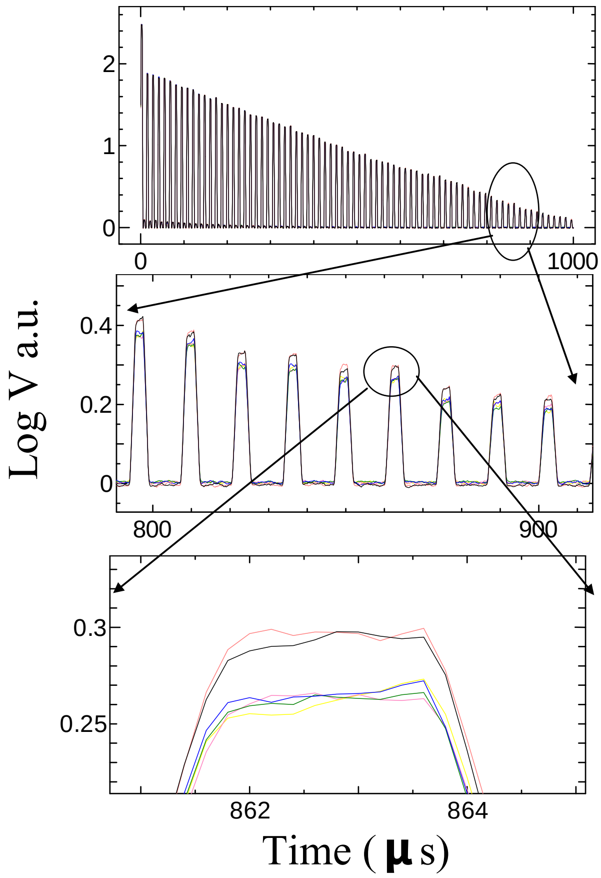

Fig. 2. Amplitude change of the tone burst envelop signal at room temperature (23 ℃).

Figure 3 shows an amplitude response obtained with the digital signal analysis of pulse waveform [1,2] for H_2 concentrations between 0.1 % and 3 %. The magnitude of the response (decrease of amplitude) increased with the H_2 concentration. Since the response was not saturated at 3% H_2, there is a possibility to differentiate H_2 concentration above 3 %, in contrast to our previous experiment [2].

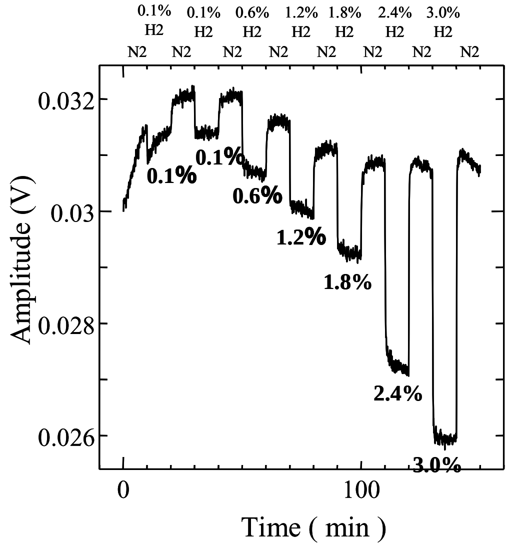

Fig. 3. Amplitude response of the sensor in H_2 from 0.1 to 3 %.

Figure 4 shows the effect of temperature on the response for low (0.6%) and medium (1.8%) concentration H_2, introduced at time t=0. The response time is defined as a time required for 90 % change of the amplitude. At 23 ℃, the response time was around 4 s at 0.6 % H_2 (a), whereas it was shorter (~2s) at 1.8 % H_2 (b). However, when the sensor was heated (124 ℃), the response time was shorter than at room temperature. It was 2 s at 0.6 % H_2 (c), whereas it was less than 2s at 1.8 % H_2 (d). This result indicates that heating to 124 ℃ reduces the response time. We also note an overshoot of the signal at room temperature where the signal first decreased rapidly and then increased slowly to the equilibrium. Such an overshoot was not present at 124 ℃, which is favorable for reliable sensor operation. Since we observed these distinct changes within a sampling interval, the flow cell response within 2s was confirmed.

As a drawback of the sensor at its present form, a base line drift was observed in Figs. 3 and 4. The possible reason may be either variation of temperature, pressure or gas atmosphere such as humidity. The drift may be eliminated by using a reference sensor without sensitive film [3,4] and by using a sensor protecting membrane.

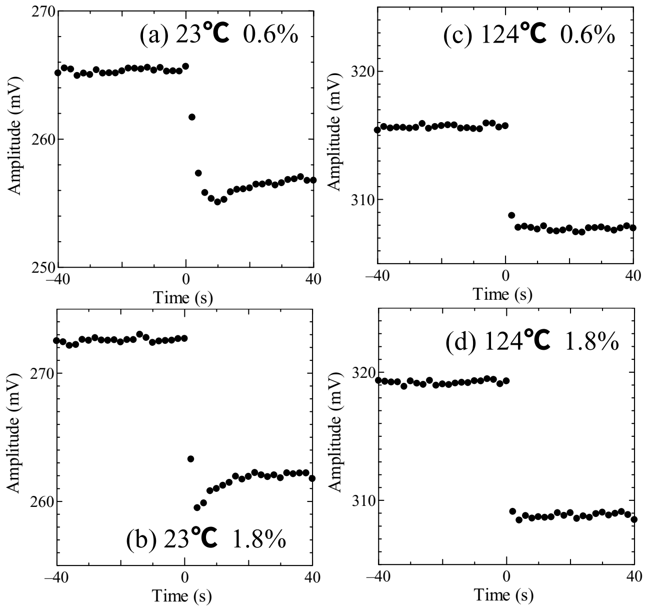

Fig. 4 Effect of temperature on the response time at room temperature (23 ℃) ((a) and (b)) and at 124 ℃ ((c) and (d)).

4. Conclusions

We investigated the effect of temperature on the response of the ball SAW H_2 sensor and found that the response time is reduced by heating to 124 ℃. The overshoot of the signal observed at room temperature was suppressed by heating.

Acknowledgement

This work was supported by the Ministry of Education, Culture, Sports, Science and Technology.

Reference

[1] K. Yamanaka, S. Ishikawa, N. Nakaso, N. Takeda, T. Mihara and Y. Tsukahara, Proc. 2003 IEEE Ultrason. Symp. 299 (2004).

[2] A. Mizukami, D. Y. Sim, I. Sato, T. Miyagishi, H. Tanaka, T. Fukiura, H. Kazato, S. Akao, T. Ohgi, N. Nakaso, H. Watanabe, T. Mihara and K. Yamanaka, Proc. Symp. Ultrason. Electron., 25, 301 (2004).

[3] A. D'Amico, A. Palma, E. Verona, 1982 IEEE Ultrasonics Symp. 308 (1982).

[4] W. P. Jakubik, M. W. Urbanczyk, S. Kochowski and J. Bodzenta, Sens. Actuators B 82, 265 (2002).

[5] R. C. Hughes and W. K. Schubert, J. Appl. Phys. 71, 542 (1992).

[6] K. Yamanaka, Y. Nagata and T. Koda Ultrasonics, 29, 159 (1991).

P2-18

Proc. Symp. Ultrason. Electron., Vol. 26, (2005) pp. 247-248
16-18 November, 2005

Electromagnetic Acoustic Resonance to Assess Creep Damage in a Cr-Mo-V Steel

◎Toshihiro Ohtani (Ebara Research Co., LTD.), Hirotsugu Ogi and Masahiko Hirao (Osaka University)

1. Introduction

Electromagnetic acoustic resonance (EMAR) [1,2] is an emerging technigue for measuring the ultrasonic velocity and attenuation of the metallic materials. It incorporated an electromagnetic acoustic transducer (EMAT) [1,2] in the resonant technique, realizing a non-contact and highly accurate measurements. In this study, the EMAR was applied to detect the creep damage process in a Cr-Mo-V steel, which is an important structual material for the thermal energy plants. The material was exposed to the temperature of 923K at various stresses. Two types of EMATs were used: the bulk-wave EMAT for plate samples and the axial-shear-wave EMAT for cylindrical samples. We measured ultrasonic attenuation in the frequency range between 1 and 7 MHz as the creep advanced. The attenuation coefficient exhibits much larger sensitivity to the damage accumulation than the velocity. It shows a peak at around 30% and a minimum value at 50 % of the creep life, being independent of the applied stress and type of EMAT. The EMAR has a potential to assess the damage advance and to predict the creep life of metals.

2. Samples and EMATs

We obtained the creep samples from two hot-rolled commercial round-bars of a Cr-Mo-V steel (JIS-SNB16). They were heated at 1283 K for 2 h, air-cooled, heated at 1223 K for 2 h, oil-quenched, and heated at 963 K for 6 h, air-cooled. One was used to make the plate specimen; its gauge section was 5 mm thick, 18 mm wide and 35 mm long. The other was cylindrical specimen; its gauge section was 14 mm in diameter and 60 mm long. Their mechanical properties are as follows; 0.2% proof stresses is 778 MPa, ultimate tensile strength 834 MPa and elongation 22 %.

We have built two types of EMATs which generate and receive the shear waves with the magnetostrictive effect of ferromagnetic materials by a non-contacting manner. One is the bulk-wave EMAT[1,2] for the plate samples, which generates the polarized shear waves traveling along the direction normal to the surfaces. This EMAT is used to excite and detect the through-thickness resonance for plate geometries. The resonant peaks appear at an equal frequency interval and at each resonant frequency; the attenuation coefficient is measured by the free-decay method, leading to the frequency dependence of attenuation. The other EMAT is for the cylindrical samples and generate the axial shear-wave; a surface shear horizontal wave, which propagates in the circumferential direction with an axial polarization [2,3]. The resonant mode of the axial shear-wave has own propagation region in the cross-section. The simultaneous measurement of the resonant frequency and attenuation of the several modes then enable us to evaluate the material inhomogeneity in radial direction [2].

3. Experiment

Creep tests were carried out at 923 K in air for various stresses between 25 and 55 MPa. Alongside the samples, the unstressed samples were placed to investigate only the effect of thermal history. We measured the resonant frequencies and the attenuation coefficients using the EMAR technique with the analog superheterodyne spectroscopy. The details of measurements and electronics can be found elsewhere [1, 4].

In creep test, we interrupted loading and furnace-cooled the samples in a furnace. After measuring the frequencies and attenuation coefficients at room temperature, we restarted the creep test. We repeated this procedure for every 20, 30 or 100 h until the rupture.

E-mail: ohtani.toshihiro@er.ebara.com

4. Results

Figure 1 shows the creep life fraction, t/t_r (the creeping time/ the rupture life), versus the attenuation coefficient, α of the 11th resonant modes (around 3.5 MHz) under four different applied stresses. It was the results for the plate samples. Rupture lives were 1018.1 h, 759.1 h , 292.0 h and 258.5 h for 25, 35, 45 and55MPa, respectively. α initially increases as creep progresses and shows a peak around t/t_r=0.3. After that, it decreases to t/t_r=0.5 and increases to the rupture. This trend is independent of the applied stress. No remarkable change occurred in the unstressed samples.

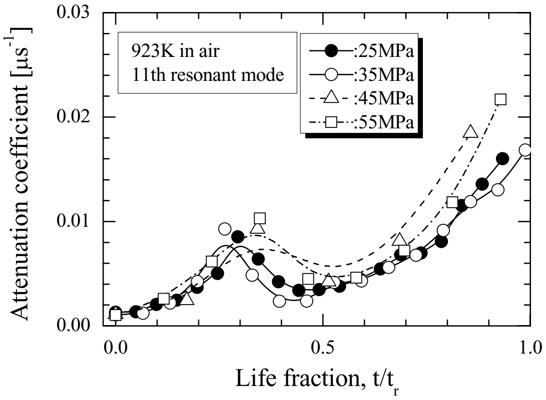

Fig.1. Relationship between the attenuation coefficient of the 11th resonant modes and life fraction with a bulk shear-wave EMAT (25, 35, 45 and 55 MPa, 923K).

Figure 2 shows the relationship between α of the first resonant mode (around 3.8 MHz) and t/t_r under three different stresses for the rod samples. Rupture lives were 774.3 h, 401.5 h and 185.0 h for 35, 45 and 55MPa, respectively. The trend of α is very similar with that observed in plate samples by the bulk-wave EMAT. Namely, α experiences the peak at 30% and the minimum at 50 % of the creep life, being independent of the applied stress and type of EMAT.

Furthermore, we observed the change of microstructure; grain size, precipitation density and dislocation structures with optical microscope, SEM and TEM. The evolution of α as creep progress is related to the microstructure change, especially, dislocation structure. At attenuation peak, many long and isolated dislocations are generated in cell and subgrains. They vibrate to absorb the ultrasonic-wave energy. However, they are absorbed into the cell walls and sub-boundaries as creep progresses to cause the minimum attenuation.

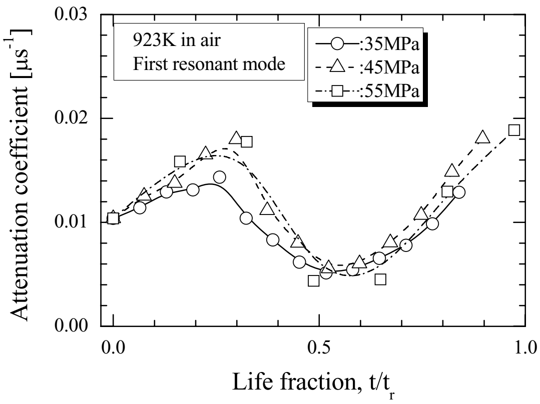

Fig.2. Relationship between the attenuation coefficient of the 1st resonant modes and life fraction with an axial shear-wave EMAT (35, 45 and 55 MPa, 923K).

4. Conclusion

Creep damage in Cr-Mo-V steel (JIS-SNB16) at 923 K in air was evaluated through ultrasonic attenuation measured with the EMAR method. Attenuation showed a peak at around 30% and a minimum value at 50 % of the creep life, being independent of the applied stress a type of EMAT, which is interpreted as resulting from microstructural changes, especially, dislocation mobility. This is supported by TEM observations. This technique has a potential to assess the damage advance and to predict the creep life of metals.

References

1. M. Hirao, H. Ogi and Fukuoka: *Rev. Sci. Instrum.* **64** (1993) 3198.
2. M. Hirao and H. Ogi: *EMATs for Science and Industry,* (Kluwer Academic Publishers, Boston, 2003), 2.
3. H. Ogi, M. Hirao and K. Minoura: *J. Appl. Phys.* **81** (1997) 3677.
4. G.L. Petersen, B. B. Chick, C.M. Fortunko and M. Hirao: *Rev. Sci. Instrum.* **64** (1993) 3198.

Proc. Symp. Ultrason. Electron., Vol. 26, (2005) pp. 249-250
16-18 November, 2005

Surface Roughness Characterization by Angular Distribution of Scattered Waves Using Air-Coupled Ultrasonic Technique

◎Deden Dian Sukmana and Ikuo IHARA (Nagaoka Univ. of Technology, Mechanical Eng.)

1. Introduction

Surface roughness is an important parameter for evaluating surface properties of materials and is typically measured by a stylus instrument that amplifies and records the vertical motions of a stylus as it moves across the surface. For soft and delicate surfaces, however, non-contact techniques such as optical methods are preferable[1)]. In this work, a novel non-contact technique using air-coupled ultrasound has been used to characterize surface roughness of the materials. The technique is based on scattering phenomenon. In our previous work [2, 3)], the scattered waves from material surfaces were measured at various reflection angles θ_2 on the *xz*-plane shown in **Fig. 1**, and the correlation between the scattered waves and the surface roughness was obtained. In this work, the scattered waves at a certain reflected angle are measured as a function of azimuthal angle θ_3 in *xy*-plane. The relationship between the intensity distribution of the scattered wave and the surface roughness is examined for various θ_3. The Kirchhoff-based scattering model is used to verify the validity of the experimental results.

2. Experimental

The measurement system is mainly consisted of a pair of broadband air coupled capacitance transducers (Micro Acoustic Co., BAT) having center frequency of 0.5 MHz, a square wave pulser (Ritec, SP-801A) and a broadband receiver (Ritec, BR-640A) [2, 3)]. The working distance between the transducer and specimen surface is 35 mm. Figure 1 shows the scattering geometry used in the experiment. Seven kinds of sandpaper sheets having different roughness were used for the specimens and were bonded on a steel plate to make flatness. A polished stainless plate was used as a reference specimen of smooth surface. **Figure 2** shows the surface profiles of each specimen obtained using a stylus profilometer. The height and lateral roughness parameters used for evaluating surface profile are the root-mean-square roughness *Rq* and the surface correlation length λ_o, respectively[4)]. The *Rq* and λ_o of the specimens are deviated from 0.04 to 115 μm and from 83 to 250 μm, respectively. The ultrasonic wave is incident onto the specimen surfaces at incident angle θ_1=30° and the scattered wave is measured at scattering angle θ_2=30° and θ_3=-90°~90°.

Email: ihara@mech.nagaokaut.ac.jp

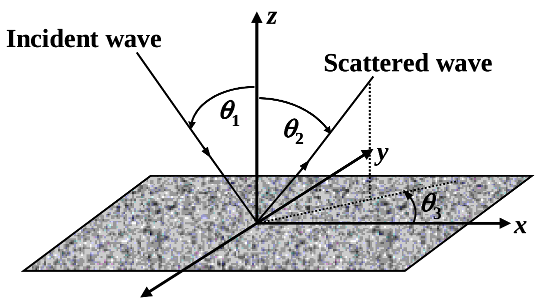

Fig. 1 The scattering geometry used in the experiment.

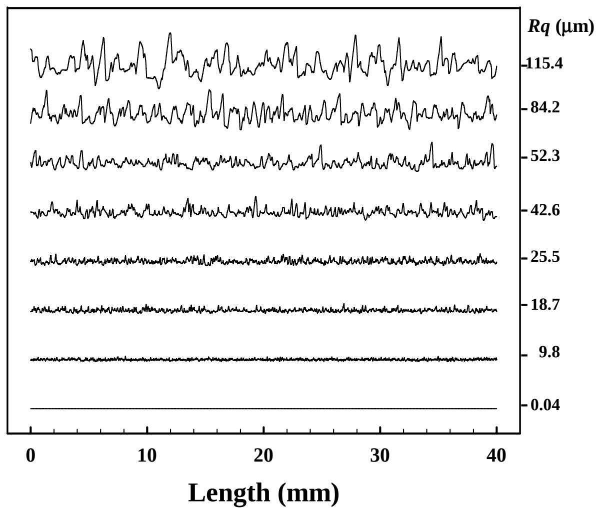

Fig. 2 Surface profiles of each specimen measured by a stylus method.

3. Results and discussion

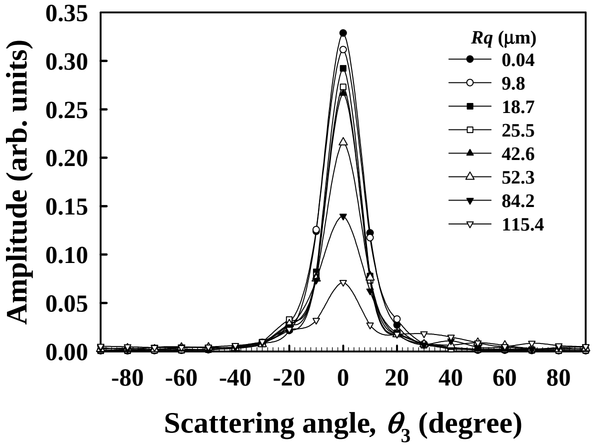

Fig. 3 The intensity distribution of the scattered waves from the surfaces having different roughness.

Figure 3 shows the change of the amplitudes of the scattered waves with the scattering angle in the azimuthal direction θ_3 for various roughnesses. At the specular reflection angle in which $\theta_1=\theta_2=30^o$ and $\theta_3=0^o$, the coherent component is dominant in the scattered waves. We can see that the amplitude decreases as roughness increases. The relationship between such the coherent component and the surface roughness was discussed in details in ref. 5. In this work, we focus on the azimuthal angle dependence of incoherent component. For $\theta_3>30^o$, the incoherent component is considered to be dominant in the measured waves. For the scattering geometry shown in Fig.1, the incoherent component can be estimated using the Kirchhoff-based scattering model and written as[6)]

$$I_{incoh} = \frac{\pi\lambda_o^2 F^2 k^2 e^{-g}}{(4\pi R)^2} A_M \sum_{m=1}^{\infty} \frac{g^m}{m!m} \exp\left(-\frac{k^2\left(A^2+B^2\right)\lambda_o^2}{4m}\right), \qquad \cdots\cdots\cdots\cdots(1)$$

where $g=k^2Rq^2(\cos\theta_1+\cos\theta_2)^2$, k is the wave number, A_M is insonified area, R is the distance between the specimen surface and the transducer, F, A and B are the angular factors defined by θ_1, θ_2 and θ_3, respectively. It is noted that the incoherent component depends on not only the roughness Rq but also the surface correlation length λ_o of the surface profile. Therefore, the correlation length λ_o can be estimated from the amplitude of incoherent component when the roughness Rq is known.

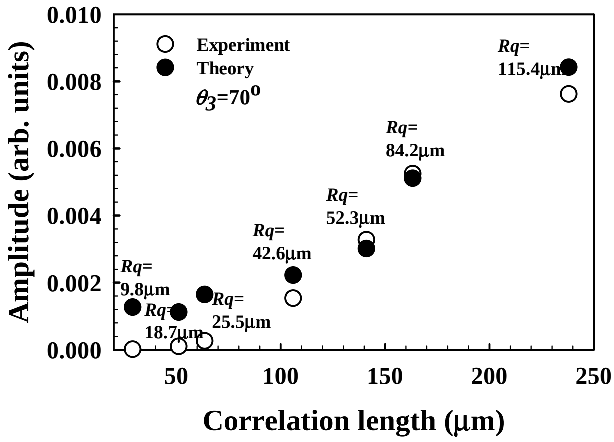

Fig. 4 Relationship between the amplitude of incoherent component and surface correlation length λ_o.

Figure 4 shows the relationship between the amplitude of the incoherent component and the correlation length λ_o obtained experimentally and theoretically. From this result, however, we have found that there is no significant difference from the previous results[3)] obtained with $\theta_3=0^o$. This is because the surface characteristic of the sandpaper is an isotropic and homogenized. The result may differ if the specimen surface being used has a directional roughness, as usually found in the surface produced by machining process in which the surface profile strongly depends on the azimuthal angle. In this case, the measurement of the scattered wave in the different azimuthal angle may give any useful information about the directional roughness.

Acknowledgment

The financial supports from Grant-In-Aid for Scientific Researches (B17360351) by JSPS are appreciated.

References

1. DJ. White House: Meas. Sci. Technol. **8** (1997) pp.955-972.
2. Deden DS, et al.: Proc. Symp. Ultrason. Electron. **24** (2003) pp.101-102.
3. Deden DS, et al.: Proc. Symp. Ultrason. Electron. **25** (2004) pp.239-240.
4. Y.P Zhao: *A Simple Introduction to Rough Surface Characterization*, 2000.
5. Deden DS, et al.: Jpn. J. Appl. Phys. **44** (2005) pp. 4417-4420.
6. J.A. Ogilvy: *Theory of Scattering from Random Rough Surfaces* (Bristol, IOP, 1991).

P2-20

Proc. Symp. Ultrason. Electron., Vol. 26, (2005) pp. 251-252
16-18 November, 2005

Electromagnetic acoustic transducer (EMAT) for generation and detection of guided wave

◎ SongSong Li[1], Toshimi Okada[1] and Xiaoming Chen[2]
1.Toyama Prefectural University, Electromagnetic Wave Laboratory, 2.Toyama University

1. Introduction

A variety of guided waves techniques have been developed and their applications in NDE have been discussed in the published articles [1]. The research effort into guided waves in plates has developed from the classical Rayleigh-Lamb wave [2]. For a given thickness and frequency, there may exist many different modes. This tends to make the received signals complex and so difficult to interpret. For NDE, it is desirable to excite a pure single mode of propagation because this will make the analysis of data become easier. In this paper, a Lorentz Force EMAT system is proposed for the excitation and detection of single Lamb wave mode and Rayleigh wave by controlling the center frequency of narrowband signals.

2. Dispersion curves of Lamb wave and EMAT design

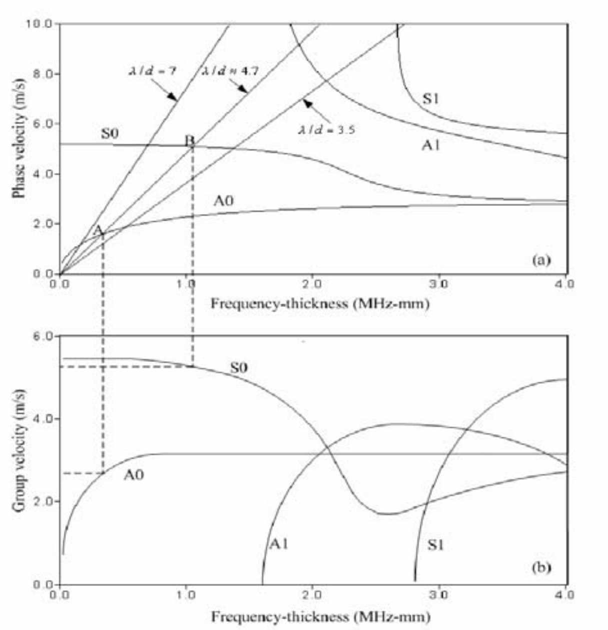

Figure 1. Lamb wave dispersion curves for steel plate: (a) phase velocity and (b) group velocity

Figure 1 (a) and (b) show the phase velocity and group velocity dispersion curves of Lamb wave in a steel plate, and the maximum limit of frequency-thickness product range is 4MHz-mm. The wavelength of Lamb wave, λ, [1]is given by $\lambda = \dfrac{c_p}{f}$, where c_p is the phase velocity of the mode and f is the frequency. By the dispersion curves, the phase velocity is the function of $f * d$. Eq. (1) is also written as $\dfrac{\lambda}{d} = \dfrac{c_p}{fd}$, where d is the plate thickness. For a given plate thickness and wavelength, the constant λ / d is the tilt of the straight line though the origin on the coordinate plane of the phase velocity dispersion curves, and the points at which the line with tilt λ / d intersect the dispersion curves of the different modes are the points at which the modes can be excited.

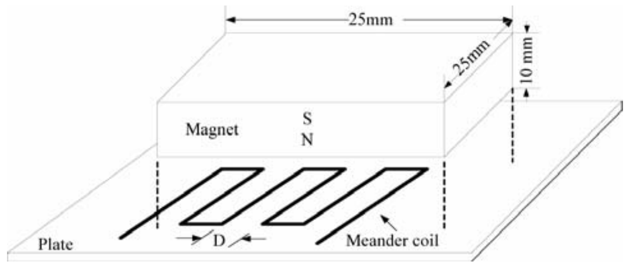

Figure 2. Configuration of Lorentz Force EMAT for generation of guided wave

The wavelength of Lamb wave is controlled by the configuration of EMAT. A Lorentz EMAT consists of a meander coil and a static permanent magnet, which is shown in figure 2, where the bias field is perpendicular to the plate and the magnet is over the meander coil that is exerted an alternating current. The meander coil creates eddy current in the plate, which then create the force in the plate by the Lorentz interaction with the biased magnetic field and hence give rise to the Lamb wave and Rayleigh wave. The process can also be used to detect Lamb wave and Rayleigh wave. In the meander coil EMAT construction, the generation of the Lamb wave and Rayleigh wave is realized by the spatially periodic stress radiating energy at an oblique angle. When the period (2D) of the meander coil line acts as an ultrasonic wavelength λ, the efficiency should be greatest, thus, the optimized Lamb wave mode can be excited. Therefore, in our experiments, the spacing size (D) of meander coil is selected as half a wavelength.

In Figure 2, the size of the magnet is 25mm x 25mm x 10mm, thus, the meander coil is

[1] Email: s-li@rdw.pu-toyama.ac.jp

designed as 6 fingers, and the spacing D between connected fingers is 3.5mm (half a wavelength). The wavelength of the Lamb wave is 7mm.For a given plate thickness, the excitation frequency of each mode is found. For example, for 1.5mm thick steel plate, the value of λ / d is about 4.7. The line with tilt of 4.7 intersects the dispersion curves of A0 and S0 mode at points A and B, indicating that the A0 mode and S0 mode can be excited at points A and B, respectively, as shown in figure 1 (a). Thus, the excitation frequency of each mode can be calculated. On the dispersion curves of phase velocity, it is known that the frequency-thickness product for the A0 mode is about 0.36MHz-mm, and the frequency-thickness product for S0 mode is about 1.02MHz-mm. Therefore, the excitation frequency for A0 is 0.24MHz, and the frequency for S0 is 0.68MHz. Similarly, for 1mm and 2mm thick steel plate, the value of λ / d is 7 and 3.5, respectively, and the excitation frequencies of each mode can be fond.

On the other hand, by the dispersion curves of group velocity, the theoretical group velocity of the corresponding mode can be known. For example, for 1.5mm thick steel plate, the group velocities of A0 mode and S0 mode are 2520m/s and 5200m/s, respectively, as shown in the figure 1 (b). These velocities can be used to compare with the real velocity of the single mode, and confirm if the desired single mode has been excited.

The operation process of the experimental setup used to excite and receive the Lamb wave is: the tone-burst pulse generated by the pulse generator, after being amplified by the power amplifier, is sent to the T-EMAT (Transmitter -EMAT). The excited Lamb wave propagates along the steel plate. The transmission wave and the reflection wave are received by the R-EMAT (Receiver -EMAT). After being amplified, the received waveforms are recorded in the digital oscilloscope, and are finally stored in computer for the data analysis.

4. Experimental results

A series of tests were performed in the different thickness steel plate. The transmitter EMAT is placed on the left side of plate to avoid the bidirectional signal, and the receiver EMAT is placed on the position that is 50cm away from the left side of plate. In order to observe easily the position where Lamb modes appear, the distance between the T-EMAT and R-EMAT is 50cm.

It is known that Lamb wave modes are successfully excited in different plate specimens, and with increasing of plate thickness, the excited Lamb modes also is increased. For example, in 1mm and 1.5mm steel plates, only A0 mode and S0 mode are excited, while in 2mm steel thick plate, A1 mode also is excited. At the same time, it is found that this EMAT configuration also excited the Rayleigh wave.

Figure 3 is a typical result using EMAT to generate each wave mode in the 1.5mm steel plate: (a) shows the Lamb wave A0 mode that it is excited at 0.24MHz, (b) shows a Rayleigh wave that is excited at 0.46MHz, and (c) shows the Lamb wave mode S0 that is excited at 0.64MHz. A0(1), R(1) and S0(1) indicate the direct wave signal, and R(2) and S0(2) indicate the reflected wave signal from the right end of plate. S(3) indicate the reflected wave from the left edge of plate, because the attenuation of the S0 mode is slow so that the reflected wave signal from the right end of plate is again reflected from the left edge of plate. From the excitation result of each mode, it is found that when one mode is excited, other modes are not excited at this frequency.

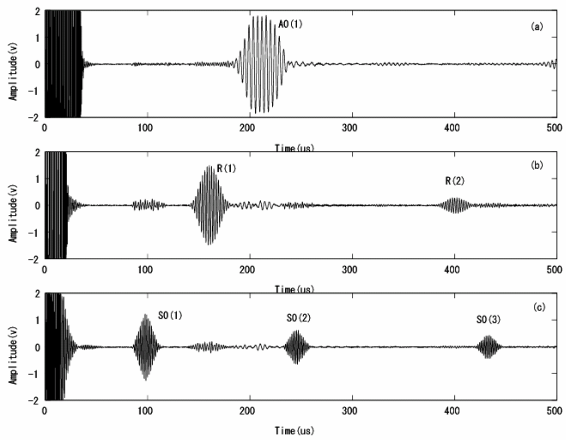

Figure 3. Waveforms of the modes excited in 1.5mm steel plate. (a) A0 mode, (b) Rayleigh wave and (c) S0 mode

5. Conclusion

In this paper, a narrowband signal EMAT system that can be used to generate and detect the pure modes is described. It has been shown that this EMAT configuration can be used successfully to excite and receive the Lamb waves and Rayleigh wave, and the results are consistent with the theoretical predictions of dispersion curve.

References

[1] Joseph L. Rose: Journal of Pressure Vessel Technology. **124** (2002) 273

[2] Viktorov I A: Rayleigh and Lamb waves-Physical Theory and Applications. (New York: Plenum) 1967

Proc. Symp. Ultrason. Electron., Vol. 26, (2005) pp. 253-254
16-18 November, 2005

Synthesis of the rejection band profile in ultrasonically induced optical fiber long-period grating

◎Norimichi Fukuma, Kentaro Nakamura, Sadayuki Ueha (P&I Lab., Tokyo Inst. of Tech.)

1. Introduction

Among various kinds of acousto-optic devices, fiber optic configuration has an advantage in insertion loss and coupling optics. An optical fiber long-period grating (LPG) is obtained by ultrasonic bending vibration propagating along the fiber [1][2]. The ultrasonic vibration generates a temporary periodic modulation in the refractive index of fiber, which causes mode couplings between the fundamental transmission mode of the fiber and the decaying modes at a certain optical wavelength determined by the spatial period of the modulation. The ultrasonically induced grating has an advantage in tunability. The rejection optical wavelength is tunable with the ultrasonic frequency. Authors experimentally investigated the vibrations excited on the fiber, as well as the optical transmission characteristics of the ultrasonically induced LPG [3]. A method to synthesize the rejection band shape is proposed in this report.

2. Experimental setup

A single mode fiber was used in our experiments. A part of the coating is removed, and the bare fiber is bonded at the top of a piezoelectric transducer as shown in Fig. 1. The transducer is driven at several hundred kHz: much higher than the fundamental resonance frequency of the transducer. Then, many longitudinal resonance modes can be utilized over the frequency range for the experiments to excite vibrations on the fiber at various frequencies. The silicon rubber coating of 400 μm in diameter on the opposite of the fiber side acts as an acoustic absorber.

3. Optical transmission characteristics

The ultrasonic vibration decays rapidly in the coated region, and a good traveling wave is excited on the bare fiber [3]. The standing wave ratio was 1.4. Flexural waves are excited along the fiber in our experiment, since the measured wavelengths well agree with the Timoshenko's beam theory. The optical transmission characteristics were measured using a super luminescent diode as a broadband light source and an optical spectrum analyzer. Transmission characteristics with the ultrasonic frequencies around 330 kHz are shown in Fig. 2. The optical center wavelength of the dip is shifted by the ultrasonic frequency. Transition of the optical center wavelength of the dips is shown in Fig. 3 as functions of the ultrasonic driving frequency. Four series of rejection center wavelength are observed and they are changed monotonously by the ultrasonic driving frequency.

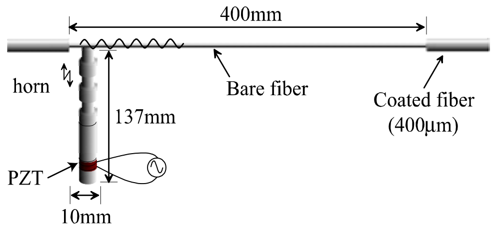

Fig. 1 Experimental setup for the ultrasonically induced optical fiber long-period grating.

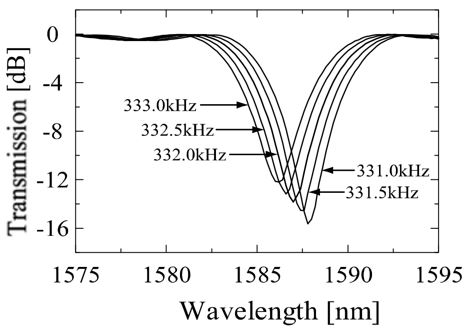

Fig. 2 Transmission characteristics at different ultrasonic frequencies.

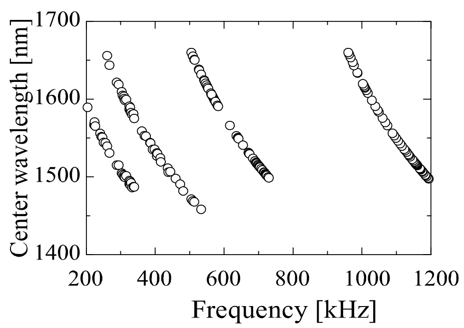

Fig. 3 Optical center wavelengths vs. the ultrasonic frequency.

----

e-mail : fukuma@sonic.pi.titech.ac.jp

4. Temporal change of the rejection band

In the previous measurements, the optical transmission characteristics were observed by an optical spectrum analyzer as time averaged results. In this section, the temporal change of the transmitted light intensity is observed. A tunable semiconductor laser is used as a light source and the transient of transmitted light intensity is recorded by a photo detector at every wavelength just after the voltage is applied to the transducer. The results are shown in Fig. 4, where the excitation of the transducer starts at t = 0. Much longer time is needed for building up the rejection band than the time for the propagation of the ultrasonic wave from the driving point to the end. The rise time of the transducer vibration is dominant, since the ultrasonic transducer is driven at its resonant frequencies.

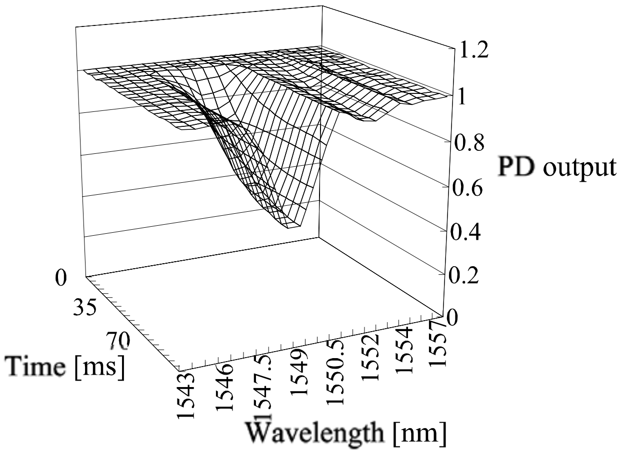

Fig. 4 Rise of the rejection band just after applying voltage to the transducer

5. Synthesis of the rejection band shape

A method to synthesize the arbitrary band shape is proposed in this section. The driving frequency is switched alternatively at a certain period so that two different vibrations exist on the fiber at the same time as illustrated in Fig. 5. The switching period is so carefully chosen that the wave should travel a half of the fiber length for the given duration, considering the propagation speed of the wave. In this experiment, vibrations at 342.4 kHz and 344.1 kHz were excited intermittently on the fiber. As a result, optical transmission characteristics shown in Fig. 6 were obtained. The rejection band was widened in width and had two attenuation peaks. In this way, the shape of rejection band can be synthesized by combining several different vibrations.

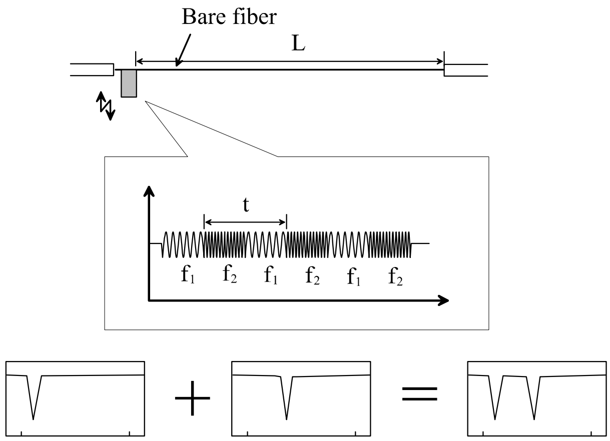

Fig. 5 A method for synthesize the rejection band shape.

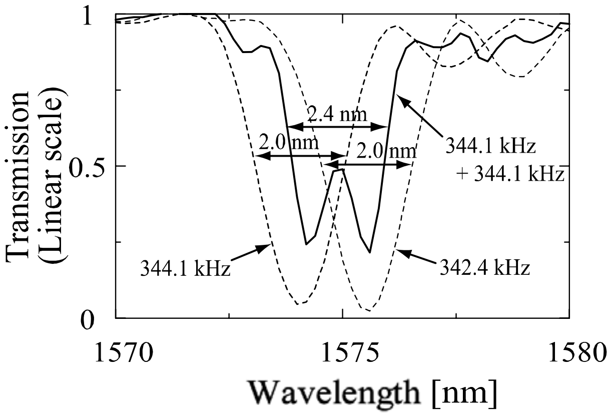

Fig. 6 An example of the rejection band synthesis.

6. Conclusions

By considering the transient characteristics of the ultrasonically induced long-period fiber grating, a method to synthesize the rejection band shape was discussed. Band width was widened by combining two vibrations with different frequencies. To excite the vibration with enough amplitude we need to utilize the resonance of the transducer. As a result, large optical rejection ratio is obtained only at discrete resonant frequencies over the whole band. Use of the resonance is the basic limitation for transient response and sweep speed. A new configuration should be introduced to achieve fully continuous sweep and arbitrary rejection band shape control.

References

1. H. E. Engan, B. Y. Kim, J. N. Blake, and H. J. Shaw: J. Lightwave Technol. **6** (1988) 428-435.
2. D. Ostling, and H. Engan: Optics Letters **20** (1995) 1247–1249.
3. N. Fukuma, K. Nakamura and S. Ueha: Proc. OFS-17, SPIE **5855** (2005) 852-855.

P2-22

Proc. Symp. Ultrason. Electron., Vol. 26, (2005) pp. 255-256
16-18 November, 2005

PIEZOELECTRIC PHOTOTHERMAL AND PHOTO-REFLECTANCE SPECTRA OF InGaN GROWN BY RADIO FREQUENCY-MOLECULAR BEAM EPITAXY

○E. Kawano, Y. Uchibori, T. Shimohara, H. Komaki, R. Katayama(1), K. Onabe(1), A. Fukuyama, and T. Ikari

Faculty of Engineering, University of Miyazaki, 1-1 Gakuen-Kibanadai-nishi, Miyazaki 889-2192, Japan
(1) Graduate School of Frontier Sciences, The University of Tokyo, 5-1-5, Kashiwanoha, Kashiwa-shi, Chiba, 277-8562, Japan

Abstract

Piezoelectric Photothermal Spectroscopy (PPTS) measurements have been carried out on InGaN (In=0~0.32) thin films grown by radio frequency molecular beam epitaxy. We found that the band energy shifts to the lower energy side (Red shift) by the increase of In composition from 0 to 0.32. For the samples with lower In composition, we could observe the exciton contribution and the obtained binding energy was estimated to be 30 meV (In=0.01). Since, the usual photo-reflectance (PR) spectroscopy could not observed the signals for the samples of higher In composition, the usefulness of the present PPTS methodology is concluded.

1. Introduction

Since band gap energy of nitride semiconductor InGaN may change by the composition in a wider range from 3.5 (GaN) to 0.7 (InN) eV, it is possible to covering from the ultraviolet to the infrared region when this material is used for optoelectronic devices. Accordingly, InGaN is very promising materials for light-emitting diode, semiconductor laser diode, light-detecting component, and optical communication devices. However, the growth of InGaN, especially for high Indium composition, is usually very difficult. Some of the reasons are the lattice mismatch and the different thermal stabilities of GaN and InN, and the bond lengths and the binding energies of each atom. These produce defects like phase separation and dislocation during the crystal growth. Therefore, physical properties of InGaN did not understand well yet. Optical absorption spectra of InGaN thin film was measured by using a Piezoelectric Photothermal Spectroscopy (PPTS) [1]. The PPTS method is known to have a high sensitivity for such thin film structures. Moreover, to clarify the advantage of the PPTS method, we also measured the same sample by using a photo-reflectance (PR) method.

2. Experimental Procedure

InGaN was grown on sapphire (0001) plane by molecular beam epitaxy with RF plasma (for N_2) cell (RF-MBE) at 575 °C for 90 min. Ga/In flux and RF plasma output were fixed at 1×10^{-4} Pa/5×10^{-5} Pa and 400 W, respectively. N_2 flow rate was varied from 1.0 to 2.0 sccm (1.0, 1.2, 1.5, 1.75, 2.0 sccm). Before InGaN growth, nitridation of sapphire substrate was performed by growing thin AlN and GaN buffer layers to stabilized the InGaN growth. The sample geometry is shown in **Fig.1.** For the PPT measurements, the probing-light from a grating monochromator was mechanically chopped and focused on the substrate side of the sample at RT.

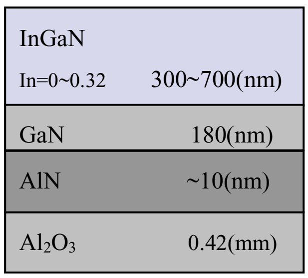

Fig.1 A schematic cross section of the InGaN thin film

The PPT signal was detected by the piezoelectric transducer (PZT) on the film side of the sample. The signal was amplified by the two-phase lock-in amplifier. The PR measurements were carried out at room temperature by using a standard experimental setup [2].

3. Results and Discussion

Figure. 2 shows the result of the PR measurements (In = 0~0.13). The PR spectrum was analyzed by the low-field ER line-shape function, i.e., third derivative functional form [3]. The energies of E0 critical point were estimated to be 2.73 eV (In=0.13), 3.18 eV (In=0.05) and 3.41 eV (In=0.01), respectively. Band energy shifts to the high energy side (Red shift) by the increase of In composition. However, the intensity of PR spectrum decreased with the increase in In composition, and fitting analysis became difficult for the sample of In>0.13. We considered that the fluctuation and phase separation of composition cause the decrease of the signal to noise ration when the In composition increased.

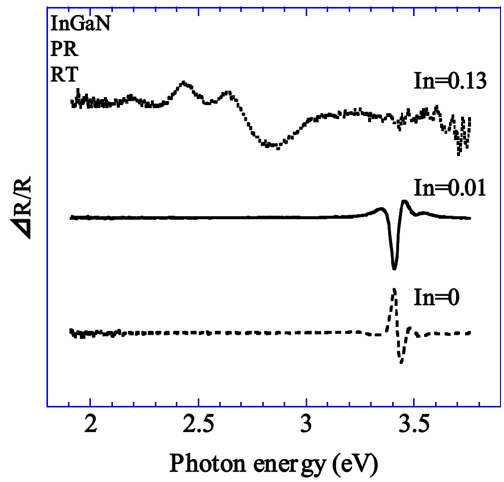

Fig.2 Photo-reflectance spectra of InGaN (0<In<0.13)

Figure. 3 shows the PPTS spectra for the samples with different In composition (0~0.32). Since the observed spectra indicate the existence of an exciton for low In compositions, the Quasi-Voigt function was used for decomposing the exciton contribution and the energies of band gap were estimated. Consequently, we obtained the binding energy of the exciton as 30 meV (In=0.01), and was almost the same as the value of 28 meV of GaN. Since the exciton contribution decreases with increasing the In composition above 0.05, the band gap was calculated from the relations of $(PPTS \times h\nu)^2$ versus hν supposing that the InGaN being a direct gap semiconductor. From the PPTS results in Fig. 3, it was found that the band gap shifted to the lower energy side by the increase of In composition (Red shift). Although the PR measurements could not reveal the band gap for In>0.13, the PPTS method could determine them. We think the present PPTS method has advantages for measuring the absorption spectra for the crystals with compositional fluctuation.

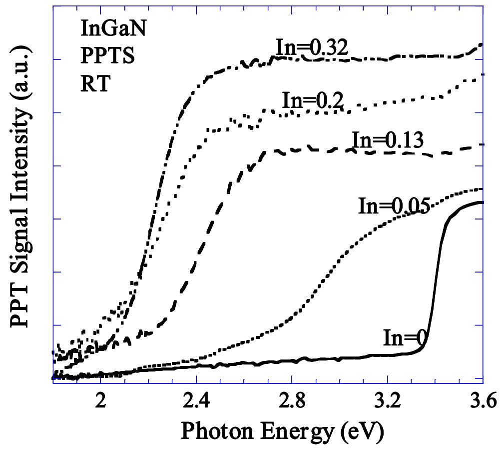

Fig.3 PPTS spectra of InGaN (0<In<0.13)

4. Conclusion

An aim of this work was to investigate the optical properties of InGaN by using a PPTS method. We found that the band energy shifts to the lower energy side (Red shift) by the increase of In composition from 0 to 0.32. Since the intensity of PR spectrum decreased with the increase of In composition, we found that PR technique is not good for the sample with compositional fluctuation. For the samples with lower In composition, we could also observe the exciton contribution and the obtained binding energy was estimated to be 30 meV (In=0.01).

5. References

[1] A. Fukuyama, A. Memon, K. Sakai, Y. Akashi and T. Ikari, J. App. Phy. 89, (2001) 1751-55.

[2] S. Chichibu, H. Okumura, S. Nakamura, Guy Feuillet, T. Azuhata, T. Sota, and S. Yoshida：Jpn. J. Appl. Phys. 36, (1997) 1976-1983.

[3]D.E.Aspnes,Surface Science 37, (1973) 418-44

---

kawano@pem.miyazaki-u.ac.jp

Proc. Symp. Ultrason. Electron., Vol. 26, (2005) pp. 257-258
16-18 November, 2005

Calibration for Measurement of Sound Fields Using Optical Probe

◎**Takeshi OHBUCHI**, **Koichi MIZUTANI, Shingo SHIBATA** (Univ. Tsukuba) and **Hiroyuki MASUYAMA** (Toba Natl. Coll. Mar. Tech.)

1. Introduction

In fields of the medical treatment diagnosis and the industrial instrumentation etc, the measurement that uses the ultrasonic wave is widely used from the characteristic such as non-contact and non-destructive. It is necessary to measure the sound fields for the calibrating of the ultrasonic probe. An optical probe is used for the noncontact measurement of sound fields [1-3]. They use phase deviation of light by the sound wave. The optical system such as interferometers is necessary for that method. And a sound field also influences light intensity [4]. In this paper, we propose the simple system for measuring of sound fields that uses the amplitude of optical intensity acquired by Avalanche photodiode (APD) module.

2. Principle

Figure 1 shows the experimental system measuring the sound fields. The experimental system consists of laser and ultrasonic transducer and APD. The laser beam passes through the water tank including sound fields emitted from transducer. Then, the laser beam is diffracted or is refracted. The light that is diffracted or refracted contain information on the sound fields. Direction emitted laser and ultrasonic from are defined *y*-axis and *z*-axis, respectively. The *x*-direction indicates the transversal direction of the sound. APD put in position on *y*-axis. Sound wave defines a sinusoidal plane wave that propagates in the *z*-direction. And the sound wave emitted to water gives a refractive index of a medium a change. The refractive index of water is given by

$$n = n_0 + kp(x, y, z, t), \tag{1}$$

$$k = \frac{(n_0 - 1)(n_0^2 + 1.4n_0 + 0.4)}{(n_0^2 + 0.8n_0 + 1)\rho_0 c_s^2}, \tag{2}$$

where n_0 is refractive index without sound fields in the medium, ρ_0 is density of the medium, c_s is velocity of pressure. k is proportionality constant concerned between amplitude of the sound pressure and change of the refractive index [5].

The change in the refractive index according to sound pressure causes refraction or diffraction. When the width of laser beam is

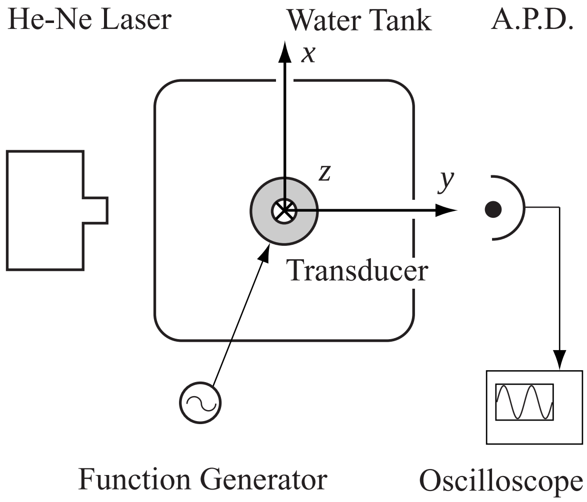

Fig.1 Experimental setup

very wide compared with the wavelength, the laser is diffracted or reflected. When frequency of the ultrasonic wave is several MHz, the light is diffracted. The intensity of incident radiation is normalized in the maximum value. The intensity of *m*-th order diffracted light I_m is given by

$$I_m = J_m^2(\nu), \tag{3}$$

where J_m and ν are the *m*-th order Bessel function of the first kind and Raman-Nath parameter. Raman -Nath parameter is given by

$$\nu = \frac{2\pi}{\lambda} \int \delta_n(y) dy, \tag{4}$$

where λ, n and $\delta_n(y)$ are the wavelength of the light, the refractive index of the medium in the measurement space and the distribution of the change of the refractive index of the medium on the direction of propagation of light, respectively.

On the other hand, when the width of laser beam is not very wide compared with the wavelength of the ultrasonic wave, the laser is refracted by refractive index gradient. Light intensity acquired by the APD includes information of sound fields. However, relation between light intensity and sound pressure is not linear. Therefore, it is necessary to calibrate.

3. Measurements and Results

The light source is a He-Ne Laser (05LHP151 / Melles Griot). The piezoelectric transducer (NEPEC

ohbuchi@aclab.esys.tsukuba.ac.jp

21 / TOKIN) is an 8.0 mm aperture in diameter at the frequency of 1.6 MHz. The transducer is set to the mechanical *x*-stage and is scanned relative to the light beam. The optical intensity is measured by the APD module (C533-03 7L-748 / Hamamatsu Photonics). The one dimensional distribution of the optical intensity along the *x*-axis is acquired by the move of the *x*-stage. The signal is observed with the oscilloscope (54645A / Hewlett Pckard). Fig.1 shows the experimental setup.

Figure 2 shows characteristic curve for calibration. Because of relation between input voltage to transducer and the sound pressure emitted by transducer is linear, the output voltage from APD and the input voltage to transducer are used for calibrating. When the characteristic curve is acquired, transducer is fixed at the point assumed origin. Regression curve of the characteristic curve became normal distribution. Intensity distribution of laser is Gaussian. It is thought to be the most likely cause of that regression curve.

Figure 3 shows projection data. The linear scanning region of x-axial direction is from −6 mm to 6 mm with 0.5 mm step length at a distance of under 10.0 mm from the vibrating surface. The input voltage to transducer is 25 Vp-p (○) and 50 Vp-p (△). The broken line is magnification. There is no change in the normalized sound fields even if the input voltage changes. Therefore, the projection data is sure to double, when the input voltage is doubled. Distribution of high sound pressure is skew.

Figure 4 shows calibrated distribution. Input voltage to transducer is estimated from Fig.1. The estimation voltage is proportional to the projection data when the laser passes the origin. Therefore, the estimated voltage is proportional to the projection data. Distribution of high sound pressure is not skew. Because of very small signal, noise thought to be cause of skew distribution at low sound pressure.

4. Conclusions

The distribution of the projection data of sound fields was measured. The system was able to simplify by use of amplitude analysis. Thanks to calibration using characteristic curve, distribution of high sound pressure was not skew. This simple system presented in this paper proved useful to measure sound fields.

References

[1] O. L. Lokberg: Applied Optics, **33** (1994) 2574.

[2] T. H. Neighbors, W. G. Mayer and H. J. Ruf: J. Acoust. Soc. Am. **98** (1995) 1751.

[2] K. Mizutani, T. Ezure, K. Nagai and M. Yoshioka: Jpn. J. Appl. Phys. **40** (2001) 3617.

[3] T. Obuchi, S. Nakanishi, K. Mizutani and H. Masuyama: Proc. Symp. Ultrason. **25** (2004) 117.

[4] T. Obuchii, K. Mizutani, S. Nakanish and H. Masuyama: Proc. ASJ. Spring Meet. (2005) 995 (in japanese).

[5] K. L. Zankel, and E. A. Hiedemann: J. Acoust. Soc. Am. **31** (1959) 44.

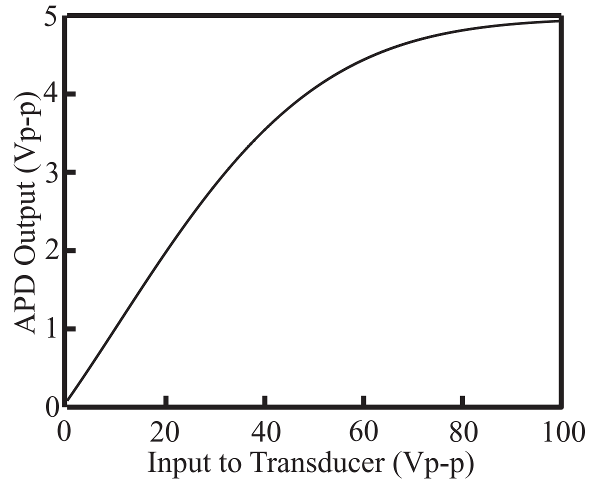

Fig.2 Regression curve of relation between intensity of light that passed sound fields and input voltage to transducer.

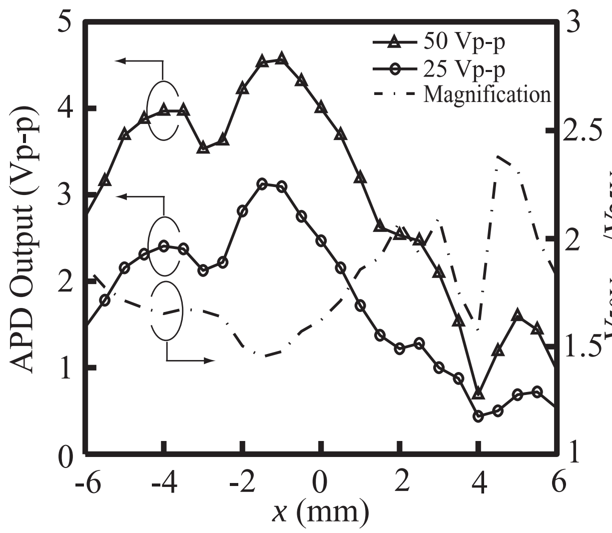

Fig.3 Experimental result of distribution of intensity of light that passed sound fields Plot by triangle: Input voltage to transducer is 50 Vp-p, circle:25 Vp-p, broken line: magnification.

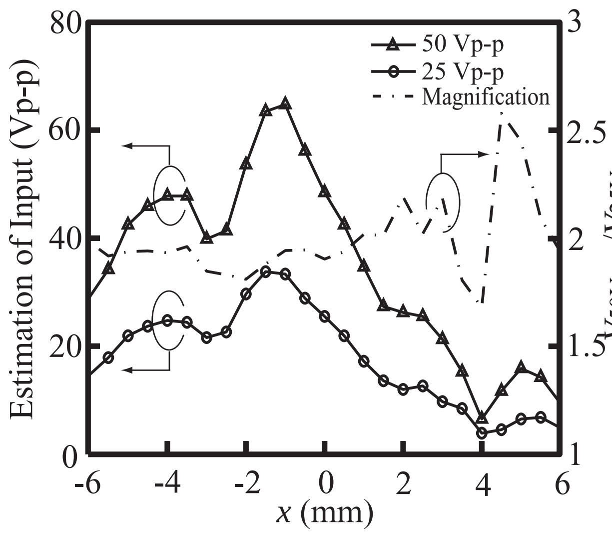

Fig.4 Calibrated result of distribution and magnification

P2-24

Proc. Symp. Ultrason. Electron., Vol. 26, (2005) pp. 259-260
16-18 November, 2005

A high frequency optical scanner using flexural vibration of an optical fiber

◎Ryoichi Isago, Shunsuke Domae, Daisuke Koyama, Kentaro Nakamura and Sadayuki Ueha
(P&I Lab., Tokyo Inst. of Tech.)

1. Introduction

Mechanical optical scanners are widely used in various applications such as bar code readers, position sensors, optically ranging devices and laser projectors. However, it is difficult to increase the scanning angle at high scanning rate with conventional methods. This report presents a method using a vibrating optical fiber where the lateral displacement and rotation of the fiber end and the acousto-optic effect due to the stress induced in the fiber core by the vibration provide a large deflection angle of the light beam. First, the configuration to excite high frequency bending vibrations on the fiber using a piezoelectric element is described, and the relationship between the resonant frequency and the fiber length is reviewed being based on the simple beam theory. Then, the principle to deflect the light beam with the vibration and a ball lens is presented. Second, the acousto-optic effect is observed. Two-dimensional scanning is demonstrated with the fiber vibration at 42 kHz and the ball lens displacement at 460 Hz.

2. Method and structure

Experimental setup for the proposed optical scanner is shown in Fig.1. A silica optical fiber without coating is bonded to the upper surface of a multilayered piezoelectric actuator. An optical fiber is vibrated in flexural mode of cantilever beam, and output light beam is collimated by a ball lens. The ball lens is bonded on the end of a stainless steel beam that is attached to another multilayered piezoelectric actuator, and vibrates in the direction perpendicular to the displacement of the optical fiber. Two-dimensional scanning is possible by the conbination of the high frequency vibration of the optical fiber and the low frequency vibration of the ball lens.

Table 1 shows the specifications of the single mode optical fiber (F-SF, Newport Co.) used in the experiments. A ball lens of 0.5 mm in diameter and a stainless steel beam of 0.7 mm in diameter are used. Table 2 shows the resonant lengths of the fiber and the stainless beam through the calculation based on the Bernoulli-Euler hypothesis [1]

$$f_n = \frac{(\beta_n L)^2}{2\pi L^2}\sqrt{\frac{EI}{\rho A}} \qquad (1)$$

for the design frequencies 40 kHz and 500 Hz, respectively. Here, EI is flexural rigidity, ρ is density, A is cross-sectional area, and $\beta_n L$ is frequency constant.

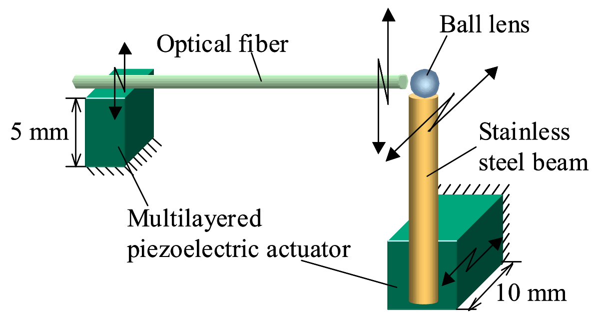

Fig.1 Experimental setup.

Table 1 Specifications of the optical fiber.

Young's modulus E	73.1 GPa
Density ρ	2220 kg/m^3
Cladding diameter	125 μm
Core diameter	7 μm
Refractive index of the cladding	1.453
Refractive index of the core	1.457

Table 2 Resonant lengths in mm.

Mode	1st	2nd	3rd
Optical fiber 40 kHz	1.6	4.0	6.7
Stainless steel beam 500 Hz	31.5	78.8	131.9

3. Optical scanning characteristics

The frequency characteristics of scanning angle in the 3rd mode flexural vibration of the optical fiber are shown in Fig.2 when the ball lens vibration is not activated. The maximum scanning angle of ±10.5 ° was obtained at 41.97 kHz when the applied voltage to the multilayered piezoelectric actuator was 24.3 V. It is considered that excess adhesive flowed to the fiber might rise the resonance frequency than the designed value.

E-mail: isago@sonic.pi.titech.ac.jp

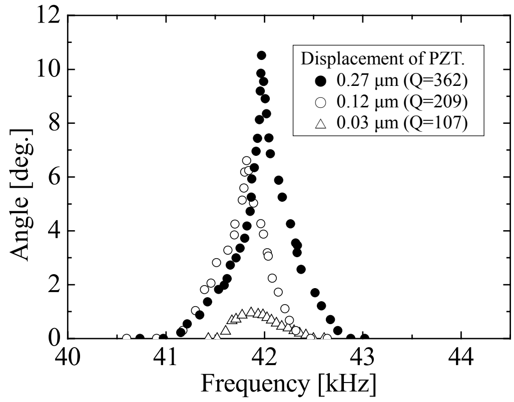

Fig.2 Frequency characteristics of the scanning angle for the vibration of an optical fiber.

4. Observation of the acousto-optic effect

The scanning angle achieved by the fiber vibration is greater than the value expected by the geometrical optics with the displacement and rotation of the fiber end due to the vibration. It is thought that the acousto-optic effect induced by the vibratory stress in the fiber may contribute the large scanning angle. The acousto-optic effect is observed for an optical fiber 16 mm in length vibrating with the 4th mode at 10 kHz. Vibration displacement and the locus of output light spot at the fiber end is observed by stroboscope method using a microscope and a blinking right emitting diode. The result is shown in Fig.3. Since the light guided by the fiber was operated in continuous wave, the locus of the light was recorded in the figure. The vibration displacement of the fiber was 8 μm, while the displacement of the output light spot was 14 μm. Then, the relative displacement of the output position to the fiber is 6 μm. This displacement of the output spot position is thought to be caused by acousto-optic effect induced by the vibration.

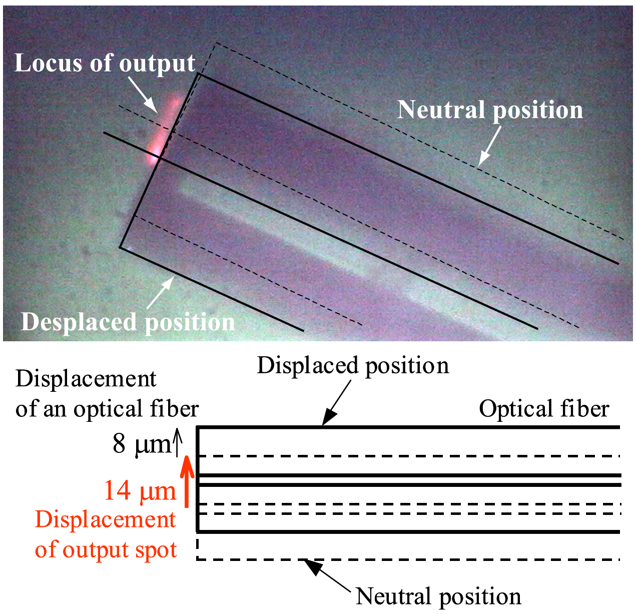

Fig.3 Picture of the vibrating fiber.

5. Two-dimensional scanning

The frequency characteristics of the scanning angle in the 1st mode flexural vibration of the stainless steel beam are shown in Fig.4. The maximum scanning angle is ±6.8 ° at 462 Hz when the applied voltage to the multilayered piezoelectric actuator is 55.3 V. The ball lens mass lowered the resonance frequency than the designed frequency. When both the fiber and ball lens vibrations are activated simultaneously, the collimated light projected on a screen at the distance of 258 mm is shown in Fig.5. The outer edges are brighter because of the sinusoidal vibrations.

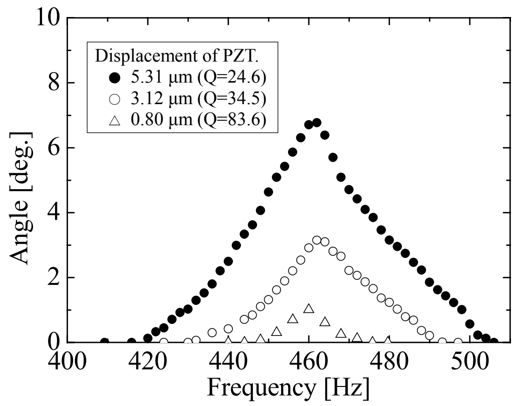

Fig.4 Frequency characteristics of scanning angle by the vibration of a stainless steel beam.

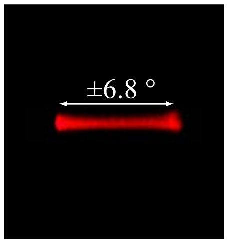

(a) Vibration of the stainless steel beam.

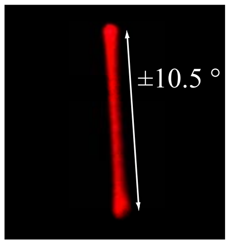

(b) Vibration of the optical fiber.

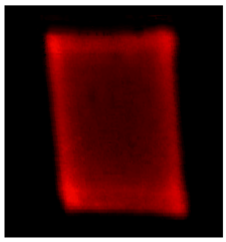

(c) Two-dimensional scanning.

Fig.5 Scanned spot on a screen at 218 mm.

6. Conclusion

The method for scanning the laser light in two dimensions by combining the vibration of an optical fiber at 42 kHz and a ball lens at 460 Hz was examined. Two-dimensional scanning of ±10.5 ° × 6.8 ° was achieved.

References

[1] Karl F Graff: *WAVE MOTION IN ELASTIC SOLIDS* (Dover Pubns, 1991) pp.140-158.

P2-25

Proc. Symp. Ultrason. Electron., Vol. 26, (2005) pp. 261-262
16-18 November, 2005

Trapping of particles on radiation surfaces of an ultrasonic actuator

Junhui Hu, Jianbo Yang, Jun Xu (Nanyang Technological University, Singapore)

1. INTRODUCTION

Improved particle separation techniques are increasingly important in biotechnology, water treatment and many other areas. Ultrasonic separation of particles, which includes trapping and transportation of particles, is very competitive in this area because it has the advantages such as being able to handle almost all materials and having a low cost compared to the magnetic and electrophoretic methods. In this paper, we report a method of trapping small particles on the radiation surfaces of an ultrasonic actuator.

2. CONSTRUCTION AND PRINCIPLE

Fig. 1 shows the structure and size of the actuator for trapping particles. A tapered aluminum strip with a width of 4.5 mm and length of 30 mm is mechanically driven by a rectangular-sandwich-shaped ultrasonic transducer at one of its four corners. Two piezoelectric rings are sandwiched between two square aluminum plates by a bolt structure. The piezoelectric rings have inner diameter of 6 mm, outer diameter of 12 mm and thickness of 1.2 mm. The actuator has a resonance frequency of about 105 kHz. It was observed that particles such as shrimp eggs, mint seeds and grass seeds may be trapped on the two radiation surfaces near the tip of the strip at the operation close to the resonance point.

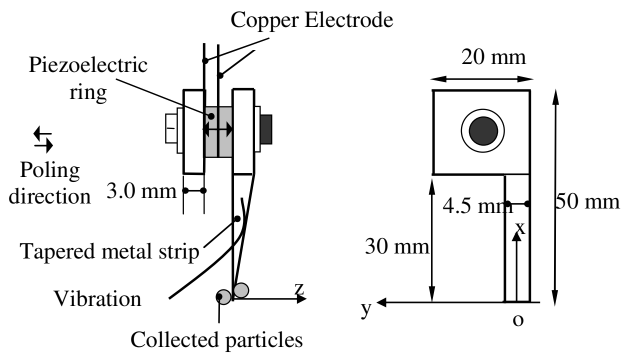

Fig. 1 Structure and size of the actuator.

The out-of-plane vibration of the tip of the aluminum strip was clearly observed by microscope system (Olympus BX-51), measuring the position change of the metal surface in the z direction due to vibration. Using the method, it was qualitatively found that the vibration amplitude is maximum at the tip ($x = 0$), and decreases as x increases in the vicinity of the tip. So the strip operates at a flexural vibration mode.

Using a 1mm needle hydrophone (SN945, Precision Acoustics, UK), it was observed that the acoustic pressure p just under the vibrating tip in water is much smaller than that near the radiation surfaces. Hence, we may assume $p\ (0, y, 0) \approx 0$ (1) for $-2.25\text{mm} \le y \le 2.25\text{mm}$. On the other hand, an acoustic boundary layer exists on the radiation surfaces [1], as shown in Fig. 2. If V_h, V_w and V_n are L_1, L_2 and L_3 components of the fluid vibration velocity at the interface between the boundary layer and the metal strip (L_3 = 0), respectively, then $V_n \neq 0$ (2) $V_h \approx 0$ (3) $V_w \approx 0$ (4). Using Eqs. (1)-(4) and $grad\ p = -\rho_0 \frac{\partial \mathbf{V_f}}{\partial t}$ (5), where $\mathbf{V_f}$ is the fluid vibration velocity, one can deduce that the acoustic pressure at the interface between the boundary layer and the metal strip is approximately zero. Due to this nodal plane, small particles are sucked to the radiation surfaces [2, 3]. To verify the existence of the acoustic radiation force which pushes small particles onto the vibrating strip, an experiment was conducted, as shown in Fig. 3. In the experiment, the radiation surfaces were perpendicular to

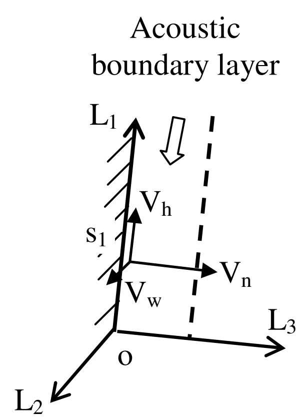

Fig.2 Acoustic boundary layer on the radiation surface and a local coordinate system.

gravitation. The trapping of shrimp eggs on the lower radiation surface due to the strip's vibration was observed in air.

3. EXPERIMENTAL METHODS AND MATERIALS

In the following experiments, the length direction of the metal strip is parallel to the gravitation; mint seeds were used, which has an average density of 0.7 g/cm^3, volume per particle of 0.07×10^{-3} cm^3, mass per particle of 4.9×10^{-5} g and diameter of 513 μm in a dry state.

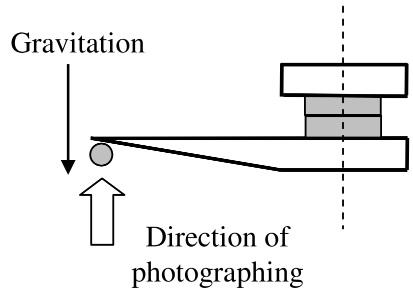

(a)

(b)

Fig.3 Verification of the existence of the acoustic force for trapping. (a) Experimental setup; (b) photo of the trapped particles.

4. CHARACTERISTICS AND DISCUSSION

Fig. 4 shows the trapping of mint seeds in water. It was observed that the distribution of trapped particles is quite uniform in the trapping area. This provides another experimental evidence of the existence of the nodal plane of acoustic pressure on the metal strip. Such a distribution would be impossible if the trapping were due to some isolated nodal points or lines in the near field or far field. Fig. 5 shows the number of trapped mint seeds versus operating frequency in water and air for a given driving voltage. It is seen that more mint seeds can be trapped in water than in air and the frequency range in which the actuator can trap particles is wider for the collection in water than in air. There are two possible reasons for these phenomena. One is that the matching of acoustic impedance between water and aluminum is better than that between air and aluminum. Another is that the buoyancy acting on the particles improves the capability of trapping particles.

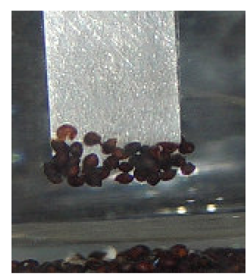

Fig. 5 Trapping of mint seeds in water.

5. SUMMARY

We have proposed a new method which uses the radiation surfaces of an ultrasonic actuator to trap small particles. Compared with other techniques of trapping particles, our technique does not need a specially designed chamber to generate the necessary sound field, and can easily transport trapped particles to a desired location for separation by simply moving the actuator.

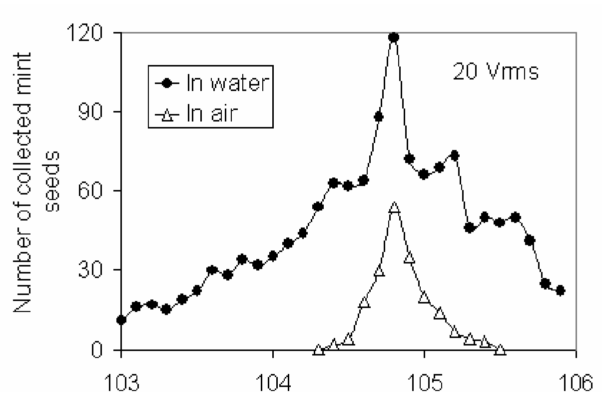

Fig. 6 Number of trapped mint seeds versus driving frequency.

REFERENCE:

[1] P. M. Morse and K. U. Ingard, *Theoretical Acoustics*. NY: McGraw-Hill, 1968, p. 243 and p. 279-287.

[2] T. Hasegawa and K. Yosioka, *J. Acoust. Soc. Am.*, vol.46, pp.1139-1143, 1969.

[3] K. Beissner, *J. Sound and Vibration*, vol. 93, No.4, pp. 537-548, 1984.

P2-26

Proc. Symp. Ultrason. Electron., Vol. 26, (2005) pp. 263-264
16-18 November, 2005

Phase shift of Rayleigh wave beneath slider with preload

◎ Yoshito Miyazaki, Takashi Shigematsu, Minoru Kuribayashi Kurosawa (Tokyo Inst. of Tech.)

1. Introduction

An extremely high performance surface acoustic wave (SAW) linear motor operating at 10 MHz has been already demonstrated [1,2]. However, the efficiency from the electrical input to mechanical output is still low. To improve the efficiency, an energy circulation driving method has proposed and demonstrated [3]. For the energy circulation driving method, forward scattering beneath a silicon slider was found to be a problem, due to the shift of the phase relation. Numerical simulation was carried out to investigate the relationship between the phase shift and slider parameters using the finite element method.

2. Energy Circulation And Wave Scattering

The schematic view of the Rayleigh wave motor stator using the energy circulation driving method is shown in Fig 1.[3] The traveling SAW is excited by putting a sine signal and a cosine signal into the driving IDTs respectively. The excited traveling wave is received by one unidirectional IDT, and converted into electric energy. The converted electric energy is returned to the after unidirectional IDT. Using this electric energy, the other unidirectional IDT excites a circulated traveling wave. The circulated wave is propagated, and received by the initial unidirectional IDT again. Then the circulated wave and the initially excited wave are superposed. It is very important that these two waves are in phase at a designed value to efficiently excite the Rayleigh wave.

On the other hand, many projections were fabricated on the contact surface by dry etching. Because of these projections, the sufficient contact pressure is generated and the better contact condition is obtained. The Rayleigh wave beneath the slider is scattered by these projections when the slider is preloaded. As the result, the phase of the wave at the rear of the slider shifts from the designed value. This phase shift affects on the superposition of the circulated wave and the initially excited wave. Namely, the power of the Rayleigh wave decreases compared to the complete accord phase condition. As a result, this phase shift decreases the efficiency of the motor.

y.miyazaki@ae.titech.ac.jp

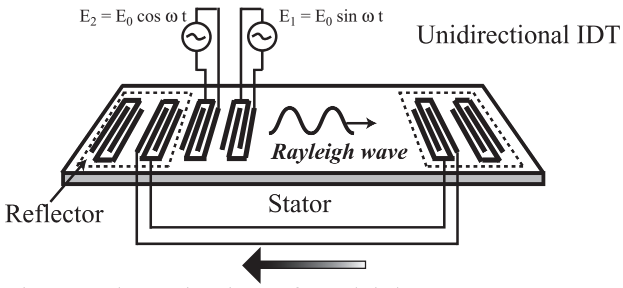

Fig. 1: Schematic view of Rayleigh wave motor stator using an energy circulation driving method.

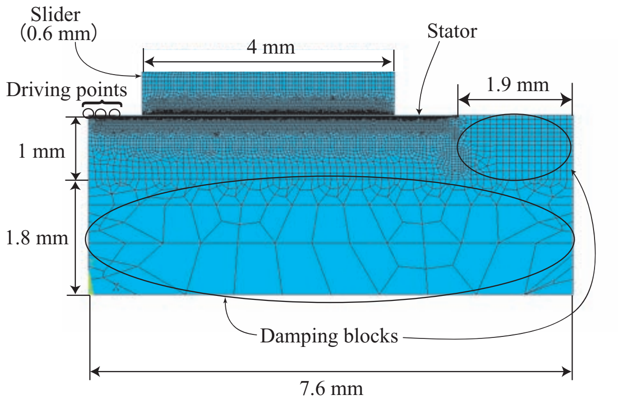

Fig. 2: FEM simulation mesh model of Rayleigh wave propagation.

3. Simulation

To investigate the phase shift of Rayleigh wave, simulation was carried out using the finite element method. The software was ANSYS 7.0.

The FEM stator and slider model is shown in Fig. 2. The model consisted of slider, stator and damping block. To prevent the reflection wave, the left side of the model had symmetrical boundary condition and damping elements were attached on the bottom and the right side of the stator. The dimensions of the damping element areas were 1.8 x 7.6 mm^2 on the bottom and 1.0 x 1.9 mm^2 on the right. Four nodes 2-D plane elements were used in the whole model. The mesh size of the surface of the stator was 5 μm, that was 1/80 of the 400 μm wave length.

The stator was made of 127.8 degrees Y-rotating X-propagation $LiNbO_3$ [4]. The slider was made of silicon. Its density was 2.33 x 10^3 kg/m^3 , Young's modulus was 1.66 x 10^{11} Pa, shear modulus was 0.639 x 10^{11} Pa. Many projections whose height were 1 μm were fabricated on the surface of the slider.

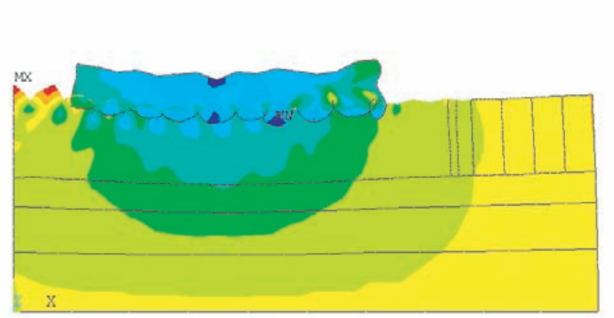

Fig. 3: FEM simulation of Reyleigh wave scattered by slider projections.

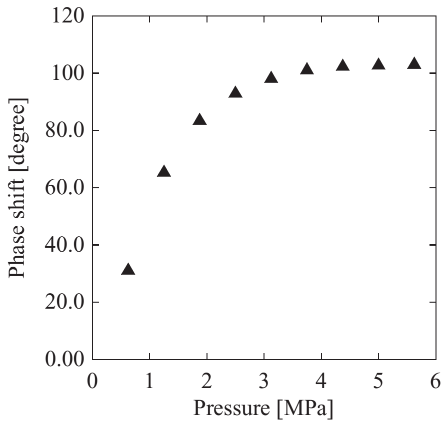

Fig. 4: Phase shift against preload caused by the silder projections.

The diameter of the projections was 50 μm, the pitch of the projections was 100 μm. Contact elements were mounted the surface of the slider and the surface of the slider projections. Its contact stiffness was 0.001.

The simulation type was two dimensional strain structural-piezoelectric analysis, transient analysis. The amplitude of 20 nm vertical sinusoidal displacement at 9.945MHz was given at 5 driving points.

4. Results of Simulation

The integral time span was 3ns which was about 1/ 30 of 1 cycle of the wave. The simulation was carried out for about 1.7 msec, that was the 17 cycles of the wave motion. On this condition, we could obtain the traveling Rayleigh wave. The phase velocity of the Rayleigh wave of this simulation was 4150 m/sec with no slider.

The deformation model of the simulation result with slider preload at 1.875 MPa is shown in Fig. 3. The phase shift against the preload is shown in Fig. 4. The large preload caused the large phase shit.

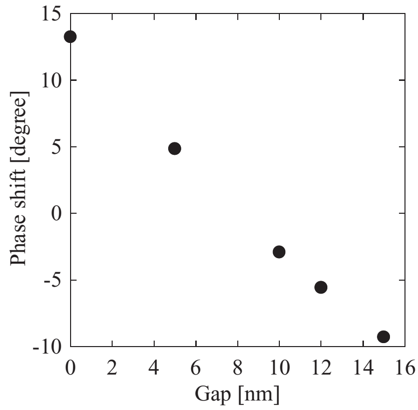

Fig. 5: Phase shift aginst gap between the stator and the slider caused by the silder projections.

When the preload was too low, the slider was pushed by Rayleigh wave and took off the stator. So soft damping block was mounted on the slider and the upper surface of the block was fixed. The preload could be controlled by changing the gap between the stator surface and the slider projections. Phase shift against gap between the stator and the slider is shown in Fig. 5. Large gaps, namely low preloads, caused the minus phase shit.

5. Conclusion

The FEM simulations were carried out to investigate the relationship between the phase shift and the projection parameters of the slider. Phase shift was caused by the contact of the slider projections. It is necessary to determinate the relationship between the phase shift and the projection parameters of the slider quantitatively for the next step.

Refference

[1] Y. Nakamura, M. K. Kurosawa, T. Shigematsu, and K. Asai, “Effects of Ceramic Thin Film Coating on Friction Surfaces for Surface Acoustic Wave Linear Motor,” Proc. of IEEE Ultrasonics Symp, P2M-3, pp. 1766-1769. Honolulu, Oct 5-8, 2003.

[2] T. Shigematsu, M. K. Kurosawa and Katsuhiko Asai, “Sub-nanometer Stepping Drive of Surface Acoustic Wave Motor,” Proc. IEEE-NANO 2003, WE 3, San Francisco, August 12-14, 2003.

[3] K. Asai, M. K. Kurosawa, “Surface acoustic wave motro using an energy circulation driving method,” Proc. of IEEE Ultrasonic Symp. , P2H-5, pp. 525-529 , Atlanta, Oct. 7-10, 2001.

[4] J. Kushibiki, I. Takanaga, M. Arakawa, and T. Sannomiya, “Accurate Measurements of the Acoustical Physical Constants of $LiNbO_{33}$ and $LiTaO^{3}_{3}$ Single Crystals,” IEEE Transactions on UFFC, VOL. 46, No. 5, Sep. 1999, pp.1315-1323.

P2-27

Proc. Symp. Ultrason. Electron., Vol. 26, (2005) pp. 265-266
16-18 November, 2005

Study of a mini-ultrasonic motor with square metal bar and piezoelectric plate hybrid

Yu Chen, Kai Lu, Tieying Zhou, Tao Liu, Cunyue Lu
Department of physics , Tsinghua University ,Beijing 100084, P R China

A new mini ultrasonic motor with metal bar and piezoelectric plate hybrid as a stator has been studied. Four piezoelectric plates are bonded to four sides of the metal bar. The metal bar is made of brass and the piezoelectric plates are made of PZT-4. The polarization direction is vertical to the piezoelectric plate. Compared with the cylindrical type of the motor, the square cross-section motor makes polarization more sufficient and signal wire easier to be welded. In this paper, the modal and harmonic analysis of the stator were performed by using FEM. The resonance frequency of the motor is about 100 kHz, the no-load revolution is above 6000 r/min and maximum torque is about 60 uNm. This new mini ultrasonic motor is of potential applications.

KEYWORDS: metal bar, ultrasonic motor, piezoelectric plate, bending vibrating

The ultrasonic motor has many excellent performance features, such as high torque at low speed, quick response, position with high accuracy, simple construction, as a result it has the extensively applied foreground in the fields of industry control, precise instrument, automobile electric appliances etc. The bending vibration piezoelectric motor makes use of the vibration and friction force to drive the rotor. Its outstanding characters are small volume, working with low energy input and easy to fabricate compared with other types of ultrasonic motors. [1-6]. In our early work a 1mm cylindrical ultrasonic motor was used in an endoscope OCT [7,8].

There are various types of bending vibrating ultrasonic motors, e.g. using piezoelectric slice, piezoelectric cylinder and tube. Although the types USM of piezoelectric cylinder and tube have high density of torque and high speed, they both have a curved surface. A novel ultrasonic motor with square cross section metal bar and piezoelectric plate hybrid is proposed in this paper. Compared with the above two, the metal bar one is easier to fabricate and the thin piezoelectric plates can be polarized more sufficient; signal wires are easier to be welded , so that the ultrasonic motor with a square cross section is easy to be mass-produced.

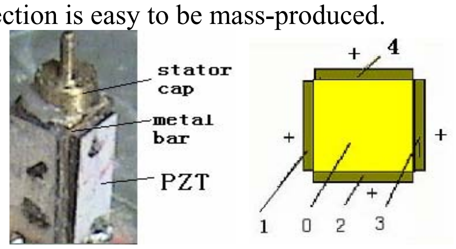

(a) (b)

Fig.1(a)the photo of stator (b)the cross section of stator

The size of the metal bar is 1.6x1.6x6.6mm^3. Figure 1(b) illustrates the cross section of the stator. Four piezoelectric plates denoted by 1,2,3,4 in Fig.1(b) are bonded to four sides of the metal bar. The size of each plate is 1.6x6x0.3mm^3. The metal bar is made of brass denoted by 0 in Fig.1(b) and the piezoelectric plates are made of PZT-4.

The polarization direction is vertical to the piezoelectric plate and they are bonded as shown in Fig.1(b). Four signals which are sin ω t、cos ω t、-sin ω t、-cos ω t, are applied onto four piezoelectric plates respectively. Two bending modes excited at two perpendicular directions, are coupled to form a rotation bending mode. The surface motion of the stator is a traveling wave of one wavelength.

Next the rotating stability of the motor is considered. We examine the moments of inertia in each direction. A coordinate system is set as in Fig.2(a).

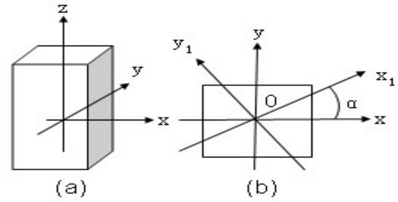

Fig.2 the coordinate system

A rotating coordinate system is x_1, y_1, as shown in Fig.2(b) and we have following relationship for two systems

$$\begin{cases} x_1 = x\cos\alpha + y\sin\alpha \\ y_1 = y\cos\alpha - x\sin\alpha \end{cases} \tag{1}$$

The moments of inertia of a bar cross section are given by [9]

$$I_x = \int_A y^2 dA, \qquad I_y = \int_A x^2 dA \tag{2}$$

where dA is the area element. The product of inertia is

$$I_{xy} = \int_A xydA \tag{3}$$

The moments of inertial in the x_1–y_1 coordinates is

$$\begin{aligned} I_{x_1} &= \int_A y_1^2 dA = \int (y\cos\alpha - x\sin\alpha)^2 dA \\ &= I_y \sin^2\alpha + I_x\cos^2\alpha - I_{xy}\sin 2\alpha \\ &= I_y\frac{1-\cos 2\alpha}{2} + I_x\frac{1+\cos 2\alpha}{2} - I_{xy}\sin 2\alpha \\ &= \frac{I_x + I_y}{2} + \frac{I_x - I_y}{2}\cos 2\alpha - I_{xy}\sin 2\alpha \end{aligned} \tag{4}$$

Similarly we have

$$I_{y_1} = \frac{I_x + I_y}{2} - \frac{I_x - I_y}{2}\cos 2\alpha + I_{xy}\sin 2\alpha \tag{5}$$

For a bar with a square cross section we have

$$I_x = I_y = \frac{h^4}{12}, I_{xy} = 0 \tag{6}$$

so that

$$I_{x_1} = I_{y_1} = \frac{h^4}{12} = I_x = I_y \qquad (7)$$

It has been proved that the moments of inertia of a metal bar are equal in all directions.

On the x-z plane, the curvature, $1/\rho_x$, caused by the bending moments M, can be calculated by the following equation

$$\frac{1}{\rho_x} = -\frac{M}{EI_y} \qquad (8)$$

where E is Young's modulus of the metal. In the x_1-y_1 coordinate system we have a same formula

$$\frac{1}{\rho_{x_1}} = -\frac{M}{EI_{y_1}} \qquad (9)$$

Since the moments of inertia of a metal bar are equal in all directions, the curvature of a square bar on the different plane is the same for a constant M. This result is the same as that of the cylindrical bar. Thus we have shown that the bending rotation of a square bar is stable.

If we apply the electrical signals on the four electrodes the particle motion track on the surface of the stator is an ellipse, which is the same as that of the cylindrical motor [10,11].

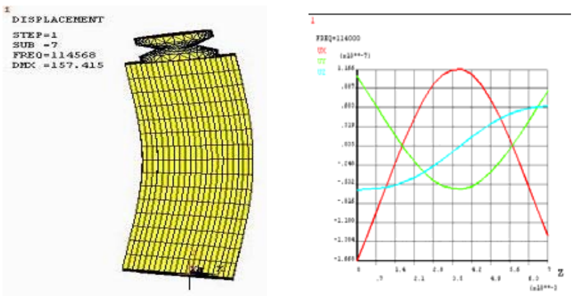

(a) (b)

Fig.3 Finite Elements Analysis (a) modal analysis (b) displacement distribution of harmonics analysis

From a Finite Elements Analysis, the result shows that the resonance frequency of the first bending mode for 2 ends free boundary condition is 114 kHz. The displacements of the surface particle of the bar along the z axis at the maximum harmonic responding is shown in fig.3(b) and its maximum displacement of an end point is about 0.2 um when the applied voltage is 5 V.

Table 1 the measurement result

Frequency	kHz	100	95	90
Effective voltage	V	93.6	90.8	88.7
Power	W	0.177	0.138	0.118
Rotating speed	rpm	6400	3800	2100

The performance of the motor was measured by use of the YOKOGAWA WT1600 power meter. The parameters obtained are listed in Table 1. The stalling torque of the motor is about 60uNm.

An ultrasonic motor with a square cross section has good potential applications in many fields such as micro-machine, medical machine. The study of using this motor in an ultrasonic gastroscope is underway.

Acknowledgements

This work was supported by NSFC 50235010.

REFERENCES :

[1]S.Ueha,Y.Tomikawa,M.Korosawa,K.Nakamura.Ultra sonic Motors: Theory and Application.Clarendon Press,Oxford,1993 p183-184

[2] T. Morita,M. Kurosawa and T.Higuchi.A Cylinder Micro-ultrasonic Motor,Ultrasonics,2000,38(1):33-36

[3] Cagatay S., Koc B., Uchino K. A 1.6-mm,metal tube ultrasonic Motor. UFFC,2003,Vol.50 No.7:782-786

[4] Shuxiang Dong etal. Piezoelectric ultrasonic micromotor with 1.5 mm diameter, UFFC,2003,Vol.50 No.4:361- 367

[5]. Zhou Tieying, Zhang Kai, Wang Huan, et al., Study on piezoelectric cylinder micro ultrasonic motor with 1mm diameter, ACTA ACUSTICA (in Chinese) 2004, 29(3): 258-261.

[6]. Zhou Tieying, Zhang Kai, Jiang kaili, Bending vibration piezoelectric cylindrical-type micro ultrasonic motor, Chinese Patent , Application No. 01109049.9（in Chinese）2001-01-09.

[7] Zhou Tieying, Liu Xinguo, Chen Yu, etal. ultrasound electromotor as the endoscopes driving system, International Medical Devices （in Chinese）, 2004, 10 (1): 10-13.

[8] ZHOU Tieying, ZHANG Kai, CHEN Yu etal, A cylindrical rod ultrasonic motor with 1 mm diameter and its application in endoscopic OCT, Chinese Science Bulletin Vol. 50, No. 8,April 2005 pp826-830 (in English)

[9] Hand Book of Material Mechanics, interpreted by Fan Xinshan Architecture industry published 1987 (in Chinese)

[10]. Zhao Xiangdong, Liu Changqing, Zhao Chunsheng, The movement mechanism research of cylinder bending travelling wave piezoelectric ultrasonic motor, Journal of Applied Mechanics （in Chinese）, 2000，17（3）: 120-123

[11]. Yang Quangang, Zhang Kai， Zhou Tieying，et al., Analysis and experiment on the taper angle of contact surface of cylindrical USM, ACTA ACUSTICA. （in Chinese） 2002, 9(5): 413-419.

P2-28

Proc. Symp. Ultrason. Electron., Vol. 26, (2005) pp. 267-268
16-18 November, 2005

Analysis of tiny piezoelectric ultrasonic linear motor

◎*Hyun-Phill Ko,Chong-Yun Kang, *Sangsig Kim and Seok-Jin Yoon
(Korea Institute of Science and Technology, *Dept. of Electrical Eng. Korea Univ.)

1. Introduction

In recent years, a novel tiny piezoelectric ultrasonic linear motor converting a radial mode vibration to a longitudinal vibration mode driven by impulse force has been developed for a camera optical module. In this work, the motors are investigated with various shaft materials in order to improve the dynamic properties of the motors. The shaft material has direct influence on efficiency, reliability and quality of the motors and their dynamic properties. In this study the frictional properties of the shaft materials were intensively considered by changing the materials which have different coefficient of friction, and the optimal combinations of material for shaft were recommended[1]. The characteristic of movement with applied voltage waveforms was also investigated to suggest optimized movement condition of the developed tin piezoelectric linear motor. Finally, the tiny ultrasonic linear motors' performance with various shaft materials in terms of velocity, maximum force, ideal working frequency and displacement of the shaft is investigated and discussed.

2. Construction and Experiment

The tiny piezoelectric linear motor using the inertia movement described above is shown in Fig.1.

The motor consists of three parts which are a transducing part, shaft and mobile element. Te transducing part consists of a piezoelectric ceramic disk, and a metal disk attached on the piezoelectric ceramic disk. The transducing part is driven by the sawtooth electrical potential applied to the electrode on the piezoelectric disk. The piezoelectric ceramic disk generates the one of the radial modes which is periodical extension and construction on the radius direction of the piezoelectric ceramic disk. The transducing part is made of round plate, generating flexural vibration by means of the piezoelectric

Author E-mail: ryanko@kist.re.kr

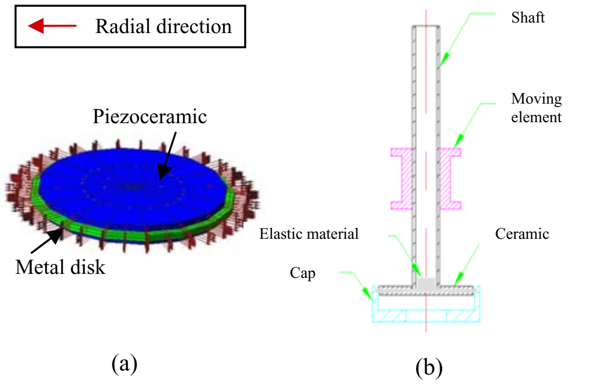

Fig. 1. Configuration of the (a) transducing part and (b) tiny ultrasonic linear motor

ceramic disk and metal disk together. The flexural vibration which has negative influence on movement of the transducing part without the constraint. Constraining the side of piezoelectric ceramic in this motor, radial mode movement, which is one of the vibration modes, is converted into up-and-down movement [2].

In this investigation, four types of materials are used for the shaft, stainless steel coated with DLC (Diamond Like Carbon), uncoated stainless steel, Pyrex and Graphite As a moving element, a rectangular stainless steel, which is compressed to a surface of the shaft by rubber tube, is used. The position of the moving element is detected with laser interferometer and the position data are converted into velocity data by using a home developed frequency to voltage converting circuit. The finite element method (FEM) is used for the vibration analysis of the motor. The finite element code ATILA is applied to the design of this motor because it takes into account piezoelectric effect and electromechanical coupling coefficients of the motor. As we use the FEM, we can assume to the

Table 1.Mechanical resonant frequency

Shaft material type	Stainless steel	DLC	Pyrex	Graphite
T Freq. (kHz)	**48**	**50**	**55**	**64**
E Freq. (kHz)	**45**	**47**	**52**	**63**

*$T_{Feq.}$: *Theoretical mechanical resonant freq. (ATILA)*
E_{Feq} : *Experimental mechanical resonant freq.(HP4192)*

theoretical resonant frequencies of the motors.

3. Experimental Result and Discussion

To operate motors with various shafts, operating frequencies of motors with the moving element are measured by impedance analyzer as shown in Table 1. The displacement characteristics of the moving element are measured with a laser interferometer. A laser beam is irradiated to the mirror attached to the moving element of each motor. The velocity of the moving element is measured at each position of the shaft, as shown in Fig.2. The length of each shaft of motors is 6mm. As indicated in Fig.2, the results show that the moving element of the motor performed a stable linear motion at pyrex shaft, as expected. Also, Fig 2 shows slightly unstable speed and linear motion characteristics of motors with DLC coated and Sus shaft. Fig. 3 shows the velocity and the force of the moving element of motors according to various shaft materials. We operated each motor with its own operating frequency shown in Fig. 3 and measured the dynamic characteristic of each motor.

As shown in Fig. 3, when the motor with stainless steel shaft is driven at 37 kHz, the motor showed the velocity and force of 10mm/sec, 90mN-m, respectively. In the motor with stainless steel coated with DLC at 35 kHz, its velocity is 15mm/s and its force is 75 mN-m. When the motor used the Pyrex shaft, the force of 110mN-m is reached at 37 kHz. This motor has a high force and stable velocity value, because the shaft with Pyrex materials has a sleek surface condition. Although the motor with stainless coated with graphite shaft is shows good dynamic characteristics, after few times operating, motor shows the unstable movements again because the wear starts and occurs between graphite shaft and moving element.

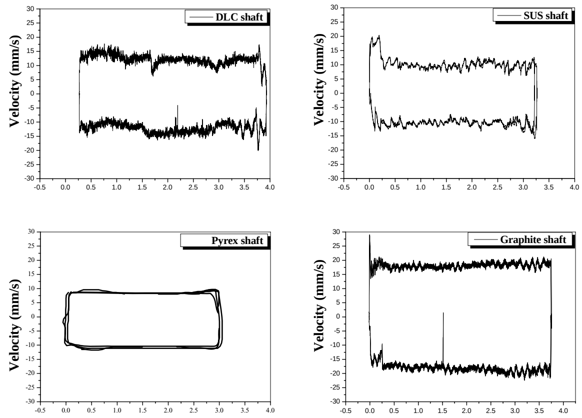

Fig. 2. The velocity of the moving element at each position of the shaft

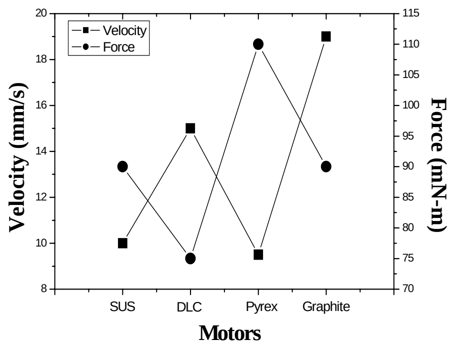

Fig. 3. The velocity and the force of the moving element of motors

4. Conclusion

We investigated the velocity and force between the shaft and moving element with a various shaft materials. When being compared with the previously proposed prototype motor, the overall size of the motor decreases but dynamic properties and stable operation are improved. The experimental results confirm that our present motor has significantly enhanced performance over the previous motor. It was found that two combinations, namely Pyrex or graphite for shaft and stainless steel for the moving element, exhibits good and stable dynamic behaviors in an ultrasonic linear motor.

References

1. H.P.Ko et al. Mater. Chem.and Phys., **90** (2005) 322.
2. H.P.Ko, C.Y.Kang ,S.Kim and S.J.Yoon : Sensors an Actuators:A (accepted SNA4867)

Proc. Symp. Ultrason. Electron., Vol. 26, (2005) pp. 269-270
16-18 November, 2005

講演取消

講演取消

Proc. Symp. Ultrason. Electron., Vol. 26, (2005) pp. 271-272
16-18 November, 2005

講演取消

講演取消

P2-31

Proc. Symp. Ultrason. Electron., Vol. 26, (2005) pp. 273-274
16-18 November, 2005

Tunable Vibration Absorber Incorporating Piezoceramic Sensoriactuator

Deyu Li, Siu Wing Or* and Helen Lai Wa Chan (The Hong Kong Polytechnic University)
Ping Kong Choy and Peter Chou Kee Liu (ASM Assembly Automation Ltd.)

1. Introduction

Tuned vibration absorbers are pre-tuned passive vibration absorption devices comprising predetermined sets of passively damped masses and springs to reduce the susceptibility to vibrations of a structure at a particular resonance frequency [1]. Tunable vibration absorbers (TVAs) often utilize smart materials as the principal tuning means to provide the distinct feature of tunable stiffness via an external tuning signal [2–4]. With such tuning means, one may easily and precisely adjust the natural frequencies of such TVAs to optimally match the targeted resonance frequencies of the corresponding under-damped structures so that additional energy absorption can properly be introduced to the structures without adding any extra component and affecting the vibration levels of the structures at other frequencies.

While effectiveness and usefulness, the existing TVAs are incapable of self-sensing structural vibrations for implementing real-time, closed-loop tuning of their natural frequencies; they are limited to an open-loop mode of operation instead. Although it is possible to establish a closed-loop operation via an installation of vibration sensors (e.g., accelerometers) on the vibrating structures, this method not only increases the engineering cost, but also leads to difficulties in assuring a reasonably high degree of absorber-sensor collocation. In view of this, we have developed a smart TVA, consisting of a piezoceramic sensoriactuator suspended in a rigid frame by two flexible beams coupled longitudinally to the axial ends of the sensoriactuator and the frame, to provide the real-time, closed-loop tuning capability in a simple, cost-effective and reliable manner [5]. In this paper, the working principle and structure of the smart TVA are described and its tunability and sensibility are reported.

2. Working Principle

The smart TVA is conceptualized using the sensitivity of the bending stiffness and natural frequency of a pair of flexible beams in response to a force exerted axially to the beams. Figure 1 shows the conceptual design of the smart TVA. It basically consists of a lumped, damped mass (2*M*), two flexible beams and two rigid bases. Each of the beams serves as a spring in the transverse direction (i.e., the y-direction) to support the damped mass at one side. These beams, at the same time, are subject to an axial actuation force (*F*) provided by the damped mass. The beams are assumed to be made of the same material having Young's modulus *E* and density r. Besides, they have the same length *L* and the same rectangular cross-section *A* of width *b* and height *h*. The axial actuation force on the beams is taken to be compressive (i.e., *F* is positive). In fact the axial stiffness of the beams (*EA*/*L*) is much larger than its bending stiffness ($48EI/L^3$). The first axial natural frequency of such a beam-mass system is much higher than its first bending natural frequency so that the TVA essentially operates in its first bending mode with the suspended damped mass vibrating along the transverse direction. The natural frequency *f* of the TVA can be calculated using [6]

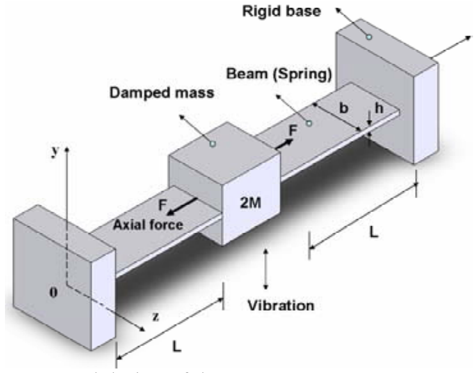

Fig. 1. Conceptual design of the smart TVA.

$$f = \frac{1}{2p}\sqrt{\frac{\frac{p^2}{L}\left[EI\left(\frac{p}{L}\right)^2 - F\right]}{3rAL + 8M}}, \tag{1}$$

where $I = bh^3/12$ is the inertial moment of the rectangular cross-sectional area.

3. Design Prototype

The fabricated smart TVA is shown in Fig. 3. It has dimensions 110 mm (length) × 40 mm (wide) × 40 mm (height). The lumped, damped mass illustrated in Fig. 1 was replaced by a piezoceramic sensoriactuator to provide the attractive functionality of tuning-while-sensing. The sensoriactuator was formed by sandwiching a CETC WTYD1012010 PZT multilayer-stack actuator (20 mm × 10 mm × 10 mm) between two PKI502 PZT patch sensors (1 mm × 10 mm × 10 mm) and then clamping the whole actuator-sensor assembly by two SST304 back plates. The sensoriactuator not only is used to provide an axial actuation force to the beams (i.e., via the stack actuator) and to monitor the amount of the axial actuation force exerted on the beams (i.e., via the two patch sensors), but also is to serve as a damped mass for the TVA. Through adjusting the electrical voltage (i.e., a

* E-mail: apswor@polyu.edu.hk

tuning signal) applied to the stack actuator of the sensoriactuator to change the axial actuation force to the beams, the transverse bending stiffness of the beams is changed and the natural frequency of the TVA is tuned. The variation of the axial actuation force and hence the transverse bending stiffness and natural frequency are automatically monitored by the patch sensors. It is important to note that when the targeted resonance frequency of the corresponding under-damped structure is reached, the outputs of the patch sensors are at maximum, indicating that the TVA has been absorbing the vibrational energy of the structure. The two flexible beams were fabricated with SST304 and have the same dimensions of 32 mm long, 6.5 mm wide and 0.56 mm thick. The rigid bases mounted on the rigid frame were also made of SST304.

4. Tunability and Sensibility Measurements

The smart TVA was installed on a LDS V406 shaker for evaluating its tunability and sensibility. A SigLab 50-84 dynamic signal analyzer was used to generate a random analog signal ranging from 0 to 1 kHz to a LDS PA100E power amplifier so as to excite the shaker to provide a reference vibration to the smart TVD. An ENDEVCO ISOTRON 256HX-10 accelerometer was mounted on the surface of the sensoriactuator of the TVA to measure the acceleration responses along the transverse direction. The SigLab was also used to gather the frequency response functions (FRFs) of both the input (i.e., the excitation signal) and output (i.e., the patch sensors and accelerometer signals) signals. A DC signal generator (Stanford Research DS340) and a power amplifier (NF 4025) were employed to drive the stack actuator of the sensoriactuator to produce a compressive axial force for tuning the natural frequency of the TVA.

Figure 3 shows the measured FRFs of the smart TVA with different tuning voltages. The observed natural frequency of the TVA at zero tuning voltages is 152.5 Hz. As the tuning voltage is increased, the stack actuator expands and exerts a larger compressive axial actuation force on the beams, thereby reducing the bending stiffness of the beams and hence the natural frequency of the TVA. It is clear that the measured natural frequency of the TVA is 135.0 Hz at an increased tuning voltage of 92 V, giving a large frequency tunability of ~12%.

The FRFs measured from the patch sensors and the accelerometer at a tuning voltage of 62 V are plotted in Fig. 4. The resonance frequency (i.e., 137.5 Hz) detected by the patch sensors is the same as that captured by the accelerometer. This good agreement suggests that the patch sensors can effectively replace the commercial accelerometer for automatic tuning purposes.

5. Conclusion

A novel TVA has been developed and experimentally evaluated. The TVA consists of a piezoceramic sensoriactuator suspended in a rigid frame by two flexible beams coupled mechanically to the axial ends of the sensoriactuator and the frame. The measured natural frequency of the TVA is 152.5 Hz at zero volts. A significantly reduced natural frequency of 135 Hz, corresponding to a high tunability of natural frequency of ~12%, has been achieved upon the application of a relatively low tuning voltage of 92 V. The FRFs as measured using the patch sensors agree well with those obtained using a commercial accelerometer, indicating a great promise of deploying the proposed TVA for real-time, closed-loop vibration absorption.

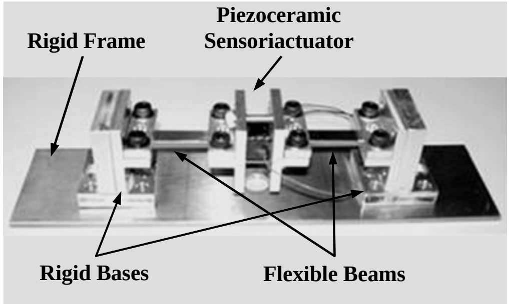

Fig. 2. A smart TVA prototype.

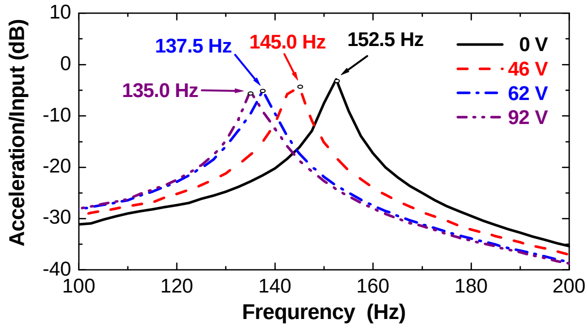

Fig. 3. Measured FRFs of the smart TVA with different tuning voltages.

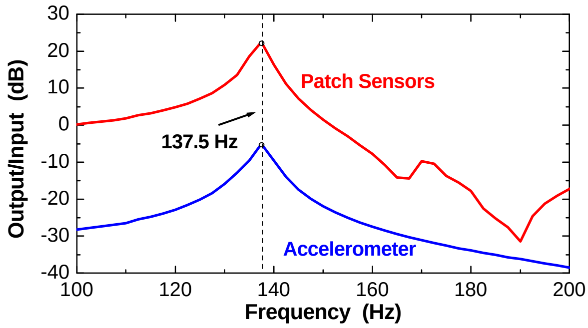

Fig. 4. Representative FRFs measured from the patch sensors and the accelerometer at a tuning voltage of 62 V.

Acknowledgments

This work was supported by the Innovation and Technology Fund (UIM/117) of the HKSAR Government and the Centre for Smart Materials of The Hong Kong Polytechnic University.

References

1. J.B. Hunt: Dynamic Vibration Absorbers (The Garden City Press Limited, Great Britain, 1979).
2. A.B. Flatau, M.J. Dapino and F.T. Calkins: J. Intell. Mater. Syst. Struct. **11** (2000) 923.
3. N. Jalili and D.W. Knowles IV: Smart Mater. Struct. **13** (2004) 998.
4. E. Rustighi, M.J. Brennan and B.R. Mace, Smart Mater. Struct. **14** (2005) 19.
5. S.W. Or, D. Li, H.L.W. Chan, P.K. Choy and P.C.K. Liu: US Patent **11/051,155** (2005).
6. D. Li, S.W. Or, C.S. Yung, H.L.W. Chan, P.K. Choy and P.C.K. Liu: Proc. 12th SPIE Annual Int. Symp. on Smart Struct. Mater. (2005) 5760.

Proc. Symp. Ultrason. Electron., Vol. 26, (2005) pp. 275-276
16-18 November, 2005

講演取消

講演取消

P2-33

Proc. Symp. Ultrason. Electron., Vol. 26, (2005) pp. 277-278
16-18 November, 2005

Characteristics of High Frequency Sound Irradiated from Electromagnetically Driven Plate

Masashi Ohara, Takashi Kubo, Jian Yang, and Mamoru Kuwabara
(Dept. of Materials, Physics and Energy Eng. Nagoya Univ.)

Abstract

An ultrasonic oscillator, which electromagnetically generates ultrasound by vibration of an iron plate in the alternating magnetic field, is newly proposed for high temperature use. Low Curie point for a normal transducer made of piezoelectric material is overcome by use of a ferromagnetic iron plate that has a high magnetic Curie temperature (1043 K). The joule heating of a ferromagnetic iron plate is observed by the infrared camera, and the heating rate of a ferromagnetic iron plate is calculated. The rate of the Joule heating is closely related to the Lorentz force with which the plate is electromagnetically vibrated. From the viewpoint of Joule heating, the effects of various process parameters on the sound pressure are discussed. The magnetic field can be concentrated on the center of the iron plate by setting the water-cooled iron pole in the induction coil, and it is expected that the iron plate can be vibrated more strongly.

1. Introduction

In recent years, the present authors [1] have devoted to developing ultrasonic technologies for material processing, which is named “Sonoprocessing of materials”. It is considered that various applied technologies in material processing, such as convection control of molten metal and inclusion removal in refining processes, dispersion of reinforced particles and orientation control of reinforced fibers in composite material engineering, can be developed by using the external force of an ultrasonic wave effectively[2]. The transducers made of piezoelectric materials are usually used for generating ultrasonic waves. But they cannot be directly used in a high temperature field because its Curie temperature is relatively low (about 600 K). An alternative way may be possible by use of a ferromagnetic iron plate which has a high magnetic Curie temperature of about 1043 K and introducing liquid coolant in order to cool the steel plate below the Curie temperature. In this study, an ultrasonic oscillator, which electromagnetically irradiates ultrasound by vibrating a steel plate in an alternating magnetic field generated from an induction coil, is newly proposed.

In the present paper, the iron plate is vibrated by the strong electromagnetic field. Transient change in temperature of the electromagnetically driven plate is measured by an infrared camera, and the heating rate of the plate is calculated. From the viewpoint of the Joule heating associated with the Lorentz force to drive the plate, the effects of various process parameters on the sound pressure are investigated.

2. Experimental setup

The experimental setup is shown in Fig.1. The alternate current, which was generated by a high frequency (440 kHz) and high power (4 kHz) signal generator, was fed to the water-cooled coil (7 turns, 60 mm in height, 50 mm in diameter). Circular iron plate with different thickness was horizontally placed above the coil. The iron plate was vibrated by the Lorentz force and heated with electromagnetically induced current, which was generated by an alternating magnetic field from the coil. Distributed thermal level of the iron plate was observed by an infrared camera. Temperature change with time was also measured at specified positions from the center of the iron plate, which were changed at intervals of 30 mm, and the heating rate of the iron plate was calculated. The measurements described above were performed by changing the iron plate thickness t and the distance between the coil and the iron plate d.

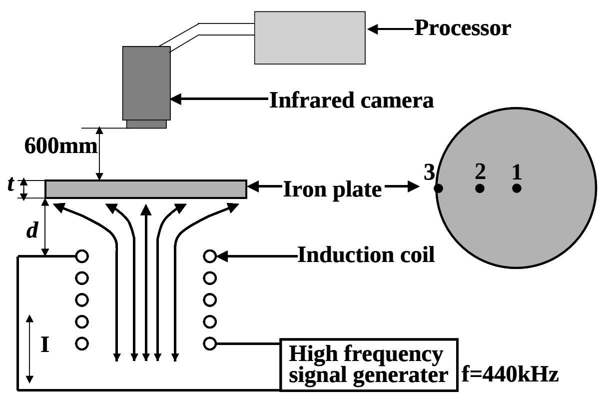

Fig.1. Experimental setup.

3. Results and discussion

Typical thermal images of the iron plate during heating is shown in Fig.2. Stressed temperature range in Fig.2 is between 15 ℃ and 100 ℃. Operating conditions and geometries employed are as follows: the distance between the iron plate and the coil: d=37 mm, the thickness of the iron plate: t=0.7 mm, the diameter of the iron plate: 120 mm, the imposed frequency: f=440 kHz, and the alternate current: I=2 A. From this figure, it is found that the iron plate was heated from the circular edge. Also transient change in temperature of the iron plate is shown in Fig.3. The approximated heating on different positions curves were obtained from plots in this figure. Local heat balance of the electromagnetic oscillating plate is expressed as the following equation:

$$CM\frac{dT}{d\theta} = QV - hA(T - T_a) \qquad (1)$$

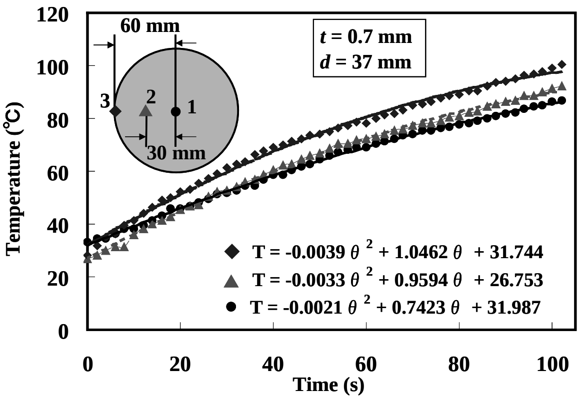

Fig.3. Transient change in temperature of the iron plate.

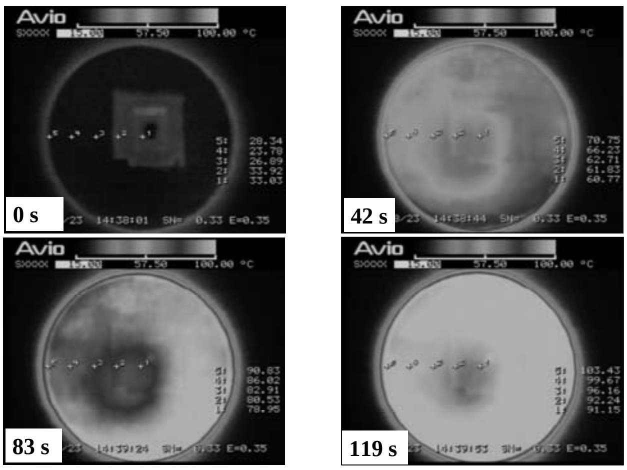

Fig.2. Thermal image of the iron plate.

where C is the specific heat, M is the mass, T is the local temperature, θ is the time, Q is the local heating rate, h is heat transfer coefficient, A is the surface area, V is volume, and T_a is the initial and ambient temperature. Since (T-T_a) is zero at θ =0, the local heating rate Q can be estimated by substituting the temperature gradient at θ =0 in Eq. (1) for corresponding observed one given by Fig.3. The local heating rates Q thus estimated are shown in Table.1.

Table.1. Heating rates of the iron plate

position	1	2	3
Q (W/m^3)	2.74×10^6	3.54×10^6	3.86×10^6

The specific heat and the density of the iron plate, which were employed in this calculation, were given as 486.6 J/kg・K and 7870 kg/m^3, respectively. Table.1 and Fig.2 indicated that the heating rate and thus the alternating magnetic field were both increased with increased radial distance. This fact implies the existence of insufficient profile of the magnetic flux density under the iron plate to be driven. However, the difference of the local heating rates between the radial positions was not so large. Induced current is generated by an alternating magnetic field that is parallel to the radial direction of the iron plate. From the Fleming's law, Lorentz force that works on the iron plate is proportional to the induced current. So, in order to increase the magnetic field that is parallel to the radial direction of the iron plate, it is important that the magnetic field is concentrated around the center of the iron plate. In this experiment, the air-cored induction coil was used. However, when the water-cooled iron pole is set in the induction coil in order to concentrate the magnetic field around the center of the iron plate, it is expected that the iron plate could be vibrated more strongly. Detailed design of the new system to generate a more strong magnetic field and its effect on the electromagnetic vibration of the iron plate will be also described in the conference venue.

4. Conclusion

An ultrasonic oscillator, which electromagnetically generates an ultrasound of the frequency of 440 kHz by vibration of a ferromagnetic plate in the alternating magnetic field, has been newly designed. The iron plate was vibrated by the strong electromagnetic field. The Joule heating of the iron plate was observed by the infrared camera to connect the local heating rate of the plate with the local Lorentz force that causes electromagnetic vibration. The heating rate of the iron plate and the Lorentz force that works on the iron plate were not so different between the radial positions on the iron plate. The iron plate can be vibrated more strongly when the magnetic flux is concentrated by using the water-cooled iron pole in the induction coil.

References

[1] M. Kuwabara et al.: International session, "Recent Innovation in Material Processes", CAMP-ISIJ, 16(2004).

[2] M. Kuwabara, et al.: Proc.8th Japan- China Sympo, Science and Technology of Iron and Steel, Chiba, Japan, 1998, p.175.

P2-34

Proc. Symp. Ultrason. Electron., Vol. 26, (2005) pp. 279-280
16-18 November, 2005

Acoustic Cavitation Based Production of Foamed Metallic Material

◎Yasuo Saiki, Takashi Kubo, Mamoru Kuwabara and Jian Yang

(Dept. of Materials, Physics and Energy Eng. Nagoya Univ.)

Abstract

An experiment has been carried out to solidify the Wood's alloy in an ultrasonic field. The ultrasonic wave employed in this experiment is of output power of 600 W and of frequency of 60 kHz, respectively. Microstructures and micro-defects in the solidified samples are observed by the scanning electron microscope (SEM). It is found that many microbubbles and microjets acoustically induced during solidification of the metal can result in microvoids in the solidified structure.

1. Introduction

Foamed materials have several interesting features. There are several methods of production of the foamed materials[1]. However in the conventional methods, additives are needed or gas is generated in the foamed materials such as hydrogen, nitrogen and so on. It is difficult to spread pores uniformly in foamed materials, and mechanical properties of a foamed material whose pores spread non-uniformly must be inferior to that of original material. Acoustic cavitation should become more attractive also in this field if cavitation malutibubble during solidification of a metal can be trapped in its solidified structure. Foamed materials with microstructures and microvoids, which are acoustically generated, can have innovative thermal and mechanical properties.

In this study, an experiment was carried out to solidify the Wood's alloy in an ultrasonic field to find microvoids in the solidified structure.

2. Experimental setup

The experimental setup is shown in Fig.1. The molten wood's alloy of 80 grams was charged into the test tube made of polypropylene, and an ultrasonic wave-guide through which ultrasound with frequency of 20 kHz and an U.S.P. of 600 W could be imposed, was set into the melt by the depth of 15 mm. Initial superheat of the melt above the melting point of wood's alloy (344～349 K) was about 5 K.

During ultrasonic irradiation, cooling water at 303K started to be flown around the test tube. Even after irradiation of ultrasound for 90 s, the flow of cooling water was continued till the whole solidification of the molten Wood's alloy was finished. And the area of square in Fig.2 was observed by SEM.

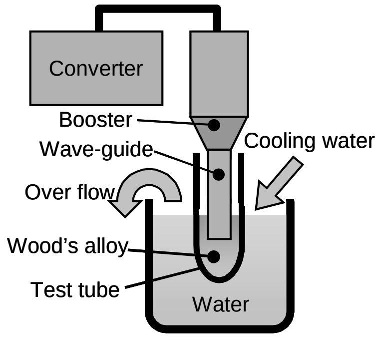

Fig. 1 Experimental setup for ultrasonic solidification.

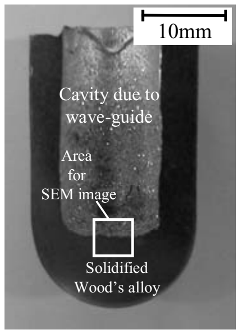

Fig. 2 Solidified alloy and area for SEM image.

3. Result and discussion

Fig.3 shows SEM images of the solidification structure of Wood's alloy solidified without ultrasonic irradiation. In order to keep the heat transfer conditions as same as with ultrasound irradiation (Fig.4), the ultrasonic waveguide was only set into the melt and the solidification experiment was carried out. Fig.3-(b) shows a magnified image of Fig.3-(a). The eutectic structures were observed in Fig.3-(b). This eutectic structure is consisted of four kinds of phases. These phases solidified in order according to the respective melting points[2].

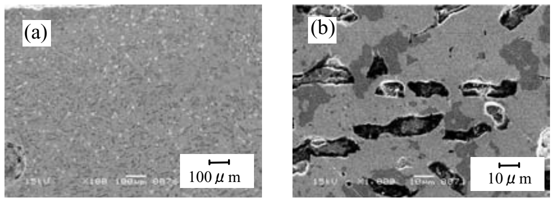

Fig.3 SEM images of the microscopic structure solidified without ultrasound.

Fig.4 shows typical SEM images of the microscopic structures solidified with ultrasonic irradiation. The elapsed time of ultrasound irradiation was 10 s and U.S.P. was 600 W. As shown in Fig.4-(a), some large spherical spaces with dark color, whose diameters were up to 3 mm, were found. It is interesting to note that several many ting defects, which in closed white frames in Fig.4-(a).These large dark colored spherical spaces should remain to be solid-liquid coexisting phase until the completion of solidification. The temperature in the large spherical spaces can be deduced to be kept homogeneously at the melting point by ultrasonic violet mixing. After nuclei of the solidification generated at the melting point, the nuclei gradually grew as small spherical particles of several tens μm in diameter and the fractional space of liquid gradually reduce. Finally they gather to become the large dark colored spherical space with many spherical particles inside.

Fig.4-(b) shows a magnified image of the white framed area (b) in Fig.4-(a), Fig.4-(c) also shows a magnified image of framed area (c) in Fig.4-(a). Fig.4-(b) shows the solidification structure which remained as the solid-liquid coexisting phase and solidified finally. The structure is composed of many small particles with a eutectic structure. The intraparticle pore is occupied by more dark substance in which alloying elements might be concentrated during growth of the nuclei in the substance at liquid state. Fig.4-(c) shows the microscopic structure, which was solidified earlier than the large dark colored spherical space. The ting defects were observed everywhere as are shown in Fig.4-(b) and Fig.4-(c).

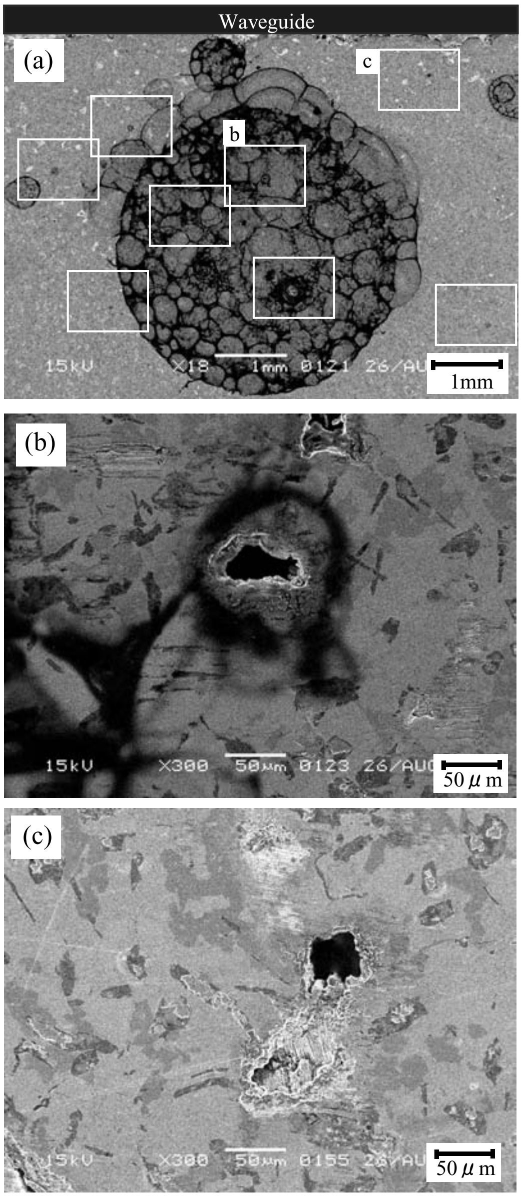

Fig. 4. SEM images of microscopic solidified with ultrasonic irradiation.

The mean size of the defect was about 50 μm. These defects were exceedingly small compared with a normal defection of solidification and had a possible dimension of acoustic cavitation. Fig.5 shows the SEM image of one indentation on aluminum foil surface attacked in water bath by an acoustic cavitation. It is interesting to note the shape and the dimension of a defect in Fig.4 is similar to this trace of indetation.

It is deduced that these defects are generated by acoustic cavitation and microjet. Although vapor pressure of the solid-liquid coexisting phase is very low and nearly zero, experimental findings in this study suggest that acoustic cavitation is generated in the liquid phase of wood's alloy during solidification. So it is expected that acoustic cavitation multibubble can be trapped in the solidifying structure and acoustic cavitation can be utilized for the production of the foamed materials.

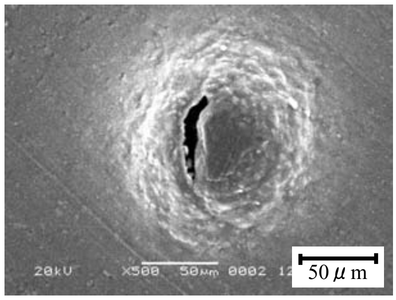

Fig.5. SEM image of one indentation on aluminum foil surface attacked by acoustic cavitation.

4. Conclusions

A laboratory experiments on the ultrasonic solidification was carried out using the Wood's alloy. Frequency and power of the ultrasound employed are 20 kHz and 600 W, respectively. Microstructures and micro-defects in the solidified samples were investigated by the SEM imaging and the optical microscope observation. The solidified structures indicated that wide area of the melt was uniformly cooled down until the temperature of the melt was kept just above its melting point because of intensified mixing due to acoustic cavitation. Finally a great many nuclei uniformly evolved and they rapidly grew in the remained melt to result in microstructures inside the area. Even during the final stage of solidification, the acoustic cavitation continued in the remaining liquid accompanied by many microbubbles and microjets to cause microvoids in the solidified structure.

References

1) H. Nkajima: Kinzoku,Vol.74, No.7, 2004, p.646
2) H. Kamioka: Jishin,Vol.2, No.30, 1977, p.463

Proc. Symp. Ultrason. Electron., Vol. 26, (2005) pp. 281-282
16-18 November, 2005

Post-Beamforming Second-Order Volterra Filters for Contrast Agent Imaging: A Frequency-Domain Aspect

Pornchai Phukpattaranont and Kanadit Chetpattananondh (Department of Electrical Eng., Prince of Songkla Univ.)

1 Introduction

Recently, many reports of the improved diagnostic capabilities exploiting ultrasound contrast agents (UCAs) in clinical applications have been published. This achievement exploits the nonlinear behavior from interaction between acoustic energy and UCAs to improve spatial and contrast resolution. In [1], we have developed post-beamforming nonlinear filtering algorithm based on the second-order Volterra filter (SVF) [2] to separate linear and quadratic components from UCA echoes. The proposed imaging method, referred to as quadratic B-mode (QB) imaging, allows for transmitting pulses optimized for maximum resolution (as in conventional B-mode) while still providing images with significant improvement of contrast between UCA and surrounding tissue. In this paper, we investigate the characteristics of QB-mode imaging in the frequency domain.

2 Theory

The QB-mode image is produced using a quadratic filter, in which the relation between input $x(n)$ and output $y(n)$ can be expressed as

$$y(n) = \sum_{k_1=0}^{N-1} \sum_{k_2=0}^{N-1} h_2(k_1, k_2) x(n-k_1) x(n-k_2), \qquad (1)$$

where $h_2(\cdot,\cdot)$ represents the quadratic kernel and N is the system memory. The quadratic kernel for contrast agent imaging is obtained by forming a system of linear equations from a segment of beamformed RF data and solving for filter coefficients to minimize the error from the linear plus quadratic predictor (For complete details of the algorithm, please see [3]). The QB-mode image is produced by applying the optimal kernel to the beamformed RF data throughout the B-mode image.

In this paper, we analyze the characteristics of the optimal quadratic kernel, which is capable of enhancing UCA over tissue, in the frequency domain. The input-output relation of the quadratic filter shown in Equation 1 in the frequency domain is given by

$$Y(e^{j\omega}) = \frac{1}{2\pi} \int_0^{2\pi} \int_0^{2\pi} H_2(e^{j\omega_1}, e^{j\omega_2}) X(e^{j\omega_1}) X(e^{j\omega_2}) d\omega_1 d\omega_2 \qquad (2)$$

under the assumption

$$\omega_1 + \omega_2 = \omega, \qquad (3)$$

where $Y(e^{j\omega})$ is the discrete-time Fourier transform (DTFT) of $y(n)$, $X(e^{j\omega})$ is the DTFT of $x(n)$, and $H_2(e^{j\omega_1}, e^{j\omega_2})$ is the 2D DTFT of $h_2(\cdot,\cdot)$. Note that the observed quadratic signal component at ω is the result of the sum of mixing all frequency components ω_1 and ω_2 such that $\omega_1 + \omega_2 = \omega$ weighted by the quadratic frequency response at $\omega_1 + \omega_2 = \omega$.

3 Results and Discussion

We use the RF data acquired *in vivo* to investigate characteristics of the optimal quadratic kernel in the frequency domain (Please see [3] for details of the experimental setup and quadratic kernel derivation). Figure 1(a) shows the B-mode image of the kidney after the injection of 0.01 mL/kg UCAs acquired using 3-cycle 1.56-MHz pulse (MI = 0.158) transmissions. Average spectra of tissue and UCA signals in the left and right boxes of Figure 1(a) are shown in Figure 1(b). We can clearly see that harmonic spectra of UCA echoes (solid) between 2 MHz and 4 MHz frequency band are broader than those from tissue echoes (dotted line). Figure 1(c) shows the optimal quadratic kernel used to produce QB-mode images. The kernel is a square matrix with size 57 by 57. The resulting QB-mode image processed with the quadratic kernel shown in Figure 1(c) is shown in Figure 1(d). One can clearly see the improvement of image quality. This significant enhancement of QB-mode image can be explained using the relation described in Equation 2.

Figure 2 shows a filled contour plot of magnitude of frequency responses in the (ω_1, ω_2) plane. The filled contour plot displays isolines calculated from the magnitude of frequency function in the (ω_1, ω_2) plane and fills the areas between the isolines using constant colors. The magnitude frequency responses obtained using RF data in the tissue ($|X_{TS}(e^{j\omega_1})X_{TS}(e^{j\omega_2})|$) and UCA ($|X_{CT}(e^{j\omega_1})X_{CT}(e^{j\omega_2})|$) regions are shown in Figure 2(a) and (b), respectively. Figure 2(c) shows the ratio of contrast to tissue magnitude, i.e. $\frac{|X_{CT}(e^{j\omega_1})X_{CT}(e^{j\omega_2})|}{|X_{TS}(e^{j\omega_1})X_{TS}(e^{j\omega_2})|}$. Four distinct peaks in the 2D plane of contrast to tissue magnitude are observed at frequencies corresponding to second harmonics due to UCA, i.e. 3 MHz. Figure 2(d) shows the magnitude of 2D frequency response of the optimal quadratic filter ($|H_2(e^{j\omega_1}, e^{j\omega_2})|$). The magnitude of frequency responses of quadratic components from tissue ($|H_2(e^{j\omega_1}, e^{j\omega_2})||X_{TS}(e^{j\omega_1})X_{TS}(e^{j\omega_2})|$) and UCA ($|H_2(e^{j\omega_1}, e^{j\omega_2})||X_{CT}(e^{j\omega_1})X_{CT}(e^{j\omega_2})|$) regions in the (ω_1, ω_2) plane are shown in Figure 2(e) and (f), respectively. We can clearly see that the quadratic kernel appropriately amplifies the region where UCA is higher than tissue at frequency (3,3) and (-3,-3) MHz.

Figure 3(a) shows a more quantitative insight of the quadratic filter in the frequency domain. Line graphs that

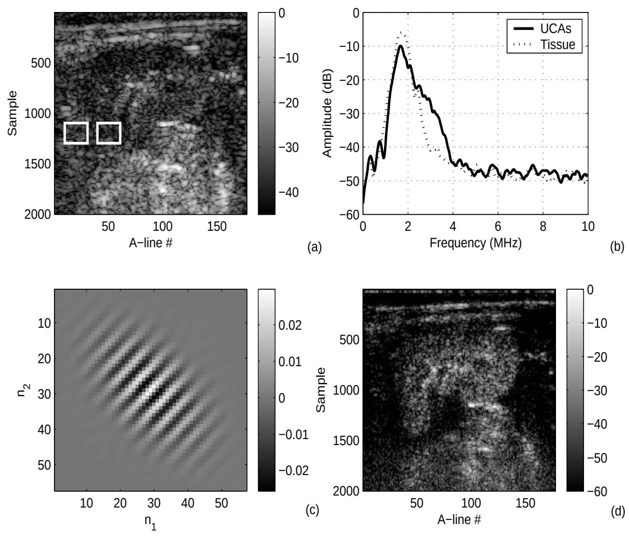

Figure 1: (a) B-mode image of the kidney. (b) Average spectra of RF data. Solid: $|X_{CT}(e^{j\omega})|$, Dotted: $|X_{TS}(e^{j\omega})|$. (c) The optimal quadratic kernel. (d) QB-mode image.

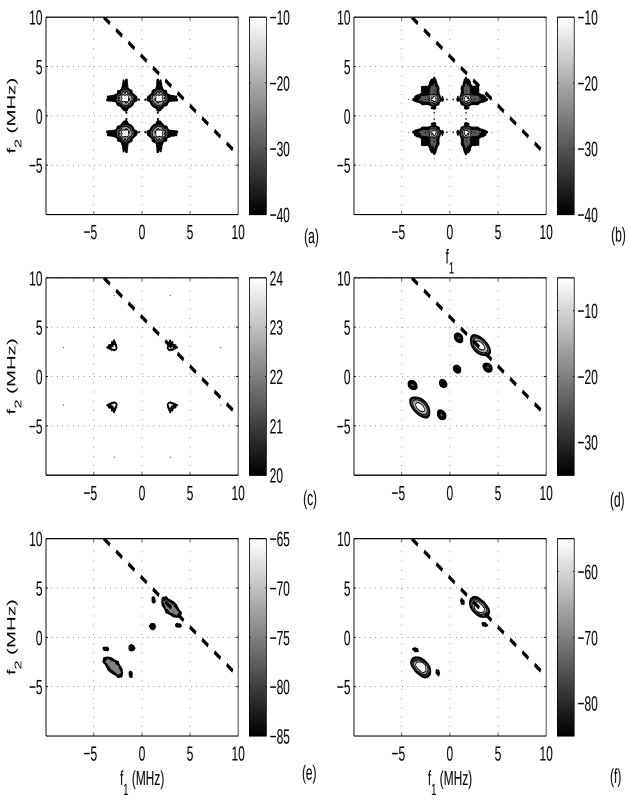

Figure 2: Filled contour plots of magnitude frequency responses in the (ω_1, ω_2) plane: (a) $|X_{TS}(e^{j\omega_1})X_{TS}(e^{j\omega_2})|$, (b) $|X_{CT}(e^{j\omega_1})X_{CT}(e^{j\omega_2})|$, $\frac{|X_{CT}(e^{j\omega_1})X_{CT}(e^{j\omega_2})|}{|X_{TS}(e^{j\omega_1})X_{TS}(e^{j\omega_2})|}$, (d) $|H_2(e^{j\omega_1}, e^{j\omega_2})|$, (e) $|H_2(e^{j\omega_1}, e^{j\omega_2})||X_{TS}(e^{j\omega_1})X_{TS}(e^{j\omega_2})|$, and (f) $|H_2(e^{j\omega_1}, e^{j\omega_2})||X_{CT}(e^{j\omega_1})X_{CT}(e^{j\omega_2})|$. In addition, the diagonal line $f_1 + f_2$ = 6 MHz is overlaid in the (ω_1, ω_2) plane.

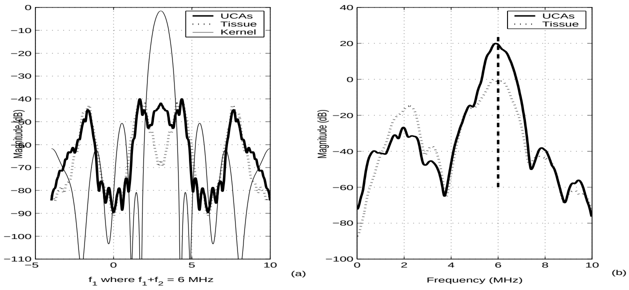

Figure 3: (a) Solid: $|X_{CT}(e^{j\omega_1})X_{CT}(e^{j\omega_2})|$, Dotted: $|X_{TS}(e^{j\omega_1})X_{TS}(e^{j\omega_2})|$, and Thin: $|H_2(e^{j\omega_1}, e^{j\omega_2})|$ where $f_1 + f_2$= 6 MHz. (b) Solid: $|Y_{CT}(e^{j\omega})|$, Dotted: $|Y_{TS}(e^{j\omega})|$.

corresponding to magnitude frequency where $f_1 + f_2 = 6$ MHz in the (ω_1, ω_2) plane of the UCA, tissue, and kernel are shown using, thick, dotted, and thin lines, respectively. One can see that the kernel has a high gain where UCA is higher than tissue. Figure 3(b) show average spectra of data from the QB-mode image in UCA ($|Y_{CT}(e^{j\omega})|$) and tissue ($|Y_{TS}(e^{j\omega})|$) regions using solid and dotted lines, respectively. The intersection points between the dashed vertical line and other two horizontally spectral lines are from the integration along the diagonal line $f_1 + f_2$= 6 MHz, i.e. $\int_0^{2\pi}\int_0^{2\pi} H_2(e^{j\omega_1}, e^{j\omega_2})X_{CT}(e^{j\omega_1})X_{CT}(e^{j\omega_2})d\omega_1 d\omega_2$ and $\int_0^{2\pi}\int_0^{2\pi} H_2(e^{j\omega_1}, e^{j\omega_2})X_{TS}(e^{j\omega_1})X_{TS}(e^{j\omega_2})d\omega_1 d\omega_2$ where $f_1 + f_2$= 6 MHz.

4 Conclusions

We analyze frequency-domain characteristics of the quadratic kernel that is able to separate quadratic components from UCA signals. QB-mode images produced using those quadratic components show significant improvement in both contrast and spatial resolution as shown in Section 3. The understanding of the quadratic kernel in the frequency domain allows for the improved filter design in term of both kernel size and contrast enhancement capability.

Acknowledgments

The authors thank ESAOTE S.p.A, Genoa, Italy for supporting the *in vivo* data used in this paper.

References

[1] P. Phukpattaranont and E. S. Ebbini, "Post-beamforming second-order volterra filter for pulse-echo ultrasonic imaging," *IEEE Trans. Ultrason., Ferroelect., Freq. Contr.*, vol. 50, no. 8, pp. 987–1001, Aug. 2003.

[2] G. L. Sicuranza, "Quadratic filters for signal processing," *Proc. of the IEEE*, vol. 80, no. 8, pp. 1263–1285, Aug. 1992.

[3] P. Phukpattaranont and E. S. Ebbini, "Post-beamforming volterra filters for contrast-assisted ultrasonic imaging: *in-vivo* results," in *Proc. IEEE Ultrason. Symp.*, 2003, vol. 2, pp. 1191–1194.

P2-36

Proc. Symp. Ultrason. Electron., Vol. 26, (2005) pp. 283-284
16-18 November, 2005

Development of a novel ultrasonic bone densitometry using acoustic parameters of cancellous bone for fast and slow waves

○Isao MANO*, Kaoru HORII (OYO Electric co., ltd.), Shinro TAKAI (Teikyo Univ., Faculty of Medicine), Takuji SUZAKI, Hiroki NAGAOKA (Horiba, Ltd.) and Takahiko OTANI (Doshisha Univ., Faculty of Engineering)

1. Introduction

An X-ray method is now widely used for noninvasive measurement of bone mineral density for the assessment of osteoporosis. An ultrasonic method has been proposed as an alternative for the diagnosis of osteoporosis. Ultrasonic measurements of bone status or bone mass density are generally performed using the following ultrasonic parameters, the slope of frequency dependent attenuation (or broadband ultrasonic attenuation, BUA [dB/MHz]) and the speed of sound (SOS [m/s]). The ultrasonic method has several advantages over X-ray bone densitometry as it is radiation free, inexpensive and portable and has the potential to evaluate the elastic or mechanical properties of bone which the X-ray method does not. However, a problem is inherent in the ultrasonic method regarding the reproducibility and the uncertainty in measured ultrasonic parameters. A novel ultrasonic bone densitometry have been developed to overcome the ploblem inherent in the ultrasonic method, and to obtain both the bone density in the real unit [mg/cm^3] or [kg/m^3] (not in the form of ultrasonic parameters) and the elasticity with a comparable space resolution to the pQCT system.

2. Measurement system and method

The authors have previously reported a peculiar propagation phenomena of ultrasonic wave in cancellous bone (two distinct longitudinal waves, fast and slow waves, propagating through cancellous bone),[1~3] and theoretically formulated the propagated ultrasonic signals in measurement site for the fast and slow waves.[4] This formulation is applied to the developed system to obtain real quantitative bone density and elasticity of cancellous bone *in vivo* clinical measurements. The peripheral quantitative computed tomography (pQCT, a micro focus X-ray system) is characterized, above all X-ray methods of bone densitometry, by measurements of a 2 dimensional local bone mass density and its imaging at 4% distal radius site. The same measurement site as pQCT is selected to compare the characteristics between the newly developed ultrasonic system and the pQCT system. The site to be measured, or a left distal radius (a left-hand wrist) is set between a pair of broadband-focused transducers (transmitter and receiver) through water-filled bags. The transmitter is driven by a single sinusoidal pulse voltage at a frequency of 1MHz. The beam width at the focus is approximately 3mm for a single sinusoidal pulse. Both transducers are coaxially and confocally aligned and move simultaneously for scanning. The ultrasound beam scans mechanically in a raster pattern through the measurement site. The ultrasonic measurement consists of two scanning processes, the first and the second scannings. In the first scannings, transmitted ultrasonic signals are taken and recorded every 2mm over a scanning area in both X-Y directions 28×28mm. Overall amplitude of the transmitted signals including both the fast and slow waves are analyzed to obtain a local attenuation distribution of the measurement site. The psuedo-bone density image obtained by the first scanning is used for confirming the bone geometry of measurement site and for determining the second scanning position to measure the bone density and the bone elasticity. The second scanning position is automatically selected by a specially developed algorithm at almost the same measurement site of pQCT in the distal radius and at a good likelihood site of the fast wave in cancellous bone. The second scanning area is 4×4mm. During the second scanning, transmitted signals are recorded every 1mm and analyzed in transmission mode to obtain the amplitudes and the propagation times for the both fast and slow waves. Echo signals are analyzed in echo mode of the second scanning to obtain the thicknesses of soft tissue, cortical bone and cancellous of the measurement site.

3. Evaluation of bone density and elasticity

The ultrasonic wave is separated into two longitudinal waves, the fast and slow waves, during the propagation in cancellous bone at distal radius. Assuming that the received signal voltage of the receiver is E_2 for the fast wave and E_2' for the slow wave, and that the received signal voltage without the subject (the propagation through water) is E_0. The ultrasonic parameters for the cancellous bone density are expressed for the fast wave as

$$T_{34}T_{45} = \left[B_0 / ATe^{-\alpha_4 x_4}\right](E_2 / E_0) \qquad (1)$$

and for the slow wave as

* E-mail address: imano@oyoe.jp

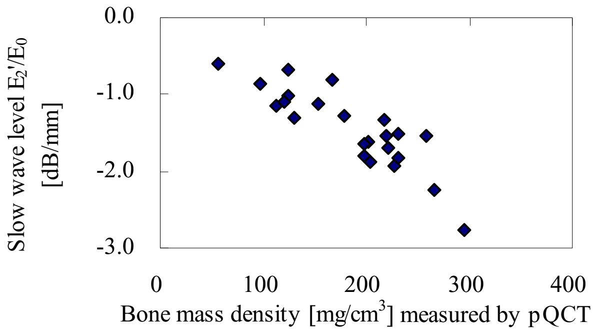

Fig.1 Slow wave level E_2'/E_0 normalized by radius thickness and bone mass density measured by pQCT.

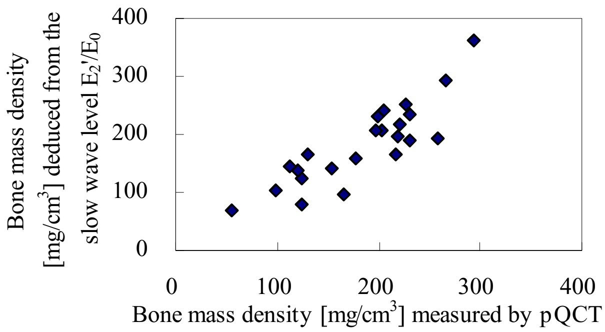

Fig.2 Bone density deduced from the slow wave level and bone mass density measured by pQCT.

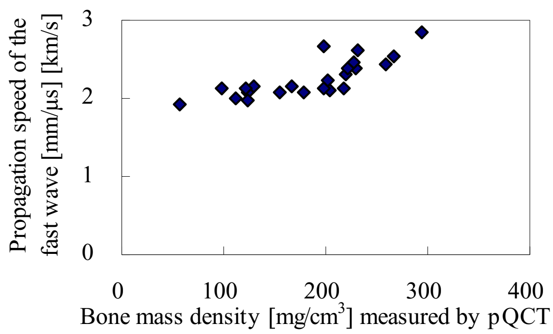

Fig.3 Propagation speed of the fast wave in cancellous bone of radius and bone mass density measured by pQCT.

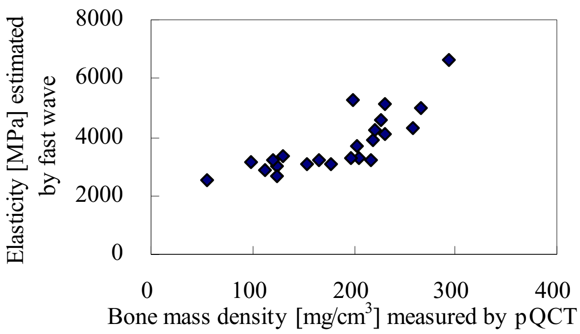

Fig.4 Elasticity corresponding to the fast wave and bone mass density measured by pQCT.

$$e^{-\alpha_4' x_4} T_{34}' T_{45}' = \left[B_0 / AT\right]\left(E_2' / E_0\right) \qquad (2)$$

where A is the total attenuation except cancellous bone, T is the product of the transmission coefficients of all medium boundaries except cancellous bone, B_0 is the attenuation in water (without the measurement site), T_{34} T_{45} and T_{34}' T_{45}' are the products of transmission coefficients of both boundaries of cancellous bone for the fast and slow waves.

The dependence of the parameters for the fast and slow waves, eqs.(1) and (2) on the bone density should be experimentally established a priori. Then the bone density of cancellous bone is evaluated using eqs.(1) and (2). The propagation speed of the fast wave in cancellous bone is given by

$$c_4 = x_4 / t_4 \qquad (3)$$

x_4 and t_4 are obtained by measured signals during the second scanning in both transmission and echo modes. The elasticity of cancellous bone is evaluated using c_4.

4. Measured results

Some examples of measured results obtained by the developed system LD100 are shown from Fig.1 to Fig.4. The slow wave level normalized by cancellous bone thickness and the bone density deduced from eq.(2) are shown in **Fig.1** and **Fig.2**. The propagation speed of the fast wave and the elasticity for the fast wave are shown in **Fig.3** and **Fig.4**. All measured values are shown as a function of the bone mass density measured by pQCT system (Stratec XCT-960).

5. Remarks and conclusions

The bone density and the elasticity of *in vivo* cancellous bone are evaluated by the developed ultrasonic bone densitometry, prototype LD100.

1) Measured values of the developed system LD100 are given with the real unit of density [mg/cm^3]or [kg/m^3] and of elasticity [MPa].

2) Measured densities obtained by the developed ultrasonic system agree well with that obtained by pQCT system and the correlation coefficient between both systems attains 0.9.

3) A possibility of 2 dimensional imaging of the bone density, comparable to the pQCT system is confirmed by measured results.

Acknowledgments

This study is supported by the Japan Science and Technology Agency as a development project of new technologies.

References

1. A. Hosokawa and T. Otani : J. Acoust. Soc. Am. **101** (1997) 558.
2. A. Hosokawa, T. Otani, T. Suzaki, Y. Kubo and S. Takai,: Jpn. J. Appl. Phys. **36**, 5B (1997) 3233.
3. A. Hosokawa and T. Otani : J. Acoust. Soc. Am. **103** (1998) 2718.
4. T.Otani,: Jpn. J. Appl. Phys. **44**, 6B (2005) 4578.

P2-37

Proc. Symp. Ultrason. Electron., Vol. 26, (2005) pp. 285-286
16-18 November, 2005

Ultrasonic Beam Steering for Accurate Measurement of Intima-Media Thickness at Carotid Sinus

○ Takashi Mashiyama, Hideyuki Hasegawa and Hiroshi Kanai
(Dept. of Electronic Eng., Tohoku University)

1. Introduction

Recently, the number of patients who died due to cardiovascular diseases are in the second place following the malignant neoplasm. Since atherosclerosis is one of main causes of these diseases, it is necessary to diagnose atherosclerosis in an early stage. The carotid sinus is a site which is easily affected by atherosclerosis [1]. However, it is impossible to diagnose atherosclerosis accurately using the conventional ultrasonography because the carotid sinus is not flat along the axis of the vessel, and ultrasonic beams of linear scanning are orthogonal to the arterial wall in a limited region. The reflection intensity in a non-orthogonal region is very weak and the arterial wall in such a region is hardly recognized. In this paper, the rough position of the arterial wall is determined from the B-mode image obtained by conventional linear scanning, then ultrasonic beams are transmitted again so that all beams are orthogonal to the arterial wall.

2. Principle

Figure 1 shows schematic diagram of beam steering. The ultrasonic beam was scanned at M positions along the x-axis by conventional linear scanning. The depth of the arterial wall, y_i $(i = 1, 2, ..., M)$, at each beam position, x_i $(i = 1, 2, ..., M)$, is detected from the B-mode image obtained by conventional linear scanning. The interval of ultrasonic beams, $\Delta x = x_{i+1} - x_i$, is 0.2 mm. With respect to a position, (x_i, y_i), of i-th ultrasonic beam, a regional slope, a_i, of the arterial wall to the surface of the ultrasonic probe is estimated by the least-squares method using the positions of the arterial wall, $\{(x_i, y_i)\}$, at neighboring $\pm N$ ultrasonic beams, as follows:

$$\theta_i = \tan^{-1} a_i \quad \text{[rad]}, \tag{1}$$

$$b_i = x_i - \frac{y_i}{\tan\theta_i} = x_i - \frac{y_i}{a_i} \quad \text{[mm]}, \tag{2}$$

where θ_i is the angle of beam which is perpendicular to the position, (x_i, y_i), of the arterial wall. From the determined beam angle, θ_i, and the position, (x_i, y_i), of the arterial wall, the transmitting position, b_i, of the ultrasonic beam, which perpendicularly passes through the position, (x_i, y_i), is determined. By determining θ_i and b_i for all positions, $\{(x_i, y_i)\}$, all beams are designed so as to be orthogonal to the arterial wall.

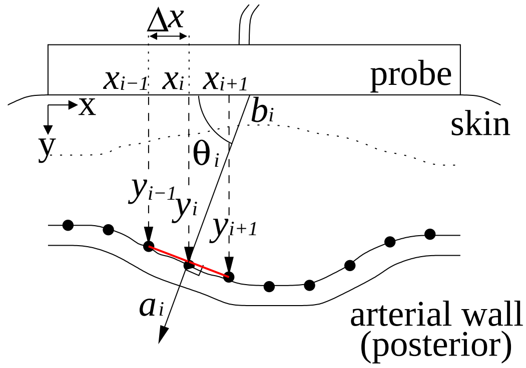

Figure 1: Determination of optimum beam position and angle ($N = 1$).

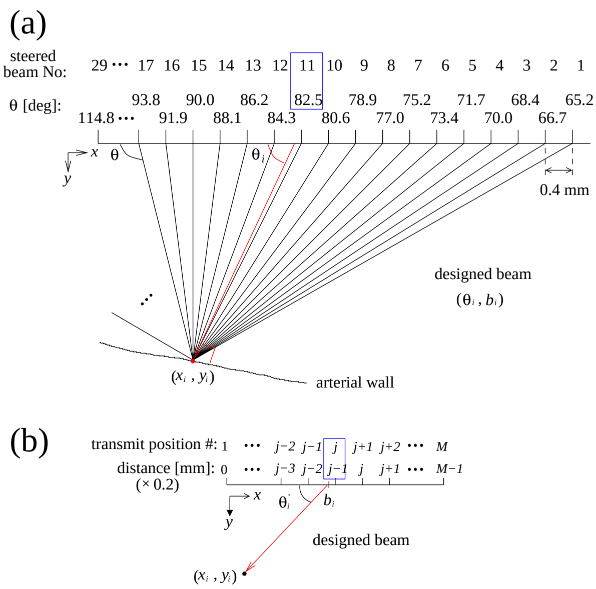

Figure 2: (a) Determination of the discrete beam angle (red line: designed beam). (b) Determination of the discrete transmit position.

In the actual diagnostic equipment, the beam angle, θ_i, has a discrete value. Therefore, a discrete beam angle, θ_i', that is the nearest to the angle, θ_i, is selected from pre-assigned angles of 29 beams (**Fig. 2**(a)). The transmit position, b_i, is calculated again using the discrete beam angle, θ_i'. The transmit position, b_i, is also a discrete value which depends on the element pitch of the ultrasonic probe. As shown in Fig. 2(b), the discrete transmit position, b_i', which is the nearest to b_i, is selected as well as the angle, θ_i'. In this way, a beam transmitted to the position, where is the nearest to (x_i, y_i), is selected.

e-mail: masiyama@us.ecei.tohoku.ac.jp

3. Basic experiments using silicone rubber

As shown in **Fig. 3**(a), a silicone rubber tube which was open up was fixed in a water bath and it was measured by a linear ultrasonic probe at 10 MHz of the diagnostic equipment (Aloka SSD-6500). The size of the silicone rubber was configured to be 13 mm because the size of the carotid sinus in the longitudinal direction is 10-13 mm. Using the beam scanning method [2], all ultrasonic beams are transmitted so as to pass the point, O, and 29 beams are transmitted at various angles θ_i (65-115 deg). The ultrasonic probe was moved in the x-axis direction at 3 mm/s for 4 s, and the point, O, was moved as shown in Fig. 3(b). Ultrasonic RF echos were obtained 60 times by moving the point, O, with a pitch of 0.2 mm along x-axis.

A B-mode image of conventional linear scanning (**Fig. 4**(a)) was composed of 60 ultrasonic beams. 60 positions of the silicone rubber surface $\{(x_i, y_i)\}$ $(i = 1, 2, ..., 60)$ were assigned on the B-mode image (red line in Fig. 4(a)). Based on the principle in Sec. 2, beams (angle θ_i, transmit position b_i) which are orthogonal to the surface of the silicone rubber were calculated using $\{(x_i, y_i)\}$. The yellow line in Fig. 4(a) shows a designed optimum beam $(i = 9)$. Designed beam angle θ_9 is 67.8 degrees and transmit position b_9 is 7.77 mm. Then, a beam with a discrete beam angle of $\theta'_9 = 68.4$ degrees and a discrete transmit position of $b'_9 = 7.6$ mm was selected.

Figure 4(b) shows a B-mode image composed by ultrasonic RF echos obtained by the designed beams. The ultrasonic beam inclines from a vertical direction by 22.2 degrees at the surface position (x_9, y_9). At this position (x_9, y_9), the silicone rubber cannot be imaged by the conventional linear scanning as shown in Fig. 4(a). On the other hand, a strong reflected echo was obtained from such a position (x_9, y_9) using the proposed method, and the silicone rubber was imaged in the entire scanned area as shown in Fig. 4(b).

4. Conclusion

In this paper, a method for designing beam steering which makes ultrasonic beams orthogonal to the arterial wall at the carotid sinus was proposed. In basic experiments, it was shown that it was possible to image a nonflat object in the entire scanned area using the proposed beam steering.

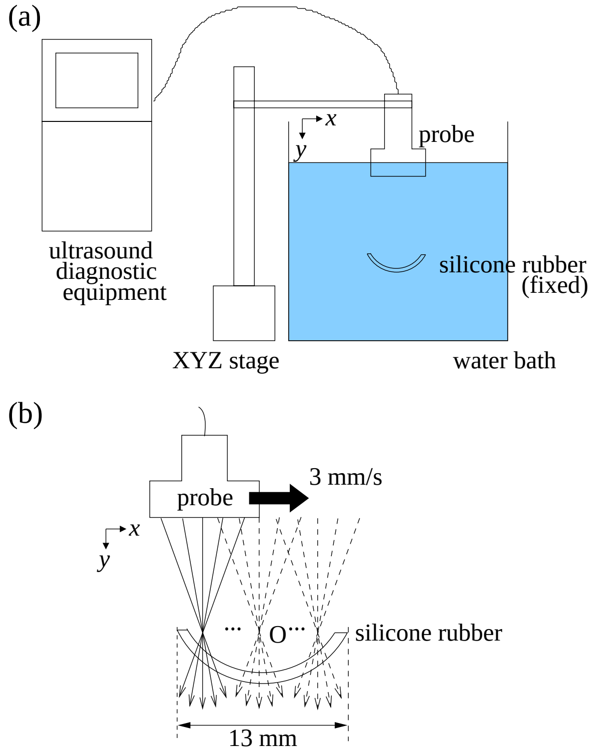

Figure 3: (a) Experimental system. (b) Schematic diagram of measurement.

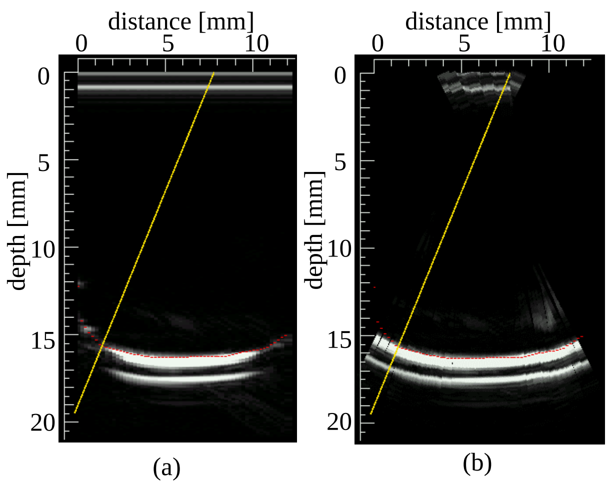

Figure 4: (a) B-mode image obtained by conventional linear scanning (red line: assigned silicone rubber surface, yellow line: designed beam $(i = 9)$). (b) B-mode image obtained by the proposed steered beams.

References

[1] C. K. Zarins, D. P. Giddens, B. K. Bharadvaj, V. S. Sottiurai, R. F. Mabon and S. Glagov: Circ. Res. **53** (1983) 502.

[2] N. Nakagawa, H. Hasegawa and H. Kanai: Jpn. J. Appl. Phys. **43** (2004) 3220.

P2-38

Proc. Symp. Ultrason. Electron., Vol. 26, (2005) pp. 287-288
16-18 November, 2005

Accurate Ultrasonic Measurement of Surface Profile by Detecting Phase Shift During Scanning

○ Chihiro Arihara, Hideyuki Hasegawa, and Hiroshi Kanai
(Dept. of Electronic Eng., Tohoku University)

1. Introduction

Recently, increasing circulatory disease such as myocardial infarction and cerebral infarction becomes a serious problem. It is important to diagnose atherosclerosis, which is a main cause of diseases in an early stage.

Luminal surface of clinically normal artery is covered with a piece of endothelial cells and will be smooth. In an early stage of atherosclerosis, luminal surface is damaged [1], edema develops under endothelium, endothelial cell is separated, and then luminal surface becomes rough. To detect atherosclerosis in an early stage, roughness of luminal surface needs to be detected with an accuracy of micrometer that cannot be achieved by traditional ultrasonic diagnostic equipments.

Interval of the ultrasonic beams is about 100 μm, and B-mode image is created using the amplitude of the received wave. Therefore, resolution of B-mode image of ultrasonic diagnostic equipment is 100 μm in a lateral direction and is 150 μm, which corresponds to the wavelength at 10 MHz, in the depth direction. In this paper, accurate detection of roughness in the depth direction was achieved using the phase of the received wave. Furthermore, the lateral resolution, which is deteriorated by a finite beam diameter, is improved by an inverse filter.

2. Principle

2.1 Method

A linear-type ultrasonic probe of ultrasonic diagnostic equipment (Aloka SSD-6500) used in this experiment transmits and receives ultrasonic pulse by scanning the ultrasonic beam along the surface of an object (center frequency f_0=10 MHz, scanning pitch L=0.1 mm, and number of beams M=70 (beam position: $l_1, l_2, \cdots, l_m, \cdots, l_M$)). Ultrasonic RF signals are sampled with 40 MHz. B-mode images consist of sampled points, which are obtained every 19.25 μm in the depth direction (sound speed c_0=1,540 m/s) and 0.1 mm in the lateral direction (a set of two dimensional discrete data: frame).

Figure 1 shows the experimental system and size of an object (extension board: 0.5 mm pitch). The object was stuck to rubber board with thumbtacks. Water was boiled to expel any remaining air, and the wall of the tank was covered with acoustic absorbing material.

The object was measured with a frame rate FR=188 frames/s while the probe moved automatically at the

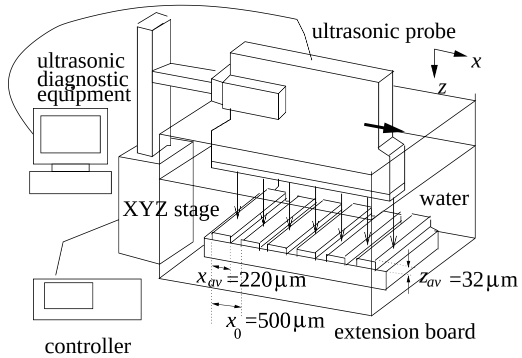

Figure 1: Experimental system for measurement of surface of object by ultrasound.

constant speed v_{stg} =50 μm/s for 2 seconds. The distance moved L=100 μm, which corresponds to the scanning interval of ultrasonic beam, in x-direction with an XYZ stage. Let us define the measurement location of beam l_1 of the first frame by $x(1,1)$=0 mm, the measurement location of beam l_m of nth frame is obtained as follows:

$$x(n,m) = (m-1)\cdot L + \frac{(n-1)\cdot v_{stg}}{FR}. \qquad (1)$$

In this paper, the phase difference $\Delta\phi(x)$ of the received wave at each measurement location was calculated as interval of frame ΔN=19. In this case, the probe moved Δx=5 μm during ΔN. Therefore, in the x direction, interval of measured location was smaller than scanning interval of L=100 μm.

The demodulated signal of received RF echo was used to measure surface profile with an accuracy of micrometer in the depth direction. When the phase difference of received wave between locations, x and $x+\Delta x$, is $\Delta\phi(x)$, the surface profile, $z(x)$, is obtained as follows:

$$\Delta z(x) = \frac{c_0 \Delta\phi(x)}{4\pi f_0}, \qquad (2)$$

$$z(x) = \int_0^x \Delta z(x')dx'. \qquad (3)$$

At this time, the measured depth, $d(x)$, corresponds to the surface of the object (about 11 mm), and focal point was about 14 mm from the surface of the probe.

It is difficult that the surface of the ultrasonic probe moves in a direction perfectly parallel to the surface of the object. Therefore, the angle between the surface of the ultrasonic probe and the surface of the object needs to be compensated. The compensated surface profile, $g(x)$, is obtained by subtracting the measure line, which is calculated by the least-square method from $z(x)$.

2.2 Improvement of deteriorated lateral resolution using inverse filter

Beam diameter deteriorates the lateral resolution. The actual surface profile, $f(x)$, of the object is expressed by the measured surface profile, $g(x)$, the beam diameter (point spread function), $h(x)$, noise $n(x)$, and their Fourier spectra, $F(u)$, $G(u)$, $H(u)$, and $N(u)$, as follows:

$$
\begin{aligned}
g(x) &= f(x) * h(x) + n(x), &(4)\\
G(u) &= F(u) \cdot H(u) + N(u), &(5)
\end{aligned}
$$

where u is spatial frequency.

In this paper, the measured signal is assumed to be noise free. The estimate of the surface profile, $\widehat{f}(x)$, is calculated by the inverse Fourier transform of $\widehat{F}(u)$, after applying the inverse filter $M(u)$, named Wiener filter to $G(u)$ as follows [2]:

$$\widehat{F}(u) = G(u) \cdot M(u), \qquad (6)$$

$$M(u) = \frac{1}{H(u)} \frac{|H(u)|^2}{|H(u)|^2 + P_{nn}(u)/P_{ff}(u)}. \qquad (7)$$

3. Experimental Results

Figure 2(a) shows a B-mode image obtained of the object by ultrasonic diagnostic equipment. Figure 2(b) shows the measured surface of the object $g(x)$. Roughness, which could not be found in Fig. 2(a), could be found easily in Fig. 2(b). The step width of $g(x)$ was equivalent to the actual pitch of the surface of the object (500 μm).

Figure 2(c) shows power spectra, $|F(u)|$, $|G(u)|$, $|H(u)|$, and $|\widehat{F}(u)|$, of the point spread function, $h(x)$, and surface profiles, $f(x)$, $g(x)$, and $\widehat{f}(x)$, respectively. In this paper, $H(u)$ is obtained by analyzing the profile of acoustic pressure within the width (500 μm) where the acoustic pressure is larger than 10% of the maximum. Figure 2(d) shows the measured surface profile, $g(x)$, the estimated surface profile, $\widehat{f}(x)$, using the inverse filter, and the actual surface profile $f(x)$. The shape of $\widehat{f}(x)$ was more similar to that of $f(x)$ in comparison with $g(x)$.

4. Conclusion

In this paper, the surface profile of an object with a surface roughness in micrometer order was detected using the phase of the RF signal. By applying an inverse filter as point spread function to the measured surface profile, the estimated surface profile shows higher accuracy than the measured surface profile without the filter.

References

[1] R. Ross: N. Engl. J. Med., **340** (2004) 115.

[2] H. C. Andrews, B. R. Hunt: Digital Image Restoration, (1977) 126.

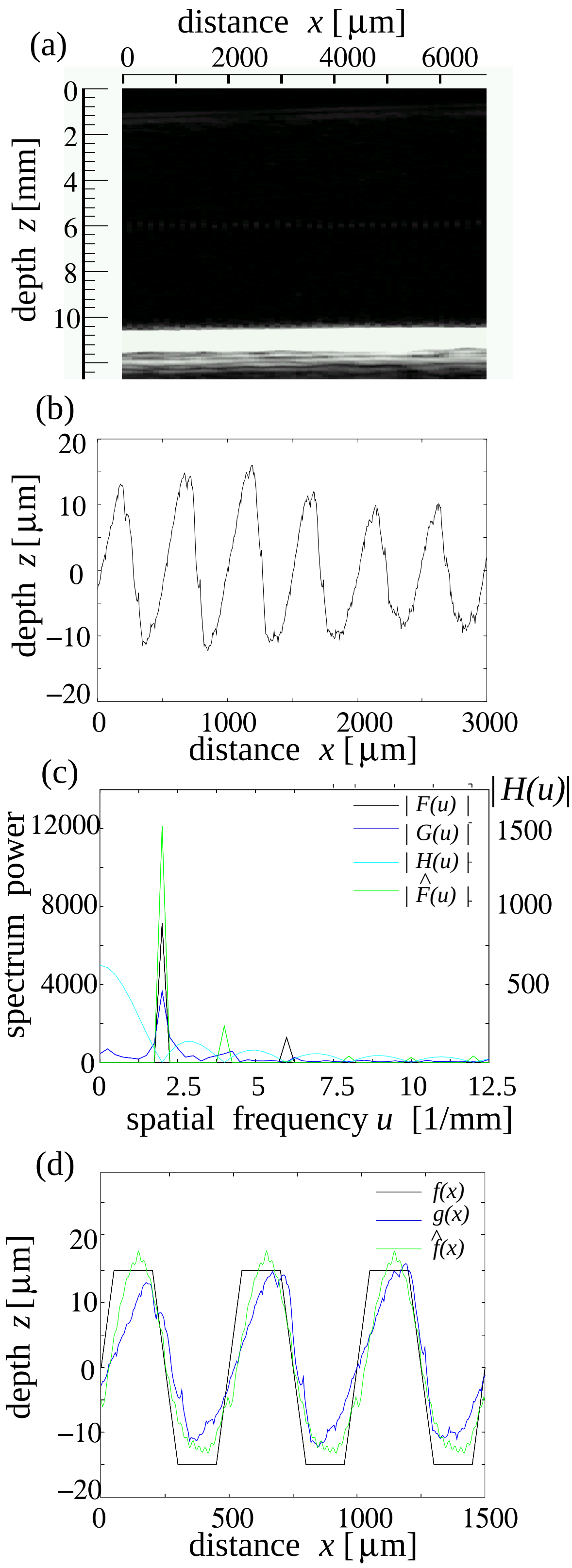

Figure 2: (a) B-mode image. (b) Surface profile, $g(x)$. (c) Spectra of point spread function and surface profiles , $f(x)$, $g(x)$, and $\widehat{f}(x)$. (d) Surface profiles, $f(x)$, $g(x)$, and $\widehat{f}(x)$.

P2-39

Proc. Symp. Ultrason. Electron., Vol. 26, (2005) pp. 289-290
16-18 November, 2005

In Vitro Measurement of Ultrasonic Scattering Dependence on Myocardial Direction

○ Hiroaki Kamada, Hideyuki Hasegawa and Hiroshi Kanai
(Dept. of Electronic Eng., Tohoku University)

1. Introduction

The direction of myocardial fiber of normal human heart wall changes gradually from the epicardium to the endocardium [1]. However, in hypertrophic heart disease, the myocardial direction becomes disarrayed. It is supposed that ultrasonic backscatter from heart wall reflects such a change of myocardial direction. Therefore, basic researches have been conducted for quantitative estimation of myocardial tissue [2]. In order to quantify the correspondence between acoustic properties of a object and ultrasonic backscattering, Knipp *et al.* made use of a reference phantom of known acoustic properties for measuring ultrasonic backscattering with eliminating influences of the measurement system [3].

In this paper, ultrasonic echoes from cloth fibers mimicking myocardium and from a porcine ventricular wall were measured with changing the angle of insonification relative to the fiber direction. From these measurements, ultrasonic scattering dependence on the fiber direction was investigated.

2. Measurement Methods

In this paper, an ultrasonic echo from an object was measured with changing the angle of insonification relative to the fiber direction by rotating the object. As shown in **Fig. 1**, the reflected signal was measured at every 10 degrees by rotating the object.

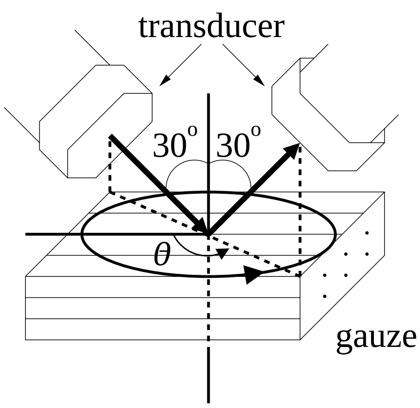

Figure 1: Schematic diagram of the measurement.

The measurement system is shown in **Fig. 2**. Both transducers for transmission and reception are single element concave transducers. Focal distance of the transducers was 30 mm and the transducers were inclined from the vertical direction by 30 degrees. A burst sine wave of seven cycle was applied to transmit transducer. The reflected signal from the object was received by receiving transducer. The digitized data were acquired after averaging the reflected signals 128 times.

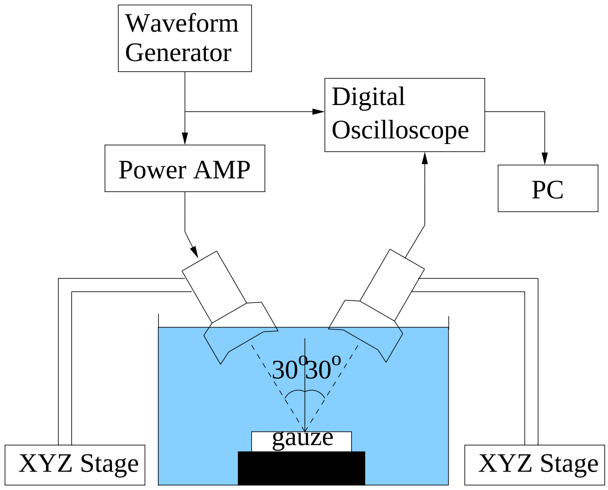

Figure 2: Measurement System.

3. Basic Experiment Using Cloth Fibers

The object made of cloth fibers consists of 16 layers of gauze. Unnecessary fibers were removed from gauzes so that fibers becomes homogeneously lined along one direction. The diameter of a human myocardial fiber is smaller than the wavelength of ultrasound used in ultrasonic diagnostic equipment. Therefore, ultrasonic echoes from a human myocardium becomes scattered waves. To make echoes from the cloth fibers scattered waves as in the case of human myocardium, the diameter of the used fiber was about 150 μm, which is smaller than the wavelength of ultrasound (214 μm) used in this basic experiment. The thickness of the whole gauze is about 9 mm.

At first, the ultrasonic echoes from the gauze were measured with setting the focal position at the surface of the gauze. Secondly, the focal position was set inside the gauze by moving both transducers to depth direction by 4.5 mm. **Figure 3** shows the maximum amplitude of the reflected signal from the surface and the inside of the gauze at each insonification angle relative to fibers. In both cases, the amplitude of the reflected signal changed due to the direction

E-mail: kamada@us.ecei.tohoku.ac.jp

of fibers. In the case of the parallel insonification relative to the direction of fibers (θ = 0 degrees and 180 degrees), the amplitude of the reflected signal became the maximum.

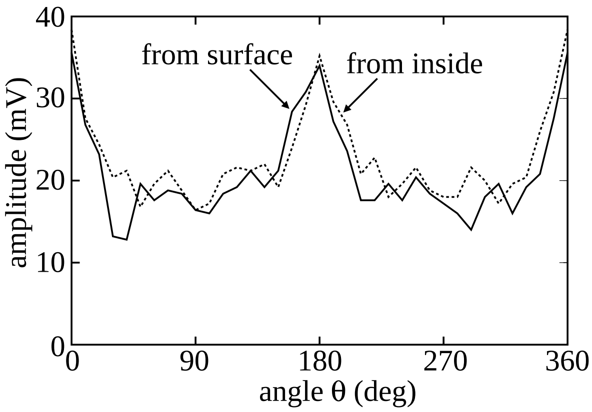

Figure 3: Changes in the maximum amplitude of the reflected signal due to the direction of the fiber. The solid and dotted lines show the maximum amplitudes of the reflected signals from the surface and the inside of the gauze, respectively.

The insonification angle dependence of ultrasonic echo is significant in the case where an object is larger than the wavelength of ultrasound. However, in the case of scattering, the angle dependence is less significant. However, when scatterers which are smaller than wavelength of ultrasound are located at a constant pitch, ultrasonic echo changes due to the angle of insonification relative to the fiber direction. Though the gauze used in this measurement was composed of fibers which are smaller than the wavelength of ultrasound, the fibers were located at a constant pitch and were lined only along one direction. Therefore, the reflected signals from the gauze showed the change due to the direction of the fiber.

4. *In Vitro* Experiment Using Excised Porcine Heart

The ultrasonic echoes from an excised porcine heart wall were measured. In the porcine heart wall, the direction of myocardium changes gradually from the epicardium to the endocardium as well as the human heart wall [1]. Therefore, the angle dependence of the echo reflected from the porcine heart wall was investigated. After slaughter, the porcine heart was measured within a half day. A part of the left ventricular wall was excised from the porcine heart and was put the epicardium side up in the water tank which was filled with the normal saline solution. The focal position was set at the surface of the specimen (epicardium), the reflected signal was measured at every 10 degrees by rotating the specimen as well as in the case of the gauze. **Figure 4** shows the maximum amplitude of the reflected signal from the specimen. The reflected signal seemed to change randomly with respect to the insonification angle. However, in the case of θ = 20 degrees and 350 degrees, the reflected signal was significantly large in comparison with those at other insonification angles. It is supposed that the directions of myocardial fibers were homogeneously lined along one direction at each depth because the porcine heart measured in this experiment was excised from the normal pig (considered not to have any heart disease). Therefore, the reflected signal from the porcine heart wall showed the angular dependence as well as the basic experiments using cloth fibers.

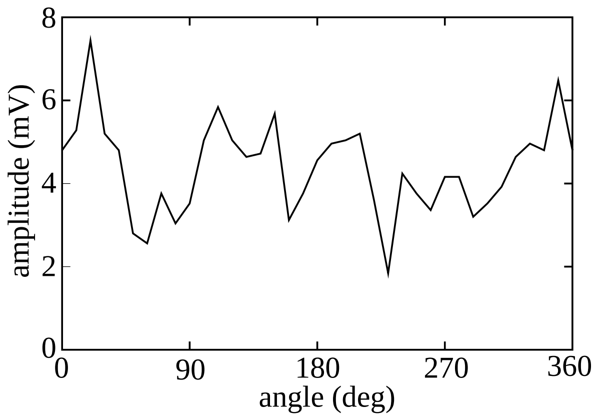

Figure 4: Change in the maximum amplitude of the reflected signal from the porcine ventricular wall.

5. Conclusion

In this study, in basic experiments using cloth fibers, it showed that the amplitude of the reflected signal changed due to the angle of insonification relative to the fiber direction. As well as the basic experiments, in the case of the porcine heart wall, the reflected signal showed the angle dependence. Since the direction of myocardial fibers becomes disarrayed in patients with hypertrophic heart disease, it is possible to estimate the condition of myocardial fibers using the feature of the change in ultrasonic scattering due to the directions of fibers.

References

[1] F. Rushmer: WB Saunders (1976) 76.

[2] L. Baldwin, R. Marutyan, M. Yang, D. Wallace, R. Holland, and G. Miller: Ultrasound in Med. & Biol. **31** (2005) 477.

[3] S. Knipp, A. Zagzebski, A. Wilson, F. Dong and L. Madsen: Ultrason Imaging **19** (1997) 221.

P2-40

Proc. Symp. Ultrason. Electron., Vol. 26, (2005) pp. 291-292
16-18 November, 2005

Measurement of Spatial Distribution of Strain Generated by Dual Acoustic Radiation Forces

○ Mikito Takahashi, Hideyuki Hasegawa, and Hiroshi Kanai
(Dept. of Electronic Eng., Tohoku University)

1. Introduction

In recent years, some remote actuation methods based on acoustic radiation forces have been reported. Fatemi and Greenleaf proposed an imaging modality that uses the acoustic response of the object to a localized dynamic radiation force [1].

In this paper, the spatial distribution of strain generated by dual acoustic radiation forces was measured by the ultrasonic phased tracking method [2].

2. Principle

When the ultrasound propagates in the medium, a constant force is generated in the direction of propagation. This force is called as the acoustic radiation force. The acoustic radiation pressure is defined as the acoustic radiation force per unit area.

When two ultrasonic beams of the amplitude of sound pressure, p_0, at slightly different frequencies, f and $f + \Delta f$, are crossed each other [1, 3, 4], an acoustic radiation pressure which fluctuates at the frequency difference, Δf, is generated. The sound pressure, p_{sum}, on the surface of the object is expressed as follows:

$$p_{sum}=p_0 \cos(2\pi f t + \theta) + p_0 \cos 2\pi (f + \Delta f)t, \quad (1)$$

where f and θ are the frequency of the transmitted pulse and the phase difference between sinusoidal waves at f and $f+\Delta f$, respectively. The energy density, $e(t)$, is expressed as follows:

$$\begin{aligned} e(t) &= \frac{1}{\rho_1 c_1^2}\{p_{sum}(t)\}^2 \\ &= \frac{1}{\rho_1 c_1^2}\{p_0 \cos(2\pi f t + \theta) \\ &\quad + p_0 \cos 2\pi(f + \Delta f)t\}^2 \\ &= \frac{p_0^2}{\rho_1 c_1^2}[1 + \cos(2\pi \Delta f t - \theta) \\ &\quad + \cos 2\pi\{(2f + \Delta f)t + \theta\} \\ &\quad + \frac{1}{2}\cos 2(2\pi f t + \theta) \\ &\quad + \frac{1}{2}\cos 4\pi(f + \Delta f)t], \end{aligned} \quad (2)$$

where ρ_1 and c_1 are the density and sound speed of the medium, respectively. From the second term of the right-hand side of eq. (2), it is found that the energy density, $e(t)$, has a component at the frequency difference Δf. With respect to the low-frequency component, the acoustic radiation pressure, $P_R(t)$, acting on the interface is given by

$$P_R(t) = (1 + R^2)\frac{p_0^2}{\rho_1 c_1^2}[1 + \cos(2\pi \Delta f t - \theta)], \quad (3)$$

where R is the pressure reflection coefficient on the surface of the object. When multiple acoustic radiation pressures, $P_R(t)$, are employed, the phase of an radiation pressure relative to the other radiation pressures can be controlled by changing θ in eq. (3).

3. Experiments

The measurement system is illustrated in **Fig. 1** [4]. Insonification angles, ϕ_1 and ϕ_2, of two ultrasound beams for actuation were set at 25 and 155 degrees, respectively. The object made of gel (45 mm×45 mm×17 mm, containing carbon powder to obtain a reflection from the inside of gel) was used.

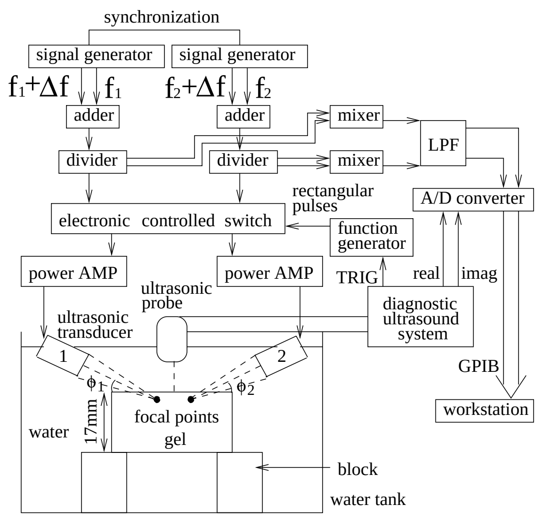

Figure 1: Measurement system.

The spatial distribution of strain generated by phase-controlled dual acoustic radiation forces ($\theta = 0$) is illustrated in **Fig. 2**. Two ultrasonic transducers for actuation (center frequency: 1 MHz, focal point: 52 mm from the surface of the transducer) were driven by a sum of two continuous waves at two slightly different frequencies of 1 MHz and 1 M+Δf Hz. Phase-controlled dual acoustic radiation forces ($\theta = 0$) were applied by setting the focal points at two different positions in the object. These two applied radiation forces cyclically compress the region between two focal points at the frequency difference, Δf, in the horizontal direction. Therefore, this region is cyclically thickened in the vertical direction.

The displacement distribution is also measured with ultrasound combined with the phased tracking method [2].

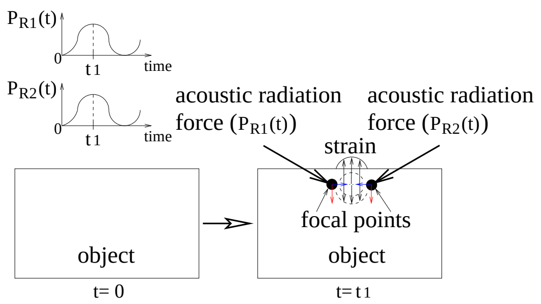

Figure 2: Generation of strain.

Positions where displacements were measured are illustrated in **Fig. 3**. The ultrasonic probe for measurement was moved with a pitch of 0.3 mm in the direction of the x axis and the displacement distribution was measured at nine positions (a, b, c, $\cdots$, i). A position e is the center between two focal points. The frequency difference, Δf, was set at 10 Hz.

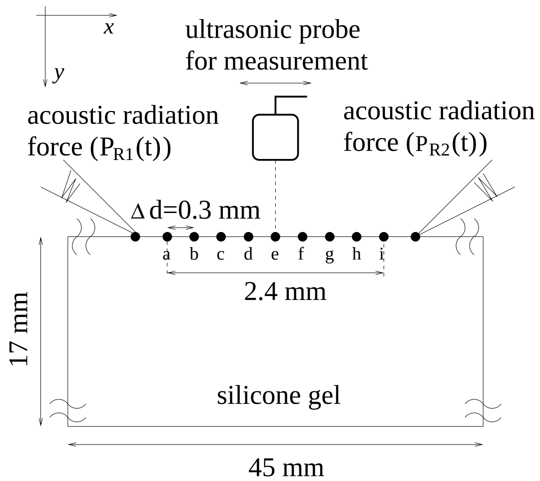

Figure 3: Illustration of positions where displacements were measured.

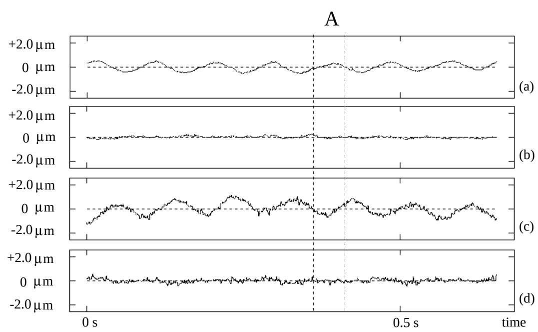

Figure 4: Measured displacements at depths of 0 mm (a), 2.7 mm (b), 4.0 mm (c), and 4.7 mm (d).

Figure 4 shows the measured displacement at each depth at position e. From the results shown in Fig. 4, it is found that when radiation pressure increases (period A in Fig. 4), points at depths of 0 mm and 4.0 mm move upward and downward, respectively. This phenomenon shows that the thickness along the ultrasonic beam at position e increases by application of radiation pressures.

Figure 5 shows the spatial distribution of the maximum displacements. Lengths and directions up-arrows and down-arrows show the magnitudes and directions of the measured displacements.

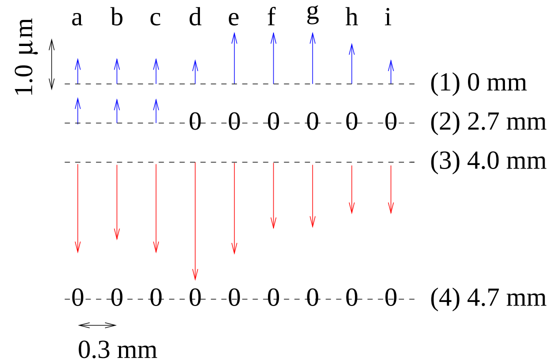

Figure 5: Spatial distribution of the maximum displacements.

As well as Fig. 4, the displacement distribution shows the thickness in the region between two focal points increases by radiation forces. In Fig. 5, it is found that displacements measured at a depth of 4.0 mm was larger than those measured at 0 mm. Ultrasonic beams for actuation were insonified along the oblique directions, and the applied radiation forces have components acting downward.

These results show that the change in thickness (strain) inside the object was successfully generated using phase-controlled dual acoustic radiation forces ($\theta = 0$).

4. Conclusion

In this paper, it was confirmed that the strain could be generated by applying phase-controlled dual acoustic radiation forces. Furthermore, it was shown that the generated strain was measurable by the ultrasonic phased tracking method.

References

[1] M. Fatemi and J. F. Greenleaf: IEEE Trans. on Med. Imag. **21** (2002) 1.

[2] H. Kanai, M. Sato, Y. Koiwa, N. Chubachi: IEEE Trans. on Ultrason. Ferroelectr. Freq. Control. **43** (1996) 791.

[3] K. Michishita, H. Hasegawa and H. Kanai: Jpn. J. Appl. Phys. **42** (2003) 4608.

[4] Y. Nishio, N. Hashimoto, H. Hasegawa and H. Kanai: IEEE Intnl. Ultrasonic Symp. (2004) 1773.

P2-41

Proc. Symp. Ultrason. Electron., Vol. 26, (2005) pp. 293-294
16-18 November, 2005

Tissue Classification of Arterial Wall Based on Correlation Between Regional Elasticity Distributions and Elasticity Histograms of Tissues

○Jun Inagaki, Hideyuki Hasegawa, Hiroshi Kanai (Dept of Electronic Eng., Tohoku University)
Masataka Ichiki (Sendai Hospital of East Railway Company)
Fumiaki Tezuka (Sendai Medical Center)

1. Introduction

Cerebral infarction and myocardial infarction are mainly caused as terminal symptoms of atherosclerosis by occlusion of the artery due to blood clots which are generated by the rupture of atherosclerotic plaque [1]. Direct characterization of the composition and vulnerability of atherosclerotic plaque may offer insight into the mechanism of plaque regression and progression [2, 3]. The change in elasticity is caused greatly by the change in composition of the arterial wall due to development of atherosclerosis [5]. Therefore, the measurement of elasticity has potential for tissue characterization of plaque.

The elasticity histograms of respective tissues (lipid, blood clot, fibrous tissue, and calcified tissue) in artery were constructed to classify arterial tissue based on elasticity [6]. In this paper, tissue classification based on correlation between the elasticity distribution of each small region in an elasticity image and elasticity histograms of respective tissues is investigated to improve tissue classification based on elasticity.

2. Method

2.1 Construction of Elasticity Histograms of Respective Tissues

In the experimental setup for *in vitro* experiments using excised femoral arteries of patients with arteriosclerosis obliterans, the change in internal pressure was generated using an artificial heart, and the internal pressure was measured by a pressure detector placed in lumen of the artery. The artery fixed in the water tank was measured in the long-axis plane with a linear-type probe (center frequency: 7.5 MHz). From the measured change in thickness and pressure, the elasticity of arterial wall was estimated at intervals of 75 μm in depth direction and 300 μm in axial direction.

After ultrasonic elasticity measurement, the pathological images were made to identify tissue component of the arterial wall in the scanned plane. The plane scanned by ultrasound was identified by imaging a needle fixed on the external surface of the posterior wall. By referring the pathological images, the regions which corresponding to one of the respective tissues (lipid, blood clot, fibrous tissue and calcified tissue) were assigned on the elasticity images. From the regions assigned for respective tissues, the elasticity histograms were obtained. Figure 1(c) shows the respective elasticity histograms of tissues.

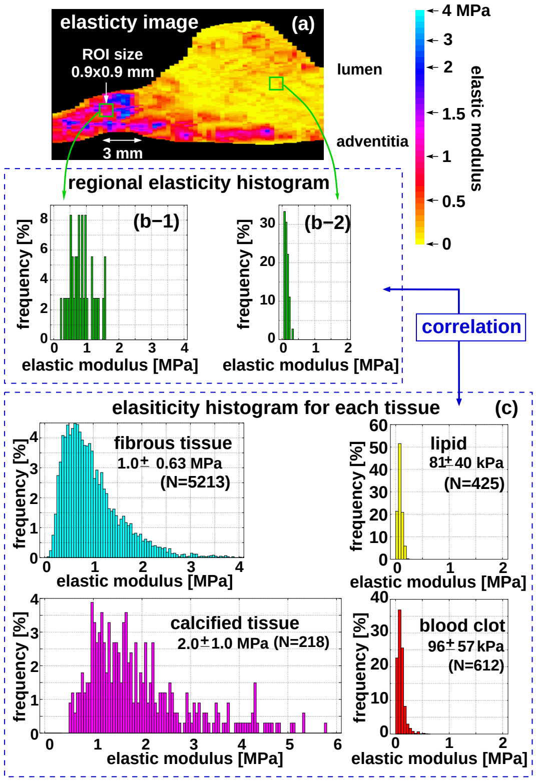

Figure 1: (a) Elasticity image of arterial wall. (b) Regional elasticity distributions in elasticity image. (c) Elasticity histograms of lipid, blood clot, fibrous tissue, and calcified tissue.

2.2 Tissue Classification Based on Correlation Between Elasticity Histograms

The region of interest (ROI) was assigned on the elasticity image (regions surrounded by green rectangles in Fig. 1(a)) which was obtained by ultrasonic measurement, and the elasticity distributions within the ROI were obtained (Fig. 1(b)). The size of ROI was 900 μm in the depth direction and 900 μm in the arterial axial direction. Therefore, 36 elasticity values were included in each ROI. Although the number of elasticity values within a ROI whose center located at the edge of the elasticity image becomes less than 36, the elasticity distribution within each ROI was also obtained.

The ROI was scanned in the entire elasticity image at the intervals of 75 μm in the depth direction and

inagaki@us.ecei.tohoku.ac.jp

300 μm in the axial direction, and the correlation coefficients between the regional elasticity distribution at each position and elasticity histograms of respective tissues were calculated. The correlation images were obtained by color coding corresponding to the correlation coefficient of each ROI.

3. Results

Table 1 shows the correlation coefficients (r_l: lipid, r_b: blood clot, r_f: fibrous tissue, r_c: calcified tissue) between regional elasticity distributions (Figs. 1(b-1) and 1(b-2)) and elasticity histogram of each tissue. Regional elasticity distributions of Figs. 1(b-1) and 1(b-2) showed the highest correlation with fibrous tissue and blood clot, respectively.

Figures 2(a) and 2(b) show the elasticity image and the corresponding pathological image, respectively. Lipid, blood clot, and fibrous tissue were identified by referring to the pathological image. Figure 2(c) shows the correlation image for each tissue. The color bar indicates the correlation coefficient for each tissue.

In Figs. 2(c-1), 2(c-2) and 2(c-3), the region of lipid, blood clot and fibrous tissue was superimposed on the correlation images by yellow, red, and green broken line, respectively. As shown in Figs. 2(c-1), 2(c-2), and 2(c-3), elasticity histograms for lipid, blood clot, and fibrous tissue give high correlation coefficient in the regions which were identified to be respective tissues. Althogh it is difficult to classify a region to be lipid or blood clot, it is possible to differentiate lipid and blood clot from fibrous tissue and calcified tissue as shown in Fig. 2(c).

4. Conclusion

In this paper, the tissue classification based on the correlation between the measured elasticity distribution and the pre-determined elasticity distribution of each tissue components was investigated. Fibrous tissue was found to be differentiated from lipids or blood clots. However, differentiation of lipids and blood clots seemed to be still difficult.

References

[1] P. R. Moreno, E. Falk, I. F. Palacios, et al: Circulation **90** (1994) 775.

[2] H. M. Loree, R. D. Kamm, R. G. Stringfellow, et al: Circ. Res. **71** (1992) 850.

[3] E. Falk, K. Prediman, P. K. Shah, at al: Circulation **92** (1995) 657.

[4] R. T. Lee, A. J. Grodzinsky, E. H. Frank, et al: Circulation **83** (1991) 1764.

[5] J. Inagaki, H. Hasegawa, H. Kanai, et al: Jpn. J. Appl. Phys. **44** (2005) 4593.

[6] H. Kanai, H. Hasegawa, M. Ichiki, et al: Circulation **107** (2003) 3018.

Table 1: Correlation between regional elasticity distribution and elasticity histogram of each tissue.

	r_l	r_b	r_f	r_c
b-1	-0.07	-0.06	0.80	0.35
b-2	0.80	0.84	-0.04	-0.15

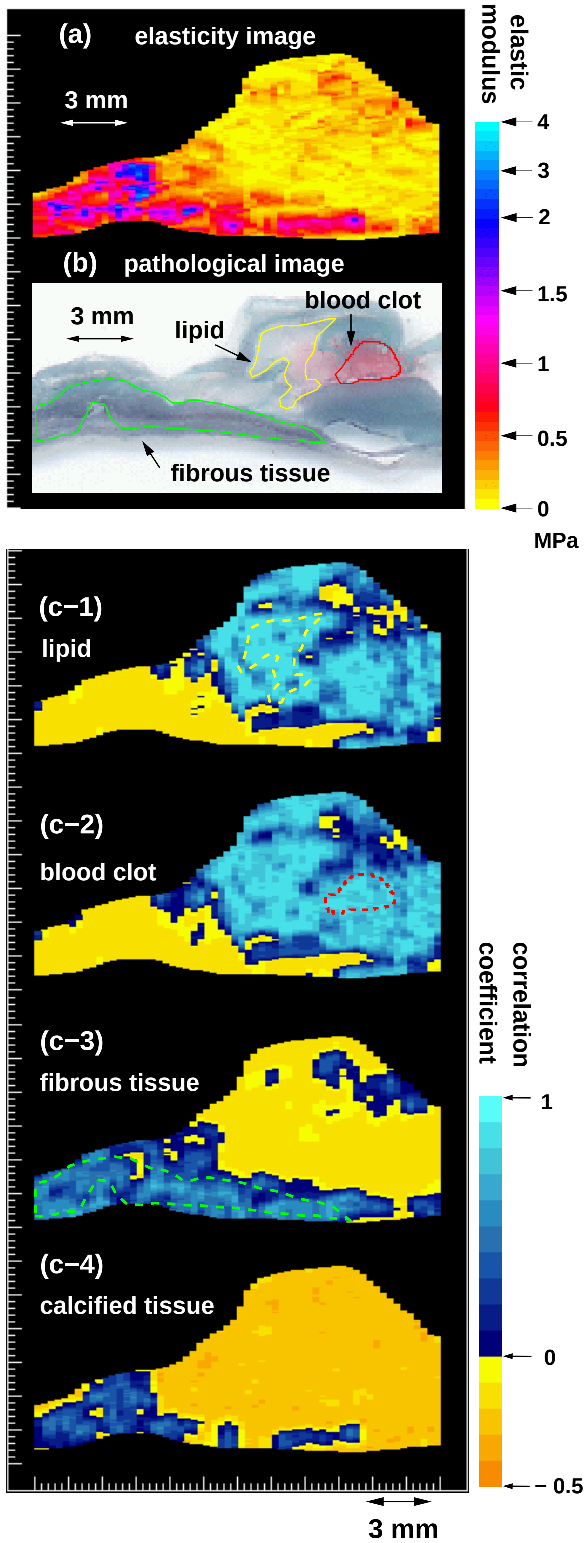

Figure 2: (a) Elasticity image of arterial wall. (b) Pathological image of corresponding section. (c) Correlation between regional elasticity distribution and elasticity histogram of each tissue.

P2-42

Proc. Symp. Ultrason. Electron., Vol. 26, (2005) pp. 295-296
16-18 November, 2005

Measurement of the amount of embolic using transesophageal echocardiography

◎Tadashi YAMAGUCHI, Kazuki HIRAI, Masami AOKI, Jin MIYAGI, Masahiko SUZUKI, Hideshige MORIYA and Hiroyuki HACHIYA (Chiba Univ.)

1. INTRODUCTION

Deep venous Thrombosisi (DVT) and Pulmonary Thromboembolism (PTE) are serious complications after Total Knee Replacement (TKR). The tight tourniquet usually used in TKR placed around the patient's leg caused blood stasis and encourage the formation of a thrombus. This thrombus may travel through the blood stream, embolizes the pulmonary arte and causes DVT. Therefore, understanding of the flowing thrombus volume is important to curing and prevention DVT.

In this study, we propose the measurement method of the amount of embolus that are carried from the leg to lung by the bloodstream.

2. DATA ACQUISITION

We acquired transeophageal echocardiography (TEE) data of right atrium of heart by ultrasonic diagnosis equipment (Hewlett Packard SONOS5500) in the period throughout the operation end out of TKR. The center frequency of ultrasound is 4 MHz. TEE datasets are saved as S-VHS movies (frame rate is 30fps). Each movie are converted to the sequence of TIFF images for data analysis and image processing.

3. EXTRACTION OF EMBOLUS

We tried to extract embolus information from TEE image by Fiber Structure Extraction Technique (FSET)[1]. In heart chamber that contains no embolus, the background echoes from each randomly distributed scatter interfere mutually, and it is well known that the probability density function (PDF) of echo envelope amplitude can be mostly approximated by the Rayleigh distribution. On the other hand, the echo envelope amplitude from embolus is larger than that from surrounding area. Hence, the PDF will not obey with Rayleigh distribution. By constraining the Rayleigh elements and accent non-Rayleigh elements, we can extract the embolus information from TEE images.

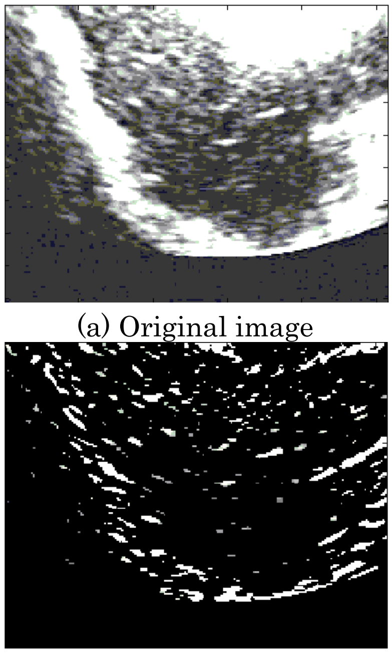

(a) Original image

(b) Image of afer FSET. Non Rayleigh elements are extracted as high echo.

Fig.1 Result of FSET for TEE image

Figure1(b) is the result of extracting the embolus information from Fig.1(a) by FSET. The punctuate structures seems like embolus are extracted in the right atrium of heart. FSET leverages the statistical property of echo signals, so it can extract elements that can't be extracted by simply threshold processing.

4. VOLMETRIC RATIO OF THE EMBOLUS

Figure 2 shows the time change of extracted images. The time tourniquet became loose after KTC operation is 0 second in Fig.2. It is shown amounts of embolus are different in each result. Then, we appropriated about time rate of change of the embolus. To measure the amount of the embolus, it is necessary to extract the endocardium from TEE images. We used Brain Extract Tool (BET) method[2][3] , it is one of the active contour model to endocardium extraction. Fig.3 shows the result of endocardium extraction by BET method. The endocardium of right atrium of heart were extracted clearly regardless of the existence of embolus.

(a) 20 second

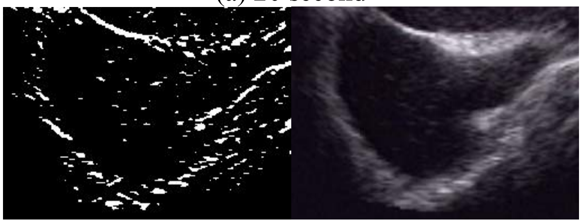

(b) 60 second

Fig.2 Time change of the result of FSET.

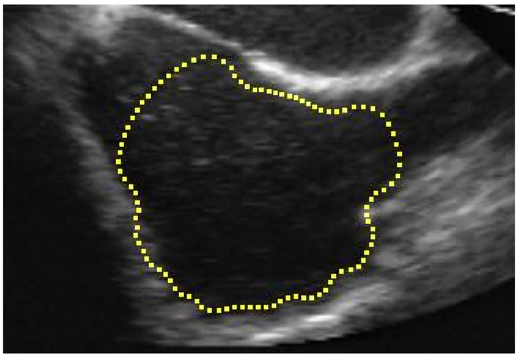

(a) Case A: there are no embolus in heart chamber.

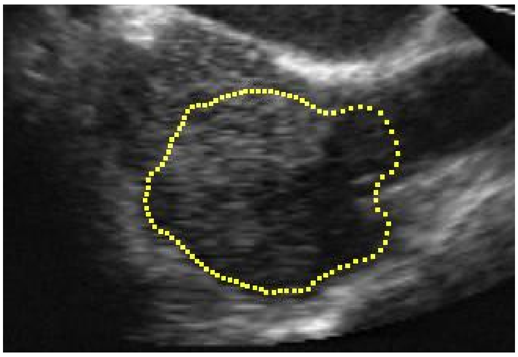

(b) Case B: many embolus are shown in heart chamber.

Fig.3 Result of endocardium extraction

Fig.4 is the time series graph of volumetric ratio of the embolus. In fig. 4(a), the rate of embolus starts increase after about 10 seconds from blood-flow resumption. As for after 20 seconds, there are most embolus, and it decreases gradually after that. In addition, the rate of embolus is changing finely at intervals of short time through the whole observation period. This minute change synchronizes with the heart beat.

5. CONCLUSION

We proposed the method to measuring the amount of embolus, and demonstrated that our method can detect the variation of embolus flow in the right atrium of heart.

The processing speed of each operation is important to achieve the real-time measurement of embolus flow. In the actual condition, FSET operates approximately in real time, but BET method doesn't. So, we examine about extraction method of an endocardium by two kinds of the processing methods of BET method and the move distance pursuing method in the next step.

REFERENCES

1. T. Yamaguchi et. al.: JJAP, Vol.44, No.6B (2005) 4615.
2. S. M. Smith: Human Brain Mapping 17 (2002) 143
3. T. Yamaguchi et. al.: IEICE Rep. US2004-103 (2005) 7

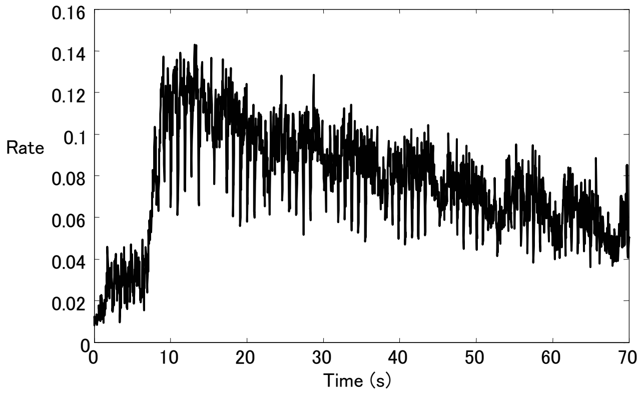

(a) long period case (100s)

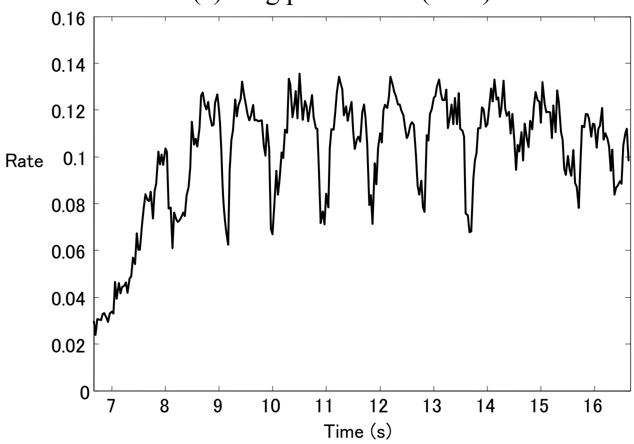

(b) short period case (10s)

Fig.4 Measurement result of rate of the embolus in the right atrium of heart

P2-43

Proc. Symp. Ultrason. Electron., Vol. 26, (2005) pp. 297-298
16-18 November, 2005

Dynamic and Precise Visualization of Contrast Agent in Blood Vessels with Motion Correction

Hideki Yoshikawa, Takashi Azuma, Kazuaki Sasaki, Ken-ichi Kawabata and Shin-ichiro Umemura

Central Research Laboratory, Hitachi, Ltd. Tokyo, Japan

1. INTRODUCTION

Vascularity gives very important information on properties of tumors such as borders or stages. Especially for detecting borders between normal and tumor tissues, not only large vessels but also minute ones are to be visualized because large portions of vessels into tumors are minute at the end. One can obtain precise information on tumor tissues with detailed tumor vasucularity which may lead to accurate diagnoses. Also, such information would be useful in monitoring the effect of tumor therapy.

As a relatively low invasive method to visualize tumor vascularity, ultrasound echography is commonly uses with contrast agents made of stabilized microbubbles. Conventional ultrasonic imaging, however, cannot clearly visualize minute vessels mentioned above, because too small numbers of contrast media can pass the vessels at a time.

Moriyasu et. al, reported on a method to visualize minute vessels by averaging multiple frames[1]. Although each contrast agent in the minute vessels is imaged as an individual dot signal in the conventional contrast image, their method makes virtual flow lines of contrast agents by overlapping the dots signals. Using this method, the minute vessels can be imaged as a line structure (upper images in Fig. 1).

Such approach enables an operator to clearly identify the minute vessels and observing dynamic inflow to the vessels of the contrast agents. However, this approach cannot simply be applied to objects with large motion, which may lead to the motion artifacts. In the lower image of Fig. 1, the motion artifact is demonstrated. If the minute vessels in each frame are moved by the tissue motion, the signals from the agent cannot be accurately connected to form a line structure. This motion artifact may lead to misdiagnosis and potential prescription of inappropriate treatment. To average signals in a specific region, both measurement and correction methods of the tissue motion, which are caused by normal physiological nature, such as the breathing or the cardiac motion, are needed.

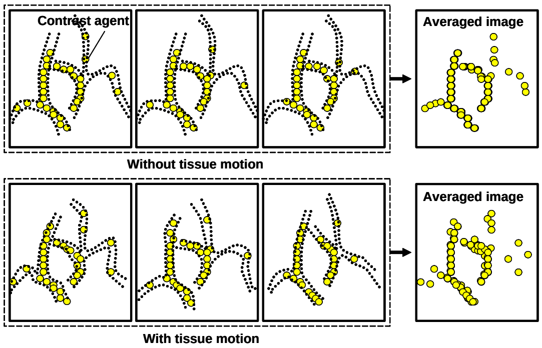

Fig. 1 Influence of the tissue motion for averaging frames.

We propose a method to produce a clear image of the vascularity of both large and minute vessels by using the time-averaging method with multiple frames which can be applied to the moving objects.

The purpose of this study is 1) to investigate the feasibility of our tissue-motion measurement and correction method[2], and 2) to apply the correction method to the time-averaging technique in *in vivo* situation including visualizing the vascularity of the minute vessels using the time-averaging method with multiple contrast images.

2. METHODS

We performed *in vivo* experiments with rabbit kidney filled with the contrast agent Definity®. Contrast image frames were obtained from an ultrasonic scanner EUB-8500 (Hitachi Medical Corp.,

---

hi-yoshi@crl.hitachi.co.jp

Chiba, Japan) and linear array probes which were fixed by hand. The Base-frame was set from the obtained frames, and other frames were then added to the Base-frame by using motion correction. Then, subregions were set on the Base-frame to measure tissue motions[2]. The subregion size was 3×3 mm laterally and longitudinally, which was larger than speckle size in this experimental condition. Tissue motion was measured between each subregion on the Base-frame and obtained other frames using the least square method. The region that best matches the set subregion was extracted and then added to the Base-frame. This extraction and addition of matching region was performed in all subregions and in all obtained frames.

3. RESULTS AND DISCUSSION

Figure 2 shows the time-averaging results of a rabbit kidney using contrast images with motion correction. Figure 2 (a) is the averaged image obtained using 100 frames, and Fig. 2 (b) is a typical conventional contrast image used to obtain Fig. 2 (a).

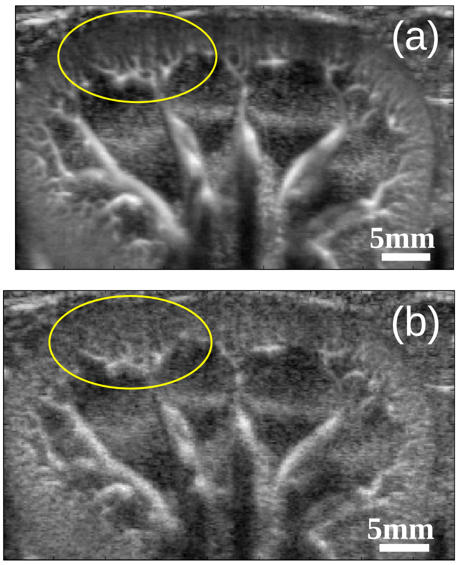

Fig. 2 Comparison between time-averaged image with motion correction (a) and single frame (b) of the contrast mode.

When comparing both images, minute vascularity was visualized more clearly in Fig. 2 (a) than in Fig. 2 (b). Especially, the peripheral vessels in the renal cortex were imaged as a precise line structure in Fig. 2 (a), which cannot be seen in Fig. 2 (b).

Figure 3 (a) is the time-averaged image obtained with motion correction of mesenterium vessels using 150 frames and Fig. 3 (b) is the time-averaged image obtained without motion correction. The vascularity in Fig. 3 (a) can be imaged more precise and clearer than in Fig. 3 (b). We also found that the tissue-motion measurement and correction method were performed accurately by comparing both images in Fig. 3.

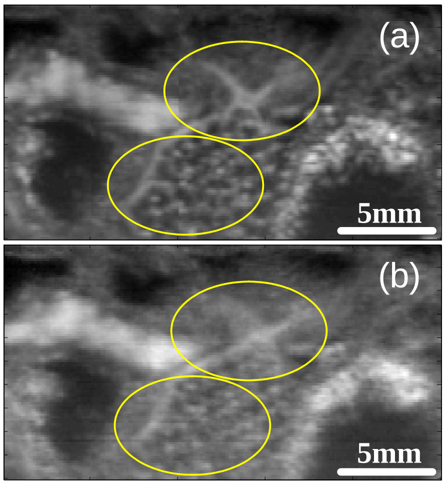

Fig. 3 Comparison of time-averaged images obtained with (a) and without (b) tissue motion correction.

The results of the precise imaging of the minute vascularity shown in Fig. 2 (a) and in Fig. 3 (a) were caused by the slight tissue motion in the slice direction. Tissue normally moves three-dimensionally and an ultrasound beam scanning an object has a slice direction range so that signals from various angles in the slice direction are included in obtained multiple frames. Therefore, dynamic signals that were less than the slice range, like speckle signals, were reduced and static signals, like vessels, were clearly imaged as a continuous line protectively and the high contrast imaging of vascularity could be performed.

REFERENCES

[1] F. Moriyasu et. al, Jpn. J. Med. Ultrason. **31** (2004) 241.

[2] H. Yoshikawa et. al, J. Appl. Phys. **44** (2005) 4561.

P2-44

Proc. Symp. Ultrason. Electron., Vol. 26, (2005) pp. 299-300
16-18 November, 2005

Behavior of Marine Animals Using Underwater Acoustic Camera

○Kohji IIDA[1)], Yong Tang[1)], Tohru MUKAI[1)], Rika Takahashi[1)], and Masanori SATO[2)]
1)Graduate School of Fisheries Sciences, Hokkaido University, 2)Honda Electronics Company, Ltd.

1. INTRODUCTION

A high resolution underwater acoustic camera enclosed in a pressure-resistant case was developed to observe underwater animals. It enables to measure size, shape, and movement of living marine animals. Acoustic camera is originally used for medical diagnosis. A convex type transducer array is driven by 3.5 MHz ultrasonic signals and the echo from an object is displayed as an acoustic tomogram. It covers a range up to 240cm in waters. The acoustical B mode image and an optical image by an underwater camera were transferred through underwater cable.

Special features of the underwater acoustic camera are, 1) To observe marine animals in dark or opaque water, 2) To observe the tissue and shape of internal organ, 3) To observe the shape and movement of marine animals in natural conditions.

The underwater acoustic camera was set on a sea bottom to observe behavior of marine animals. Several species of marine animals including zooplankton were observed during the periods.

2. METHODS

Underwater acoustic camera: To observe marine organisms in natural condition, an underwater acoustic animal observation system was developed. The system consists of acoustic camera and underwater optical camera in the pressure-resistant case as shown in Fig. 1.

Fig.1. Underwater acoustic camera.

An acoustic camera uses convex type ultrasonic probes which works at 3.5 MHz and forms fan shaped acoustical beam using 192 elemental beams with the coverage angle of 60 degrees and the range of 240 cm. Acoustical image has a dynamic range of 95dB, is displayed on a CRT monitor as a 256 levels monochrome image, and is outputted the video signal as NTSC format. An optical camera consists of a CCD color video camera and an infrared LED projector in a cylindrical waterproof case. An optical camera was set beside the acoustic camera directed to the forward.

Both acoustic and optical camera were enclosed in a cylindrical pressure-resist case (100m in maximum) which was made of aluminum alloy with 480mm of diameter and 450mm of length. It was placed on the 1m height of aluminum frame stand and set at the sea bottom. The length of 300m underwater cables was used to supply electric power to the underwater system and to transmit the video signals to facilities on shore.

Table 1. Specification of underwater observation system.

Component	Item	Specification
Acoustic Camera	Frequency	3.5MHz / 5.0MHz
	Resolution	Direction 2mm / Distance 3mm
	Range	0.24～1m
	Probe type	Linear / Convex
	Display mode	B-mode, M-mode
	Video format	NTSC
	Power supply	AC100V
Optical Camera	Camera type	CCD camera
	Video format	NTSC
	Lighting	Infrared LED Projector
	Power supply	DC12V
Casing	Size	500W×450D×1260H (480ϕ)
	Cable	300mCoaxial cable
	Pressure-resistant	Depth 50m
Monitor	Display	CRT Display
	Video recorder	DV, VHS, Computer

Observation of marine animals in natural condition at sea: Field experiments were conducted in July 2004 and June 2005 at the east coast of Oshima Peninsula, northern Japan where is Usujiri Fisheries Experiment Station, Hokkaido University. An acoustical/optical underwater animal observation system was installed on the sea bottom at the depth of 12m. Both acoustical and optical images of marine organisms were continuously recorded to VCR for 5 days in natural condition. And the tapes were replayed simultaneously to compare two images for analyzing species, size, and swimming behavior of animals.

3. RESULTS

Several marine organisms in the video tapes were recorded. Generally, marine animals appeared more in nighttime than in

daytime. In the daytime fish were appeared in optical camera and some of them were also displayed in acoustic camera as shown in Fig.2. In the night time many animals including zooplankton were observed in acoustic camera. However, the optical camera with an infrared light projector was restricted short range. However a large number of marine organisms including zooplanktons were recorded by acoustic camera.
Main animals which appeared in daytime were sand lance, sea smelt, jelly fish, Arabesque greenling, etc. Especially a couple of sand lance was showed spawning behavior and looked like holding territory to other male individuals.

Many different kinds of animals were observed in nighttime by both acoustical and optical cameras. Swarms of small organisms such as zooplankton were intermittently appeared. Fish, zooplankton, and unknown animals with long tail were also observed. Since an infrared light was attenuated dramatically in water, it was difficult to confirm that the animals of optical images were the same as those in acoustical camera. Only few fish who were passed through in short distance from the camera was identified.

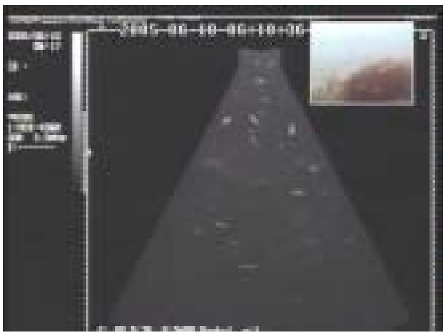

Fig.2. Fishes appeared in an acoustic camera.

Figure 3 shows a diurnal variation of organisms appeared in acoustical image. Appearances of zooplankton were concentrated between sunset and sunrise. The other fishlike images were increased after sunset and before sunrise during the field experiment.

Even though it was difficult to measure the sizes of animals by optical images due to distortion, acoustical images could provide correct shape and size of the animals in a display. Swimming speeds of animals were also measured. Internal structures including a vertebra and a swimbladder of swimming fish were recorded as shown in Fig. 4. This animal was thought to be a bladdered fish having a large gill and the body length was estimated to 18 cm.

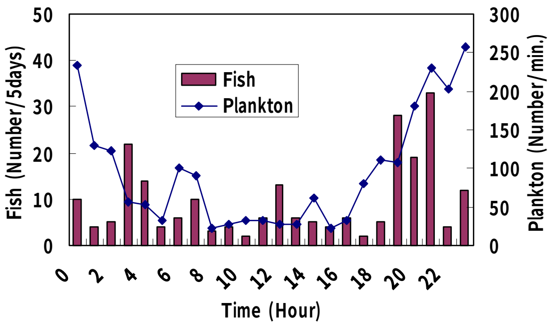

Fig.3. Variation of marine animals in acoustic camera.

4. DISCUSSION

Another merit of an acoustic camera is to observe marine organisms under dark and muddy waters. Especially as an acoustic camera provides B-mode image which can be measured certain distance from camera to the object, the size and the shape of animals can be measured, whereas an optical camera only provides an apparent shape depending on the distance to an object. Shapes, sizes and swimming speeds of fish and zooplankton were observed by acoustical image in the field experiment. These functions are applicable to monitor behaviors of marine animals in the underwater facilities.

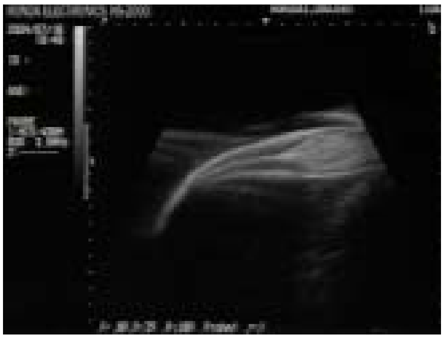

Fig. 4. Unknown animals passed through in short range.

Acknowledgments

This research was supported by the Ministry of Education, Science, Sports and Culture, Grant-in-Aid for Exploratory Research, 15658057, 2003-2005.

REFERENCES

1. Kohji Iida, Tohru Mukai, Donhyug Kang, Masanori Sato, “Morphological Observation of Marine Organism by Underwater Ultrasonography”, Proceeding of OCEANS‘04, 357-36 (2004)

2. P. N. T. Wells, "State-of-art of ultrasound imaging in medicine and biology", Acoustical Imaging, Vol. 22, 137-144(1995)

3. R. K. Hansen and P. A. Andersen, "A 3D underwater acoustic camera - Properties and applications," Acoustical Imaging, 22, 607-611(1995)

Proc. Symp. Ultrason. Electron., Vol. 26, (2005) pp. 301-302
16-18 November, 2005

講演取消

講演取消

P2-46

Proc. Symp. Ultrason. Electron., Vol. 26, (2005) pp. 303-304
16-18 November, 2005

Adaptive Equalization for Underwater Acoustic Communication in Multipath Channel

◎ Chun-Dan Lin*, Seongwook Lee**, Jong Rak Yoon*, (*: Dept. of telecommunication engineering, Pukyong National Univ., Korea **: Institute of acoustic and vibration engineering, Pukyong National Univ., Korea)

1. Introduction

Adaptive equalizers are always realized in the underwater acoustic time-dispersion channel. In this paper we proposed that for the channels having large eigenlvalue spread the equalizer first adopts RLS (recursive least square) algorithm during training period and then employs LMS(least mean square) algorithm after switched to decision direct mode, and the numerical simulation results demonstrate this equalizer's superior performance.

In shallow water acoustic communication multipath time dispersion is the major obstacle to achieve reliable high data rate transmission. To mitigate the intersymbol interference (ISI) effects caused by multipath, equalization technique will be employed. LMS (least mean squares) and RLS (recursive least squares) are the most commonly algorithms in equalization. The major advantage of LMS algorithm is its computational simplicity, however, its convergence rate depends on the eigenvalue spread caused by the channel characteristics, whereas RLS is invariant to eigenvalue spread. Consequently we propose for a channel having large eigenvalue spread with severe ISI RLS algorithm can be used for training, LMS equalizer is then employed to remove ISI after transmission being switched to decision-direct mode.

2. Communication System

The system configuration utilizing QPSK modulation is depicted in Fig. 1. The four-level data streams pass the I-channel and Q-channel pulse shaping filter to match the channel bandwidth for the ideal band-limited under-water acoustic system. At the receiver the received signal will be demodulated, processed by equalizer, finally detected and decoded generating streams of data.

3. Simulation results

E-mail : jryoon@pknu.ac.kr

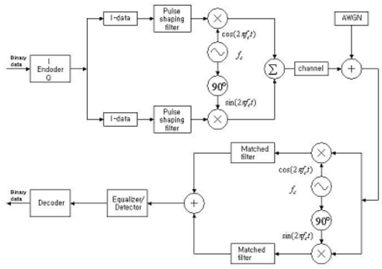

Fig. 1. Block diagram of QPSK system

In our simulation the parameters are shown in Table I and the training sequence is selected as 300 symbols in all the cases. The signal to noise ratio(SNR) is 30dB unless it is noted. We consider three channels whose transfer functions are given by

$$H_a(z) = 0.58 + 0.23z^{-8} - 0.41^{-13} + 0.16z^{-21} \quad (1)$$

$$H_b(z) = 0.7 - 055z^{-1} + 0.29z^{-2} - 0.22z^{-3} - 0.2z^{-80} + 0.16z^{-84} - 0.08z^{-87} \quad (2)$$

$$H_c(z) = 0.7 - 0.54z^{-1} + 0.29z^{-2} - 0.22z^{-3} - 0.21z^{-51} + 0.17z^{-53} - 0.12z^{-54} \quad (3)$$

For the first channel when we employ a linear equalizer with 22 taps the eigenvalue spread is 3.75. The second channel model has the eigenvalue spread of 49.17 using a linear equalizer with 88 taps. The third channel model for R=1000m corresponds to eigenvalue ratio of 39.85 for the number of equalizer taps is chosen to be 55. Due to decision feedback equalizer's (DFE) nonlinear characteristics it does not give rise to noise enhancement during equalization processing. For the purpose of comparison, we employ LMS DFE and RLS-LMS DFE (first RLS algorithm, then LMS algorithm) to investigate their performance to reduce ISI imposed on the channels with various eigenvalue spreads.

Here we show the equalization outputs for the channel R=10m with smaller eigenvalue ratio and the channel R=1000m with large eigenvalue ratio. Fig. 2 depicts the constellation plots for channel R=10m. It's clear that RLS-LMS DFE performs better than LMS since RLS-LMS DFE output can reach convergence more rapidly. For channel R=1000m as shown in Fig 3 LMS DFE output is much more scattered than that of RLS-LMS DFE, in addition for this channel RLS-LMS DFE results in a big enhancement compared with the former channel. Consequently for the channels with larger eigenvalue spread the proposed method can be an effective way to make a tradeoff between convergence and excess mean square error since LMS algorithm is very sensitive to the choice of step size.

Table Ⅰ

Modulation format	QPSK		
Carrier frequency	20kHz		
Symbol rate	2ksym/s		
Water depth(d)	100m		
Sound speed	1500m/s		
Transmitter depth	5m		
Receiver depth	97m		
Horizontal range (r)	10m	600m	1000m

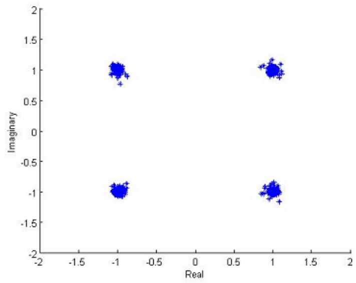

Fig. 2a. LMS DFE output for R=10m

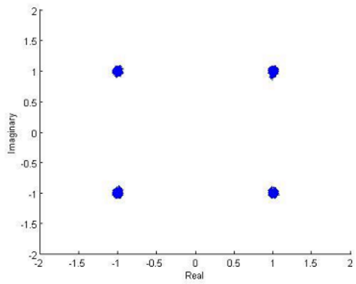

Fig. 2b. RLS-LMS DFE output for R=10m

Fig. 4 plots the mean squared error as a function of input SNR for RLS-LMS and LMS DFE. At high SNR all the DFE performance meets the demands of communication: BER$\leq 10^{-4}$. Moreover, for the channels with larger eigenvalue ratio RLS-LMS DFE outperforms LMS DFE apparently. At low SNR for different channels neither of RLS-LMS and LMS DFE supplies good performance. This implies that when SNR is higher a good way for removing ISI caused by channel time dispersion is to use adaptive equalization technique.

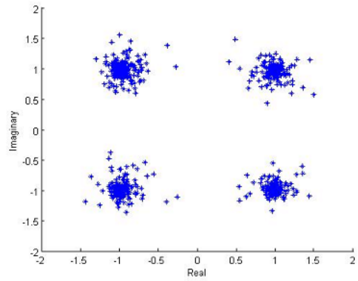

Fig. 3a. LMS DFE output for R=1000m

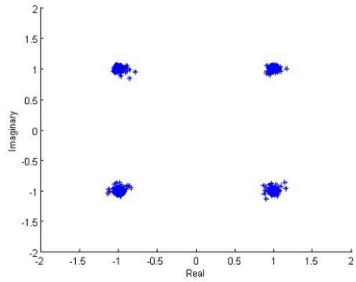

Fig. 3b. RLS-LMS DFE output for R=1000m

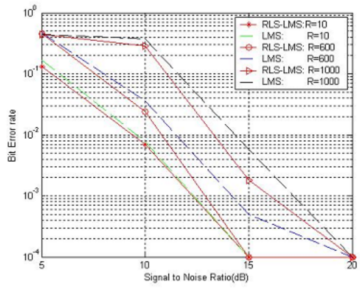

Fig. 4. MSE vs. SNR after RLS-LMS or LMS DFE

4. Conclusions

Through the simulation we present that the three channel 's characteristics and aiming at choosing appropriate equalization method to achieve ideal transmission effects we propose that using RLS algorithm during the training period especially for the channel having large eigenvalue spread, LMS algorithm is used to take over the update task. The simulation results prove that it's an effective scheme to speed training and tracking efficiently not improving the computation complexity largely.

Acknowledgment

This work was supported by Brain Busan 21 Project.

References

1 J. G.. Proakis: *Digital Communications* (McGraw Hill, 2001) p.668.

2. S. Haykin: *Adaptive Equalizer* (Prentice Hall, 2002) p.289.

3. L. Freitag, M. Johnson and M. Stojanovic: Oceanic **1** (1997) 580.

Proc. Symp. Ultrason. Electron., Vol. 26, (2005) pp. 305-306
16-18 November, 2005

An Approach for Tonal Signal Automatic Recognition of Ship Radiated Noise

◎ Kyu-Chil Park, Phil-Ho Lee* and Jong-Rak Yoon
(Pukyong National University, Korea, * Agency for Defense Development, Korea)

1. Introduction

The ship-radiated noise appear the various characteristic signals due to the mechanic system in the ship, the propeller and the interaction between ship body and sea water. It is important informations for the ship's design, the maintenance, the operating condition dignosis and machinery monitering. Generally, it is classified the speed dependent component and the speed independent component.[1-3] Therefore, it is required that some procedures to classify the signal origin from the ship-radiated noise.

This paper presents a technique to detect the tonal signal and classify the tonal signals from ship radiated noise, using peak extraction and Q-factor. [4]

2. Detection of tonal signals

Fig. 1 shows an example of a line spectrum and a LOFAR-gram from ship-radiated noise. It is required to classify what tonal signal is important and what origin of tonal signal is. As shown Fig. 1, the tonal signals have some characteristics – peaks and higher amplitudes. And the speed dependent components have some frequency variation width in some time zone. In this paper, we approach the study as following:

1) Peak extraction from line spectrum
2) Selection of tonal signals exceed threshold among results of step 1)
3) Classification of tonal signal by checking the frequency variation width (by Q-factor)

In step 1), the peaks are extracted by differential coefficients ($\Delta x_1 - \Delta x_2 \geq 0$) from adjacent two points shown as Fig. 2.

E-mail : kcpark@pknu.ac.kr

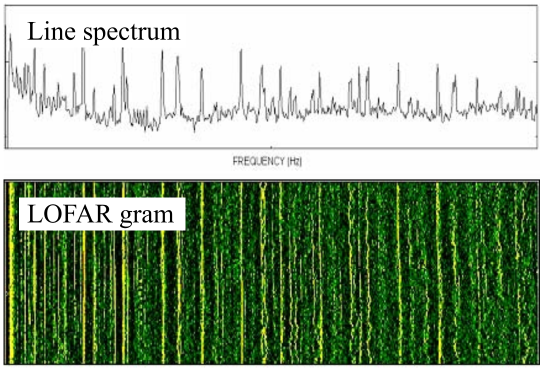

Fig. 1 An example of line spectrum and LOFAR gram from ship-radiated noise.

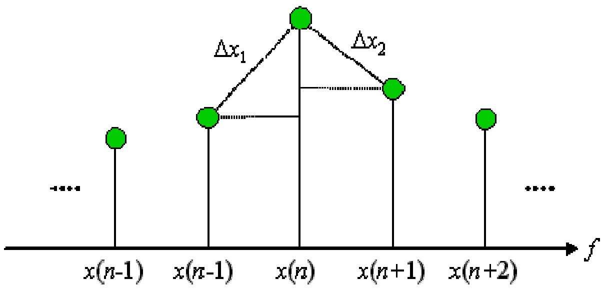

Fig. 2 Peak extraction of tonal signal by differential coefficients

For step 2), the threshold value is given the half of maximum spectrum amplitude.

For step 3), we apply the Q-factor to classify two components - the speed dependent component (SDC) and the speed independent component (SIDC). Fig. 3 shows an example of the bandwidth calculation from a test signal with Gaussian distribution of 20Hz divergence. At the top, from left, the frequency variations are 0, 1, 2, …, 7Hz. The rest show the amplitudes variations and the bandwidth variations. From Fig. 3, we obtain that the frequency variation in the SDC is larger than the SIDC. The frequency variation width of the tonal signals are calculated in 22 frames. We classify the tonal signals by counting the number of the peak extracted signal in each frequency domain.

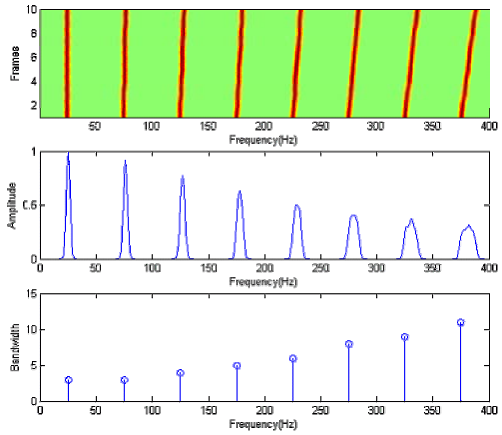

Fig. 3 An example of the bandwidth calculation

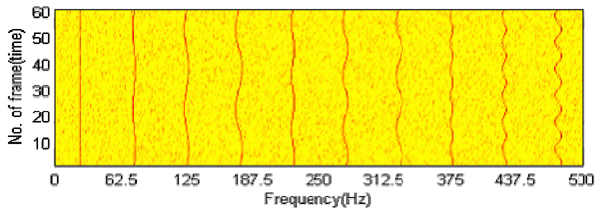

(a) Test ship signal's spectrogram

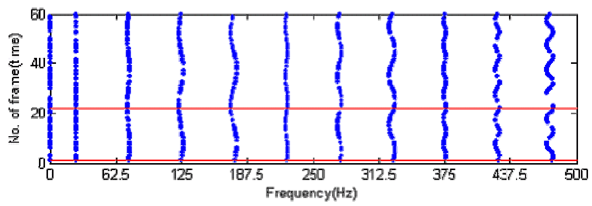

(b) Exceeding threshold and peak extraction signal

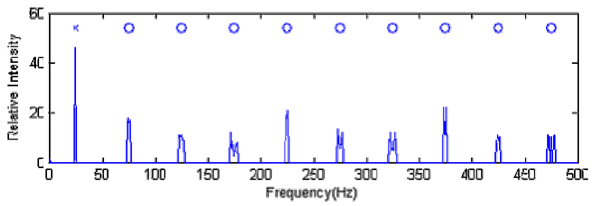

(c) Classified signal by Q-factor

Fig. 4 Simulation result for test ship signal applied by Q-factor

3. Numerical experiments and results

For the numerical simulation, we made test signals with 1 SIDC and 9 SDCs and 20% Gaussian noise such as Fig. 4. We exactly classified 1 SIDC marked 'o' and 9 SDCs marked 'x'.

At next, we apply this approach to real achieved noise data from ship radiated as shown Fig. 5. The horizontal two lines represent 22 frames for classification around CPA(Closest Point of Approach). We successfully classified 3 SIDCs marked 'o' and 10 SDCs marked 'x' except very low frequency components below 50Hz.

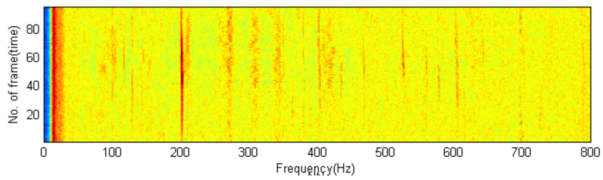

(a) Real ship signal's spectrogram

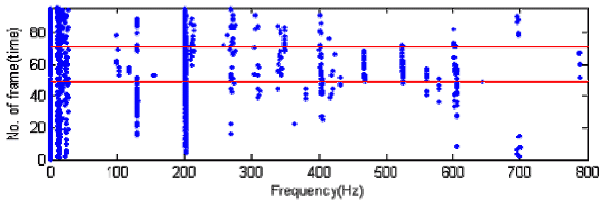

(b) Exceeding threshold and peak extraction signal

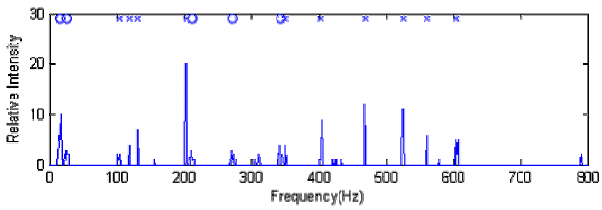

(c) Classified signal by Q-factor

Fig. 5 Classification result for real ship signal applied by Q-factor

4. Conclusions

This paper presents techniques to detect and classify the tonal signals from ship-radiated noise, using peak extraction and Q-factor. We obtained the reasonable results of the classification of tonal signals using frequency variation width in frequency domain.

Acknowledgment

This work was supported by STX Engine Co.,Ltd. and the Brain Busan 21 Project.

References

1. Chu-Kuei Tu, Huang-Chia Huang: Underwater Technology (1998) 253.
2. Phil-Ho Lee, Jong-Rak Yoon, Kyu-Chil Park, Ki-Hun Lim: Acoustical Society of Korea, **23**, (2004) 175.
3. Thomas L. Hemminger, Yoh-Han Pao: IEEE **5** (1994) 712.
4. C.K.Alexander and M.N.O.Sadiku: *Fundamental of Electric Circuits* 2nd Edition (McGRAW HILL, 2003) p.632.

Proc. Symp. Ultrason. Electron., Vol. 26, (2005) pp. 307-308
16-18 November, 2005

Bit Error Characteristics of Passive Time Reversal Underwater Acoustic Communication due to a Moving Source

◎Jong Rak Yoon and Ji-Hyun Park (Pukyong Nat'l Univ., Korea),

Daniel Rouseff (Applied Physics Lab., Univ. of Washington)

1. Introduction

The underwater acoustic communications(UWA) using passive time reversal process(PTRP) or passive phase conjugation has shown that the bit error rate(BER) on BPSK UWA depends on the relative distance change between the source and receiver. The mismatch between the initial channel impulse response and the subsequent response after the source or receiver moving causes this effect. In this study, the BER is qualified as a function of source moving distance and source-receiver range.

2. PTRP communication

Fig. 1 shows the experimental geometry. A probe pulse at initial source location is transmitted and then the signal corresponding to the information data stream. Therefore, the PTRP UWA using the initial probe pulse channel response has the mismatch effect on the coherent sum of the PTRP. This results the coherence degrade and BER increase. The probe signal $p(t)$ is given as

$$p(t) = \cos(2\pi f_c t)(1 - \cos(2\pi t / T_b)), \quad 0 \le t \le T_b \qquad (1)$$

where f_c and T_b are carrier frequency and bit interval, respectively. We use the M array elements processed signals to get spatial diversity gain. The sum of each element processed signal is given as

$$\begin{aligned} y(t) &= \sum_{i=1}^{M} r_{pi}(t) r_{pi}(-t) \\ &= \sum_{i=1}^{M}\sum_{k=1}^{K}(\alpha_{ik})^2 R_{pp}(t) + \sum_{i=1}^{M}\sum_{\substack{k_1=1 \\ k_1\neq k_2}}^{K}\sum_{k_2}^{K}\alpha_{ik_1}\alpha_{ik_2}R_{pp}(t+\tau_{ik_1}-\tau_{ik_2}) \end{aligned} \qquad (2)$$

where, $r_{pi}(t)$ and $R_{pp}(t)$ are the probe response signal at the i th receiver and the autocorrelation of probe. The α_{ik} is the amplitude of the k th path and τ_{ik} is the time difference between the direct and reflected path signals. The signal for moving source is given as

$$\begin{aligned} y'(t) &= \sum_{i=1}^{M} y_i'(t) = \sum_{i=1}^{M} r_{pi}(t) r_{pi}'(-t) \\ &= \sum_{i=1}^{M}\sum_{k=1}^{K}(\alpha_{ik}\alpha_{ik}')R_{pp}(t+\tau_{ik}-\tau_{ik}') + \sum_{i=1}^{M}\sum_{\substack{k_1=1 \\ k_1\neq k_2}}^{K}\sum_{k_2=1}^{K}\alpha_{ik_1}\alpha_{ik_2}'R_{pp}(t+\tau_{ik_1}-\tau_{ik_2}') \end{aligned} \qquad (3)$$

where, the prime denotes the matched signal version of the displaced source position. The first term in (2) and (3) is defined as the main lobe which is the desired signal and the second terms as the side lobe which is the destructive interference signal. We apply (1)-(3) to the BPSK information data signal which is given as

$$I(t) = \sum_{n} I_n p(t - nT_b), \quad I_n = +1 \text{ or } -1 \qquad (4)$$

The sum of all elements processed signals for a fixed source and a receiver $Iy(t)$ and that for the moving source $I_y'(t)$ are given as

$$\begin{aligned} Iy(t) &= \sum_{i=1}^{M}\sum_{n} I_n \sum_{k=1}^{K}(\alpha_{ik})^2 R_{pp}(t - nT_b) \\ &+ \sum_{i=1}^{M}\sum_{n}\sum_{\substack{k_1=1 \\ k_1\neq k_2}}^{K}\sum_{k_2=1}^{K}\alpha_{ik_1}\alpha_{ik_2}R_{pp}(t+\tau_{ik_1}-\tau_{ik_2}-nT_b) \end{aligned} \qquad (5)$$

$$\begin{aligned} Iy'(t) &= \sum_{i=1}^{M}\sum_{n} I_n \sum_{k=1}^{K}(\alpha_{ik}\alpha_{ik}')R_{pp}(t+\tau_{ik}-\tau_{ik}'-nT_b) \\ &+ \sum_{i=1}^{M}\sum_{n}\sum_{\substack{k_1=1 \\ k_1\neq k_2}}^{K}\sum_{k_2=1}^{K}\alpha_{ik_1}\alpha_{ik_2}'R_{pp}(t+\tau_{ik_1}-\tau_{ik_2}'-nT_b) \end{aligned} \qquad (6)$$

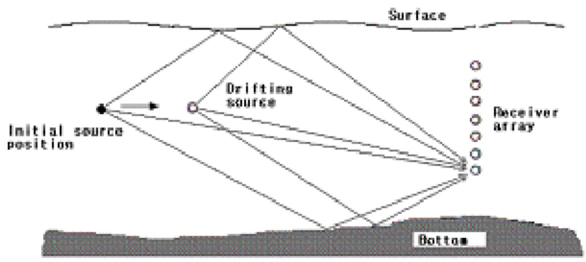

Fig. 1. Experimental configuration .

E-mail : jryoon@pknu.ac.kr

In (6), the main lobe will show interference since $(\tau_{ik} - \tau_{ik}')$ is not equal to zero. In the correlation demodulation, the one bit signal of $Iy(t)$ (or $Iy'(t)$) is correlated with probe signal and this gives the Euclidean distance d between the information sequence +1 and -1 as

$$d = \{2E(1-\rho_{I_y p})\}^{1/2} \tag{7}$$

where E denotes the energy of one bit signal.. The correlation $\rho_{I_y p}$ between $I_y(t)$ and $p(t)$ is defined as

$$\rho_{I_y p} = (E_{I_y} E_p)^{-1/2} \int_0^{T_b} I_y(t) p(t) dt \tag{8}$$

where, E_{I_y} and E_p denote the energy of $I_y(t)$ and $p(t)$. Since $\rho_{I_y p}$ is always less than one for moving source, the bit error increases to that for the fixed source-receiver range.

3. Experimental results

Bit error due to source moving was examined considering the experiment in the Puget Sound near Seattle. The water depth is about to be as 40-60m and surface and bottom reflection coefficients are assumed to be -0.8 and 0.6 in simulation. Fig. 2 is one of the sea trial and the simulation results for fixed source-receiver. A mark '*' corresponds to a transmitted

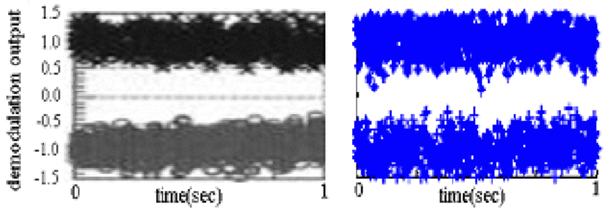

Fig. 2. Demodulation outputs of the sea trial(left) and the simulation(right).

'one' while a mark '+' to a transmitted 'zero'. Successful communication is possible. Fig. 3 shows one of the results for moving source in sea trial. The water depth and the initial source-receiver range were 60m and 1500m, respectively. As time elapsed, distance between +1 and -1 is decreased, so that bit error increase.

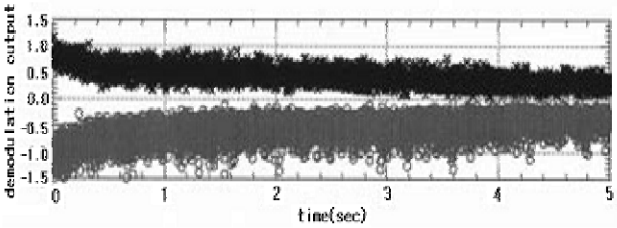

Fig. 3. Source moving effect on demodulation output. Drift rate 0.4m/sec, SNR=11.8dB.

Fig. 4 shows the correlation coefficient with respect to drifting distance for two different given initial source-receiver ranges. At short source-receiver range, the correlation changes more rapidly than at long range and induces more rapid variation of correlation. Fig. 5 is the corresponding bit error characteristics. Demodulation output is analysed in 1m range step. As shown,

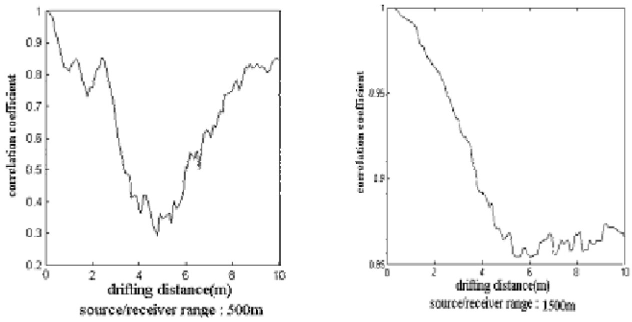

Fig. 4. The correlation coefficient with respect to horizontal source moving distance for two different initial source-receiver ranges.

correlation degrade matches with the demodulation output characteristics i.e. the bit error nature. Comparing Fig. 4 to Fig. 5, correlation agrees well with the bit error characteristics. The demodulation output is degraded with drifting distance increase.

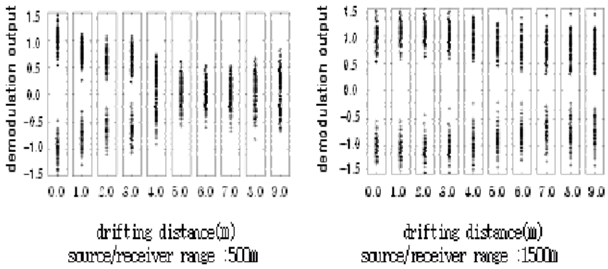

Fig. 5. BER corresponding to Fig. 4 for source moving.

4. Conclusions

The effect of moving source on passive time reversal process BPSK UWA has been presented. The increase of source moving distance induces the decrease of the correlation coefficient and results in smaller Euclidean distance in demodulation signal space. The correlation degrade by source moving agrees well with the bit error rate and the distant source-receiver range gives slower change of bit error variation than short source-receiver range with the same source moving rate. The sea trial and simulation results agree well each other in general trend such that the demodulation output is degraded with moving distance increase.

Acknowledgement

This work was supported by Pukyong National Univ. Research Abroad Fund in 2003 and Brain Busan 21 Project.

References

1. D. Rouseff, D. R. Jackson, W. L. J. Fox, C. D. Jones, J. A. Ritcey, and D. R. Dowling : IEEE J. Oceanic Eng. **26**(2001) 821.
2. D. R. Dowling : J. Acoust. Soc. Am. **95**(1994) 1450.
3. J. A. Catipovic and L. E. Freitag : IEEE J. Oceanic Eng. **16**(1991) 86.
4. Q. Wen and J. A. Ritcey : IEEE J. Oceanic Eng. **19**(1994) 227.
5. A. Parvulescu : J. Acoust. Soc. Am. **98**(1995) 943.
6. T. C. Yang : IEEE J. Oceanic Eng.**29**(2004) 472.

P2-49

Proc. Symp. Ultrason. Electron., Vol. 26, (2005) pp. 308a-308b
16-18 November, 2005

Dynamic Behavior of Multibubble Cavitation During Ultrasonic Degassing

○Takashi Kubo, Noriyasu Kawakita, Mamoru Kuwabara and Jian Yang
(Dept. of Material Processing Eng. Nagoya Univ.)

Abstract

A water model experiment has been carried out to clarify the effects of atmospheric pressure, the power of ultrasound imposed and concentration of suspended fine particles on the rate of degassing with acoustic cavitation. It is clarified that operating factors described above accelerate the rate of ultrasonic degassing. Furthermore dynamic behaviors of acoustic cavitation during degassing have been visualized by a high-speed digital video camera, and the observed behaviors were well correlated to the rates of ultrasonic degassing for corresponding operating conditions.

1. Introduction

Sonoprocessing of Materials in which ultrasound is applied to material processing operations can create many innovative technologies [1,2]. Acoustically induced cavitation multibubble is especially expected to cause high efficient degassing, because of increase in gas-liquid interface generated as acoustic cavitation multibubble, and because of intensive mixing of liquid by microjets generated when the bubbles collapse [3]. For high efficient ultrasonic degassing, it is important to investigate the operating factors described below. In this study, a water model experiment has been carried out to clarify the effects of atmospheric pressure, frequency, the power of ultrasound imposed and the amount of suspended fine particles on the rate of ultrasonic degassing.

2. Experimental Setup

Fig. 1 shows a basic experimental setup for the ultrasonic degassing of liquid. A continuous sinusoidal signal generated by a function generator was amplified by a power amplifier. Its electric output was fed to a bolted Langevin-type transducer (resonant frequency: 25, 46 kHz nominal maximum input power: 55 W) or to a plate-type circular piezoelectric ceramic transducer (resonant frequency: 250 kHz) of 45 mm diameter. The transducer was fixed to a stainless steel plate of 3 mm thickness at the bottom of the vessel. The vessel was made of a cylindrical acrylic resin of 3 mm in thickness and 74 mm in inner diameter. It was filled with an aqueous 0.01N NaOH solution to a resonance depth. Distilled water, which was prepared for the solution, was pre-degassed by stirring it for about 1.5 hours under the vacuum atmosphere. Atmospheric pressure above the solution was adjusted at a specified level with a vacuum pump. The pH meter to indicate variation of CO_2 concentration in the NaOH solution intermittently detected its transitional change. The influences of the atmospheric pressure, frequency and the concentration of dispersed fine particles on the degassing speed were investigated. The fine particles used in this experiment were polystyrene balls of 241μm in diameter and 1050kg/m^3 in density. Furthermore, the behavior of the cavitation during irradiation of ultrasound was photographed with a

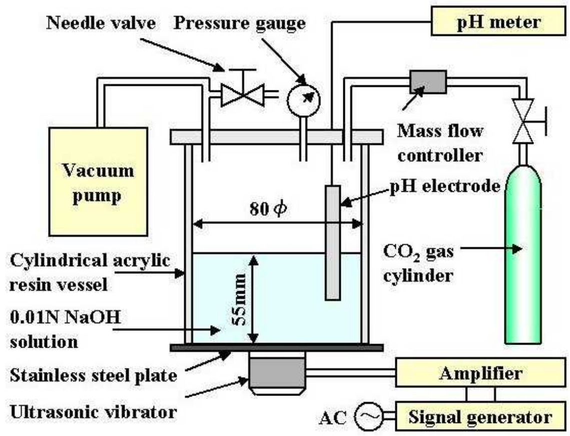

Fig.1 Experimental setup.

digital camera.

3. Results and discussion

Fig.2 shows the influence of the atmospheric pressure on the rate of degassing with or without ultrasound of a frequency of 42.3 kHz and a power of 18 W. In the case of ultrasonic degassing, it was observed that many small bubbles evolved quietly and flew up orderly at the initial stage, and the acoustic cavitation after several minutes became noisy and caused violent motion of the liquid accompanied by microjets. From Fig. 2, it was shown that the rate of ultrasonic degassing was drastically higher than that of degassing without ultrasound, and was also shown that the degassing rate was accelerated by the decrease in atmospheric pressure in both cases. This result is caused by the decrease in cavitation threshold with decreased atmospheric pressure. Particularly at the initial stage, acoustic cavitation remarkably accelerated the rate of degassing and the rate became moderate after an elapse of several minutes. These findings suggest transition from gaseous acoustic cavitation conditions to vaporous acoustic cavitation

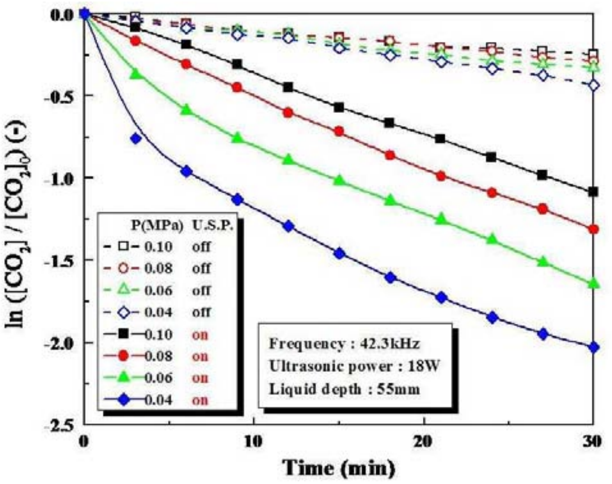

Fig.2 Effect of atmospheric pressure on the rate of degassing with or without irradiation of ultrasound.

ones.

Fig.3 shows the comparison of low and high frequencies of ultrasounds on the rate of degassing. Imposed frequencies were 42.3 kHz and 245.5 kHz keeping a power of ultrasound as 18 W, and the liquid depth was set in resonant condition for each working frequency. At the initial stage, the rate of degassing with low frequency of ultrasound was higher than that with high frequency, and finally the degassing ceased. Whereas, in the case of degassing with high frequency ultrasound, the rate of degassing was lower than that with low frequency of ultrasound at the initial stage of degassing. However the degassing continued till the final stage of experiment. In the case of high frequency ultrasound, acoustic streaming was generated toward direction of ultrasound irradiated, and acoustic cavitation multibubble was continuously removed by the acoustic streaming.

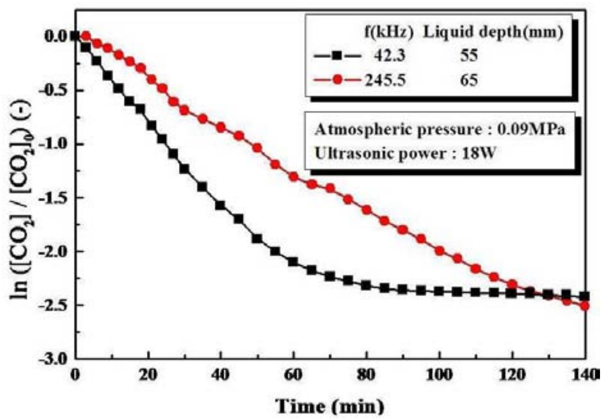

Fig,3 Effect of frequency of ultrasound on the rate of degassing at constant atmospheric pressure.

Fig.4 shows the influence of fine particles dispersed in liquid on the rate of ultrasonic degassing. In order to adjust the density with the particles and to disperse them uniformly, sugar was mixed with the NaOH solution to prepare a sugar solution of 12 mass% and 0.01 N. An ultrasound of 41.9 kHz was irradiated into the liquid with depth of 55 mm. It is found from Fig.4 that the rate of degassing was promoted by the dispersed fine particles whose surfaces might favor nucleation of cavitation bubbles. The promotion of degassing with the dispersed particles was remarkable at the initial stage. This is why the surface of fine particles can provide the effective nucleation sites only during the period of gaseous cavitation. Additional effect can be expected such that dispersed particles move from around antinodes of sound pressure, where no acoustic cavitation bubbles are generated, to low sound pressure area such as nodes of sound pressure or surface in the vessel, where acoustic cavitation bubbles substantially exist. Figure 4 show that the influence of dispersed particles tended to saturate when the particle concentration C_p exceeded 0.032 mass%.

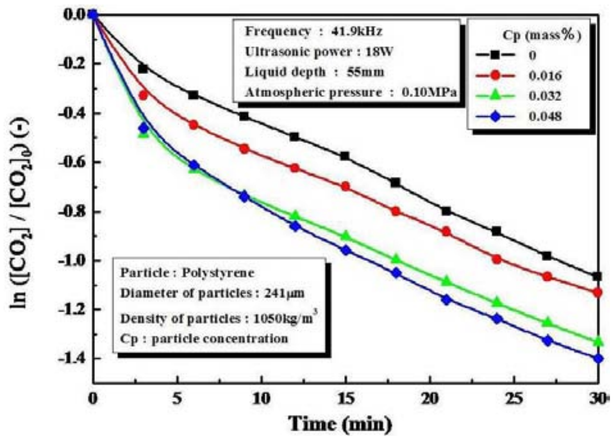

Fig,4 Effect of particles on the rate of degassing with irradiated ultrasound.

4. Conclusion

In this paper, the effects of atmospheric pressure, frequency and concentration of dispersed particles on ultrasonic degassing have been investigated. The acoustic cavitation plays an important role in the degassing process, and the decreased atmospheric pressure, the power of ultrasound imposed, and the dispersed fine particles all accelerate the degassing rate. The behaviors of cavitation multibubble during ultrasonic degassing were observed by a high-speed digital video camera in the same experimental conditions described above. Observed behaviors of acoustic cavitation bubbles were well correlated to the rates of degassing of melt for corresponding operating conditions.

Reference

[1] M. Kuwabara, S. Sano, S. Yamahira, and M. Sano: Proc. Int. Conf. World Congress of Ultrasonic (1997) p.408.

[2] M.Kuwabara, S. Komarov and M.Sano: Proc. 8th Japan-China. Symp. Science and Technology of Iron and Steel (1997) p.175.

[3] T. Kubo, M. Kuwabara and Jian Yang: Jpn. J. Appl. Phys. **44** (2005) 4647.

G-1

Proc. Symp. Ultrason. Electron., Vol. 26, (2005) pp. 309-310
16-18 November, 2005

Applicability of FDTD method on the wave propagation in the cancellous bone

◎Yoshiki NAGATANI, Hirotaka IMAIZUMI, Takashi FUKUDA, Mami MATSUKAWA, Yoshiaki WATANABE and Takahiko OTANI (Doshisha Univ.)

1. Introduction

Longitudinal wave propagating in the cancellous bone separates into fast and slow waves depending on the conditions[1-3]. This interesting phenomenon becomes a strong tool for the diagnosis of osteoporosis because the wave behavior depends on the bone structure.

However, there are a few studies applying FDTD (Finite Difference Time Domain) method to such complex coexistent models of liquid and solid.

In this study, the applicability of FDTD method to the cancellous bone is discussed focusing on the propagation of fast and slow waves.

2. Elastic FDTD method[4]

The governing equations of elastic FDTD for the isotropic medium are;

$$\frac{\partial \sigma_{xx}}{\partial t} = (\lambda + 2\mu)\frac{\partial v_x}{\partial x} + \lambda\frac{\partial v_y}{\partial y} + \lambda\frac{\partial v_z}{\partial z} \quad (1)$$

$$\frac{\partial \sigma_{xy}}{\partial t} = \mu\left(\frac{\partial v_x}{\partial y} + \frac{\partial v_y}{\partial x}\right) \quad (2)$$

$$\frac{\partial v_x}{\partial t} = \frac{1}{\rho}\left(\frac{\partial \sigma_{xx}}{\partial x} + \frac{\partial \sigma_{xy}}{\partial y} + \frac{\partial \sigma_{zx}}{\partial z}\right) \quad (3)$$

where σ_{ij} is normal and shear stresses, v_i is particle velocity, λ and μ are Lame coefficient, and ρ is density of the medium.

The transformation of these equations into difference equations enables the alternate calculation of stress and particle velocity, which realizes the numerical simulation of the field.

3. Simulation Model

The size of bovine cancellous bone used was 14×14×7[mm]. **Figure 1(a)** is the x-ray micro focus CT image and **(b)** is the distribution of averaged volume fraction of the sample.

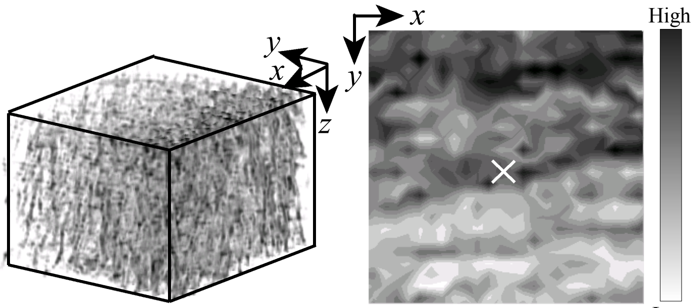

(a) X-ray micro focus CT image. (b) Distribution of averaged bone volume fraction.

Figure 1 Cancellous bone.

Simulation field is 17×17×13[mm] with cube lattice of 46[μm]. Time step is 5[ns]. As an initial particle velocity at the surface of the concave source, a single sinusoidal wave of **Fig. 2** is used. The surface of the transmitter is star-shaped in order to decrease the edge effect.

$$v(t) = \begin{cases} \sin\omega t \times \sin^2\left(\omega t/2\right) & \left(\text{for } 0 \le t \le 2\pi/\omega\right) \\ 0 & \left(\text{for } 2\pi/\omega < t\right) \end{cases} \quad [m/s]$$

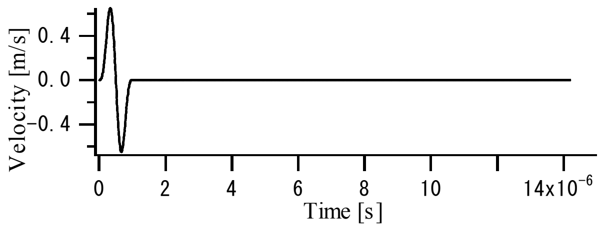

Figure 2 Waveform of initial particle velocity.

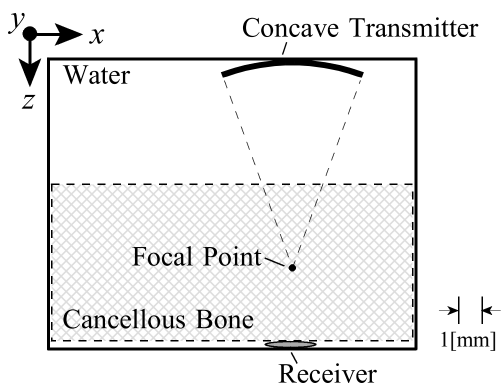

Figure 3 FDTD simulation model.

E-mail: nagatani@usl.doshisha.ac.jp

The sample is fully immersed in water. The z axis position of the transmitter is fixed to keep the focal point at the half length of the sample thickness. Changing positions of transmitter and sensor in the x-y plane, the distribution of wave propagation was investigated. As the acoustic constants of cancellous bone, the experimentally observed values of the cortical bone are appropriated.

4. Results and Discussion

4.1. FDTD Simulation

Figure 4(a) is the calculated pressure waveform of the model without the sample. The wave observed at the cross(×) point of Fig. 1(b) is shown in **Fig. 4(b)**. Both fast and slow waves can be seen. The fast wave is considered to propagate mainly in the hard structure of bone sample. Moreover, the amplitude of the fast wave was much smaller than the slow wave, which has also been reported experimentally[1-2].

Figure 5(a) is the distribution of arrival time of the fast wave. The amplitude of slow wave is shown in **Fig. 5(b)**. Figure 1(b) and Figs. 5(a)(b) indicate that the arrival time of fast wave and the amplitude of slow wave have good correlations with the distribution of bone volume fraction in Fig. 1(b).

4.2. Experiments

Distributions of fast and slow waves are experimentally observed using PVDF hydrophone. The focal length of transmitter is 40[mm] and the radius is 10[mm]. A single sinusoidal wave at 1[MHz] is transmitted. The radius of the receiver is 2.5[mm].

The result shown in **Fig. 6** shows similar tendency with the FDTD data.

5. Conclusion

Using the CT model of the actual cancellous bone, the generation of fast and slow waves is confirmed by elastic FDTD method. This clearly shows the applicability of FDTD method to understand the complicated wave propagation in cancellous bone.

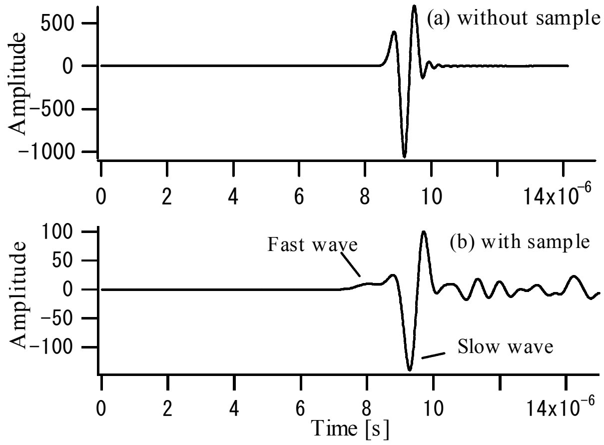

Figure 4 Simulated waveforms.

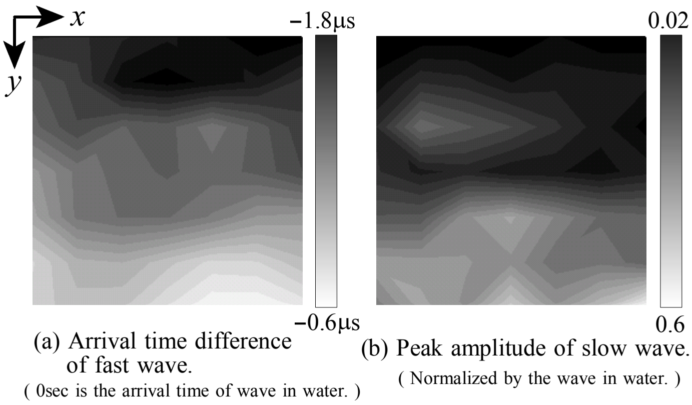

Figure 5 Distribution of arrival time and amplitude of simulated waveforms.

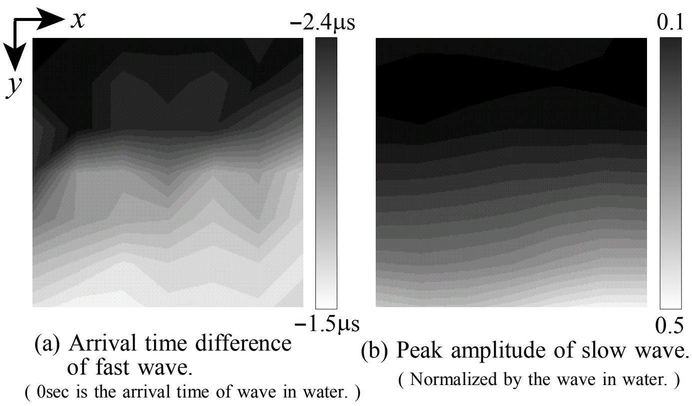

Figure 6 Distribution of arrival time and amplitude of experimentally observed waveforms.

Acknowledgment

Authors would appreciate the measurement of x-ray micro focus CT to Dr. Murata and Dr. Takada at Shiga University of Medical Science.

References

1. A. Hosokawa, T. Otani : J. Acoust. Soc. Am, **101** (1997) 558.
2. A. Hosokawa, T. Otani, T. Suzuki, Y. Kubo, S. Takai : Jpn. J. Appl. Phys. **36** (1997) 3233.
3. T. Otani : Jpn. J. Appl. Phys. **44** (2005) 4578.
4. Y. Tanikaga, K. Takaki, Y. Watanabe, T. Sakaguchi : IEICE Technical Report, US2003-3 (2003).

Proc. Symp. Ultrason. Electron., Vol. 26, (2005) pp. 311-312
16-18 November, 2005

Simulation of ultrasound propagation trough three-dimensional trabecular bone structures

Frederic Padilla[1 a], Emmanuel Bossy[b] and Pascal Laugier[a] (a:Laboratoire d'Imagerie Parametrique CNRS Universite Paris 6, b: Laboratoire d'Optique Physique, ESPCI, CNRS)

1. Introduction

Quantitative ultrasound are now well established techniques for the assessment of bone status, mainly in a context of osteoporosis. The most developed techniques use the transmission on ultrasound waves through trabecular bone at the calcaneus (heel bone). The measurement is based on the estimation of the speed of sound and slope of the frequency dependent attenuation of the wave that has propagated through the bone [1].
However, the physics underlying the interaction between ultrasound and trabecular bone structure is still not fully understood. The difficulties of elaborating a general theoretical framework come from the complex nature of the propagation medium : trabecular bone is a network of interconnected solid trabeculae saturated with fluid, it is anisotropic and heterogeneous (both intra and inter specimens), and at clinical frequency (MHZ range) features of the micro architecture have typical dimensions of the order of the US wavelength.
While analytical approaches that would take into account a large number of these micro architectural parameters as well as different physical mechanisms quickly become inextricable, numerical simulation offers a powerful alternative.
In this paper, 3D numerical simulations of ultrasound transmission are performed through 31 trabecular bone samples measured by high resolution synchrotron microtomography. We show that the simulations yield signals which characteristics (attenuation, speed of sound, possible existence of two types of waves) are consistent with those observed experimentally. In particular, we compare the simulated attenuation to that measured experimentally, and discuss the relative contribution of scattering and absorption to the total attenuation.

2. Numerical simulations

The numerical computations were coupled to 3D numerical models of trabecular structures. 32 trabecular bone specimens from human femur were imaged using SR-µCT [2] at the ESRF (European Synchrotron Radiation Facility, France). Parallelepiped domains with dimensions 5.6x5.6 mm² in the transverse dimensions (X,Y) and 30 µm along the Z axis were extracted from each synchrotron acquisitions (fig. 1).

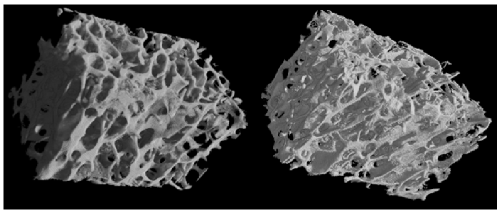

Fig. 1 : Three dimensional views of synchrotron microtomographic reconstruction of trabecular bone micro-architecture.

Simulations of wave propagation through trabecular bone were performed using a software developed by our group (SimSonic), based on a finite-difference time-domain (FDTD) algorithm [3]. A numerical solution to the 3D linear elastic wave propagation equation is computed in both fluid and solid materials. However, it does not account for absorption phenomena such as viscous effects. Perfectly matched layers [4] have been implemented, avoiding unphysical reflections from the boundaries of the simulation mesh.
The ultrasonic pressure source was defined over the whole XY plane at z = 0 mm and a plane receiver was set at z = 10 mm, recording the pressure averaged over its whole surface. The source emits a broadband pressure pulse centered at 1 MHz.
For the computations, the following parameters were used for density ρ_{water}=1 g/cm^3, ρ_{bone}=1.85 g/cm^3; logitudinal velocity cL_{water}=1500 m/s, cL_{bone}=4000 m/s; and transverse wave velocity in bone cT_{bone}=1800 m/s.
For each simulation, attenuation coefficient and speed of sound were computed from the ratio of the spectrum of the signal transmitted through bone to that of the reference signal [5]. The BUA (Broadband Ultrasound Attenuation) was derived

[1] Laboratoire d'Imagerie Parametrique, CNRS Universite Paris 6, 15 rue de l'Ecole de Medecine, 75006 Paris, France.

as the slope of a linear fit of the attenuation coefficient as a function of frequency in the frequency bandwidth 0.3-1.3 MHz. Speed of sound (SOS) was defined as the value taken by the phase velocity at 1 MHz.

3. Results and discussion

The first very important result was obtained when looking at the frequency dependence of the attenuation coefficient : it was observed that the simulation yield linear frequency dependent attenuation coefficient in all the specimens. Moreover, it was found that the BUA was an increasing function of porosity (Fig. 2-left), and that the quantitative simulated effect of BV/TV on nBUA was of the order of 2 dB/cm/MHz per % of BV/TV, in agreement with experimental reports [6].

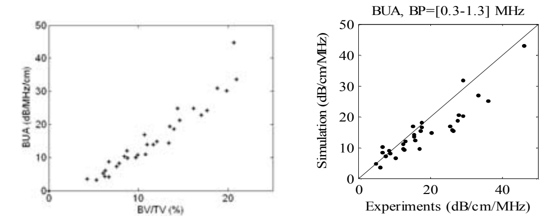

Fig. 2. Left : BUA as a function of bone volume fraction (BV/TV = (1-porosity)*100). Right : Simulated Vs measured BUA.

We also observed a close agreement between simulated and experimental values of BUA measured on the same specimens prior to µ-CT experiments (Fig. 2-right). Assuming the difference in simulated and experimental attenuation is caused by the contribution of absorption (that is not taken into account in the simulation), the consistently lower simulated BUA values than experimental ones indicate that scattering alone is not enough to explain the increase of attenuation with frequency. Nevertheless, this graph also shows that scattering explains a major part of the observed BUA. The maximum relative difference between simulated BUA and experimental BUA occurs around experimental values of about 30 dB/cm/MHz and is less than 30 %. The graph also suggests that the contribution of absorption to BUA is only significant for high values of BUA, i.e. for denser bone.
Looking at the phase velocities, two important results were obtained. It was observed that simulated SOS was positively correlated with the bone volume fraction, and that a majority of specimens (25 out of the 31 samples) exhibited negative phase velocity dispersion. This strongly suggests that scattering by the complex 3D trabecular network yield mainly negative dispersion.
Finally, a last simulation was performed to test the influence of the orientation of the trabecular with respect to the direction of propagation of the ultrasound wave. For the simulation results discussed above, the main orientation of the trabecular network happened to be consistently perpendicular to the propagation direction (Z axis), and only one single ballistic arrival is recorded at the receiver. When rotating the specimens, in order to have the direction of ultrasound propagation parallelel to the main orientation of the trabecular network, we observed the existence of two waves (Fig. 3), similar to those observed experimentally [7]: the fast wave is low pass-filtered and travels faster than waves in water, and the slow wave travels lower.

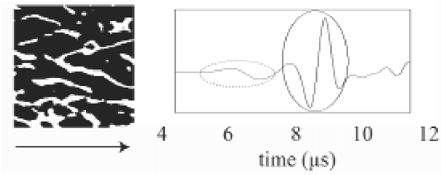

Fig. 3 : A fast wave (dashed circle) and slow wave (dotted line) are observed after propagation in a direction parallel to the main orientation of the trabeculae.

4. Conclusion

Simulations performed through 3D trabecular bone geometry, without taking into account absorption, yield major phenomena observed experimentally : attenuation varies linearly with frequency, BUA and velocity increase with the amount of bone, velocity dispersion can be negative, and two types of wave can be observed for appropriate propagation direction relative to the main orientation of the structure. Therefore, such simulations provide a powerful tool to study the effect of several cancellous bone parameters on ultrasound propagation.
The close correlation between simulated and experimental BUA, obtained without taking into account the absorption, also suggest that scattering phenomena may play a major role in attenuation.

References

1. Njeh et al., Quantitative Ultrasound : assessment of osteoporosis and bone status. 1999, London: Martin Dunitz
2. Salome et al. Med Phys **26** (1999) 2194.
3. Bossy et al. J. Acoust Soc Am **115** (2004) 2314.
4. Collino and Tsogka. Geophysics **66** (2001) 294.
5. Laugier et al. Bone **20** (1997) 157.
6. Chaffai et al., Bone **30** (2002) 229.
7. Hosokawa and Otani. J. Acoust Soc Am **103** (1998) 2718.

G-3

Proc. Symp. Ultrason. Electron., Vol. 26, (2005) pp. 313-314
16-18 November, 2005

Quantifying and Qualifying Sea Bottom Backscattering Strength by Quantitative Echo Sounder

◎ Henry M. Manik, Masahiko Furusawa, and Kazuo Amakasu
(Tokyo University of Marine Science and Technology)

1. Introduction

Underwater acoustic technologies are most effective and useful for characterization of sea bottom due to their reliability and versatility. They are based on the measurement, analysis, and interpretation of characteristics of signal reflected or scattered by the sea bottom.

One of the effective and promising acoustic methods to measure bottom surface backscattering strength (SS) is to use a quantitative echo sounder (QES) originally developed for fisheries surveys. The QES can rather easily measure echoes due primarily to scattering from the water-bottom interface. A sea bottom backscattering strength theory was developed by one of the authors [1] for checking the QES performance.

In our previous study [2] we developed a ring surface scattering (RSS) model for sea bottom scattering as an extension of the above theory and compared the SS values obtained by the RSS model with the results from the bottom echo integration model to confirm the reliability of the theory. In this study, we apply our bottom echo integration model and RSS model extensively to a bottom survey by QES off Jawa Island and examine the effectiveness of our models.

2. Methods

A QES (KaijoSonic, KFC3000) installed onboard the research and training vessel "Umitaka-maru" of Tokyo University of Marine Science and Technology was used to measure SS. The simplified block diagram of the QES to measure SS is shown in **Fig. 1**. The QES was calibrated with a 38.1 mm ϕ tungsten carbide sphere following the standard method.[3]

In the bottom echo integration method, [1] we average the bottom echoes for a predefined depth layer (r to $r + r_w$) including the bottom echoes and for a ping sequence or integration period to obtain the average bottom echo integration strength ("bottom SV") as

$$\langle S_{VB} \rangle = \frac{\langle E_{TB}{}^2 \rangle}{K_M{}^2} \tag{1}$$

where E_{TB} is the time varied gain (TVG) amplifier output, K_M is the multiple echo coefficient, and < · > exhibits the averaging. The simple relationship between the average SS and the bottom SV is given by [1]

$$\langle S_s \rangle = r_w \langle S_{VB} \rangle \tag{2}$$

where r_w is the integration width.

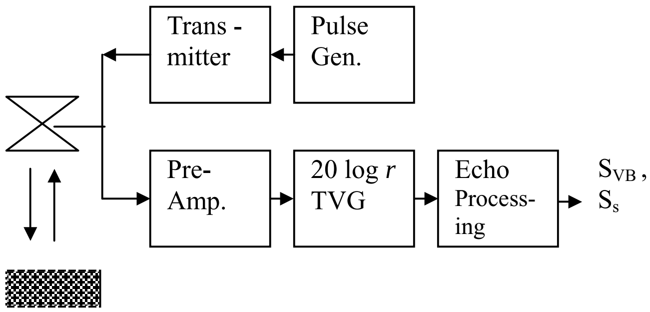

Fig. 1 Simplified block diagram of QES to measure SS

Using the RSS Model we have a relationship between the raw SV value of the bottom echo, S_{VB} , and the raw surface scattering strength, S_s, as

$$S_{VB} = \frac{S_s\, \Phi}{\Psi\, (c\,\tau/2)} \tag{3}$$

where Φ and Ψ are the equivalent beam angle for surface and volume scattering, respectively, c is the sound speed, and τ is the pulse width. At the peak of the bottom echo, we have

$$\Phi \simeq \Phi_o \tag{4}$$

where Φ_o is the asymptotic value of the equivalent beam angle for surface scattering. In the case of a sharp beam we have [4]

$$\Phi_o \cong \Psi\,. \tag{5}$$

Introducing Eqs. (4) and (5) into Eq. (3) gives

$$S_s = (c\,\tau/2)\, S_{VB} \tag{6}$$

and we can easily convert the raw SV to raw SS.

A bottom survey was conducted from 9 to 24 December 2003 in the Indian Ocean, southern coast of Jawa, Indonesia in conjunction with the oceanographic and exploratory fishing.

email : md02207@edu.s.kaiyodai.ac.jp

3. Results and Discussions

An example of the average SS map obtained by the echo integration of bottom echo with integration period of 0.1 nmi of bottom echo is shown in **Fig. 2** with depth contour deduced from the QES data ; the SS of this area are ranging from -23 to -12 dB. We observe an evident correlation between the bottom slope and the SS value : SS values are generally high where the bottom slope is large as seen at the south-west corner of Fig. 2.

The instantaneous SS derived from RSS model at point A of Fig. 2 is shown in **Fig. 3.**

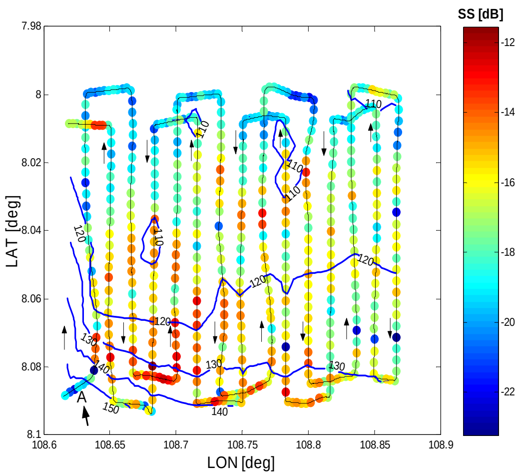

Fig. 2 The average SS map along the acoustic track

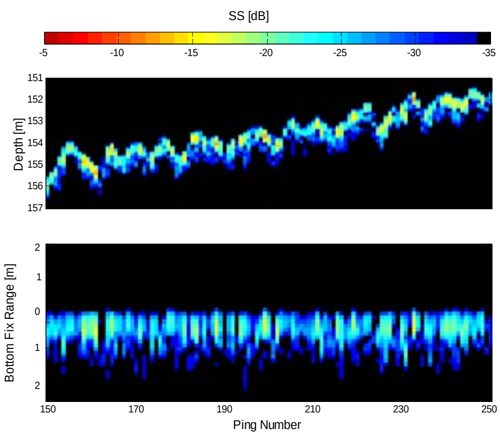

Fig. 3 The instantaneous SS of point A (upper) with the fixed and expanded bottom (lower)

The upper figure is the sea bottom image with undulation caused by the ship motion and the lower figure is the bottom image after bottom fixing and expansion. The SS value read from this figure is about -20 dB and the value by bottom echo integration methods seen in Fig. 2 are in good agreement.

It is shown that the QES can rather easily measure echoes by reflection of sounding pulse from the bottom. The QES is especially useful when both fish and sea bottom should be quantified. **Figure 4** shows simultaneously the scattering from fish (SV) close to the sea bottom and the SS values by Eq. (6) of the fixed and expanded bottom.

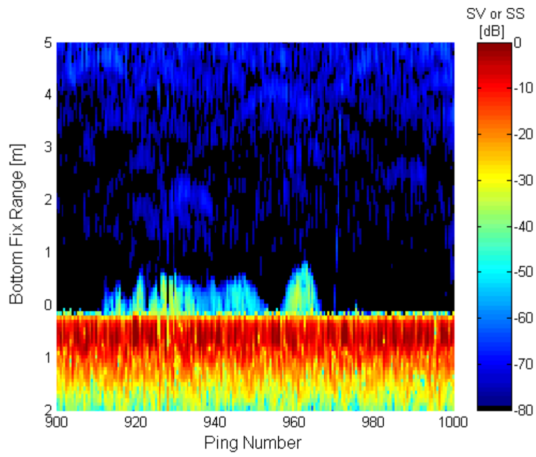

Fig. 4 Measured scattering strength of fish (SV) close to the sea bottom and the SS sea bottom

We can correlate the bottom material estimated by the SS value and bottom fish. From the measured SS value, the bottom type is estimated as sand. The SV values of fish close to the sea bottom are ranging from -60 to -30 dB. From this like display, the assessment of fish and their habitat by bottom material is possible.

We summarize our study as follows :

The SS values can be measured by the bottom echo integration method and the RSS model.

The efficiency of QES to measure scatterings both from fish (SV) and bottom (SS) was shown.

4. Acknowledgment

We acknowledge JSPS-DGHE Core University Program for Fisheries Science for the collaborative research between Tokyo University of Marine Science and Technology and Bogor Agricultural University (Indonesia).

References

1. C. Aoyama, E. Hamada and M. Furusawa : Nippon Suisan Gakkaishi. **65** (1999) 78-85.
2. H.M. Manik, M. Furusawa and K. Amakasu : J. Fish. Sci (submitted).
3. Y. Miyanohana, K. Ishii and M. Furusawa : Nippon Suisan Gakkaishi. **59** (1993) 933-942.
4. C. Aoyama, E. Hamada and M. Furusawa : Nippon Suisan Gakkaishi. **63** (1997) 570-577.

G-4

Proc. Symp. Ultrason. Electron., Vol. 26, (2005) pp. 315-316
16-18 November, 2005

Measurement of Fish School Volume Using Omnidirectional Multi-Beam Sonar, -Scanning Mode and Algorithm-

○Yong Tang, Kohji Iida, Tohru Mukai, (Univ. Hokkaido, Fish. Sci.) Yasushi Nishimori (Furuno Co., LTD)

1. Introduction

Since the pelagic fishes show features that tend to gather into larger stocks and swim near sea surface, it is difficult to investigate by using a quantitative echo sounder with a sharp vertical beam, because a smaller sampling and fish avoid approaching vessels [1]. Therefore, the quantitative sonar (Furuno FSV30 research version) which have omni directional multi-beam was developed, and makes it's possible to measure both the volume backscattering strength (SV) and volume of fish school simultaneously. In this study, the method for estimating the volume of fish school is proposed using various scanning modes of sonar. A computer simulation is conducted to clear the characteristic of measured volume, and the valid selection is discussed for estimating the volume of pelagic fish school.

2. Quantitative sonar and measurement method of fish school

The quantitative sonar is constructed by FSV30 sonar (24kHz), a data recording unit and analysis tool [2]. There are six modes for investigating fish school radiating 64 beams from the spherical transducer, including on cruise scan (DA-1,2,3), beam scan (DA-4,5) and biplane scan (DA-6)(Fig. 1).

The volume can be estimated by integrating the plural projective of echo area on y-z plane along x-axis assigned to the course of ship at mode DA-2(Fig. 2a), expressed as

$$V_S = \int_{x_1}^{x_2} \int_{\theta_{b1}}^{\theta_{b2}} \int_{r_1}^{r_2} r \cos \alpha_x dr d\theta_b dx \qquad (1)$$

where x is cruising distance, r and θ_b are distance and azimuth of echo respectively, α_x is the angle of normal line $\boldsymbol{n}_x$ of scanning plane to the x-axis. Otherwise, at mode DA-1 α_x is zero.

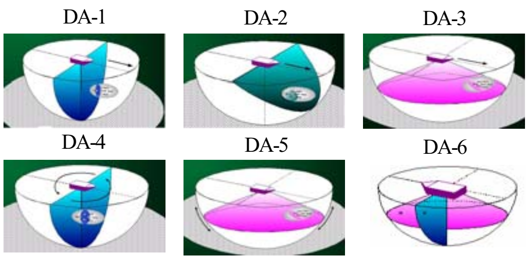

Fig. 1 Schematic diagram of six measurement modes of FSV30 sonar

Yong TANG , tang@echo.fish.hokudai.ac.jp

For the circular mode DA-3, since the fish school is scanned with a conic plane, as shown in Fig. 2b, the angle α_x which between $\boldsymbol{n}_x$ of dS and x-axis can be described as

$$\cos \alpha_x = \cos \theta_b \cos(\pi/2 - \beta) \qquad (2)$$

and the volume can be expressed as

$$V_H = \cos \beta \sin \beta \int_{x_1}^{x_2} \int_{\theta_{b1}}^{\theta_{b2}} \int_{r_1}^{r_2} r \cos \theta_b dr d\theta_b dx \,. \qquad (3)$$

At anchored modes DA-4 or 5, the volume can be estimated by volume integration method (Fig. 2c), with the formula

$$V_{BT} = \int_{\theta_{b1}}^{\theta_{b2}} \int_{\beta_1}^{\beta_2} \int_{r_1}^{r_2} r^2 \,|\sin(\pi/2 - \beta)|\, dr d\beta d\theta_b \qquad (4)$$

where the β and θ_b are zenith and azimuth angle respectively.

Also these formulas could be used for biplane mode in terms of the states of ship at curious or anchor.

3. Simulation of measuring fish school volume

A simulation was conducted for measuring the volume of spherical scatterer. The parameters of acoustic and fish school are showed on Table 1. The insonified acoustic pressure to transducer by individual scatterer of fish school which given a random orientation, and for each beam, can be expressed using the sonar equation as

$$P_{rij}^2(t) = P_0^2 r_i^{-4} 10^{-0.2\alpha r_i} D_{sij}^2 D_{rij}^2 T_{si} u^2 \left(t - \frac{2r_i}{c}\right) \qquad (5)$$

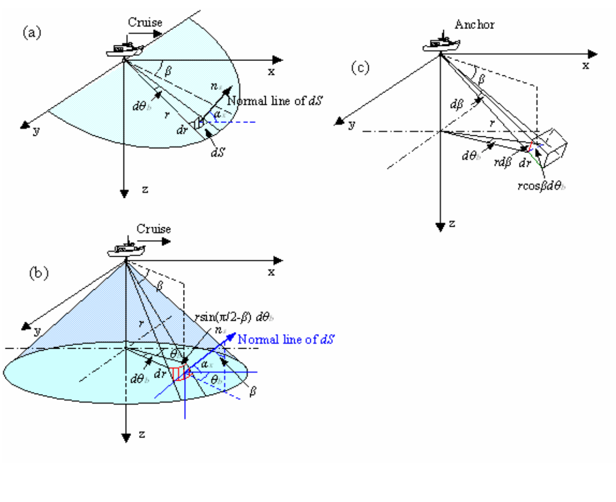

Fig. 2 Integration method for various modes of sonar. a shows integral area at mode DA-1,2, b is for mode DA-3, c shows integral volume of echo at mode DA-4,5.

Table 1 Parameters of sonar and spherical scatterer for computer simulation

Measure mode		mode DA-2,3,4,5
Beam width	transmission	180°×12.4° (360°×11.9° at DA-3,5)
	reception	13.6° (11.9° at DA-2, 4)
Pulse width		2ms
Source level		216dB
Displayed angular resolution		2.86° (5.71°at DA-3, 5)
Displayed range resolution		0.375m
distance at ping ratio		4m
Target strength		-40dB (normal distribution)
Diameter of spherical scatterer		20m
Interval of individual scatterer		1m (random distribution)
Threshold of signal level		-75dB, -70dB, -65dB

where P_0 is source level, r is distance, α is absorption coefficient, D_s and D_r are directivity functions of transmission and reception respectively, u is the function of wave shape [3], i and j are indexes of scatterer and beam respectively. So, the insonified acoustical pressure for each beam could be synthesized by all scatterers, and it can be estimated using the amplitude of carrier signal expressed as

$$P_{Mj}^2(t) = (\sum_{i=1}^{n} P_{rij}(t)\cos\gamma_j)^2 + (\sum_{i=1}^{n} P_{rij}(t)\sin\gamma_j)^2 \qquad (6)$$

where γ is the phase with a random distribution between 0~2π.

The directivity functions of linear and circular transducer are used for transmission and reception approximately. Finally, the P_M is amplified with 20log$r$ TVG to generate the raw SV signal and be displayed the same at a polar coordinate as a sonar.

4. Results

As shown in Fig. 3, we estimated the volume of spherical scatterer which ahead of ship at 30m depth using mode DA-2 and DA-3. The measured volumes normalized theoretical value show the stabilizing feature between 30°~90° tilt angle at mode DA-2 and 30°~60° at mode DA-3. So the small tilt is not useful for measuring the fish ship volume. Also the azimuthal characteristics were examined using 30° tilt angle. The volume can be measured within 30° azimuth from ship head for mode DA-3, and within 70° for mode DA-2(Fig. 4). So mode DA-2 is more available to estimate the volume of pelagic fish school, although mode DA-3 can search for fish school at a broad circular area.

For anchor mode, Fig. 5 shows the precision of estimated volume is higher at mode DA-4 than that at mode DA-5. Furthermore, the anchor mode has a better precision than that at cruise mode (Fig. 3, 4, 5).

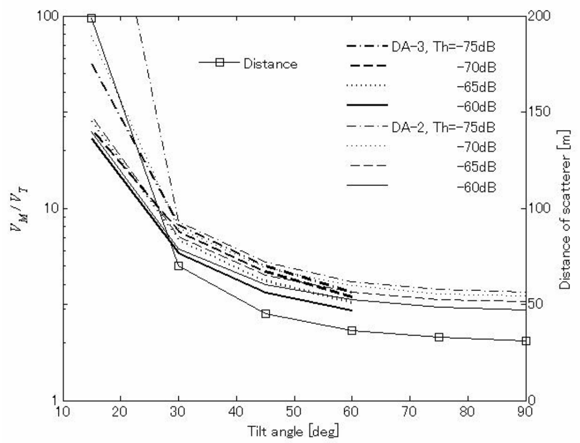

Fig. 3 Measured volumes of spherical scatterer at 30m depth using various tilt angles and threshold of signal level at mode DA-2, 3

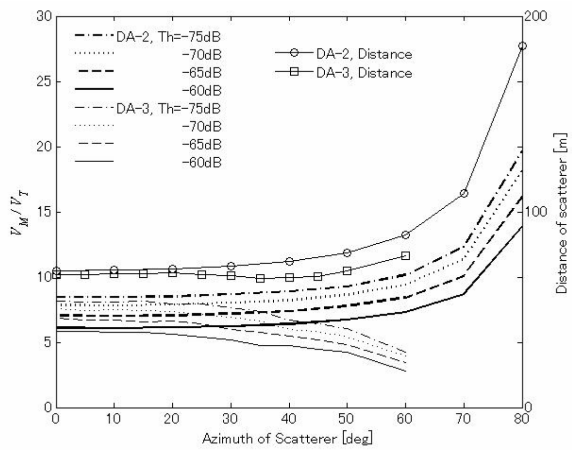

Fig. 4 Measured volumes of spherical scatterer at 30m depth and various azimuths using 30° tilt angle at mode DA-2 ,3

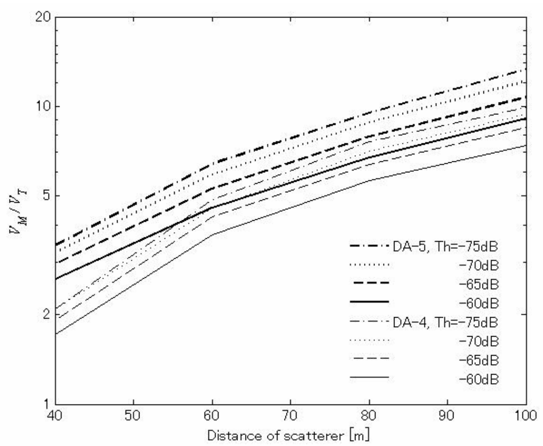

Fig. 5 Measured volume of spherical scatterer at 30m depth and various distances using mode DA-4 and DA-5

Reference

1. F.Gerlotto, J. Castillo, A. Saavedra, M.Barbieri, M.Espejo and P.Cotel: ICES J. Mar. Sci. **61** (2004)1120.
2. K. Iida, Y. Tang, T. Mukai and Y. Nisimori: OCEANS'04, Proceeding, (2004) 401.
3. M.Furusawa, K. Isii and Y. Maniwa: J. Acoustical Soc. Jpn. **42** (1986) 2. (in Japanese with English captain)

H-1

Proc. Symp. Ultrason. Electron., Vol. 26, (2005) pp. 317-318
16-18 November, 2005

Integrated Ultrasonic Transducers Made by Sol-Gel Spray Technique

◎ Makiko Kobayashi and Cheng-Kuei Jen
(Industrial Materials Institute, National Research Council of Canada)

1. Introduction

In-situ structural health monitoring, on-line and off-line nondestructive testing (NDT), and on-line real-time diagnosis of industrial material processing are desired to identify, characterize, assess the voids, defects and damages in many materials and structures for applications in aerospace vehicles, marine vessels, automobiles, nuclear power plants, gas, water and oil pipelines, etc and also ensure the quality of manufactured products of polymer and metal extrusion and molding (or casting), etc [1-3]. Ultrasonic techniques are frequently used for these purposes because of their subsurface inspection capabilities, fast inspection speed, simplicity, cost effectiveness and ease of operation. The common limitations of the use of the conventional and non-integratable UTs are (1) the requirement of couplant, (2) complicated for curved surfaces, (3) difficult for pulse-echo mode and (4) not efficient for temperature higher than 60°C. In this investigation, our technology focuses on optimizing the fabrication process of sol-gel sprayed piezoelectric thick (>40 μm) film UTs with handheld equipments and no furnaces that are significantly different from the fabrication method reported in [4] in order to integrate them onto flat and curved surfaces of metal and graphite/epoxy (Gr/Ep) composites at the desired sensor locations without the displacement of and harming substrates.

2. Fabrication and characterization of UTs

Bismuth titanate (BIT) or lead zirconate titanate (PZT) powders were purchased with a particle size distribution of about 80 and 2 μm, respectively. BIT is chosen because of high 675°C Curie temperature (T_c) and reasonable piezoelectric strength, which are suitable for high (>350°C) temperature operations. PZT is chosen because of relatively high T_c ~350°C, high piezoelectric strength and dielectric constant. The powders were dispersed into PZT sol-gel solution by ball milling method to achieve the paint. The final BIT or PZT powders were estimated of sub-micron size. An airbrush was then used to spray the sol-gel composite directly onto steel, stainless steel (SS), Gr/Ep substrates, etc. In this way the films can be produced at desired locations through a shadow mask onto the samples. After spray coating, thermal treatments such as drying and firing were carried out using a heat gun or a gas torch. Multiple layers were made in order to reach the desired thickness and frequency (1 – 30 MHz) of interest. The films were then electrically poled using the corona discharging technique. For corona poling, the top surface temperature of the substrate was kept around 300 and 120°C, respectively. A high positive voltage supplied from a 28 kV DC power supply was fed into a thin and sharp needle located several centimeters above the films coated on the substrates, which serves as the ground electrode. The poling time was about 10 minutes. Finally, silver paste painting was used to form the top electrode at room temperature. This convenient approach makes the selection of electrode size, i.e. the sensor size, simple. The silver paste had been tested and its operating temperature could be up to at least 200°C. It is noted that PZT sol-gel solution contributed as bonding material between the BIT or PZT powder and the substrates. The dielectric constants of the BIT/PZT and PZT/PZT films were 15-90 and 60-340, respectively, measured by a Hewlett Packard 4192A LF Impedance Analyzer at 1 kHz and the difference in each UT comes from the heating methods used. The measured piezoelectric coupling constant k_t was 4 and 24% for BIT/PZT and PZT/PZT film UT, respectively.

3. Ultrasonic performances of UTs

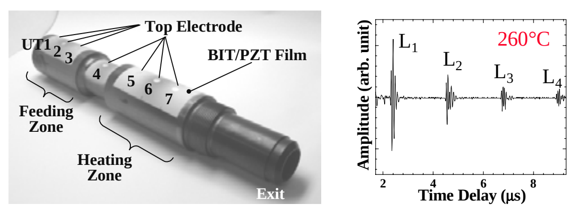

(a) (b)

Fig. 1 (a) Integrated 90μm BIT/PZT composite film UT arrays on barrel for diagnostics of micro-molding and (b) its ultrasonic performance in time domain at 260°C.

Figure 1a shows seven BIT/PZT composite film UTs (UT1-7) fabricated directly on the external surface of the cylindrical barrel for a micro-molding device; Microsystem50 from Battenfeld, Austria. The diameter of the top electrode was 5 mm, which is the active area size of the UT. The length of the steel barrel was 265mm, the internal diameter was 14 mm, and the external diameters at the areas of UT1-3, 5-7 and at that of UT4 were 40 mm and 30 mm, respectively. In Fig.1b L^1, L^2, L^3 and L^4 are respectively the 1st, 2nd, 3rd and 4th round-trip reflected echoes through the thickness of the barrel wall at UT6 location. The pulse-echo mode was used. The measured center frequency, 6 dB bandwidth and signal-to-noise ratio (SNR) of the L^1, by the UT6 at 260°C, were 13MHz, 13MHz and 31dB, respectively. The SNR is defined as the ratio of the amplitude of the first echo

L^1 over that of the signals, which are undesired, between the echoes traversing back and forth in the substrate. The amplitude and time delay variation of L^1 can be used for monitoring the properties such as viscosity, filler composition, melt quality, average temperature etc. of molten polymer in the gap between the inner barrel wall and the rotation screw inside the barrel. The performance of UT1-7 array was almost the same. The BIT/PZT UT can operate up to more than 440°C [3]. The integrated UTs have also been deposited onto aluminum and titanium substrates and their performance is equally to that shown in Fig.1b.

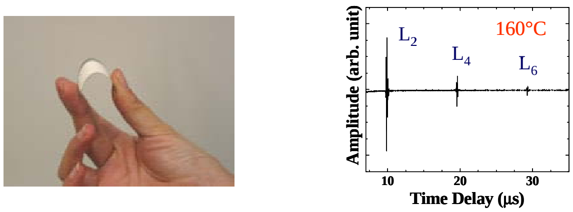

(a) (b)

Fig. 2 (a) Integrated 40µm PZT/PZT composite UT on a 75µm thick SS membrane and (b) its ultrasonic performance in time domain at 160°C when attached to a steel pipe with outer diameter of 102 mm.

Flexible ultrasonic transducers (UTs) consisting of a metal foil, a piezoelectric ceramic film and a top electrode are also developed. Here, a 75µm thick SS, a 40 µm thick PZT/PZT composite film and silver paste was chosen as metal foil, piezoelectric film and top electrode materials, respectively. The SS foil serves both as substrate and bottom electrode. The flexibility is realized owing to the porosity of piezoelectric film and the thinness of metal foil as shown in Fig.2a. This flexible UT was attached by a mechanical holder onto the steel pipe with outer diameter of 102 mm, inner diameter of 46 mm, and a length of 205 mm. A viscous oil ultrasonic couplant was placed between the SS foil and the outer surface of the pipe. The pulse-echo mode was used. The steel pipe was heated up by a hot plate. The ultrasonic performance in the time domains at 160°C is shown in Fig.2b and L_2, L_4 and L_6 are respectively the 1st, 2nd and 3rd round-trip reflected echoes through the thin SS foil, couplant and the wall thickness of the steel pipe. The measured SNR of L_2 was 28 dB. Thus in-situ or off-line NDT using such flexible UTs attached or glued to substrates are feasible and convenient. In addition, the test results show that this particular flexible UT can be bended into a curvature of a radius of 15 mm without damaging the ultrasonic performance. It is expected that further reduction of the thickness of metal foil and piezoelectric composite film will enhance the flexibility.

Gr/Ep composites are now increasingly used for large structures due to their high strength over weight ratio. In the manufacturer's recommended curing technique the highest temperature in the curing stage was only 176°C and the duration was two hours. For this kind of substrate the PZT/PZT composite film UT was fabricated with all the thermal treatment carried out by a heat-gun, which produced gentle heat in order not to harm the Gr/Ep substrate. A 70µm thick PZT/PZT film UT deposited on such a composite of 12.7 mm thick is shown in Fig.3a.This Gr/Ep has sufficient conductivity to serve as the bottom electrode of the UT. Figures 3b shows the ultrasonic performance of this integrated UT operated in pulse-echo mode in the time domain at 22°C. The measured SNR, center frequency and 6 dB bandwidth of ultrasonic signal L^1 were 15 dB, 1.6 MHz and 1.5 MHz, respectively. The low center frequency and bandwidth were caused by the high ultrasonic attenuation within the thick specimen. The result demonstrates the capability of integrated UT for in-situ real-time NDT application of Gr/Ep substrates.

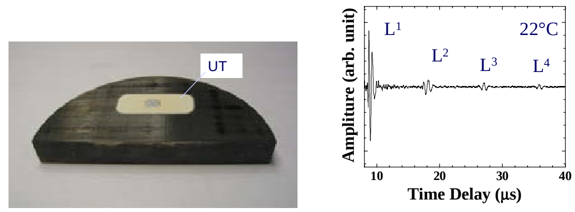

(a) (b)

Fig. 3 (a) Integrated 70 µm thick PZT/PZT composite film UT on a 12.7 mm thick Gr/Ep composite and (b) its ultrasonic performance in time domain at 22°C.

4. Conclusions

Integrated UTs have been developed for in-situ structural health monitoring, on-line and off-line NDT and on-line real-time manufacturing process monitoring. Fabrication techniques focused on the use of handheld equipments to perform sol-gel spray coating including using a torch or heat gun to carry out drying and firing, poling and electrode fabrication in the production of these UTs. These UTs can be fabricated in arrays and operated at desired NDT sites even of curved surfaces at high temperatures. Metal and Gr/Ep composites substrates were used.

Acknowledgment

The authors are grateful to H. Hébert, Y. Ono, S.B. Nguyen and J.-F. Moisan for their technical assistance.

References

1. T. Arakawa, K. Yoshikawa, S. Chiba, K. Muto, and Y. Atsuta : Nondestr. Test. Eval., **7** (1992) 263.
2. H. Karasawa, M. Izumi, T. Suzuki, S. Nagai, M. Tamura, and S. Fujimori : Journal of Nuclear Science and Technology, **37** (2000) 769.
3. M. Kobayashi and C.-K. Jen : Smart Mater. Struct., **13** (2004) 271.
4. D. Barrow, T.E. Petroff, R.P. Tandon, R.P. and M. Sayer : J. Apply. Phys., **81** (1997) 876.

H-2

Proc. Symp. Ultrason. Electron., Vol. 26, (2005) pp. 319-320
16-18 November, 2005

Evaluation of closed cracks by nonlinear ultrasonic phased array

◎Yoshikazu Ohara, Ryouta Sasaki, Toshihiro Ogata, Tsuyoshi Mihara and Kazushi Yamanaka
(Tohoku Univ.)

1. Introduction

Although closed cracks can propagate under applied stress resulting in catastrophic accidents e.g. in atomic power plants, it is difficult to detect them since the intensity of scattering waves is much lower than that from open cracks. Recently, nonlinear ultrasound is expected to have a potential of detecting and evaluating them, and subharmonic wave [1,2] with half-frequency of input signal is particularly useful because of its selectivity for cracks. Thus far, we have observed subharmonics in closed cracks and developed a model to analytically reproduce the observed waveform [3]. Also, we observed a peculiar wave at the tail part of received wave and explained it as a free oscillation of cracks [4]. However, fast and reliable test was not realized due to the lack of imaging capability.

In this study, we propose a novel nonlinear ultrasonic phased array (PA) to image closed and open cracks using digital signal processing (DSP) for filtering at linear and nonlinear frequency. To interpret the results and ascertain the mechanism of subharmonic resonance [5,6], we examine the frequency dependence of subharmonic generation in closed cracks.

2. Nonlinear Ultrasonic Phased Array

As a fast and reliable method for the evaluation of closed cracks, we constructed nonlinear ultrasonic PA with DSP, as shown in Fig. 1. Since transducers in conventional PA can not generate an intense ultrasound required in nonlinear testing of cracks, we developed a LiNbO3 single crystal transmitter, which can endure against high voltage input, with an appropriate wedge made of polyimide. It is driven by a short tone burst amplified by a gated amplifier, whereas the PA with 32 elements at 5 MHz center frequency is utilized as a receiver. Before the process of imaging, DSP extracts linear or nonlinear components. For example, closed cracks can be imaged by DSP which passes only subharmonic or superharmonic component. On the other hand, open cracks can be imaged by DSP which passes only fundamental components.

To realize such a measurement system, the calculation of a time shift of waveforms arriving from focal point is required, since the transmitter and receiver are separated contrary to conventional PA. The formulation of the propagation time and time delay has been already reported in Ref. [7].

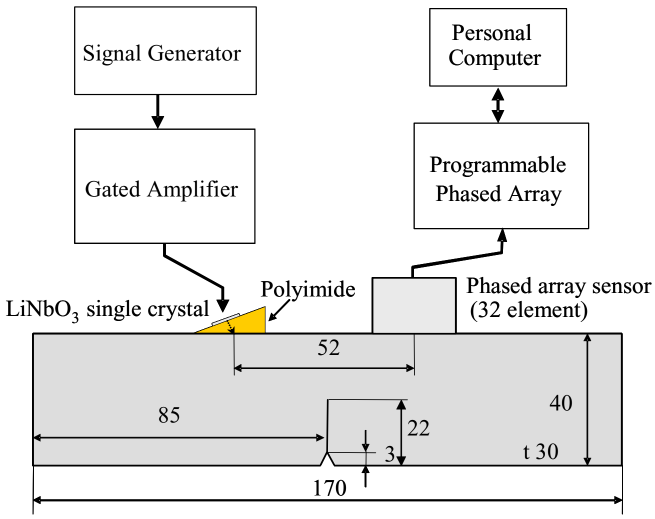

Fig. 1. Nonlinear ultrasonic phased array.

3. Results and Discussions

We prepared well-defined fatigue cracks in an aluminum alloy (A7075). The crack was extended from a notch in a three-point bending fatigue test under two conditions in Table I [8].

Table I. Maximum and minimum stress intensity factor for fatigue test.

	K_{max} (kgf/mm$^{3/2}$)	K_{min} (kgf/mm$^{3/2}$)
Sample A	17	2
Sample B	14	2

Figure 2 shows a linear image for sample A, where scan area is from 14 to 50 mm (2 mm step) in depth and from 10 to 60° (2° step) in angle. It is confirmed that the position of crack tip in the image agreed with that of the actual crack tip. Therefore, the validity of the developed ultrasonic PA was verified.

Next, we examined the frequency dependence of subharmonic generation in closed crack of sample B by sweeping the input frequency.

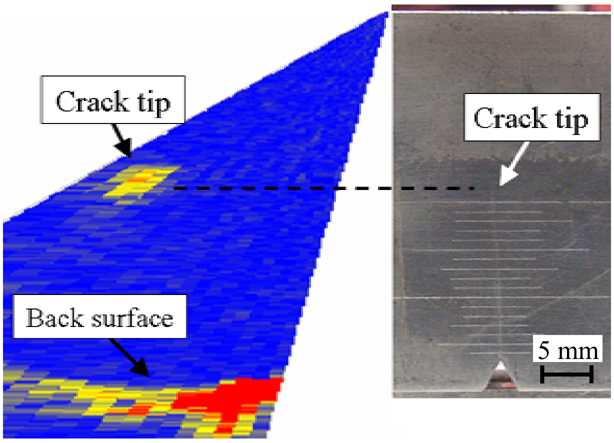

Fig. 2. Comparison of linear image obtained by nonlinear ultrasonic PA with actual fatigue crack of sample A.

A tone-burst of 3 cycles with peak-to-peak displacement amplitude of 20 nm was used. The parameters of the band pass filter are shown in Table II.

As shown in Figs. 3(b) and 3(c), a clear difference between 7.2 and 10.2 MHz was observed, whereas crack tip was not observed in linear image of Fig. 3(a) probably because the crack is closed. In Fig. 3(c), the subharmonic waves were generated not only at the crack tip but also at a part below crack tip. On the other hand, it was generated only at crack tip in Fig. 3(b). Thus, the frequency dependence of subharmonic generation in closed cracks was observed for the first time by applying the nonlinear ultrasonic PA to the well-defined crack. As a means of interpreting the frequency dependence of subharmonic generation in closed cracks, we proposed a new concept [6] as follows.

In medical ultrasonic imaging, it has been clarified that the subharmonic generation at micro bubble is maximized when the input frequency is close to twice the resonant frequency of bubble [5]. Accordingly, in the case of subharmonic generation in closed cracks, the intensity will take a maximum when the input frequency is close to twice the resonant frequency of closed crack.

In linear ultrasound, the frequency dependence of scattered wave from a crack was examined by the boundary integral equation method and the resonant condition was shown that crack length is close to the odd multiple of a quarter Rayleigh wavelength [9]. In the case of closed cracks, although the same resonant vibration as the above is not excited, the subharmonic vibration can be resonantly excited if the input frequency is close to twice the resonant frequency of the crack. On the basis of this concept, the local variation in Figs. 3(b) and 3(c) may be interpreted as the frequency dependence of subharmonic excitation of a part of the closed crack with dimension comparable to the Rayleigh wavelength in submillimeter to millimeter range.

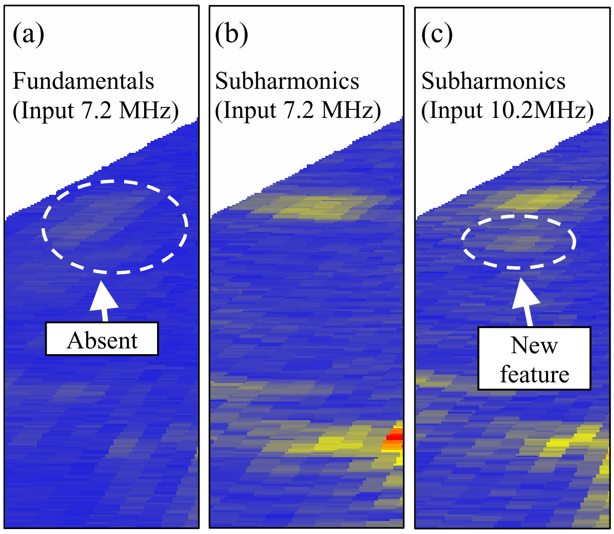

Fig. 3. Images of fatigued crack tips in sample B obtained by nonlinear ultrasonic PA with DSP.

Table II. Cutoff frequency, attenuation rate and stopband attenuation of selected band pass filters.

Frequency to extract (MHz)	Cutoff frequency (MHz)		Attenuation Rate (dB/octave)		Stopband Attenuation (dB)
7.2	6.2	8.2	281	261	60
3.6	2.6	4.6	170	121	60
5.1	4.1	6.1	217	177	60

4. Conclusions

We proposed a novel nonlinear ultrasonic phased array. We expect that this approach is significantly useful in detecting and quantitatively evaluating closed cracks. In our future works, we will quantitatively verify the model for subharmonic generation.

References

1. A. Moussatov, V. Gusev and B. Castagnede : Phys. Rev. Lett. **90-12** (2003) 124301-1.
2. I. Solodov, J. Wackerl, K. Pfleiderer and G. Busse : Appl. Phys. Lett. **84** (2004) 5386.
3. K. Yamanaka, T. Mihara and T. Tsuji : Jpn. J. Appl. Phys. **43-5B** (2004) 3082.
4. R. Sasaki, T. Ogata, Y. Ohara, T. Mihara and K. Yamanaka : Jpn. J. Appl. Phys. **43-5B** (2004) 3082.
5. P. M. Shanker, P. D. Krishna and V. L. Newhouse : J. Acoust. Soc. Am. **106** (1999) 2104.
6. K. Yamanaka, R. Sasaki, T. Ogata, Y. Ohara and T. Mihara : Rev. Prog. QNDE (2006), submitted.
7. Y. Ohara, T. Mihara and K. Yamanaka : The third US-Jpn. Symp. in NDE, (2005) 229.
8. M. Akino, T. Mihara and K. Yamanaka : Rev. Prog. QNDE **23B** (2004) 1256.
9. D. E. Budreck and J. D. Achenbach : J. Appl. Mech. **55** (1988) 405.

H-3

Proc. Symp. Ultrason. Electron., Vol. 26, (2005) pp. 321-322
16-18 November, 2005

On the Photoacoustic Nondestructive Instrumentation with a Line-Focus Laser Beam and a Planar Specimen Combination

○Tsutomu Hoshimiya[1], Mika Hatake-yama, Naoki Ohtaki and Haruo Endoh
(Tohoku Gakuin Univ., Fac. Eng.)

1. Introduction

In the field of photoacoustic (PA) imaging, a point-focus (PF) laser beam is dominantly used to make thermal or acoustic image for inspection of the specimens such as welded steel plates [1]. However, a line-focus (LF) laser beam is also useful to achieve quick inspection of the solid specimen, as pointed by the first author as a Japanese patent [2].

In this paper, the inspection of the welded steel plates by rotating a LF laser beam around the center of the welded region was done. The PA signal dependence on rotation angle is measured for inspection [3]. The feasibility to apply the LF laser beam to achieve photoacoustic tomography (PAT) [4] is also described.

2. Experimental apparatus

The PA imaging system is similar to that of the Photoacoustic microscope (PAM). The PA signal was detected by a highly sensitive condenser microphone (Brewer & Kaejer 4166), and it was processed with a lock-in amplifier, reconstructed as amplitude and phase images, and displayed and recorded by a computer. Amplitude and phase PA images were stored as spread-sheet data, and those are available to be processed such as integration or noise reduction easily.

A laser diode (LD) pumped YAG laser was used as an optical excitation source with a LF beam shape. Its beam was previously diffused with a concave lens and then focus as a line image by a cylindrical lens. Laser beam size was 8 mm in length was 8 mm in length and 1 mm in width.

---

[1] e-mail: tpth@tjcc.tohoku-gakuin.ac.jp

The specimen used was a pair of welded steel plates with a thickness of 1.5 mm (maximum turn-on current of welding: 8kA). A drill hole was made by drilling with a diameter 1.5mmϕ along interface surface of the welded two plates from the edge of one side to the center of the specimen.

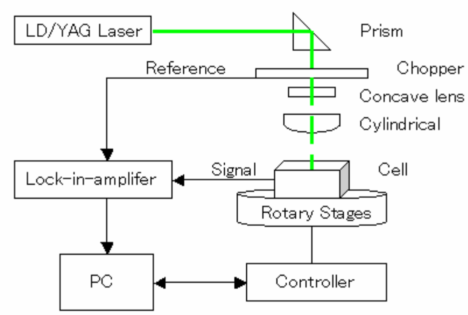

Fig. 1 Basic experimental setup.

3. Experimental results

The step of the rotation angle and the time needed for a measurement were one degree and seven minutes, respectively. Laser power and modulation frequency were 28mW and 8 Hz, respectively. The thermal diffusion length was about 77 μ m such that it is enough for the thermal wave to reach the drilled hole made at the welded interface.

The time needed for inspection of the welded specimen by the use of a point-focus laser beam with the resolution of 50 x 50 pixels was about 30 minutes so that a simple inspection using a LF laser beam shortened measurement time in about four times.

The dependence of the obtained PA signal on the rotation angle was shown in Fig. 2. In Fig. 2 (a), PA signal dependence of the specimen without an artificial undersurface defect is shown, whereas that corresponding to the specimen with undersurface defect is shown in Fig. 2 (b). It shows the PA signal maximum around the angle of 90 degrees, at which the overlap of the LF laser beam and a drill hole maximizes.

4. Discussion

The PA signal generated in the solid specimens in most case is proportional to the absorption coefficient of the specimen α and laser intensity I_0, and inversely proportional to the modulation frequency f. If we irradiate plane solid specimen with a LF laser beam, the generated PA signal is proportional to the summation of the absorption coefficient of the irradiated area so that this combinations useful to realize two-dimensional (2D) CT PA imaging or 2D-PAT as pointed in ref [2].

The feasibility to use a LF laser beam to realize non-contact photothermal radiometry, such as active thermography, is also pointed out in the patent [2].

5. Conclusion

Simple nondestructive inspection (NDI) of the welded specimen with an artificially made was achieved by rotating a LF laser beam. Combination of LF laser beam with CT technique is the next step purpose of the current study.

Acknowledgement

The first author (TH) is grateful to Suzuki Motor Company for the financial support and sample preparation.

References

[1]K. Miyamoto, M. Suzuki, T. San-nomiya, T. Hoshimiya and N. Chubachi: Jpn. J. Appl. Phys., 43, 3107 (2004).

[2]T. Hoshimiya: Japanese patent, submitted No. 2005-206177（2004.3）.

[3] T. Hoshimiya and M. Suzuki : Abstract of 2005 IEEE Ultrasonics Symposium, (2005. 9, Rotterdam).

[4] X. Wang, Y. Pang, G.. Ku, G.. Stoica, and L. V. Wang: Opt. Lett., 28, (2003) 1739.

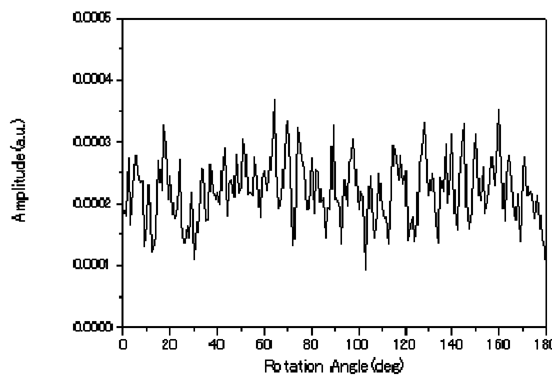

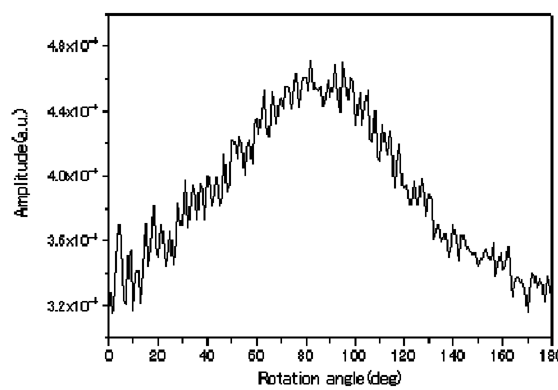

Fig. 2 PA signal dependence on rotation angle: (a) specimen without undersurface defect(upper), (b) specimen with undersurface defect (lower).